frontiers | Research Topics

# Processes and management of altered estuaries and deltas in the anthropocene

**Edited by**
Guan-hong Lee, Joseph Carlin, Daidu Fan and Timothy Dellapenna

**Published in**
Frontiers in Marine Science

ISSN 1664-8714
ISBN 978-2-8325-3218-8
DOI 10.3389/978-2-8325-3218-8

## About Frontiers

Frontiers is more than just an open access publisher of scholarly articles: it is a pioneering approach to the world of academia, radically improving the way scholarly research is managed. The grand vision of Frontiers is a world where all people have an equal opportunity to seek, share and generate knowledge. Frontiers provides immediate and permanent online open access to all its publications, but this alone is not enough to realize our grand goals.

## Frontiers journal series

The Frontiers journal series is a multi-tier and interdisciplinary set of open-access, online journals, promising a paradigm shift from the current review, selection and dissemination processes in academic publishing. All Frontiers journals are driven by researchers for researchers; therefore, they constitute a service to the scholarly community. At the same time, the *Frontiers journal series* operates on a revolutionary invention, the tiered publishing system, initially addressing specific communities of scholars, and gradually climbing up to broader public understanding, thus serving the interests of the lay society, too.

## Dedication to quality

Each Frontiers article is a landmark of the highest quality, thanks to genuinely collaborative interactions between authors and review editors, who include some of the world's best academicians. Research must be certified by peers before entering a stream of knowledge that may eventually reach the public - and shape society; therefore, Frontiers only applies the most rigorous and unbiased reviews. Frontiers revolutionizes research publishing by freely delivering the most outstanding research, evaluated with no bias from both the academic and social point of view. By applying the most advanced information technologies, Frontiers is catapulting scholarly publishing into a new generation.

## What are Frontiers Research Topics?

Frontiers Research Topics are very popular trademarks of the *Frontiers journals series*: they are collections of at least ten articles, all centered on a particular subject. With their unique mix of varied contributions from Original Research to Review Articles, Frontiers Research Topics unify the most influential researchers, the latest key findings and historical advances in a hot research area.

Find out more on how to host your own Frontiers Research Topic or contribute to one as an author by contacting the Frontiers editorial office: frontiersin.org/about/contact

# Processes and management of altered estuaries and deltas in the anthropocene

**Topic editors**

Guan-hong Lee — Inha University, Republic of Korea
Joseph Carlin — California State University, Fullerton, United States
Daidu Fan — Tongji University, China
Timothy Dellapenna — Texas A&M University at Galveston, United States

**Citation**

Lee, G.-h., Carlin, J., Fan, D., Dellapenna, T., eds. (2023). *Processes and management of altered estuaries and deltas in the anthropocene*. Lausanne: Frontiers Media SA. doi: 10.3389/978-2-8325-3218-8

# Table of contents

frontiers | Frontiers in Marine Science

TYPE Editorial
PUBLISHED 27 July 2023
DOI 10.3389/fmars.2023.1220155



OPEN ACCESS

EDITED AND REVIEWED BY
Charitha Bandula Pattiaratchi,
University of Western Australia, Australia

*CORRESPONDENCE
Guan-hong Lee
ghlee@inha.ac.kr

RECEIVED 10 May 2023
ACCEPTED 19 May 2023
PUBLISHED 27 July 2023

CITATION
Lee G, Carlin J, Fan D and Dellapenna T (2023) Editorial: Processes and management of altered estuaries and deltas in the Anthropocene.
*Front. Mar. Sci.* 10:1220155.
doi: 10.3389/fmars.2023.1220155



# Editorial: Processes and management of altered estuaries and deltas in the Anthropocene

Guan-hong Lee[1]*, Joseph Carlin[2], Daidu Fan[3] and Timothy Dellapenna[4]

[1]Department of Oceanography, Inha University, Incheon, Republic of Korea, [2]Department of Geological Sciences, California State University, Fullerton, CA, United States, [3]Sedimentology School of Ocean and Earth Sciences, Tongji University, Shanghai, China, [4]Department of Marine and Coastal Environment Science, Texas A&M University at Galveston, Galveston, TX, United States

KEYWORDS

**altered estuaries, Anthropocene, delta, process, management, estuarine dam, reclamation, Holocene**

Editorial on the Research Topic
Processes and management of altered estuaries and deltas in the Anthropocene

An estuary is an environment that provides various ecosystem services of both ecological and commercial value (Kennish, 2002). Estuaries and deltas have also been centers of human settlement due to their high biological productivity, protection from the sea, and the confluence of rivers with access to inland navigation. As a result, estuaries and deltas are subject to a wide range of human impacts, as many cities and ports around the world are constructed very close to estuaries (Kennish, 2017; McGranahan et al., 2007). Large-scale engineering projects, such as dredging, estuarine dams, and land reclamation, have significantly altered the natural properties of estuaries and deltas, leading to changes in river discharge, tidal patterns, and sediment dynamics. These alterations have caused severe ecosystem degradation over the last century (Lotze et al., 2006). Given their ecological and commercial value, it is critical that we manage estuaries and deltas in a way that balances the needs of human populations with the needs of these vital ecosystems.

Estuarine and deltaic processes are largely controlled by the interaction between climate-related sea level changes, environmental factors, such as the oceanographic regime, sediment availability, and tectonics, as well as anthropogenic impacts (Kench, 1999; van der Wal et al., 2002; Mulligan et al., 2019; Chang et al., 2020; Figueroa et al., 2020). While human impacts are indisputable in the 21th century during the Anthropocene, human influence has been also increasingly evident in the Holocene. In recent decades, efforts to restore altered estuaries and deltas have increased and it is imperative to understand the nature of the processes operating in altered estuaries and deltas and their responses to modifications. Therefore, the goal of this Research Topic is to share our increased knowledge on the nature of the altered processes, not only in the Anthropocene but also in the natural processes and altered processes in the Holocene.

Even in the Holocene, estuaries and deltas were influenced by human impact although not as significant as those during the Anthropocene. Through geochemical and grain size analysis of a long sediment core spanning more than 5500 years, Zou et al. found that the

construction of an ancient dam stabilized the sedimentary environment by regulating flash floods and providing water supply in Southern China. Guo et al. then reconstructed the human adaptations to environmental change by examining the salt production site on the southern coast of Laizhou Bay in Eastern China. On the other hand, by examining the evolutionary history of mud deposits using long cores through Holocene strata in the northwestern shelf of the South China Sea, Li et al. found that thick mud deposits initiated after 3 ka BP due to the enhanced sediment fluxes and strengthened winter monsoon. In recent years over the past millennium, heavy metals were enriched due to human activities.

In addition to human influence in the Holocene, we had contributions to the methods to reconstruct past environments. By using magnetic records of surficial sediment in the Yangtze river basin, Liu et al. found matching magnetic susceptibility between the upper basin and the lower estuary providing insights into the source-to-sink process of clastic materials. Then, Jiang et al. established, by examining the spatial distribution and composition of alive and dead benthic foraminifera (BF) in relation to different water masses off the Changjiang estuary, that taphocoenose BF in core sediments can be used to reconstruct the past marine environments. On the other hand, Song et al. reported that the shallow biogenic gas seepage in the Yangtze subaqueous delta and Hangzhou Bay is increasing due to global warming and seabed erosion related to sediment deficit.

In this Research Topic, several papers dealt with the sedimentary and geochemical responses due to the construction of an estuarine dam. Extending their earlier work on the impact of estuarine dams on the estuarine parameter space and sediment flux decomposition, Figueroa et al. examined the effect of different dam locations and freshwater discharge for four estuarine types (strongly stratified, partially mixed, periodically stratified, and well-mixed). The estuarine dam location affected the tide-dominated estuaries, while the discharge interval affected the river-dominated estuaries. Through a COAWST numerical modeling study, Chang et al. found that the impacts of the estuarine dam were highly significant over the impacts due to the land reclamation at least at the altered Nakdong estuary of Korea. Lee and An found that ammonium regeneration and uptake rates were high at the altered Yeongsan estuary by an estuarine dam. Small-size bacteria were responsible for most of the ammonium regeneration, not zooplankton because intermittent freshwater discharge prevented stable zooplankton community development. Relatively high ammonium regeneration and uptake rates indicate that the altered Yeongsan estuary has changed to an optimum condition for high ammonium regeneration as the turbidity decreased and water residence time increased after the construction of the estuarine dam. Finally, Zeng et al. tested the effectiveness of three Marine Protected Areas (MPAs) in the Yangtze River delta with the modified framework of potential drivers and conservation outcomes and found that MPAs that showed satisfactory environmental performance and that public awareness, participation, and regular monitoring and assessment can further improve management and environmental performance.

In conclusion, this Research Topic provided insight into the processes of human alterations in estuaries and deltas and data to support future sustainable management. The research focused on the nature and impacts of human alterations and subsequent reconstruction of the environments during the Holocene. In more recent years of the Anthropocene, environmental degradation due to human alterations is also becoming of greater interest. While we are understanding and improving our environment, it is suggested to require better public awareness regarding modern, rapidly changing estuaries and deltas.

## Author contributions

All authors listed have made a substantial, direct, and intellectual contribution to the work and approved it for publication.

## Funding

This research was supported by Basic Science Research Program (2017R1D1A1B05033162) and Center for Anthropocene Studies (2018R1A5A7025409) through the National Research Foundation of Korea (NRF).

## Acknowledgments

We thank all the authors for their contributions to this Research Topic. We are also thankful to all the reviewers who took their valuable time for providing constructive comments.

## Conflict of interest

The authors declare that the research was conducted in the absence of any commercial or financial relationships that could be construed as a potential conflict of interest.

## Publisher's note

# References

Chang, J., Lee, G., Harris, C. K., Song, Y., Figueroa, S. M., Schieder, N. W., et al. (2020). Sediment transport mechanisms in altered depositional environments of the anthropocene nakdong estuary: a numerical modeling study. *Mar. Geol.* 430, 106364. doi: 10.1016/j.margeo.2020.106364

Figueroa, S. M., Lee, G., Chang, J., Schieder, N. W., Kim, K., and Kim, S. Y. (2020). Evaluation of along-channel sediment flux gradients in an anthropocene estuary with an estuarine dam. *Mar. Geol.* 429, 106318. doi: 10.1016/j.margeo.2020.106318

Kench, P. S. (1999). Geomorphology of Australia estuaries: review and prospect. *Austral. Ecol.* 24, 367–380. doi: 10.1046/j.1442-9993.1999.00985.x

Kennish, M. J. (2002). Environmental threats and environmental future of estuaries. *Environ. Conserv.* 29, 78–107. doi: 10.1017/S0376892902000061

Kennish, M. J. (2017). "Estuaries: anthropogenic impacts," in *Encyclopedia of coastal science*. Eds. C. Finkl and C. Makowski (Springer). doi: 10.1007/978-3-319-48657-4_140-2

Lotze, H. K., Lenihan, H. S., Bourque, B. J., Bradbury, R. H., Cooke, R. G., Kay, M. C., et al. (2006). Depletion, degradation, and recovery potential of estuaries and coastal seas. *Science.* 312, 1806–1809. doi: 10.1126/science.1128035

McGranahan, G., Balk, D., and Anderson, B. (2007). The rising tide: assessing the risks of climate change and human settlements in low elevation coastal zones. *Environ. Urban.* 19, 17–37. doi: 10.1177/0956247807076960

Mulligan, R. P., Mallinson, D. J., Clunies, G. J., Rey, A., Culver, S. J., Zaremba, N., et al. (2019). Estuarine responses to long-term changes in inlets, morphology, and sea level rise. *J. Geophys. Res. Ocean.* 124, 9235–9257. doi: 10.1029/2018JC014732

van der Wal, D., Pye, K., and Neal, A. (2002). Long-term morphological change in the ribble estuary, northwest England. *Mar. Geol.* 189, 249–266. doi: 10.1016/S0025-3227(02)00476-0

frontiers | Frontiers in Marine Science

ORIGINAL RESEARCH
published: 14 April 2022
doi: 10.3389/fmars.2022.873220

# Environmental Evolution and Human Adaption Recorded From a Salt Production Site at the Coastal Plain of Laizhou Bay, China

*Yuanyuan Guo[1]*, Longjiang Mao[2]*, Likai Zhu[1] and Duowen Mo[3]*

*[1] Shandong Provincial Key Laboratory of Water and Soil Conservation and Environmental Protection, College of Resources and Environment, Linyi University, Linyi, China, [2] School of Marine Sciences, Nanjing University of Information Science and Technology, Nanjing, China, [3] Laboratory for Earth Surface Process, Ministry of Education, College of Urban and Environmental Sciences, Peking University, Beijing, China*

The southern coast of the Laizhou Bay is considered as one of important areas for the origin and development of sea salt production in Eastern China. Archaeologists have collected rich materials to better understand history of salt production in the region, but how environmental change influences early salt production is still unknown. Here we collected samples at the Shuangwangcheng (SWC) site in the southern plain of Laizhou Bay. We conducted grain size, mollusk and foraminifera analysis to examine the evolution of sedimentary environment and restored the human adaptions to environmental change. The results showed that the sedimentary environment of study area was lower tidal flat during 6400~5900 yr BP as indicated by coarse and well sorted grain size, high abundance of foraminifera, and the *Ammonia beccarii* vars. - *Quinqueloculina akneriana* foraminifera assemblage. Sedimentary environment changed from intertidal to supratidal flat with decreasing abundance of foraminifera and finer upward grain size at 5900~ 4300 yr BP. After 4300 yr BP, this area was less affected by seawater, which could be reflected by the appearance of freshwater mollusk and rarely discovered foraminifera. Our retrieved environment changes were closely related with ancient human activities. The Holocene transgression constrained the Dawenkou cultural sites within the inland areas with higher altitude. The exposed coast lowlands after sea retreat were initially not suitable for human survival except sporadic salt production sites of the Longshan culture. These conditions were improved during the Shang and Zhou Dynasties when humans widely used the particular natural resources of underground brine for salt production, and then a large number of salt production sites appeared, which made this region develop into an important origin center of salt production. Our research suggests that salt production was an economic activity that was adopted by people to adapt to the harsh environment, which is of great significance for understanding the evolution of the human-environmental relationship in the coastal area.

**Keywords: salt production, sedimentary environment, Laizhou Bay, the Shuangwangcheng Site, human-environment relationship**

OPEN ACCESS

***Edited by:***
*Daidu Fan,*
*Tongji University, China*

***Reviewed by:***
*Zhanghua Wang,*
*East China Normal University, China*
*Liang Zhou,*
*Jiangsu Normal University, China*

****Correspondence:***
*Yuanyuan Guo*
*yygpku@163.com*
*Longjiang Mao*
*mlj1214@sina.com*

***Specialty section:***
*This article was submitted to Coastal Ocean Processes, a section of the journal Frontiers in Marine Science*

***Received:*** *10 February 2022*
***Accepted:*** *21 March 2022*
***Published:*** *14 April 2022*

***Citation:***
*Guo Y, Mao L, Zhu L and Mo D (2022) Environmental Evolution and Human Adaption Recorded From a Salt Production Site at the Coastal Plain of Laizhou Bay, China. Front. Mar. Sci. 9:873220. doi: 10.3389/fmars.2022.873220*

## INTRODUCTION

The southern coastal plain of the Laizhou Bay in northern Shandong Province is one of the most important sea salt production areas along the eastern coast of China. This region has a long history of salt production, which can be dated back to the late Neolithic Age (Yan, 2015). Historical documents record that salt production and trade played an important role in economics and politics of this region during 1000 B.C. (Flad et al., 2005). Despite the great importance, early salt production in the southern coast of Laizhou Bay has received less attention in the studies of early civilization. Knowledge was limited to incidental archaeological discoveries and systematic research was lacking for a long time. This situation did not change until the advent of the 21th century when a joint project was carried out to advance the research on the history of salt production throughout the coastal regions of southern Laizhou Bay. There are several excavation activities in this region including the Liwu Site in Yangxin county (Yan et al., 2010b), the Nanheya Site in Guangrao county (Wang et al., 2010), the Huodao-aoli Site in Changyi county (Dang and Li, 2019), the Beiyang site (Wang et al., 2005) and the Shuangwangcheng (SWC) site (Yan et al., 2010a) in Shouguang city, which greatly enriches archaeological materials, especially about salt production during the Shang and Zhou Dynasties. Accordingly, our understanding about salt production has been improved in five aspects, including salt production ceramics, salt production technology and processes, settlement patterns and salt production relations, coastal and inland resource interaction, and the origin and development of salt production (Li, 2009; Wang, 2012; Yan, 2013; Yu, 2014). Due to the rich archaeological materials and important findings about early salt production, the southern plain of Laizhou Bay has attracted much more attention in the field of salt archaeology. However, there is still a lack of knowledge on how environmental changes influenced early salt production, making it difficult to understand human – environment interaction in coastal areas from a more integrated and systematic perspective.

The group of the SWC sites, located in the southern coastal plain of the Laizhou Bay, is one of the largest salt production site clusters discovered in the southern coast of the Bohai Sea. After field surveys, investigation and assessments for seven times in 2003, 2004, 2005 and 2008, a joint project team from the Peking University – Shandong Provincial Institute of Cultural Relics conducted excavations at three locations in the SWC site group. The archaeological excavation of the SWC site covered an area of more than 5,000 square meters. Many remains and relics related to salt production activities in the Shang, Zhou, Song and Yuan dynasties have been discovered, among which several intact salt-making workshop units with clear structures and layouts from the late Yin-Shang to the early Western Zhou period were excavated (Yan et al., 2010a). The excavations of the SWC sites provided valuable information for the study of the development of ancient Chinese salt industry. In this paper, we selected four representative profiles, and collected samples from three of them, which gave us an opportunity to reconstruct environmental evolution, and examine the relationship between salt production and regional environmental changes from the perspective of environmental archaeology. Our research aims to deepen the understanding of the evolution of the relationships between human and environment in coastal areas.

## REGIONAL SETTINGS

The southern plain of the Laizhou Bay is located on the south bank of the Bohai Sea. The area extends from the mouth of the Xiaoqing River in the west to the mouth of the Jiaolai River in the east (**Figure 1**). The elevation of the study area is high in the south and low in the north. Accordingly, landforms are composed of the piedmont diluvial tableland, alluvial plains, and marine plains from south to north. This region features the warm temperate monsoon climate, with an average annual temperature of 12.3°C and average annual precipitation of 613.2 mm. The intra-annual distribution of precipitation is uneven, with much more in summer and less in winter. The rivers in this region are short, and flows from south to north.

With the continuous development of archaeological research, the study area has reconstructed a relatively continuous Neolithic to Bronze Age cultural sequence, including the Houli culture (8500-7500 a BP), the Beixin culture (7400-6300 a BP), the Dawenkou culture (6300-4600 a BP), the Longshan Culture (4600~4000 a BP), the Yueshi Culture (3900~3500 a BP) and Shang and Zhou Dynasties Culture (3500~2200 a BP).

## MATERIALS AND METHODS

The SWC sites group is located around Shuangwangcheng Reservoir in the north of Shouguang City, Shandong Province, 27 km away from the current coastline (**Figure 1**). The area is flat and low-lying, with only 3 to 4 meters above the sea level. Archaeological survey in 2008 discovered more than 80 locations which were related to salt production. Among them, three locations were excavated in great detail, and two workshops of salt production were unearthed. In addition, some brine wells, evaporation ponds, water storage pits and large stoves boiling for salt were also found. Through field investigations, we selected 4 profiles at the SWC 014 location for stratigraphic division and lithological analysis. We collected 49 sediment samples at 5 cm intervals in the SWC-W profile, 19 samples at 10 cm intervals in the SWC-N profile, and 11 samples at 10-15 cm intervals in the SWC-S profile. We also collected three mollusk samples, one from the depth of 152-156 cm in SWC-N profile and two from the depths of 40~44 cm and 55-60 cm respectively at the SWC-S profile. The SWC-S02 profile was not sampled because its lithological characteristics were very similar to the SWC-S profile.

Grain size analysis of sediment samples were performed at the sedimentary laboratory in Peking University. Samples were preprocessed with $H_2O_2$ and 10% HCl to remove organic matters and carbonates, and dispersed with a 0.05 mol/L sodium before measured by the Mastersizer 2000 instrument. Grain size composition and parameters such as median size ($M_d$), Skewness (Sk), Kurtosis ($K_G$) and standard deviation (SD) were calculated to indicate the diverse deposition environments.

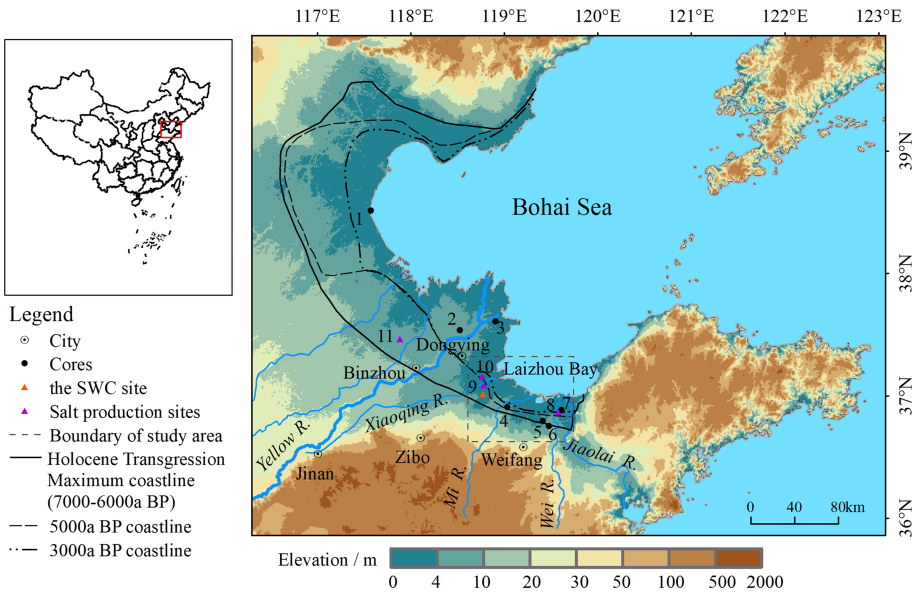


**FIGURE 1** | Topographical map and the location of the SWC site, the cores,the excavated salt production sites and coastlines of different period. (1. the BQ1 core, 2. the H9601 core, 3. the H9602 core, 4. the ZK305 core, 5. the A5 core; 6. the A1 core, 7. the ZK303 core, 8. the Huodao-aoli site, 9. the Dahuangbeiyang site, 10. the Nanheya site, 11. the Liwu site).

Mollusk samples were processed and identified at Nanjing Institute of Geology and Paleontology, Chinese Academy of Sciences. Foraminifera analysis were conducted at the Institute of Oceanology, Chinese Academy of Sciences. First, 50 grams of dried sample were filtered with a 63 μm diameter sieve and the left samples on the sieve were collected. Then the samples were dehydrated, and processed with the $CCl_4$ solution to float, separate and enrich foraminifera. At last, foraminifera were identified and counted under a Zeiss optical stereoscope. Indices were calculated, including the abundance [number of individuals per gram), simple diversity (*S*: number of species), complex diversity (*H(s)*] and percentages of all species of the foraminifera (the proportion of the number of a certain species of foraminifera to the total number of foraminifera in one sample). The complex diversity was reflected by the Shannon-Weiner index (Shannon-Weiner index) whose formula is as follows:

$$H(s) = -\sum_{i=0}^{S} P_i \ln P_i$$

where *H(s)* refers to the complex diversity; *s* refers to the number of species in the sample; $P_i$ is the ratio of the number of the *i*-th species to the total number of all species. The *H(s)* curve can well reflect the changes in paleo-salinity and paleo-sea water depth (Yao et al., 2014). The lower the *H(s)* value, the more the salinity deviates from normal seawater; the lower the *H(s)* value, the generally smaller the sea water depth.

Accelerator mass spectrometry (AMS) $^{14}C$ dating on mixed benthic foraminifers samples from the SWC-W profile was performed at the AMS$^{14}C$ Dating Laboratory of the Peking University. Radiocarbon ages in **Table 1** were calibrated using CALIB 7.0.2 (Reimer et al., 2013) with ΔR value of −178 ± 50 a (Southon et al., 2002). Based on the dating results, we set up a rough chronological framework to construct the relationship between the cultural layers and the stratigraphic sequence in the profile.

# RESULTS AND ANALYSIS

## Lithology and Grain Size Composition

The lithological characteristics of the four profiles at the SWC site were consistent with each other (**Figure 2**). From bottom to

**TABLE 1** | $^{14}C$ ages of mixed benthic foraminifera of the SWC-W profile at the SWC site.

| Sample No. | Lab No. | Depth/cm | Materials | $^{14}C$ date /BP | Calibrated date / yr BP | |
|---|---|---|---|---|---|---|
| | | | | | 1σ (68.2%) | 2σ (95.4%) |
| SWC-W-23 | BA10366 | 105-110 | foraminifera | 5135±60 | 5630-5490 | 5660-5370 |
| SWC-W-49 | BA10367 | 233-238 | foraminifera | 5945±35 | 6445-4355 | 6490-6320 |

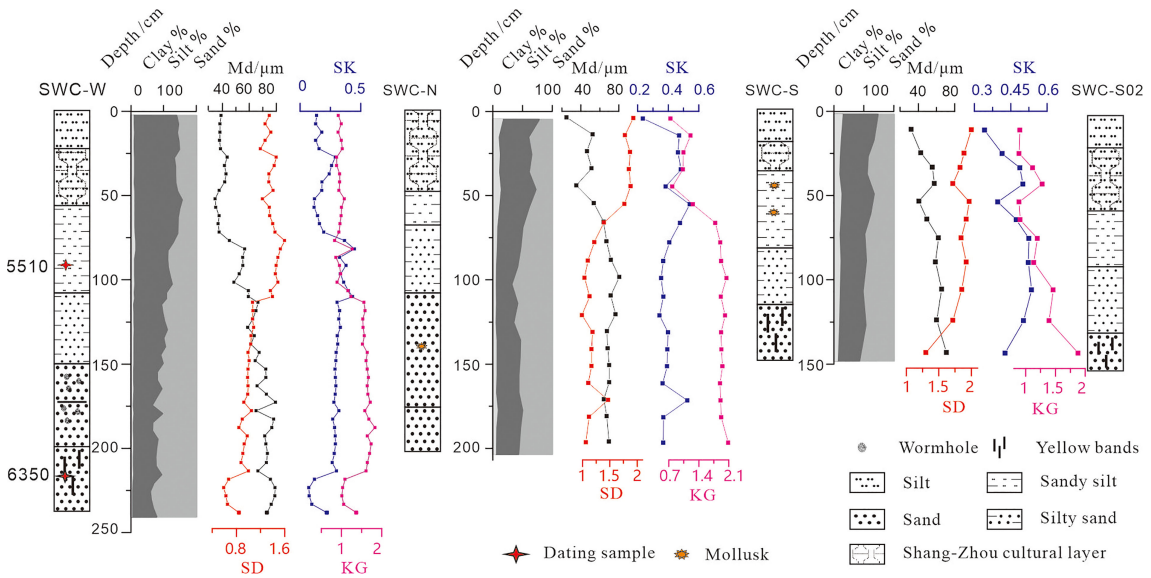


**FIGURE 2** | Stratigraphy and curves of grain size parameters of the four profiles at the SWC site.

top, the colors changed from dark to light, while the grain size became finer indicated by the gradually decrease of median grain size ($M_d$). Sediments at lower part of profiles (150-243cm in SWC-W profile, 110-200 cm in SWC-N profile, 115~150 cm in SWC-S profile, and 135~160cm in SWC-S02 profile) were characterized by a dark gray sand or yellowish gray silty sand with yellow spots or yellow vertical bands. Sediments at the overlying stratum (70-150 cm in SWC-W profile, 60-110 cm in SWC-N profile, 50-115cm in SWC-S profile, and 55-135cm in SWC-S02 profile) featured yellowish gray silty sand or yellow sandy silt. The upper layers (0-70 cm in SWC-W profile, 0-60 cm in SWC-N profile, 0-50 cm in SWC-S profile, and 0-55 cm in SWC-S02 profile) were mainly composed of gray or dark gray sandy silt, and some archaeological remains of Shang and Zhou Dynasties were discovered. Due to the high consistency of the four profiles, we chose the SWC-W profile as the benchmark and the other profiles as a supplement to reveal the changes in grain size distribution properties along the sedimentary layers.

Gain size frequency curves of sediment samples at lower parts of profiles mainly exhibited unimodal distribution (**Figure 3** SWC-W-47, SWC-N-11 and SWC-S-09), probably indicating single and strong hydro dynamics. Sediment samples from overlying stratum showed a typical bimodal pattern with a main peak at 65~75 μm and a secondary peak at 5~10 μm (**Figure 3** SWC-W-22 and SWC-N-05), which indicated that the deposition process might be affected by two forces: rivers and seawater. There were also some samples exhibited the unimodal pattern in the overlying strata with the peak at 70~80 μm (**Figure 3** SWC-N-03 and SWC-S-03). Curves of grain size parameters were shown in **Figure 2**. Sorting values (SD) ranged from 0.59 to 2, suggesting the conversion from well sorting to poor sorting (Folk and Ward, 1957). Specifically, the SD values were relatively lower at the depth of 150~243 cm, then gradually increased at the depth of 70~150 cm, and slightly decreased at the depth of 0~70 cm in SWC-W profile, indicating that the sorting of sediments showed a better-poorer-slightly better trend. Skewness values (Sk) ranged from 0.17 to 0.54, belonging to zero skewness to strongly positive skewness. The kurtosis values ($K_G$) were between 0.83 and 1.83, indicating the transitions from leptokuitic, mesokurtic to platykurtic. The trend of kurtosis value was opposite to that of SD and Sk in SWC-W profile. Overall, our analysis suggested that from the bottom to the top of the SWC profiles, the grain size composition changed from well sorted sand or silty sand to poorer sorted silty sand or sandy silt. The mean hydrodynamic force weakened with gradually weaker influence of waves and stronger influence of rivers.

## Foraminifera Assemblages

We identified a large number of foraminifera from 14 samples of the SWC-W profile which belonged to 24 taxa. The majority were eurythermal and euryhaline forms such as *Ammonia beccarii* vars, *Quinqueloculina akneriana*, *Elphidium magellanicum*, and *Cribrononion incertum* etc. whose variations could well indicate coastal environmental changes. Previous studies have found that *A. beccarii* vars lives in coastal brackish water environments such as intertidal zones, low-salt lagoons, and bays (Wang et al., 1988); *Q. akneriana* mainly lives in the lower intertidal zone and the shallow coastal waters areas at a depth of 50~200 m (Zheng, 1988; Li et al., 2010); *E. magellanicum* often lives in the shallow coastal water at a depth of 5-10m (Wang et al., 1988); and *C. incertum* is mainly distributed in the inland shelf and intertidal zone with a water depth of less than 50 m in the East China Sea (Lin et al., 2005). Based on the chronological framework of profiles and changes of foraminifera assemblage indices, three stages were divided as below (**Figure 4**):

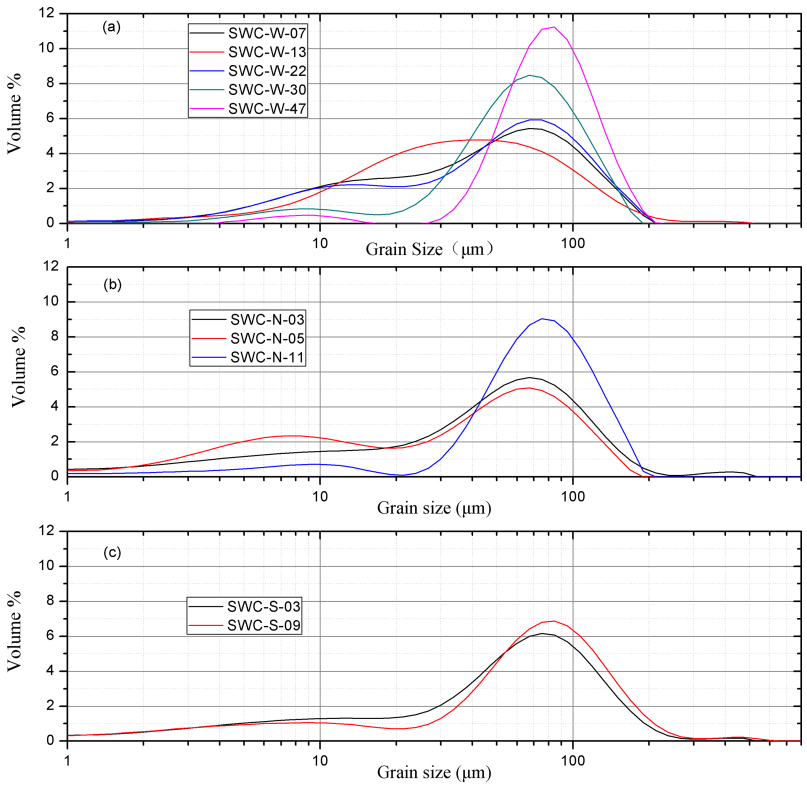


**FIGURE 3** | Grain size frequency curves of typical samples. **(A)** SWC-W profile, **(B)** SWC-N profile, **(C)** SWC-S profile.

Stage I (6400~5900 yr BP, 160-243 cm in SWC-W profile): This stage was rich in foraminifera with the abundance values between 70 and 177, the S values between 9 and 13, and the *H(s)* values between 1.52 and 2.07. Foraminifera assemblage was dominated by *A. beccarii* vars. (ranging from 13.8%~39.1%, average 33.8%) and *Q. akneriana* (ranging from 0~38.3%, average 22%), followed by *E. asiaticum* (8.1%), *C. incertum* (8%) and *N. akitaense* (6.1%).

Stage II (5900~4300 yr BP, 70-160cm at SWC-W profile): The abundance of foraminifera ranged from 7 to 20 with an

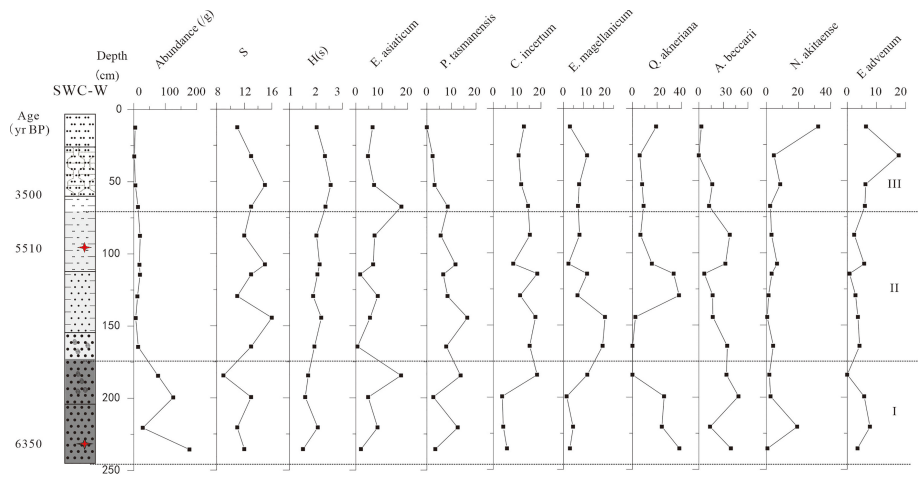


**FIGURE 4** | Curves of foraminifera indices and percentage of some typical taxa in SWC-W profile.

average of 15. The values of simple diversity and complex diversity fluctuated obviously with peaks at 16 and 2.36 respectively, suggesting that the sedimentary environment became more unstable. Compared to stage I, the percentages of *E. magellanicum* (11.6%), *C. incertum* (14.4%), and *P. tasmanensis* (9.5%) increased while that of *A. beccarii* vars. (24.3%) and *Q. Akneriana* (16.1%) decreased. Besides, *E. simplex* began to appear in this segment with a proportion of about 3%. Besides, one species of bivalve mollusk, *Sinonovacula constricta* (*Lamarck*), which often lives in the middle and lower areas of the intertidal zone or the inner bay (Xue, 2002), was found at the depth of 152-156 cm in the SWC-N profile. A gastropod species, *Cerithidea sinensis Philippi*, indicative of littoral environment, was found at 72–75 cm in SWC-S profile (An et al., 2008).

Stage III (after 4300 yr BP, 0-70cm in SWC-W profile): Foraminifera fossils were still present in the sediments of stage III in SWC-W profile, but the abundance decreased substantially to 1~4 per gram. The simple diversity and complex diversity were 11~15 and 2.03~2.56 respectively. Foraminifera assemblage were dominated by *C. incertum* (12.44%) and *Q. akneriana* (10.54%). *E. advenum* also appeared with a maximum content (17.65%) at a depth of 30-35 cm in SWC-W profile. Besides, a typical non-marine gastropod species, *Pseudamnicola opima* Yu, was found at 40-44 cm in SWC-S profile.

# DISCUSSION

## Sedimentary Environment and Coastline Change

Grain size and foraminifera analysis of the SWC profiles revealed clear pattern of sedimentary environment change since the middle Holocene in the southern Laizhou Bay region. The grain size in the four profiles from the SWC site all became finer upwards, changing from well sorted dark grey silty sand in the lower part to the yellowish brown sandy silt or clay silt in the upper part of profiles, which was consistent with the cores of ZK 305, Hsh15 and QSP near the SWC site (Zhang et al., 2004; Xue and Ding, 2008). Studies have reported that grain size in a typical aggradational tidal flat succession tends to be coarser upwards when transited from subtidal to intertidal flat and to be finer upwards when converting from intertidal into supratidal flat, and sediments are generally coarsest in the lower tidal flat (Xue et al., 2001; Fan et al., 2015). Therefore, our profiles indicated the succession from the lower tidal flat to supratidal flat. Mollusk samples at the lower parts of the SWC-N and SWC-S profiles contained species which are typical in intertidal zone, while samples at the upper part of the SWC-S profile contained typical freshwater species. Moreover, the foraminifera assemblage also supported our findings about sedimentary environment. Most species of foraminifera were coastal euryhaline forms, such as *A. beccarii* vars, *Q. akneriana*, *E. asiaticum*, and so forth. The abundance of foraminifera was high at the bottom of profile and decreased substantially at the top of SWC-W profile. Combined with the results of grain size, foraminifera and mollusk assemblages we inferred that the sedimentary environment changed from the lower tidal flat in stage I (6400-5900 yr BP), the intertidal zone in stage II (5900~4300 yr BP) to the supratidal flat in stage III (after 4300 yr BP).

Sedimentary environment evolution reconstructed in our study reflected that the coastline advanced to the SWC site area when maximum Holocene Transgression occurred and then gradually moved seaward during the mid-late Holocene in the southern Laizhou Bay. This is consistent to previous studies that the sea level in the Bohai Sea area rose to the highest at about 6500~7000 yr BP, 2~3m higher than the current level (Liu et al., 2004; Liu et al., 2010). The coastline advanced landward for dozens of kilometers to the coastal plain (**Figure 1**) during the maximum Holocene transgression (Zhuang et al., 1991; Yi et al., 2012; Bradley et al., 2016; Song et al., 2018). The landward movements of coastline can also be supported by the lithological changes (**Figure 5**) of the cores in the west coast of the Bohai Sea (BQ1 core), the Yellow River Delta (H9601 and H9602) (Xue et al., 1995; Yi et al., 2003) and in the southern coastal plain of Laizhou Bay (cores of QSP, Zk 303, ZK305, LZ908 and Hsh15) (Xue and Ding, 2008; Zhang et al., 2004; Yi et al., 2012), which demonstrated the shallow marine facies, tidal flat facies or lagoon facies in the sediments. Sedimentary environment change from the tidal flat to supratidal flat was likely controlled by the seaward retreat of coastline. The records of cores A1 and A5 in Changyi city (**Figures 1** and **5**) supported our finding that the coastline continuously moved seaward from 6000 yr BP (Zhang et al., 2008). Studies showed that the coastline retreated to the north of the Yangzi — Fengtai line in Weifang city at around 3500 yr BP (**Figure 1**) where a shell bank was formed (Zhuang et al., 1991). With the continuous seaward movement of the coastline, several lakes that were formed in the middle Holocene such as Biehua Lake, Judian Lake, and so forth gradually disappeared. The deposition in these areas were characterized by shallow marine facies, lagoon facies, and fluvial facies from bottom to top (Han et al., 2002; Han and Zhang, 2005; Zou et al., 2020).

## The Development of Salt Production in Coast Lowlands Due to Environmental Change

Our research highlights the close relationships between environmental evolution and ancient human activity in the coastal areas. Given that the southern plain of Laizhou Bay experienced a large-scale transgression process in the middle of the Holocene, and a large area of land was submerged by seawater, our previous study revealed that the distribution of sites during the Dawenkou Culture period was limited to the inland alluvial plain areas at higher altitudes (Guo et al., 2013) (**Figure 6**). Marine influence terminated after 4300 yr BP, approximately in the Longshan culture period, and the environment around the SWC site hasn't changed a lot since then, which gave more chance for human settlement. Specifically, it was likely that the coastline retreat promoted the early salt production activity in this region during the Longshan culture period. Archaeological studies have reported that ten salt

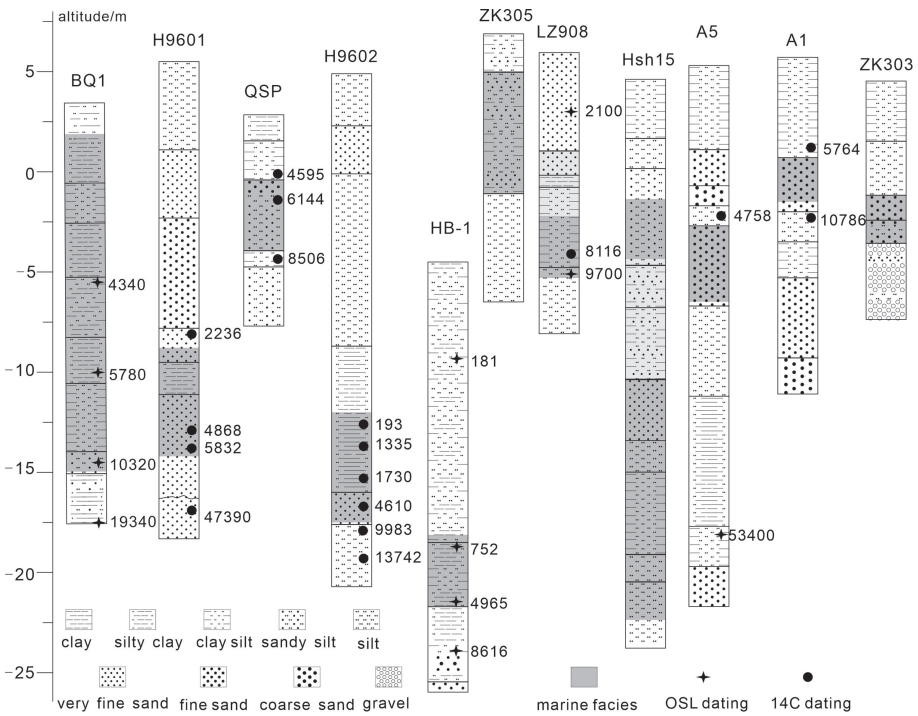


**FIGURE 5** | Diagram of sediment cores around the Bohai Sea.

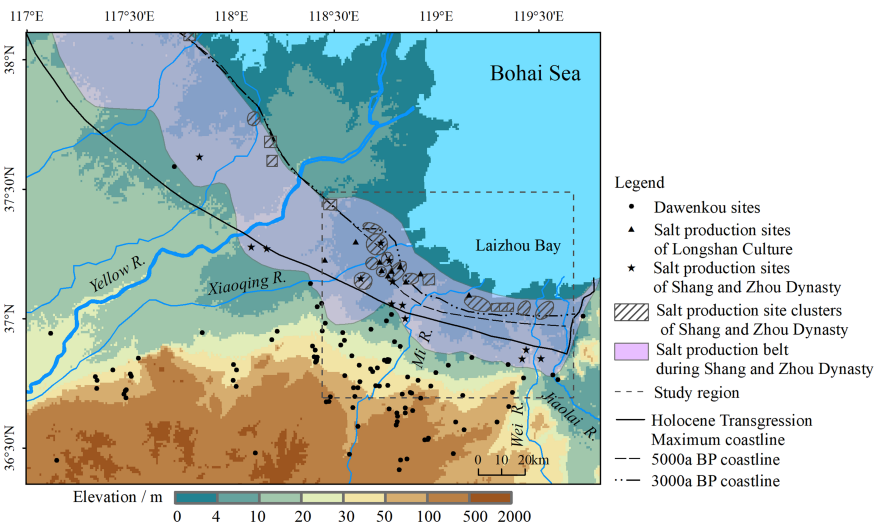


**FIGURE 6** | Distribution of the Dawenkou cultural sites, and the salt production sites of the Longshan cultural period and the Shang and Zhou Dynasties.

production sites of the Longshan culture period were discovered sporadically at the coast of the Laizhou Bay (**Figure 6**). However, these sites were small in scale, had short history and the salt production process of this period was at relatively lower level and had no specialized vessels for production (Li and Wang, 2007; Yan, 2015). However, the cultural relics of plant ash, burnt soils and white calcareous remains that were common in salt production sites of the Shang and Zhou Dynasties signified the appearance of early salt production activities in the Longshan culture period.

Our research highlights the great improvement of the salt production technology during the Shang and Zhou Dynasties. There are much convincing evidence supporting our findings.

Specialized helmet-shaped potteries characterized by simple style, thick texture, thick tires, popular shape bottom were used for salt production (**Figure 7**), and this type of potteries for salt production always occupied almost 90% of the unearthed potteries in the salt production sites (Li, 2019). Intact salt production workshop units, including brine wells, salt hearths, hearth shelter, the working rooms, the brine cisterns, groups of settling ponds, evaporating ponds, were restored at the SWC site (Yan et al., 2010a). Stable isotopes (O/C/Sr) analysis on the white calcareous remains (**Figure 7**) collected from salt production potteries demonstrated that raw material was underground brine which had high paleosalinity formed during marine transgression (Cui et al., 2010; Cui, 2011). Brine wells with a depth of 5~10 m (**Figure 8**) often appeared in groups to extract raw materials for salt production (Dang and Li, 2019). The brine layer at the bottom of the brine well found at the SWC site was shown in **Figure 8A**. Salt production sites increased substantially in quantity and scale during the Shang and Zhou Dynasties as indicated by the densely distributed salt-making sites in marine plains (Wang et al., 2006; Ma et al., 2012; Dang and Li, 2019). Charcoal records also revealed frequent anthropogenic biomass burning of large quantities of woods as fuels for salt-making in this area (Tan et al., 2022). In sum, we concluded that salt production in the southern plain of Laizhou Bay during the Shang and Zhou Dynasties became a specialized and large-scale economic activity, and facilitated cultural thriving and prosperity in this region. Therefore, environmental changes provide a favorable and indispensable background for human development in the coastal areas, although technological progress plays an important role in promoting the coordinated development of the ancient human-land relationship.

It is worth mentioning that there may be some connections between salt-making sites in coastal plain of Laizhou Bay and the farming settlements in the inland areas during the Shang and Zhou dynasties. First, the inland areas probably provided coastal salt workers with salt-making tools (Wang, 2012). The specialized salt making tools were found in both the coastal salt production sites and the inland farming sites, but the proportion of *briquetages* in the salt production sites was much higher than that in the inland sites (Wang et al., 2006). Moreover, inland areas are rich in pottery clay suitable for making *briquetages*, and there were pottery kilns found in inland settlements such as the Zhaopu site in Qingzhou city (Wang, 2012). Second, analysis of the animal bones unearthed from coastal salt production sites showed that the domestic mammals mainly consisted of limb bones and mandibles, but very few ribs and no skull and vertebrae were found (Yan, 2013). The evidence might indicate that these mammals were not slaughtered locally in the coastal areas but were transported from inland farming areas. So this could support our finding that inland sites might provide necessities to people in coastal areas. Third, in exchange, the coastal salt-making sites might provide salt products to inland people, because these areas had abundant underground brine


**FIGURE 7** | Helmet-shaped potteries and white calcareous remains unearthed in southern plain of Laizhou Bay. **(A)** Helmet-shaped pottery of the Shang Dynasty unearthed at the Huangtuya site in Zibo city (provided by Zimeng Wang), **(B)** Helmet-shaped potteries unearthed at the SWC site, **(C, D)** White calcareous remains adhering to the inner wall of the helmet-shaped pottery at the SWC site (Yan, 2013).


**FIGURE 8** | Brine wells discovered in salt production sites. **(A)** Brine well showing the underground brine layer at the SWC site of the Shang and Zhou Dynasties. **(B)** Brine well discovered at the Jixielinchang site of the Eastern Zhou Dynasty (provided by Zimeng Wang).

resources for salt production. Therefore, there might be a trade based on salt between the inland sites and the coastal sites during the Shang and Zhou dynasties. Literature also recorded that during the Eastern Zhou Dynasty, the state of Qi had already implemented the official control on the production and trade of salt to connect with surrounding areas (Fang, 2004). In sum, the development of salt-making activities during the Shang and Zhou Dynasties is a typical example of the comprehensive utilization of regional resources and the adaption to environmental conditions.

## CONCLUSION

We reconstructed the sedimentary environments during the middle and late Holocene based on four profiles around the SWC site. Our analysis of the grain size and foraminifera of samples from the SWC site suggests that the stratigraphy was structured by the sea-level changes in the Holocene. The sedimentary environment has undergone changes from lower tidal flat to supratidal flat since 6000 years ago. The landward and seaward movements of coastline during Holocene caused significant changes in the geographical environment of the southern plain of Laizhou Bay, which had a profound impact on the human activities. When the landward movement of the coastline occurred due to the Holocene transgression, human activities were restricted to the inland plains. With the continuous recession of the coastline and the development of salt production especially the use of specialized salt making tools and raw materials of underground brine, the coast plain of the Laizhou Bay became an important center of salt production during the Shang and Zhou Dynasties, which contributed to the social and economic prosperity of the area. Salt production activities indicated the high ability to comprehensively use of resources and environmental conditions in the area, which showed the active adaptation of human beings to the environment.

## DATA AVAILABILITY STATEMENT

The original contributions presented in the study are included in the article/supplementary material. Further inquiries can be directed to the corresponding authors.

## AUTHOR CONTRIBUTIONS

YG: Conceptualization, Formal analysis, Investigation, Resources, Writing - original draft, Funding acquisition. LM: Formal analysis, Investigation, Editing, Funding acquisition. LZ: Formal analysis, Editing. DM: Formal analysis, Investigation, Funding acquisition. All authors contributed to the article and approved the submitted version.

## FUNDING

This work was supported by the National Natural Science Foundation of China [41701220; 41771218], the National Key R&D program of China [2020YFC1521605], and Major Program of National Social Science Foundation of China [19ZDA231].

## REFERENCES

An C. G., Zhao Y. L., Lin L., Li J. Y., Cui L. L., Ma C. Y. (2008). The Biodiversity of Marobenthos of Intertidal Zone on Chongming Island in Summer. *Acta Ecol. Sin.* 28, 577–586. doi: 10.3321/j.issn:1000-0933.2008.02.016

Bradley S. L., Milne G. A., Horton B. P., Zong Y. (2016). Modelling Sea Level Data From China and Malay-Thailand to Estimate Holocene Ice-Volume Equivalent Sea Level Change. *Quat. Sci. Rev.* 137, 54–68. doi: 10.1016/j.quascirev.2016.02.002

Cui J. (2011). Archaeological Research of Science and Technology of Salt Making Site in Shuangwangcheng, Shouguang City, Shandong Province. *Cult. Reli. South China* (1), 116–119. doi: doi: 10.3969/j.issn.1004-6275.2011.01.014

Cui J., Yan S., Li S., Dang H., Wang S. (2010). Some Issues on Ancient Salt Making Technology of Shuangwangcheng Site in Shouguang City, Shandong Province. *Archaeology* (3), 50-56.

Dang H., Li F. (2019). Discussion on Salt Production Industry and Related Issues at the Changyi County. *Reli. Museolgy* (6), 62–68. doi: doi: 10.3969/j.issn.1000-7954.2019.06.008

Fang H. (2004). Archaeological Research on Sea Salt Industry of the Shang and Zhou Period in Northern Shandong Area. *Archaeology* (4), 53–67.

Fan D., Shang S., Cai G., Tu J. (2015). Distinction and Grain-Size Characteristics of Intertidal Heterolithic Deposits in the Middle Qiantang Estuary (East China Sea). *Geo-Marine Lett.* 35, 161–174. doi: 10.1007/s00367-015-0398-2

Flad R., Zhu J., Wang C., Chen P., Von Falkenhausen L., Sun Z., et al. (2005). Archaeological and Chemical Evidence for Early Salt Production in China. *Proc. Natl. Acad. Sci. USA* 102, 12618–12622. doi: 10.1073/pnas.0502985102

Folk R. L., Ward W. C. (1957). Brazos River Bar: A Study in the Significance of Grain Size Parameters. *J. Sediment. Petrol.* 27, 3–26. doi: 10.1306/74D70646-2B21-11D7-8648000102C1865D

Guo Y., Mo D., Mao L., Wang S., Li S. (2013). Settlement Distribution and its Relationship With Environmental Changes From the Neolithic to Shang-Zhou Dynasties in Northern Shandong, China. *J. Geogr. Sci.* 23, 679–694. doi: 10.1007/s11442-013-1037-3

Han M., Zhang L. (2005). Sedimentary Analysis and Environmental Evolvement of Judian Lake in the Sounth Coastal Plain of Laizhou Bay. *Scentia Geogr. Sin.* 25, 678–682. doi: 10.3969/j.issn.1000-0690.2005.06.005

Han M., Zhang W., Li Y., Zhang L. (2002). Formation and Change of Ancient Lake on South Coast Plain of Laizhou Bay. *Sci. Geogr. Sin.* 22, 430–435. doi: 10.13249/j.cnki.sgs.2002.04.009

Li S. (2009). China's Salt Industry Archaeology in 2008. *Cult. Reli. South China* (1), 54–56. doi: 10.3969/j.issn.1004-6275.2009.01.008

Lin F., Wang J., Li J., Pei Y., Kang H. (2005). Character Istics of Microfossil Assemblages and Evolution of the Sedi- Mentary Environment Since the Late Quaternary in the Laizhou Bay, Bohai Sea. *Geol. Bull. China* 24, 879–884. doi: 10.3969/j.issn.1671-2552.2005.09.016

Li J., Shang Z., Wang H., Pei Y., Wang F., Tian L. (2010). Modern Foraminifera Assemblages: Vertical Zonation and its Indi- Cation for Holocene Sea Level and Geoenvironmental Reconstruction in Bohai Bay, China. *Geol. Bull. China* 29, 650–659. doi: 10.3969/j.issn.1671-2552.2010.05.003

Liu J., Li A., Chen M. (2010). Environmental Evolution and Impact of the Yellow River Sediments on Deposition in the Bohai Sea During the Last Deglaciation. *J. Asian Earth Sci.* 38, 26–33. doi: 10.1016/j.jseaes.2009.12.013

Liu E., Zhang Z., Shen J. (2004). Spore-Pollen Records of Environmental Change on South Coast Plain of Laizhou Bay Since the Late Pleisstocene. *J. Palaeogeogr.* 6, 78–84. doi: 10.3969/j.issn.1671-1505.2004.01.009

Li H., Wang Q. (2007). The History of Sea-Salt Production in Northern Shangdong and Archeological Research. *Guan Zi J.* (2), 43–47. doi: 10.19321/j.cnki.gzxk.2007.02.013

Ma S., Wang Q., Li H., Yu C., Fu Y., Xu Q. (2012). Brief Report of the Survey on Salt Industry Archaeology in the Low Xiaoqinghe River in Northern Shandong Province. *Huaxia Archaeol.* (3), 3–22. doi: 10.16143/j.cnki.1001-9928.2012.03.003

Reimer P. J., Edouard Bard B., Alex Bayliss B., Warren Beck B. J., Paul Blackwell B. G., Christopher Bronk Ramsey B. (2013). Intcal13 and Marine13 Radiocarbon Age Calibration Curves 0–50,000 Years Cal Bp. *Radiocarbon* 55, 1869–1887. doi: 10.2458/azu_js_rc.55.16947

Song B., Yi S., Yu S. Y., Nahm W. H., Lee J. Y., Lim J., et al. (2018). Holocene Relative Sea-Level Changes Inferred From Multiple Proxies on the West Coast of South Korea. *Palaeogeogr. Palaeoclimatol. Palaeoecol.* 496, 268–281. doi: 10.1016/j.palaeo.2018.01.044

Southon J., Kashgarian M., Fontugne M., Metivier B., Yim W. W. S. (2002). Marine Reservoir Corrections for the Indian Ocean and Southeast Asia. *Radiocarbon* 44, 167–180. doi: 10.1017/S0033822200064778

Tan Z., Gu M., Han Y., Mao L., Zhou L., Liu L., et al. (2022). Records of Fire and its Controls on Coastal Plain of Laizhou Bay, China Since 5000 Years. *Palaeogeogr. Palaeoclimatol. Palaeoecol.* 585, 110702. doi: 10.1016/j.palaeo.2021.110702

Wang Q. (2012). Retrospect and Prospect of Salt Industry Archaeology in Shandong Province, China. *Huaxia Archaeol.* (4), 59–69. doi: 10.16143/j.cnki.1001-9928.2012.04.014

Wang Q., Li R., Zheng B. (2005). Excavation on the Dahuagnbeiyang Site of the Western Zhou Dynasty Site in Shouguang City, Shandong Province. *Archaeology* (12), 41–47.

Wang Q., Rong Z., Wang L., Zhao J. (2010). A Breif Report of the Western Zhou Dynasty Salt Production Site at the Nanheya in Dongying City, Shandong Province, China. *Archaeology* (3), 37–49.

Wang P., Zhang J., Zhao Q., Min Q., Bian Y., Zheng L., et al. (1988). *Foraminifera and Ostracodes in Surfacee Sediments of the East China* (Beijing: China Ocean Press).

Wang Q., Zhu J., Shi B. (2006). Man-Nature Relationship Evolution During the Holocene In Northern Shandong Evidenced From Coastline Changes and Seasalt Production. *Quat. Sci.* 26, 589–596. doi: 10.3321/j.issn:1001-7410.2006.04.014

Xue C. (2002). Holocene Sedimentary Environments and Sea Level Change Based on Qingfeng Section, Jianhu, Jiangsu, China. *Acta Sedimentol. Sin.* 20, 184–177. doi: 10.14027/j.cnki.cjxb.2002.01.030

Xue C., Ding D. (2008). Weihe River - Mihe River Delta in South Coast of Bohai Sea, China: Sedimentary Sequence and Architecture. *Scentia Geogr. Sin.* 28, 672–676. doi: 10.13249/j.cnki.sgs.2008.05.672

Xue Y., Yin Y., Gao S. (2001). Grain Size Characteristics of Tidal Flat Sediments, Northern Yellow River Delta. *Mar. Sci.* 25, 50–54. doi: 10.3969/j.issn.1000-3096.2001.05.016

Xue C., Zhu Z., Lin H. (1995). Holocene Sedimentary Sequence, Foraminifera and Ostracoda in West Coastal Lowland of Bohai Sea, China. *Quat. Sci. Rev.* 14, 521–530. doi: 10.1016/0277-3791(95)00013-F

Yan S. (2013). *The Salt Archaeology of Shang and Western Zhou Period in the Coastal Region of the Bohai Gulf. 1st ed*. Ed. S. Yan (Beijing: Cultural Relics Press).

Yan S. (2015). Salt Making Remains of the Longshan Age at the South Coast of the Laizhou Bay. *Archaeology* (12), 107–114.

Yan S., Dang H., Wang S., Li S., Wang D. (2010a). Excavation of Shuangwangcheng Salt Industry Site in Shouguang City, Shandong Province in 2008. *Archaeology* (3), 18–35.

Yan S., Zhang Z., Tong P. (2010b). A Brief Report on the Excavation of the Shang Dynasty Remains at the Liwu Site in Yangxin County, Shandong Peovince, China. *Archaeology* (3), 3–17.

Yao J., Yu H., Xu X., Yi L., Chen G., Su Q. (2014). Paleoenvironmental Changes During the Late Quaternary as Inferred From Foraminifera Assemblages in the Laizhou Bay. *Acta Oceanol. Sin.* 33, 10–18. doi: 10.1007/s13131-014-0536-0

Yi S., Saito Y., Oshima H., Zhou Y., Wei H. (2003). Holocene Environmental History Inferred From Pollen Assemblages in the Huanghe (Yellow River) Delta, China: Climatic Change and Human Impact. *Quat. Sci. Rev.* 22, 609–628. doi: 10.1016/S0277-3791(02)00086-0

Yi L., Yu H. J., Ortiz J. D., Xu X. Y., Chen S. L., Ge J. Y., et al. (2012). Late Quaternary Linkage of Sedimentary Records to Three Astronomical Rhythms and the Asian Monsoon, Inferred From a Coastal Borehole in the South Bohai Sea, China. *Palaeogeogr. Palaeoclimatol. Palaeoecol.* 329–330, 101–117. doi: 10.1016/j.palaeo.2012.02.020

Yu Y. (2014). The Development of Salt Industry on South Coast of Laizhou Bay in Northern Shandong. *Salt Ind. Hist. Res.* (2), 8–16. doi: 10.3969/j.issn.1003-9864.2014.02.002

Zhang Z., Nie X., Bian X. (2004). Environmental change of lakes in Xiaoqinghe River drainage, Shandong Province.. *J. Palaeogeogr.* 6, 226–233. doi: 10.3969/j.issn.1671-1505.2004.02.011

Zhang Z., Liu E., Zhang Y., Xin L. (2008). Environmental Evolution in the Salt-Water Intrusion Area South of Laizhou Bay Since Late Pleistocene. *J. Geogr. Sci.* 18, 37–45. doi: 10.1007/s11442-008-0037-1

Zheng S. (1988). *Cement and Porcellaneous Foraminifera in the East China Sea* (Beijing: Science Press).

Zhuang Z., Xu W., Li X. (1991). The Coastline Evolution on the South Coast of the Bohai Sea Since 6 Ka BP. *J. Ocean Univ. Qingdao* 21, 99–110. doi: 10.16441/j.cnki.hdxb.1991.02.010

Zou C., Zhao Q., Mao L. (2020). Holocene Environmental Evolution Recorded by Core Sediments of Judian Lake in the East of Lubei Plain Shandong Province. *J. Palaeogeogr.* 22, 1209–1220. doi: 10.7605/gdlxb.2020.06.083

**Conflict of Interest:** The authors declare that the research was conducted in the absence of any commercial or financial relationships that could be construed as a potential conflict of interest.

this article, or claim that may be made by its manufacturer, is not guaranteed or endorsed by the publisher.

frontiers | Frontiers in Marine Science

ORIGINAL RESEARCH
published: 09 June 2022
doi: 10.3389/fmars.2022.910125

# Holocene Environmental Evolution Response to the Human Activities and East Asian Summer Monsoon Variation in the Liangzhu Ancient City Complex, Eastern China

*Chunhui Zou*[1], *Longjiang Mao*[1,2*], *Siwei Shan*[3*], *Shuangping Zhaocheng*[4] *and Duowen Mo*[4]

[1] Institute of Scientific and Technical History, Nanjing University of Information Science and Technology, Nanjing, China, [2] School of Marine Science, Nanjing University of Information Science and Technology, Nanjing, China, [3] Department of Archaeology, School of History, Wuhan University, Wuhan, China, [4] College of Urban and Environmental Sciences, Peking University, Peking, China

OPEN ACCESS

**Edited by:**
Joseph Carlin,
California State University, Fullerton, United States

**Reviewed by:**
Xinxin Zuo,
Fujian Normal University, China
Li Wu,
Anhui Normal University, China

***Correspondence:**
Longjiang Mao
mlj1214@nuist.edu.cn
Siwei Shan
swshan@whu.edu.cn

**Specialty section:**
This article was submitted to Coastal Ocean Processes, a section of the journal Frontiers in Marine Science

**Received:** 31 March 2022
**Accepted:** 09 May 2022
**Published:** 09 June 2022

**Citation:**
Zou C, Mao L, Shan S, Zhaocheng S and Mo D (2022) Holocene Environmental Evolution Response to the Human Activities and East Asian Summer Monsoon Variation in the Liangzhu Ancient City Complex, Eastern China. Front. Mar. Sci. 9:910125. doi: 10.3389/fmars.2022.910125

The Liangzhu Ancient City Complex is located in a low-lying coastal delta area, and its environmental evolution would have had a significant impact on the human-environment interactions. In this study, element geochemistry and grain size of the sediment sequence from a dam section in Ganggongling (GGL) reveal crucial aspects of sedimentary dynamics, environmental evolution, human activities, and East Asian Summer Monsoon (EASM) variation in the Liangzhu area since 5500 a. Starting from the middle-to-late Holocene, the GGL section shows an overall transition from warm humidity to cold-dry, which is consistent with the climate record dimension in southern China. Through comprehensive analysis of the sedimentary environment before and after the dam's completion, it can be found that the Ganggongling dam has played a positive role in regulating mountain torrents and met the needs of production and domestic water, such as rice planting through water storage. Further applications on the multi-decadal to centennial time scale demonstrate that variations in solar activity may control the EASM intensity mainly in southern China, which is subject to ENSO intensity changes.

**Keywords: environmental evolution, human activities, East Asian summer monsoon, Liangzhu Ancient City Complex, dam section**

## INTRODUCTION

The river basins and their deltas are areas that are very sensitive to global and regional climate and environmental changes, and their environmental changes have largely influenced and constrained the rise and fall of civilizations in these areas during historical periods (Zong et al., 2007; Rolett et al., 2011; Timmermann and Friedrich, 2016; Dong et al., 2019). Studying environmental changes in estuaries and deltas and the corresponding adaptation and response to human activities has become a central issue of widespread scholarly interest in the past decades. Previous studies have primarily

focused on the relationship between climate and vegetation and human activities in environmental elements, as well as sudden disaster events that have a direct impact on human activities, such as earthquakes and floods (Cullen et al., 2000; Yi et al., 2003; González-Sampériz et al., 2008; Kennett et al., 2012; Amorosi et al., 2013; Dixit et al., 2014; Sun et al., 2019). In addition, the hydrogeomorphic environment, such as sea-level change and river and lake evolution, are closely related to human activities, and their evolutionary processes significantly affect the activities of ancient humans, which also become a current research hotspot (Turney and Brown, 2007; Chen et al., 2008; Innes et al., 2014; Nienhuis et al., 2020). For example, in the Atacama desert region of northern Chile, the Mississippi River basin, and the Nile River basin, cultural decline at certain times has been attributed to several events of the river, lake, and floodplain shrinkage and reduced river flows (Núñez et al., 2002; Kidder et al., 2008; Macklin et al., 2015; Munoz et al., 2015). Thus, understanding past human-nature interactions is essential for exploring long-term human culture and agriculture and provides important information for human adaptation to future climate change.

As an important component of the global climate system, the East Asian monsoon affects nearly 60% of the world's inhabitants (Yao et al., 2015). Only by studying the response of the East Asian monsoon to the overall behavior of the global climate system in the framework of global change can we fully understand the patterns and mechanisms of the East Asian monsoon climate change. In recent years, scholars have reconstructed the Holocene monsoon climate and environmental characteristics of different regions, divided them into stages and analyzed the relationship between the environment and monsoon evolution (Kutzbach, 1981). In addition, the historical evolution of the East Asian Summer Monsoon (EASM) has been extensively studied using a variety of geological archives, including loess-paleosol sequences, marine and lake sediments, peat sediments, and stalagmites, revealing the cycle of changes in the East Asian Monsoon and its driving mechanisms (Huang et al., 2018; Liu et al., 2013; Mu et al., 2016; Goldsmith et al., 2017; Gai et al., 2020; Li et al., 2022). Geochemical elements in lacustrine sediments can provide a continuous, high-resolution record of changes in terrestrial and aquatic ecosystems (Colman et al., 2007; Fu et al., 2013). Geochemical elements also provide key information on environmental changes in lakes, such as erosion history and soil and slope cover formation processes, as well as the climate history of continental areas and regional responses to large-scale climate change, which can then be used to infer climate conditions (Oldfield et al., 1979; Rosenbaum and Reynolds, 2004). However, the reconstruction of the East Asian Summer Monsoon in eastern China relies heavily on high-resolution oxygen isotope records preserved in cave stalagmites. This is because stalagmites grow in closed and stable cave systems, and the environmental information obtained is fidelity-rich and sensitive to environmental changes. Therefore, we urgently need other higher resolution proxies (e.g., geochemical elements, etc.) to enhance the understanding of the East Asian summer monsoon in eastern China.

The Neolithic culture of the lower Yangtze River region, one of the birthplaces of Chinese culture, has undergone a long and complex development process in the Holocene (Stanley and Chen, 1996). As the last stage of the prehistoric culture in the region, Liangzhu culture is famous for its rice cultivation and large water engineering constructions, representing the pinnacle of the Neolithic culture in the lower Yangtze River region (Liu B et al., 2017a). The Liangzhu site was also inscribed on the UNESCO World Heritage List in 2019. Geographically, the Liangzhu area is located in a low-lying coastal area on the north coast of Hangzhou Bay, which is significantly affected by the East Asian monsoon and is also highly susceptible to extreme climatic and environmental events such as typhoons, storms, floods, and seawater intrusion, and scholars consider this as a possible reason for the interrupted disappearance of Liangzhu culture (Nicholls and Cazenave, 2010; Kirwan and Megonigal, 2013; Fan et al., 2017). During the Liangzhu culture, more evergreen, moisture-loving genera, such as *Cyclobalanopsis Oerst* and *Castanopsis armata*, were found in the sporulation record, reflecting a climate that remained warm and humid in general (Wang and Zhang, 1981; Shi, 2011). However, systematic studies on the Holocene environmental evolution and monsoonal changes in the Liangzhu area are lacking. In recent years, archaeological work has revealed the existence of a large and complex hydraulic system at the periphery of the ancient city of Liangzhu, consisting of a group of nearly ten dams of different sizes stacked in the ravine between the mountains, which range in age from the early to the middle of the Liangzhu culture (Wang and Liu, 2015; Huan et al., 2022). However, little research has been conducted on the Holocene environmental evolution process within the dam system and the environmental significance of prehistoric dams. For this purpose, we selected Ganggongling Dam, one of the closest dams in the high dam system to the Hangjiahu Plain, and analyzed the sediment sequence by stratigraphy, sedimentology, chronology, and geoarchaeology of the sediments sampled from the reservoir area within the dam. The resulting lithology, geochemical element abundance, and grain size distribution were obtained and compared with other regional proxies. The objectives are 1) to recover the Holocene environmental evolution of the reservoir area, 2) to discuss the environmental significance of prehistoric dams and their relationship with human activities, and 3) to reconstruct the regional precipitation processes and to explore their relationship with changes in EASM intensity.

## REGIONAL SETTING

The Hangzhou-Jiaxing-Huzhou Plain (Hangjiahu Plain) is part of the southern Yangtze River Delta, bordered by Taihu Lake in the north, the hilly areas of western Zhejiang in the west, Qiantang River and Hangzhou Bay in the south, and Wujiang to Jinshan in the east, and is an alluvial plain of rivers and lakes with low topography and a dense network of waterways (**Figure 1B**). The overall topography of the region is not very undulating, with elevations generally ranging from 2 to 4 m. The

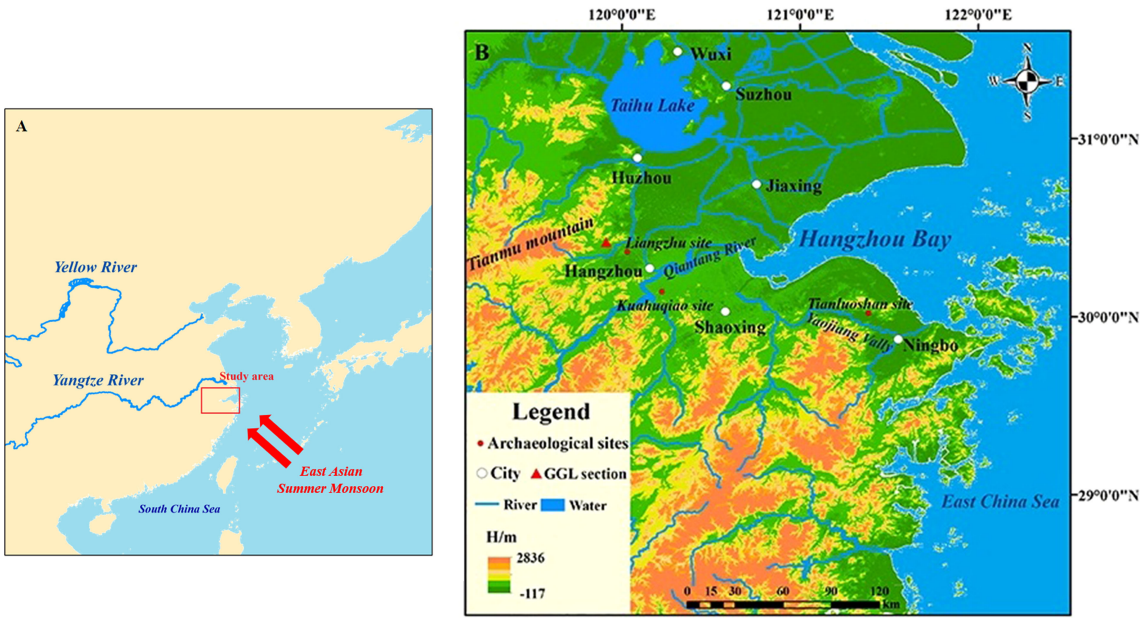


**FIGURE 1** | **(A)** Location of the study area in the lower reaches of Yangtze River; **(B)** Specific location of the GGL profile and its surrounding hydrogeomorphology.

elevation is lower in the northeast in the area in front of Tianmu Mountain and slightly higher in the southwest along the Qiantang River and Hangzhou Bay, with a general pattern of high in the southwest and low in the northeast (Yang et al., 2002). The surface sediments of the region are dominated by river-lake phase sediments composed of fine-grained clay and silt from the Yangtze River, Qiantang River, and numerous lakes, and the tidal flats phase sediments with coarser grains and loose soils on the southern edge (Lu, 2008). The study area of Liangzhu City is located between Dazhe Mountain and Daguan Mountain south of the Tiaoxi River, bordering some low mountains on the western and southwestern edges of the Hangjiahu Plain.

The Hangjiahu Plain has a well-developed water system, and most of the rivers have a small watershed area, short headwaters, and fast flow rates. Most of the water systems originate from Tianmu Mountain and Mogan Mountain, among which the Tiaoxi River belongs as one of the eight major water systems in Zhejiang Province (Yan et al., 1959; Xu, 2012). The climate of the Hangjiahu Plain is an East Asian monsoon climate with an uneven seasonal distribution of precipitation, with low rainfall in spring and winter and high precipitation in summer and autumn (**Figure 1A**). The average annual temperature in the region is 15~16°C, and the average yearly precipitation is 1000~1400mm.

# MATERIALS AND METHODS

## Section Recovery and Dating

Ganggongling Dam is at the easternmost end of the high dam system at the periphery of the ancient city of Liangzhu, located in Banyao Town, Hangzhou, Zhejiang Province. The exploratory pit shows a uniform dam body with artificial accumulation, which shows that the northern slope of the dam body slopes to the north. We took a natural sediment profile inside the dam on the north side of the dam accumulation, and the depth of the profile exceeded 227 cm without bottoming out, which is called the Ganggongling section (30°25′11″N,119°54′39″E; elevation:10m). Samples spaced 2-5 cm apart were selected for further laboratory analysis, yielding a total of 63 samples.

Photos of the GGL profile are shown in **Figure 2A**. According to the detailed lithological description, grain size distribution, and sediment structure, the GGL section can be divided into eight layers from top to bottom. The detailed description is as follows:

Zone 1 (0~22cm) is the surface paddy soil, mainly composed of gray clayey silt with some rusty brown root-whisker-like rust spots. Zone 2 (22~42cm) is the bottom of paddy soil in the upper part, which is gray clayey silt; the lower part is brownish yellowish, grayish-brown clayey silt, with undulating upper and lower interfaces. Zone 3 (42~93 cm) is brownish-gray clayey silt with rusty brown root-whisker-like rusty spots. Zone 4 (94~122 cm) and zone 5 (122~150 cm) are dark gray to grayish-brown mottled clayey silt and dark gray clayey silt, respectively. Zone 6 (122-150 cm) comprises grayish-green clayey silt and rusty yellow clayey silt. Zone 7 (203-227 cm) and Zone 8 (227 cm~) are gray clayey silt sand with brownish-yellow clayey sand and gray clayey sand with brown spots.

The photoluminescence dating was done by the Laboratory of Environmental Archaeological Photoluminescence, Institute of Geography, Henan Provincial Academy of Sciences. 4-11um quartz particles were obtained by the conventional pretreatment method for all samples, and quartz equivalent

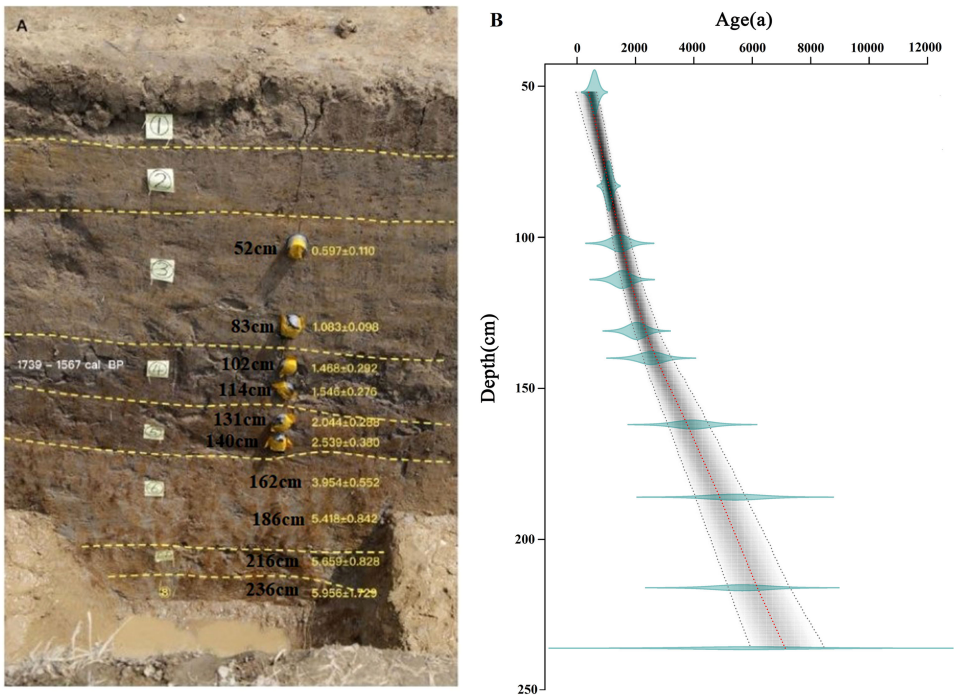


**FIGURE 2** | Stratigraphy **(A)** and age-depth model **(B)** of the GGL section.

dose (De) was tested by the single piece regenerative dose method (SAR). U, Th, and K contents were tested by neutron activation method (NAA) in the Analysis and Testing Research Center of Beijing Institute of Nuclear Industry and Geology. Water content was measured by actual water content, the absolute error of 5% was given, and dose recovery experiments at different temperatures were conducted for all samples (Lai and Brückner, 2008). A 7.5 mm thick Hoya U-340 filter was placed between the photomultiplier tube (PMT) and the sample at the top of the photoluminescence system to remove the irradiated light. De measurements were performed by the single slice regenerative dose (SAR) method (Banerjee et al., 2001). Based on the improved experimental procedure of Murray et al., the "cutheat preheat" was changed to "110°C thermoluminescence (TL) measurement". The purpose of the improvement is twofold: one is to release the thermal instability signal, and the other is to use the information of the quartz 110°C TL signal peak to examine the sensitivity change during the experiment.

## Abundance of Elements

The samples were tested for macronutrients and trace geochemical elements by the Key Laboratory of the Ministry of Education for Orogeny and Crustal Evolution, Peking University. The test element is divided into constant elements (e.g., $SiO_2$, $Al_2O_3$, $Fe_2O_3$, $TiO_2$, etc.) and trace elements (Rb, Sr, Zr, V, etc.). The naturally dried samples were sieved through a 20 mesh sieve, mixed thoroughly, and ground to less than 200 mesh using a ball mill. We took 10~20 g of the mixed sample and sealed it in a sealed bag and send it to the laboratory for testing. FeO was determined by titrimetric method, and other macronutrients and some trace elements were tested by Axios wavelength dispersive X-ray fluorescence spectrometer according to GB/T14506.28-2010 standard. The remaining trace elements were determined using an iCAPRQ inductively coupled plasma mass spectrometer. Concrete steps are as follows: (1) 0.25g sediment sample was weighed and introduced into a Teflon tank matched with the microwave digestion instrument, and heated at 85°C for 20 minutes for pre-digestion; (2) 13 ml of HNO3 and 5 ml of HF were added to the digestion tank, which was ensured to be completely sealed and placed in the microwave digester; (3) After the microwave digestion was carried out and the sample was brought to room temperature, the lid and the inner wall of the digestion tank were rinsed with ultrapure water, 5 mL of $HClO_4$ was added and then heated at 190°C on a special heating plate to remove the acid. (4) When the digestion solution was gradually evaporated to the size of soybean and no white smoke came out, the digestion tank was repeatedly rinsed with 5‰ HNO3 solution and finally diluted to 50mL for testing on the machine.

## Grain Size Analysis

The grain size data of the sediment samples were measured and analyzed at the Key Laboratory of the Ministry of Education for Surface Process Analysis and Simulation, School of Urban and Environmental Studies, Peking University, with a laser grain size

analyzer, Mastersize 2000, Malvern, UK, with a resolution of 0.15φ and a measurement range of 0.02~2000 μm with a relative error <3%. Pre-processing work is as the following: (1) in order to remove gravel, plant roots and other biological residues from the samples, naturally air-dried samples were passed through a 20-mesh sieve and 0.3-0.5 g of the sample was placed into a washed and dried 50 ml beaker after all samples were well mixed; (2) 20 ml of 10% $H_2O_2$ was added to a beaker and heated to 200° C on a hot plate until there was little $H_2O_2$ left; (3) 10 ml of 10% HCl was added to a heated beaker, the beaker was filled with pure water to room temperature, and the supernatant was removed after standing for 12 hours; (4) 10 ml of 0.05 mol/L (NaPO3)6 was added to the sample, placed in the ultrasonic shaker for 10 minutes and then put into the machine for testing.

# RESULTS

## OSL Dating Results

The ten OSL dates from the GGL section are provided in **Table 1**. The calculated ages of the GGL profiles range from 6000 to 400a BP (**Figure 2B**). GGL-OSL-07 and GGL-OSL-08 differ in depth by only 24 cm but span in age from 3954 ± 552 a to 5418 ± 842 a, with depositional interruptions that may be due to erosion or artificial dredging.

## Abundance of Elements

As shown in **Figure 3**, the relative contents of major elements are represented by the counterparts of their oxides. $Al_2O_3$, $Fe_2O_3$, and $SiO_2$ dominate the sediments in the depositional sequence of

**TABLE 1** | OSL dating results for samples in the CY section.

| Lab.N | Sample N. | Depth(cm) | Rb /ppm | U /ppm | Th /ppm | K /% | Q-De(Gy) | w.c(%) | Q-Dose rate(mGy/a) | Q-Age(ka) |
|---|---|---|---|---|---|---|---|---|---|---|
| L536 | GGL-01 | 52 | 132±3.4 | 3.81±3.6 | 14.5±2.1 | 1.97±0.55 | 2.47±0.02 | 19.93 | 4.139±0.761 | 0.597±0.110 |
| L537 | GGL-02 | 83 | 131±0.7 | 3.86±1.2 | 15.1±1.7 | 2.10±0.35 | 4.54±0.03 | 20.81 | 4.193±0.379 | 1.083±0.098 |
| L538 | GGL-03 | 102 | 137±1.3 | 4.02±3.3 | 15.8±2.6 | 1.82±0.79 | 5.76±0.03 | 24.18 | 3.925±0.780 | 1.468±0.292 |
| L539 | GGL-04 | 114 | 143±2.6 | 4.17±4.2 | 16.6±3.4 | 2.03±0.26 | 6.58±0.03 | 22.69 | 4.256±0.760 | 1.546±0.276 |
| L540 | GGL-05 | 131 | 139±2.1 | 4.07±2.9 | 16±1.3 | 1.98±0.39 | 8.52±0.02 | 21.91 | 4.167±0.587 | 2.044±0.288 |
| L541 | GGL-06 | 140 | 142±2.3 | 4.41±3.2 | 16.5±2.5 | 1.82±0.32 | 10.33±0.04 | 24.38 | 4.068±0.608 | 2.539±0.380 |
| L542 | GGL-07 | 162 | 152±2.1 | 4.2±2.6 | 17.3±2.7 | 1.93±0.48 | 16.95±0.08 | 21.28 | 4.286±0.598 | 3.954±0.552 |
| L543 | GGL-08 | 186 | 155±3.0 | 4.08±1.6 | 16.6±3.1 | 2.12±0.84 | 23.35±0.09 | 22.30 | 4.310±0.670 | 5.418±0.842 |
| L544 | GGL-09 | 216 | 146±2.9 | 3.63±2.9 | 15.2±2.9 | 2.03±0.36 | 23.01±0.13 | 20.51 | 4.066±0.594 | 5.659±0.828 |
| L545 | GGL-10 | 236 | 138±3.6 | 3.26±5.4 | 14.1±2.4 | 1.94±0.88 | 22.48±0.12 | 21.07 | 3.774±1.096 | 5.956±1.729 |

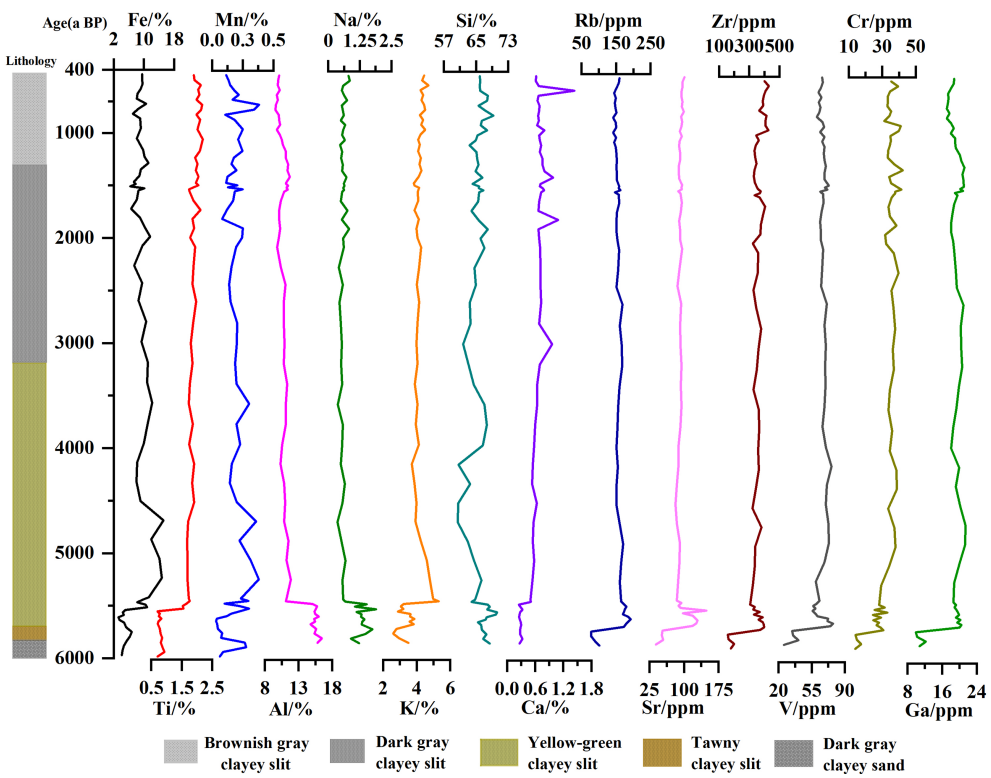


**FIGURE 3** | Stratigraphic sequence and major element concentrations of sediments in the GGL profile.

the GGL profile. The concentration of $Al_2O_3$ varies between 9.6 and 16.4% (average=11.7%), with maximum values during 219~228cm. Conversely, $Fe_2O_3$ shows a continuous reduction at the bottom of the section (average=8.54%). Similar to the trend of $Al_2O_3$, the $SiO_2$ concentration ranges between 58.6 and 70.3%, with a maximum contribution of 201cm. In terms of the trace elements, Zr, Ti, V, Sr, Cr, and Ga have relatively high average contents. V (77.9 ppm) has the highest average range among the heavy metals, followed by Cr (42.34 ppm). Moreover, the concentration of heavy metals dramatically vary in the top and lower parts of the section, while it is relatively stable in the middle part of the section.

## Grain Size Distribution Characteristics

Grain size frequency curves showing multi-peak distribution (**Figure 4A**). The grain size versus standard deviation plot shows that four sensitive grain size components can be identified based on the three standard deviation peaks at 17.4 μm, 79.4μm, and 416.9 μm in the curve (Boulay et al., 2007). Their corresponding size ranges are <45.7μm, 45.7–158.5μm, and >158.5μm, respectively (**Figure 4B**). The grain size analysis results show that the entire section is dominated by silty sand, followed by clay and sand, and the sand content fluctuates significantly from 200 cm onwards (**Figure 4C**). Therefore, we designated three different grain size groups from fine to coarse sensitive fractions 1 (SC1) to 3 (SC3), thus representing three different sensitive grain size fractions. In terms of percentage content, the content of SC1 is dominant, followed by SC2 and SC3. The trend of the median grain size is more similar to SC2 and SC3, while it is negatively correlated with SC1(**Figure 4C**).

# DISCUSSION

## Climate Interpretation From the Multiproxy Approach

Chemical weathering can alter the mineral composition of the land surface, and the resulting debris constitutes the majority of the clastic fraction in the sediment. Therefore, integrated geochemical element parameters can overcome the uncertainty of a single element's response to the environment and better reflect the degree of chemical weathering of sediments. (Kronberg et al., 1986; Fu et al., 2018; Stankevica et al., 2020). In this paper, the following chemical weathering and precipitation proxies were selected to infer the climate change in the study area since the Holocene.

In lacustrine sediments, the precipitation intensity can be inferred from Fe/Mn. The anaerobic environment created by the water-sediment interface in deep lakes favors the dissolution of iron and manganese (Davison, 1993), while manganese is more likely to precipitate in an oxidizing environment (Boyle, 2002). The relative precipitation can be inferred from lake-level proxies such as Fe/Mn. Therefore, the higher Fe/Mn ratio reflects a decrease in the oxygen content of the water body, indicating a further increase in the degree of anaerobicity of the lake water and a rise in the lake water level. Recent work has also confirmed

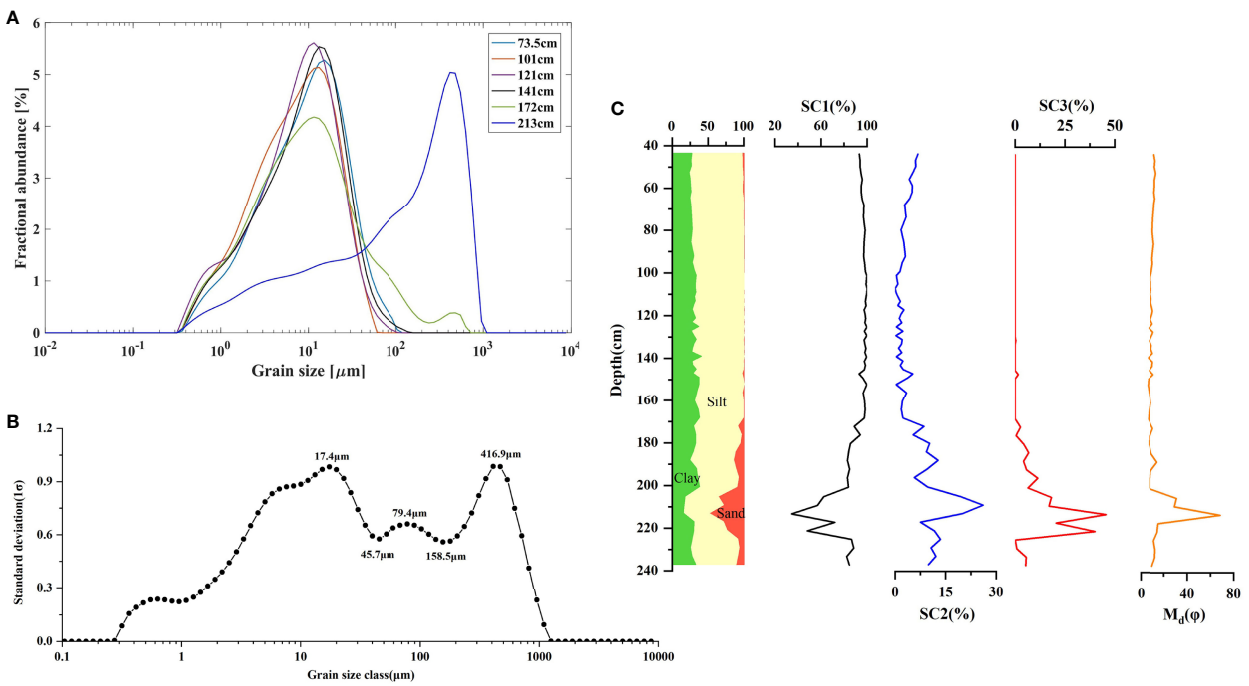


**FIGURE 4** | Grain size analysis results in the GGL section. **(A)** Grain size frequency curves at different depths; **(B)** Grain size classification with standard deviation diagram; **(C)** Depth variation of the three grain size sensitive components expressed as relative content.

that lower Fe/Ti and Mn/Ti generally occur in reducing environments because Ti is more stable in depositional environments (Boës et al., 2012), and the reduction of Fe, Mn in reducing environments Sedimentation would decrease further (Moreno et al., 2007; Kylander et al., 2011), which would also represent an increase in precipitation. In the GGL profile, the ratios of Fe/Ti and Mn/Ti show a good correlation, which in turn are negatively correlated with Fe/Mn (**Figures 5A–C**), which may provide insight into the precipitation variation in the dam supporting evidence.

In general, certain major and trace elements (e.g., K, Na, Ca, Al) behave differently during chemical weathering and can therefore be used to trace the intensity of chemical weathering. The chemical weathering index [CIA = $Al_2O_3/(Al_2O_3 + CaO + Na_2O + K_2O)$] is mainly used to reflect the degree of alteration of minerals during the weathering of sediments, and the increase of its value indicates the growth of chemical weathering of minerals (Chen et al., 2020; Perri, 2020; Wang et al.,2020). In addition, Rb, Sr, and Zr are also commonly used in the study of lacustrine sediments. Rb is easily enriched *in situ* by adsorption of clay minerals during chemical weathering or rainfall percolation, while Sr is easily left *in situ* in a free state with surface or groundwater (Jeong et al., 2006; Du et al., 2011; Chang et al., 2013). Zr is mainly found in heavy minerals such as zircon rocks, which are very stable during weathering. Existing studies have shown that with the intensification of chemical weathering, the Rb/Sr value of the *in-situ* residual sediments will gradually increase, while the Zr/Rb value will gradually decrease (Kalinin et al., 2018). Therefore, an enormous Rb/Sr value and a smaller Zr/Rb value can represent a humid environment with high rainfall and intense chemical weathering, and vice versa, a dry environment with weak chemical weathering and low rainfall. The sum of Ti+V+Cr+Zr+Ga elemental hydrolyzates marks the distribution of the landing source material and migrates into the water as part of the coarse suspension, which is positively correlated with the weathering intensity (Ryabogina et al., 2019). The Rb/Sr values in the GGL profiles showed a similar trend to the sum of CIA and Ti+V+Cr+Zr+Ga (r = 0.93, 0.98), which can well reflect the change of weathering intensity (**Figures 5D–G**).

## Holocene Paleoenvironmental Evolution of the Liangzhu Area

The Ganggongling Dam is an artificial paleodam-like relic, and the available $^{14}C$ dating results indicate that it was built around 5000 cal a BP (Wang and Liu, 2015). Before the dam was built (6000~5500aBP), the median grain size curve fluctuated violently, and the grain size was at the coarsest and best-sorted stage in the entire section. This reflects the solid hydrodynamic conditions and frequent river swings at this time, which may have accumulated some flash flood alluvium (**Figure 4C**). After the dam was built (after 5500a BP), the sedimentary environment in the dam was dominated by lacustrine facies, which well recorded the precipitation changes in this area. In this paper,

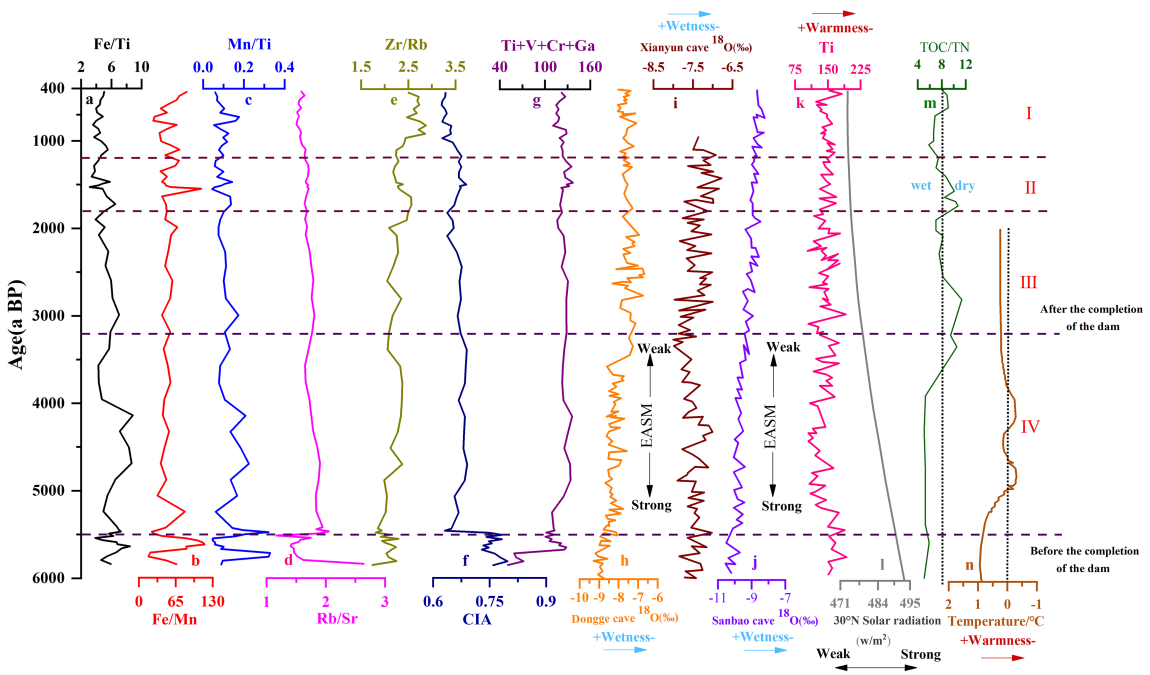


**FIGURE 5** | Comparison of EASM records from GGL section **(A–G)** and other monsoon regions records. **(H)** Stalagmite $^{18}O$ record from the Dongge Cave in China (Dykoski et al., 2005); **(I)** Stalagmite $^{18}O$ record from the Xianyun Cave in China (Che et al., 2018); **(J)** Stalagmite $^{18}O$ record from the Sanbao Cave in China (Dong et al., 2013); **(K)** Elemental intensity of Ti in Huguangyan Maar Lake (Wu et al., 2011); **(L)** 30°N June Insolation (Berger and Loutre, 1991); **(M)** Ratio of total organic carbon to total nitrogen (TOC/TN) (Yang et al., 2011); **(N)** Pollen records of Core CM97 (Yi et al., 2003).

lithologic and multi-proxy data from the GGL section is correlated with previously published literature from the study area to reveal detailed paleoenvironmental evolution and monsoonal changes in the Liangzhu region since about 5500a BP. Specifically, the mid-late Holocene paleoenvironmental evolution is grouped into Stage IV ~ Stage I.

Stage IV: From 5500 to 3200 a BP, relatively higher values for the Rb/Sr and Ti+V+Cr+Zr+Ga, with correspondingly high CIA values, indicate more variability in the intensity of chemical weathering, reflecting a humid period (**Figures 5D, F, G**). Similarly, Fe/Mn ratio from GGL sediments is more positive at this stage, possibly reflecting an intensified humidity (**Figure 5B**). During the same interval, the $^{18}O$ values at the lower levels of Dongge Cave, Xianyun Cave, and Sanbao Cave indicate an increase in precipitation, that is, an enhancement of EASM (**Figures 5H–J**; Dykoski et al., 2005; Dong et al., 2010; Cui et al., 2017). In addition, the lower Ti content in the sediments of Huguangyan Maar Lake also reveals the warm and humid climate conditions (**Figure 5K**; Wu et al., 2011). The TOC/TN values of core CM97 from the Changjiang Estuary, located in the East Asian monsoon region, also recorded an increase in precipitation during the contemporaneous period, likeness to the GGL profile (**Figure 5M**, Yang et al., 2011).

Stage III: Between 3200 and 1800 a BP, the chemical weathering intensity gradually weakened, as indicated by elemental indicators in the GGL section, and an arid climate probably caused this. The CIA values are relatively low, with comparatively small fluctuations (**Figure 5D**). Fe/Mn, Rb/Sr ratios, and Ti+V+Cr+Zr+Ga remained stable and lower, while Zr/Rb, Fe/Ti, and Mn/Ti increased significantly (**Figures 5A–C, E–G**). These data all indicate a considerably dry phase. Grain size evidence suggests that the profile shifts to a less hydrodynamic lacustrine environment (**Figure 4C**). Within this time interval, the increasing rate of the stalagmite $\delta^{18}O$ record from Dongge cave, Xianyun cave, and Sanbao cave provide additional evidence for this dry interval (**Figures 5H–J**; Dykoski et al., 2005; Dong et al., 2010; Cui et al., 2017). Furthermore, a dry period from 3000 to 2000 cal yr BP was also detected in Ti and TOC/TN record from the Huguangyan Maar Lake and core CM97 (**Figure 5K, M**, Wu et al., 2011; Yang et al., 2011). Combined with the weakening of solar radiation, the intensity of EASM in this stage remarkably decreased (Berger and Loutre, 1991).

Stage II: From 1800 to1200a BP, the intensity of chemical weathering is slightly higher than in stage III, but the overall fluctuation is not significant. As indicated by elemental ratios and CIA values in the GGL section, this could be caused by a slightly enhanced warm and humid climate. Similarly, $\delta^{18}O$ values from Dongge cave and Sanbao cave showed a slight decrease in magnitude for this time interval, possibly reflecting the increased wetness (Dykoski et al., 2005; Dong et al., 2010). Previous studies from Yangtze River estuary sediments also confirm that warm and humid climatic conditions occurred around 1500 a BP (Yao et al., 2015; Li et al., 2016). The humid-loving pollen records from the Dianshan Lake and Yangtze River Delta provide further evidence of a warm-humid period since 1800 aBP (Yi et al., 2003; Zhang, 2005; Yi et al., 2006). The intensity of EASM increased slightly in this phase.

Stage I: Between 1200 and 400 a BP, Rb/Sr, Fe/Mn, CIA, and Ti+V+Cr+Zr+Ga were further reduced. Meanwhile, the Fe/Ti, Mn/Ti, and Zr/Rb ratios notably increased. As recorded in these element ratios in GGL sediments, relatively weak chemical weathering is closely related to cold and dry climatic conditions. Similarly, in the Dongge cave and Sanbao cave, a dry climate phase was inferred from the $\delta^{18}O$ record (**Figures 5H–J**; Dykoski et al., 2005; Dong et al., 2010; Cui et al., 2017). The Ti records from Huguangyan Maar Lake also confirm that it was characterized by cold and dry climatic conditions (**Figure 5K**; Wu et al., 2011). The above evidence shows a further weakening of EASM intensity.

## Environmental Significance of Dams and the Response of Human Activities

The Liangzhu area is highly influenced by the East Asian summer winds and is also vulnerable to extreme climatic and environmental events, such as typhoons, storms, floods, and seawater intrusion (Fan et al., 2017). From the topographic location, there are several rivers in the northern mountains of the ancient city of Liangzhu. It is not difficult to speculate that when typhoons and storm events occur, flash floods or mudslides are likely to form around the area, which seriously threatens the safety of the ancient city and the ancestors living in Liangzhu (Zong et al., 2012; Long et al., 2014; Wang et al., 2018; Ling et al., 2021). The Gangongling dam in this paper was built in the late Liangzhu culture around 5000 years ago and was abandoned after the Liangzhu culture. Therefore, the environmental significance of the dam can be understood by comparing the changes in the depositional environment of the dam before and after its construction. Before the dam was built (6000-5000a BP), it was a river environment with an unstable depositional environment and a frequently oscillating river channel, with coarse sediment particles, reflecting the strong hydrodynamic conditions and the ability of flash floods to carry materials of larger grain size to accumulate here (**Figure 5**). During the use of the dam (5000-3900a BP), the depositional environment inside the dam changed from fluvial facies to floodplain facies, and the depositional environment was relatively stable. At this time, the sediment particles were smaller, and the hydrodynamic force was weak, indicating that the completion of the Ganggongling Dam had a positive significance for regulating flash floods (**Figure 4C**). After the dam was abandoned (3900~400 a BP), the hydrodynamic force gradually weakened. To about 3200~1200 aBP, dark gray lacustrine facies deposits developed, indicating that after the dam was abandoned, the lack of manual management resulted in blockage of the drainage outlet, and the water flow in the dam was not smooth and blocked.

The documentary record shows that the construction of the dam near the ancient city of Liangzhu was several hundred years later than the ancient city, probably reflecting the fact that the ancient people of Liangzhu realized the importance of building dams by summing up their experience of the development of the Majiahong and Songze cultures in the past centuries or even two thousand years (Liu, 2008). The ancients gradually realized that ancient cities and farmlands were vulnerable to flash floods under the climate and precipitation conditions of the region.

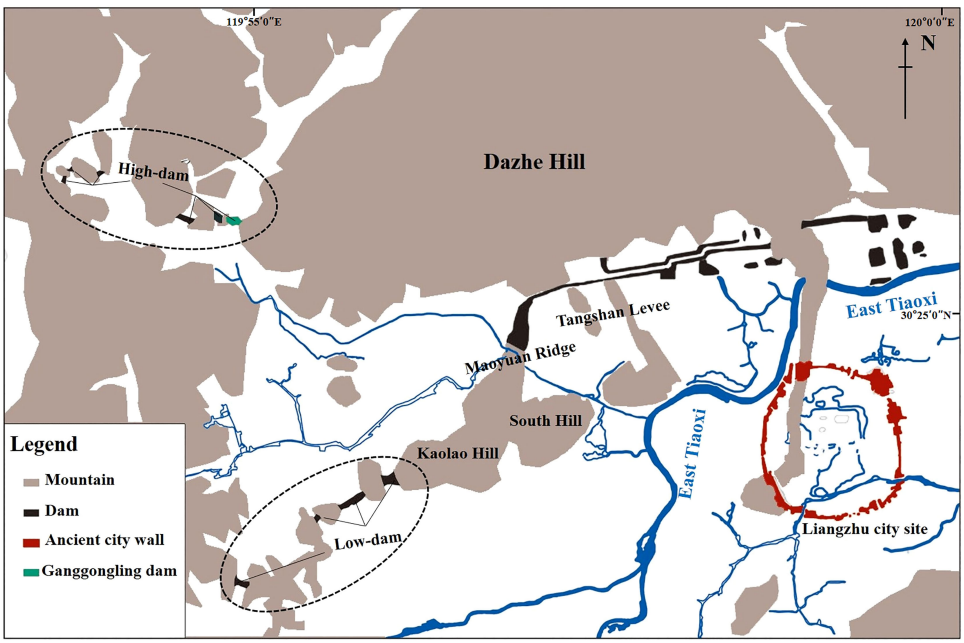


**FIGURE 6** | Topographic map showing the location of Liangzhu City and the hydraulic enterprise system (Modified by Liu et al., 2014a).

Therefore, protection against surges through the construction of dams was the most basic need to protect the ancient cities and the surrounding farmland (Liu et al., 2014a).

In addition to the function of flood control and water storage, the reservoirs formed by multi-stage dams were also important transportation channels at that time (**Figure 6**). In the high-dam system, the reservoir area formed by Ganggongling, Huoling, and Zhoujiafan dams can go up the valley about 3000m when it is complete. The low-dam system can go north about 3700m when it is done and reach below Ganggongling dam, and the northeast side is connected with the Tangshan long dike, which plays a perfect role in water transportation (Liu et al., 2014; Wang and Liu, 2015). These hydraulic facilities also facilitated the development of rice agriculture, as evidenced by evidence that organic matter lenses distributed in a chalky to clayey soil matrix in rice fields at the Maoshan site may have formed under controlled flooding or irrigation (Zhuang et al., 2014).

In general, the construction of the GGL dam reflects the qualitative change in the ideology of the ancient people during the Liangzhu culture and is an essential step in the development of Neolithic society. In the process of environmental change, the ancient people no longer simply adapted to the natural environment by migrating to higher ground but actively sought to transform it (Liu et al., 2018). Thus, the emergence of ancient cities and dams resulted from the close combination of a stable environment, developed products, and social development. It also reflects the transformation of Liangzhu culture from a rice-based agricultural civilization to a high-level society with an embryonic class and social division of labor (Shi et al., 2011; Liu et al., 2017b).

## Possible Driving Mechanisms Contributing to the Multi-Decadal to Centennial EASM Variations

Variations in the EASM on decades to centuries scales during the Holocene may be attributed to many factors, and solar activity is thought to be the dominant factor in EASM oscillations (Fleitmann et al., 2003; Jia et al., 2015; Zheng et al., 2015). The summer monsoon originates from low latitude ocean air mass and is greatly affected by solar radiation, so the summer monsoon responds better to solar radiation (Wehausen and Brumsack, 2002). The decades- to centuries-scale drought intervals recorded in the SC2 content and Na/K ratio of the GGL profile correlate with the time interval of solar radiation intensity (TSI) reduction inferred from cosmic ray-derived radionuclides (**Figures 7A–C**, Steinhilber et al., 2012), suggesting that solar activity conditions may control precipitation fluctuations during the Holocene in coastal eastern China. Further evidence for this proposition is provided by the significant similarity between the cyclic variation in SC2 content and the variation in solar radiation intensity recorded at $\Delta^{14}C$ (Damon and Sonett, 1991). However, the drive-response relationship within the monsoon system is difficult to explain by a single model (Ding et al., 1995; Gupta et al., 2003). Thus, we conclude that further amplification mechanisms such as the El Niño-Southern Oscillation (ENSO) in the equatorial Pacific (Marchitto et al., 2010; Lim and Fujiki, 2011; Jia et al., 2015; Park et al., 2016) may play an important role in enhancing the influence of solar radiation on EASM precipitation.

The tropical Pacific atmosphere-ocean system plays an important regulatory role between the Sun and the Earth's

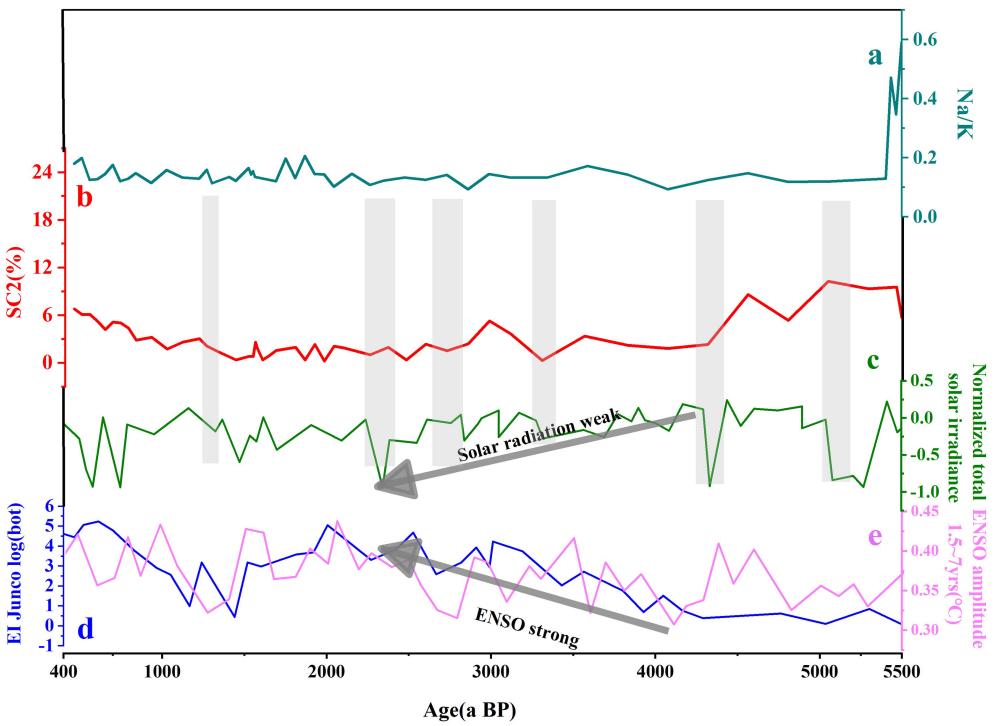


**FIGURE 7** | Comparison of multi-decadal to centennial time scale climate changes recorded in GGL section **(A, B)** with potential forcing factors **(C–E)**. **(A)** Na/K ratio in the GGL section; **(B)** grain size sensitive component 2 content in the GGL section; **(C)** normalized total solar irradiance reconstructed from a cosmic ray intensity record (Steinhilber et al., 2012); **(D)** ENSO-like record from Lake El Junco indicated by the Botryococcene concentration (Conroy et al., 2008); **(E)** ENSO amplitude simulation results in the 100-year window from CCSM3 model (Liu et al., 2014b).

climate. The sea-air feedback system produces persistent El Niño-like SST anomalies when solar radiation decreases, gradually affecting the climate worldwide (Emile-Geay et al., 2007). Previous studies have shown that ENSO strongly influenced the changes in the East Asian monsoon during the Holocene, and the intensity of ENSO activity varied greatly (Conroy et al., 2008; Chen et al., 2016). At Lake El Junco in the Galápagos Islands, strong and frequent El Niño events occurred during 4000-2000 cal a B.P. and were documented by indicators such as lake grain size, staphylococcal concentration, and $\delta^2H$ (Conroy et al., 2008; Zhang et al., 2014). In addition, sea surface temperature, photosynthetic pigments, and rocky debris material in marine sediments near the Peruvian coast collectively reflect the maximum El Niño activity during the 3000-2000 cal a B.P. period (Conroy et al., 2008; Zhang et al., 2014). Our results show that the dry periods indicated by SC2 and Na/K in the GGL profiles are broadly consistent with the weakening of ENSO activity in the late Holocene (**Figures 7A, B, D, E**). In other words, this suggests that stronger ENSO can trigger significant amounts of precipitation in the Liangzhu area and also implies that ENSO activity plays a dominant role in decades to centuries of extreme climate change. In modern observations and simulations, scholars have confirmed that the increase in rainfall in the lower Yangtze River is strongly associated with enhanced ENSO activity (Tong et al., 2006; Li et al., 2011; Zeng et al., 2011). In addition, a significant increase in the frequency of ENSO-related storm events in the middle Yangtze River during the Late Holocene provides further evidence for a strong link between enhanced ENSO activity and increased precipitation in central China (Hong et al., 2006; Zhu et al., 2017). The reason may be that the improved ENSO activity (El Niño state) and the weakened solar activity lead to the negative anomaly in the Indo-Pacific warm pool SST, which induces the formation of Kelvin waves in the cold phase in the western Pacific. This causes abnormal cyclonic activity in the northwest Pacific Ocean, preventing monsoon moisture transport to the south and north of China (Jia et al., 2015; Rao et al., 2016).

## CONCLUSIONS

Geochemical and grain size data from the GGL section from the Liangzhu city complex in eastern China provide a ~5500a record of paleoclimate evolution and the EASM precipitation variations. Two intervals of stronger chemical weathering indicate a humid-warm climate, occurring at 5500~3200 a BP and 1800~1200 a BP. Weak chemical weathering intensities during the 3200~1800 a BP and 1200~400 a BP suggest dry and cold climate conditions. Although some sedimentation information from the use of the dam is missing, a comparison of the sedimentation environment information inside Ganggongling Dam before its construction and after its abandonment clearly shows that the sedimentation

environment was significantly more stable after the dam was built than before. This reflects that the construction of the dam has played a positive role in regulating flash floods, not only by intercepting them to prevent them from entering the Hangjiahu Plain but also by storing water, thus alleviating the adverse effects of dry climatic conditions on human beings, and meeting the demand for water for production and living such as rice cultivation. Besides, our findings suggest that the multi-decadal to centennial EASM intensity fluctuations are primarily affected by solar irradiance. The amplification of internal forcing mechanisms, such as the El Niño-Southern Oscillation (ENSO) in the equatorial Pacific, may play an important role in enhancing the influence of solar radiation on EASM precipitation.

## DATA AVAILABILITY STATEMENT

The raw data supporting the conclusions of this article will be made available by the authors, without undue reservation.

## AUTHOR CONTRIBUTIONS

CZ: Conceptualization, Formal analysis, Resources, Writing original draft. LM: Formal analysis, Investigation, Editing, Funding acquisition. SS : Formal analysis, Editing. SZ: Formal analysis, Investigation, Editing. DM: Formal analysis, Investigation, Funding acquisition. All authors contributed to the article and approved the submitted version.

## ACKNOWLEDGMENTS

This work was supported by the National Natural Science Foundation of China (grant number: 41771218), the National Key Research and Development Program of China (grant number:2020YFC1521605), and the National Social Science Major Foundation of China (grant number:19ZDA231). We thank the reviewers for their constructive comments that help improve an earlier version of our manuscript.

## REFERENCES

Amorosi, A., Sammartino, I., and Sarti, G. (2013). Background Levels of Potentially Toxic Metals From Soils of the Pisa Coastal Plain (Tuscany, Italy) as Identified From Sedimentological Criteria. *Environ. Earth Sci.* 69 (5), 1661–1671. doi: 10.1007/s12665-012-2001-8

Banerjee, D., Murray, A S., Bøtter-Jensen, L., and Lang, A (2001). Equivalent Dose Estimation Using a Single Aliquot of Polymineral Fine Grains. *Radiation Measurements* 33, 73–94. doi: 10.1016/S1350-4487(00)00101-3

Berger, A., and Loutre, M. F. (1991). Insolation Values for the Climate of the Last 10 Million Years. *Quaternary Sci. Rev.* 10 (4), 297–317. doi: 10.1016/0277-3791(91)90033-Q

Boës, X., Rydberg, J., Martinez-Cortizas, A., Bindler, R., and Renberg, I. (2012). Evaluation of Conservative Lithogenic Elements (Ti, Zr, Al, and Rb) to Study Anthropogenic Element Enrichments in Lake Sediments. *J. Paleolimnol* 46, 75–87. doi: 10.1007/s10933-011-9515-z

Boulay, S., Colin, C., Trentesaux, A., Clain, S., Liu, Z., and Lauer-Leredde, C. (2007). Sedimentary Responses to the Pleistocene Climatic Variations Recorded in the South China Sea. *Quaternary Res.* 68 (1), 162—172. doi: 10.1016/j.yqres.2007.03.004

Boyle, J. F. (2002). Inorganic Geochemical Methods in Paleolimnology. *Tracking Environ. Change Using Lake Sediment* 2, 83–141. doi: 10.1007/0-306-47670-3_5

Chang, H., An, Z. S., Wu, F., Jin, Z. D., Liu, W. G., and Song, Y. G. (2013). An Rb/Sr Record of the Weathering Response to Environmental Changes in Westerly Winds Across the Tarim Basin in the Late Miocene to the Early Pleistocene. *Palaeogeography Palaeoclimatol. Palaeoecol.* 386 (6), 364–373. doi: 10.1016/j.palaeo.2013.06.006

Chen, S., Hoffmann, S. S., Lund, D. C., Cobb, K. M., Emile-Geay, J., and Adkins, J. F. (2016). A High-Resolution Speleothem Record of Western Equatorial Pacific Rainfall: Implications for Holocene ENSO Evolution. *Earth Planet. Sci. Lett.* 442, 61–71. doi: 10.1016/j.epsl.2016.02.050

Chen, C., Wang, J. S., Wang, Z., Peng, Y. B., Chen, X. H., Ma, X. C., et al. (2020). Variation of Chemical Index of Alteration (CIA) in the Ediacaran Doushantuo Formation and its Environmental Implications. *Precambrian Res.* 347, 105829. doi: 10.1016/j.precamres.2020.105829

Chen, Z., Zong, Y., Wang, Z., Wang, H., and Chen, J. (2008). Migration Patterns of Neolithic Settlements on the Abandoned Yellow and Yangtze River Deltas of China. *Quaternary Res.* 70 (2), 301–314. doi: 10.1016/j.yqres.2008.03.011

Che, Y. P., Xiao, H. Y., Cui, M. Y., Jiang, X. Y., and Cai, B. G. (2018). Age and Subrotational Characteristics of the Heinrich2 Event Recorded in the Stalagmite of Xianyun Cave, Minxi. *J. Sedimentol.* 36 (6), 9. doi: 10.14027/j.issn.1000-0550.2018.143

Colman, S. M., Yu, S. Y., An, Z. S., Shen, J., and Henderson, A. C. G. (2007). Late Cenozoic Climate Changes in China's Western Interior: A Review of Research on Lake Qinghai and Comparison With Other Records. *Quaternary Sci. Rev.* 26 (17-18), 2281–2300. doi: 10.1016/j.quascirev.2007.05.002

Conroy, J. L., Overpeck, J. T., Cole, J. E., Shanahan, T. M., and Steinitz-Kannan, M. (2008). Holocene Changes in Eastern Tropical Pacific Climate Inferred From a Galápagos Lake Sediment Record. *Quaternary Sci. Rev.* 27, 1166–1180. doi: 10.1016/j.quascirev.2008.02.015

Cui, M. Y., Xiao, H. Y., Sun, X. S., Hong, H., Jiang, X. Y., and Cai, B. G. (2017). Characteristics of the Heinrich 1 Abrupt Climate Event Inferred From a Speleothem Record From Xianyun Cave, Fujian Province. *Chin. Sci. Bull.* 62 (26), 11. doi: 10.1360/N972017-00091

Cullen, H. M., Demenocal, P. B., Hemming, S., Hemming, G., Brown, F. H., Guilderson, T., et al. (2000). Climate Change and the Collapse of the Akkadian Empire: Evidence From the Deep Sea. *Geology* 28 (4), 379–382. doi: 10.1130/0091-7613(2000)2<379:CCATCO>2.0.CO;2

Damon, P. E., and Sonett, C. P. (1991). "Solar and Terrestrial Components of Theatmospheric14c Variation Spectrum," in *The Sun in Time*. Eds. C. P. Sonett, M. S. Giampapa and M. S. Matthews (Tucson: University of Arizona Press), 360–388.

Davison, W. (1993). Iron and Manganese in Lakes. *Earth Sci. Rev.* 34 (2), 119–163. doi: 10.1016/0012-8252(93)90029-7

Ding, Z. L., and Yu, C. W. (1995). Dynamical Mechanisms of Monsoonal Changes in East Asia During the Quaternary Period. *Quaternary Res.* 15 (1), 63–74.

Dixit, Y., Hodell, D. A., and Petrie, C. A. (2014). Abrupt Weakening of the Summer Monsoon in Northwest India ~4100 Yr Ago. *Geology* 42 (4), 339–342. doi: 10.1130/G35236.1

Dong, J. G., Diao, W., and Kong, X. K. (2013). Variation in Uranium Isotopes of Stalagmites From Sanbao Cave, Hubei Province: Implications for Palaeoclimate. *Marine Geol. Quaternary Geol.* 33 (1), 129–136. doi: 10.3724/SP.J.1140.2013.01129

Dong, G. H., Ruo, L., Lu, M. X., Zhang, D. J., and Nathaniel, J. (2019). Evolution of Human-Environmental Interactions in China From the Late Paleolithic to the Bronze Age. *Prog. Phys. Geography: Earth Environ.* 44 (2), 233–250. doi: 10.1177/0309133319876802

Dong, J., Wang, Y., Cheng, H., Hardt, B., Edwards, R. L., Kong, X., et al. (2010). A High-Resolution Stalagmite Record of the Holocene East Asian Monsoon From Mt Shennongjia, Central China. *Holocene* 20 (2), 257–264. doi: 10.1177/0959683609350393

Du, S., Li, B., Niu, D., Zhang, D. D., Wen, X., Chen, D., et al. (2011). Age of the MGS5 Segment of the Milanggouwan Stratigraphical Section and Evolution of the Desert Environment on a Kiloyear Scale During the Last Interglacial in

China's Salawusu River Valley: Evidence From Rb and Sr Contents and Ratios. *Geochemistry* 71 (1), 87–95. doi: 10.1016/j.chemer.2010.07.002

Dykoski, C. A., Edwards, R. L., Cheng, H., Yuan, D. X., Cai, Y. J., Zhang, M. L., et al. (2005). A High-Resolution, Absolute-Dated Holocene and Deglacial Asian Monsoon Record From Dongge Cave, China. *Earth Planet. Sci. Lett.* 233 (1-2), 71–86. doi: 10.1016/j.epsl.2005.01.036

Emile-Geay, J., Cane, M., Seager, R., Kaplan, A., and Almasi, P. (2007). El Niño as a Mediator of the Solar Influence on Climate. *Paleoceanography* 22 (3), 3210. doi: 10.1029/2006PA001304

Fan, D. D., Wu, Y. J., Zhang, Y., Burr, G., Huo, M., and Li, J. (2017). South Flank of the Yangtze Delta: Past, Present, and Future. *Mar. Geol.* 392, 78–93. doi: 10.1016/j.margeo.2017.08.015

Fleitmann, D., Burns, S. J., Mudelsee, M., Neff, U., Kramers, J., Mangini, A., et al. (2003). Holocene Forcing of the Indian Monsoon Recorded in a Stalagmite From Southern Oman. *Science* 300 (5626), 1737–1739. doi: 10.1126/science.1083130

Fu, C.F., An, Z.S., Qiang, X., Bloemendal, J., Song, Y., and Chang, H (2013). Magnetostratigraphic Determination of the Age of Ancient Lake Qinghai, and Record of the East Asian Monsoon Since 4.63 Ma. *Geology* 41 (8), 875–78. doi: 10.1130/G34418.1

Fu, J. H., Li, S. X., and Niu, X. B. (2018). Paleo-Sedimentary Environmental Restoration and its Significance of Chang 7 Member of Triassic Yanchang Formation in Ordos Basin, NW China. *Petroleum Explor. Dev.* 45 (6), 998–1008. doi: 10.1016/S1876-3804(18)30104-6

Gai, C. C., Liu, Q. S., Roberts, A. P., Chou, Y. M., Zhao, X. X., Jiang, Z. X., et al. (2020). East Asian Monsoon Evolution Since the Late Miocene From the South China Sea. *Earth Planet. Sci. Lett.* 530, 115960. doi: 10.1016/j.epsl.2019.115960

Goldsmith, Y., Broecker , W.S., Xu, H., Polissar, P.J., deMenocal, P.B., Porat, N, et al. (2017). Northward Extent of East Asian Monsoon Covaries With Intensity on Orbital and Millennial Timescales. *Proc. Natl. Acad. Sci. U. S. A.* 114, 1817–21. doi: 10.1073/pnas.1616708114

González-Sampériz, P., Valero-Garcés, B. L., Moreno, A., Morellón, M., Navas, A., Machín, J., et al. (2008). Vegetation Changes and Hydrological Fluctuations in the Central Ebro Basin (Ne Spain) Since the Late Glacial Period: Saline Lake Records. *Palaeogeography Palaeoclimatol. Palaeoecol.* 259 (2), 157–181. doi: 10.1016/j.palaeo.2007.10.005

Gupta, A. K., Anderson, D. M., and Overpeck, J. T. (2003). Abrupt Changes in the Asian Southwest Monsoon During the Holocene and Their Links to the North Atlantic Ocean. *Nature* 421, 354–357. doi: 10.1038/nature01340

Hong, B., Lin, Q. H., and Hong, Y. T. (2006). Holocene Asian Monsoon, ENSO, and High Northern Latitude Climate Correlation. *Chin. Sci. Bull.* 51 (17), 8. doi: 10.1360/csb2006-51-17-1977

Huang, C., Wei, G., Li, W., and Liu, Y. (2018). A Geochemical Record of the Link Between Chemical Weathering and the East Asian Summer Monsoon During the Late Holocene Preserved in Lacustrine Sediments From Poyang Lake, Central China. *J. Asian Earth Sci.* 154, 17–25. doi: 10.1016/j.jseaes.2017.12.008

Huan, X. J., Zhang, J. P., Zhuang, Y. J., Fan, C., Wang, N. Y., Ji, X., et al. (2022). Intensification of Rice Farming and its Environmental Consequences Recorded in a Liangzhu Reservoir, China. *Quaternary Int.* 619, 39–45. doi: 10.1016/j.quaint.2022.01.012

Innes, J. B., Zong, Y., Wang, Z., and Chen, Z. (2014). Climatic and Palaeoecological Changes During the Mid-to-Late Holocene Transition in Eastern China: High-Resolution Pollen and non-Pollen Palynomorph Analysis at Pingwang, Yangtze Coastal Lowlands. *Quaternary Sci. Rev.* 99 (9), 164–175. doi: 10.1016/j.quascirev.2014.06.013

Jeong, G. Y., Cheong, C. S., and Kim, J. (2006). Rb-Sr and K-Ar Systems of Biotite in Surface Environments Regulated by Weathering Processes With Implications for Isotopic Dating and Hydrological Cycles of Sr Isotopes. *Geochimica Et Cosmochimica Acta* 70 (18), 4734–4749. doi: 10.1016/j.gca.2006.07.012

Jia, G., Bai, Y., Yang, X., Xie, L., Wei, G., Ouyang, T., et al. (2015). Biogeochemical Evidence of Holocene East Asian Summer and Winter Monsoon Variability From a Tropical Maar Lake in Southern China. *Quaternary Sci. Rev.* 111, 51–61. doi: 10.1016/j.quascirev.2015.01.002

Kalinin, P. I., Kudrevatykh, I. Y., Vagapov, I. M., Borisov, A. V., and Alekseev, A. O. (2018). Biogeochemical Processes in Steppe Landscapes of the Ergeni Upland in the Holocene. *Eurasian Soil Sci.* 51 (5), 495–505. doi: 10.1134/S1064229318050058

Kennett, D. J., Breitenbach, S., Aquino, V. V., Asmerom, Y., Awe, J., Baldini, J., et al. (2012). Development and Disintegration of Maya Political Systems in Response to Climate Change. *Science* 338 (6108), 788–791. doi: 10.1126/science.1226299

Kidder, T. R., Adelsberger, K. A., Arco, L. J., and Schilling, T. M. (2008). Basin-Scale Reconstruction of the Geological Context of Human Settlement: An Example From the Lower Mississippi Valley, USA. *Quaternary Sci. Rev.* 27 (11-12), 1255–1270. doi: 10.1016/j.quascirev.2008.02.012

Kirwan, M. L., and Megonigal, J. P. (2013). Tidal Wetland Stability in the Face of Human Impacts and Sea-Level Rise. *Nature* 504 (7478), 53–60. doi: 10.1038/nature12856

Kronberg, B. I., Nesbitt, H. W., and Lam, W. W. (1986). Upper Pleistocene Amazon Deep-Sea Fan Muds Reflect Intense Chemical Weathering of Their Mountainous Source Lands. *Chem. Geol.* 54 (3-4), 283–294. doi: 10.1016/0009-2541(86)90143-9

Kutzbach, J. E. (1981). Monsoon Climate of the Early Holocene: Climate Experiment With the Earth's Orbital Parameters for 9000 Years Ago. *Science* 214 (4516), 59–61. doi: 10.1126/science.214.4516.59

Kylander, M. E., Ampel, L., Wohlfarth, B., and Veres, D. (2011). High-Resolution X-Ray Fluorescence Core Scanning Analysis of Les Echets (France) Sedimentary Sequence: New Insights From Chemical Proxies. *J. Quaternary Sci.* 26 (1), 109–117. doi: 10.1002/jqs.1438

Lai, Z., and Brückner, H. (2008). Effects of Feldspar Contamination on Equivalent Dose and the Shape of Growth Curve for OSL of Silt-Sized Quartz Extracted From Chinese Loess. *Geochronometria* 30, 49–53. doi: 10.2478/v10003-008-0010-0

Lim, J., and Fujiki, T. (2011). Vegetation and Climate Variability in East Asia Driven by Low Latitude Oceanic Forcing During the Middle to Late Holocene. *Quaternary Sci. Rev.* 30 (19-20), 2487–2497. doi: 10.1016/j.quascirev.2011.05.013

Ling, G. J., Ma, C. M., Yang, Q., Hu, Z. J., Zheng, H. B., Liu, B., et al. (2021). Landscape Evolution in the Liangzhu Area Since the Early Holocene: A Comprehensive Sedimentological Approach. *Palaeogeography Palaeoclimatol. Palaeoecol.* 562, 110141. doi: 10.1016/j.palaeo.2020.110141

Liu, B. (2008). Report of Archaeological Excavation on Liangzhu City-Site in Hangzhou City for the Period 2006~2007. *Archaeology* 7, 586—579.

Liu, T., Liu, Y., Sun, Q., Zong, Y., Finlayson, B., and Chen, Z. (2017b). Early Holocene Groundwater Table Fluctuations in Relation to Rice Domestication in the Middle Yangtze River Basin, China. *Quaternary Sci. Rev.* 155, 79–85. doi: 10.1016/j.quascirev.2016.11.015

Liu, Z. Y., Lu, Z. Y., Wen, X. Y., Otto-Bliesner, B. L., Timmermann, A., and Cobb, K. M. (2014b). Evolution and Forcing Mechanisms of El Nino Over the Past 21,000 Years. *Nature* 515, 550–553. doi: 10.1038/nature13963

Liu, B., Wang, N., Chen, M., Wu, X., Mo, D., Liu, J., et al. (2017a). Earliest Hydraulic Enterprise in China 5,100 Years Ago. *Proc. Natl. Acad. Sci.* 114 (52), 13637–13642. doi: 10.1073/pnas.1710516114

Liu, B., Wang, N. Y., Zheng, Y. F., Chen, X. G., Zhou, W. L., Yan, K. K., et al. (2014a). Findings of Archaeological Survey of Prehistoric City at Liangzhu During 2006-2013. *Southeast Culture* 2, 31–38.doi: 10.3969/j.issn.1001-179X.2017.06.010

Liu, S., Shi, X., Liu, Y., Wu, Y., Yang, G., and Wang, X (2013). Holocene Paleoclimatic Reconstruction Based on Mud Deposits on the Inner Shelf of the East China Sea. *J. Asian Earth Sci.* 69 113–20. doi: 10.1016/j.jseaes.2013.01.003

Liu, Y., Sun, Q., Fan, D., Dai, B., Ma, F., Xu, L, et al. (2018). Early to Middle Holocene Sea Level Fluctuation, Coastal Progradation and the Neolithic Occupation in the Yaojiang Valley of Southern Hangzhou Bay, Eastern China. *Quat. Sci. Rev.* 189, 91–104. doi: 10.1016/j.quascirev.2018.04.010

Li, X., Yang, H., Yao, Y., Chen, Y., and Liu, W. (2016). Precipitation Changes Recorded in the Sedimentary Total Organic Carbon Isotopes From Lake Poyang in the Middle and Lower Yangtze River, Southern China Over the Last 1600 Years. *Quaternary Int.* 425 (2), 292–300. doi: 10.1016/j.quaint.2016.07.020

Li, W., Zhai, P., and Cai, J. (2011). Research on the Relationship of ENSO and the Frequency of Extreme Precipitation Events in China. *Adv. Climate Change Res.* 2 (2), 101–107. doi: 10.3724/SP.J.1248.2011.00101

Li, P., Zhang, C. X., Wu, H. B., and Gao, Z. W. (2022). Geochemical Characteristics of Holocene Loess-Paleosol Sequences in Central Chinese

Loess Plateau and Their Implications for East Asian Monsoon Evolution. *Quaternary Int.* 616, 99–108. doi: 10.1016/j.quaint.2021.10.017

Long, T., Qin, J., Atahan, P., Mooney, S., and Taylor, D. (2014). Rising Waters: New Geoarchaeological Evidence of Inundation and Early Agriculture From Former Settlement Sites on the Southern Yangtze Delta, China. *Holocene* 24 (5), 546–558. doi: 10.1177/0959683614522309

Lu, P. Y. (2008). *Study on the Sedimentary Structure and Spatial Spreading Pattern of the Quaternary in Hangzhou* (Hangzhou: Zhejiang University).

Macklin, M. G., Toonen, W. H., Woodward, J. C., Williams, M. A., Flaux, C., Marriner, N., et al. (2015). A New Model of River Dynamics, Hydroclimatic Change and Human Settlement in the Nile Valley Derived From Meta-Analysis of the Holocene Fluvial Archive. *Quaternary Sci. Rev.* 130, 109–123. doi: 10.1016/j.quascirev.2015.09.024

Marchitto, T. M., Muscheler, R., Ortiz, J. D., Carriquiry, J. D., and van Geen, A. (2010). Dynamical Response of the Tropical Pacific Ocean to Solar Forcing During the Early Holocene. *Science* 330 (6009), 1378–1381. doi: 10.1126/science.1194887

Moreno, A., Giralt, S., Valero-Garcés, B., Sáez, A., Bao, R., Prego, R., et al. (2007). A 14 Kyr Record of the Tropical Andes: The Lago Chungará Sequence (18°s, Northern Chilean Altiplano). *Quaternary Int.* 161 (1), 4–21. doi: 10.1016/j.quaint.2006.10.020

Mu, Y., Qin, X, Zhang, , and Xu, L. (2016). Holocene Climate Change Evidence From High Resolution Loess/paleosol Records and the Linkage to Fire-Climate Change-Human Activities in the Horqin Dunefield in Northern China. *J. Asian Earth Sci.* 121, 1–8. doi: 10.1016/j.jseaes.2016.01.017

Munoz, S. E., Gruley, K. E., and Massie, A. (2015). Cahokia's Emergence and Decline Coincided With Shifts of Flood Frequency on the Mississippi River. *Proc. Natl. Acad. Sci. U.S.A* 112, 6319–6324. doi: 10.1073/pnas.1501904112

Nicholls, R. J., and Cazenave, R. (2010). Sea-Level Rise and its Impact on Coastal Zones. *Science* 328 (5985), 1517–1520. doi: 10.1126/science.118578

Nienhuis, J. H., Ashton, A. D., Edmonds, D. A., Hoitink, A., and Törnqvist, T. E. (2020). Global-Scale Human Impact on Delta Morphology has Led to Net Land Area Gain. *Nature* 577 (7791), 514–518. doi: 10.1038/s41586-019-1905-9

Núñez, L., Grosjean, M., and Cartajena, I. (2002). Human Occupations and Climate Change in the Punade Atacama, Chile. *Science* 298, 821–824. doi: 10.1126/science.1076449

Oldfield, F., Bloemendal, J., and Thompson, R. (1979). Magnetic Measurements Used to Access Sediment Influx at Llyn Goddionduon. *Nature* 280, 50–53. doi: 10.1038/280050a0

Park, J., Shin, Y. H., and Byrne, R. (2016). Late-Holocene Vegetation and Climate Change in Jeju Island, Korea and its Implications for ENSO Influences. *Quaternary Sci. Rev.* 153, 40–50. doi: 10.1016/j.quascirev.2016.10.011

Perri, F. (2020). Chemical Weathering of Crystalline Rocks in Contrasting Climatic Conditions Using Geochemical Proxies: An Overview. *Palaeogeography Palaeoclimatol. Palaeoecol.* 556, 109873. doi: 10.1016/j.palaeo.2020.109873

Rao, Z., Li, Y., Zhang, J., Jia, G., and Chen, F. (2016). Investigating the Long-Term Palaeoclimatic Controls on the δd and δ18o of Precipitation During the Holocene in the Indian and East Asian Monsoonal Regions. *Earth Sci. Rev.* 159, 292–305. doi: 10.1016/j.earscirev.2016.06.007

Rolett, B. V., Zheng, Z., and Yue, Y. F. (2011). Holocene Sea-Level Change and the Emergence of Neolithic Seafaring in the Fuzhou Basin (Fujian, China). *Quaternary Sci. Rev.* 30 (7-8), 788–797. doi: 10.1016/j.quascirev.2011.01.015

Rosenbaum, J. G., and Reynolds, R. L. (2004). Basis for Paleoenvironmental Interpretation of Magnetic Properties of Sediment From Upper Klamath Lake (Oregon): Effects of Weathering and Mineralogical Sorting. *J. Paleolimnol.* 31, 253–265. doi: 10.1023/B:JOPL.0000019228.46421.f4

Ryabogina, N. E., Afonin, A. S., Ivanov, S. N., Li, H. C., and Nikolaenko, S. A. (2019). Holocene Paleoenvironmental Changes Reflected in Peat and Lake Sediment Records of Western Siberia: Geochemical and Plant Macrofossil Proxies. *Quaternary Int.* 528, 73–87. doi: 10.1016/j.quaint.2019.04.006

Shi, C. X., Mo, D. W., Li, C. H., Liu, B., Mao, L. J, and Li, M. (2011). The Relationship Between Environmental Evolution and Human Activities of the Liangzhu Site Group Zhejiang Province, China. . *Earth Sci. Front.* 18 (13), 347–56.

Stankevica, K., Klavins, M., Vincevica-Gaile, Z., Kalnina, L., and Kaup, E. (2020). Accumulation of Metals and Changes in Composition of Freshwater Lake Organic Sediments During the Holocene. *Chem. Geol.* 539, 119502. doi: 10.1016/j.chemgeo.2020.119502

Stanley, D. J., and Chen, Z. (1996). Neolithic Settlement Distributions as a Function of Sea Level Controlled to Pography in the Yangtze Delta, China. *Geology* 24 (24), 1083–1086. doi: 10.1130/0091-7613(1996)024<1083:NSDAAF>2.3.CO;2

Steinhilber, F., Abreu, J. A., Beer, J., Brunner, I., Christl, M., Fischer, H., et al. (2012). 9,400 Years of Cosmic Radiation and Solar Activity From Ice Cores and Tree Rings. *Proc. Natl. Acad. Sci.* 109 (16), 5967–5971. doi: 10.1073/pnas.1118965109

Sun, Q., Liu, Y., Wünnemann, B., Peng, Y., and Chen, Z. (2019). Climate as a Factor for Neolithic Cultural Collapses Approximately 4000 Years BP in China. *Earth Sci. Rev.* 197, 102915. doi: 10.1016/j.earscirev.2019.102915

Timmermann, A., and Friedrich, T. (2016). Late Pleistocene Climate Drivers of Early Human Migration. *Nature* 538 (7623), 92–95. doi: 10.1038/nature19365

Tong, J., Zhang, Q., Zhu, D. M., and Wu, Y. J. (2006). Yangtze Floods and Droughts (China) and Teleconnections With ENSO Activities, (1470-2003). *Quaternary Int.* 144 (1), 29–37. doi: 10.1016/j.quaint.2005.05.010

Turney, C., and Brown, H. (2007). Catastrophic Early Holocene Sea-Level Rise, Human Migration, and the Neolithic Transition in Europe. *Quaternary Sci. Rev.* 26 (17-18), 2036–2041. doi: 10.1016/j.quascirev.2007.07.003

Wang, P., Du, Y. S., Yu, W. C., Algeo, T. J., Zhou, Q., Xu, Y., et al. (2020). The Chemical Index of Alteration (CIA) as a Proxy for Climate Change During Glacial-Interglacial Transitions in Earth History. *Earth Sci. Rev.* 201, 103032. doi: 10.1016/j.earscirev.2019.103032

Wang, N. Y., and Liu, B. (2015). Archaeological Investigation of the Peripheral Hydraulic System of the Ancient City of Liangzhu in Hangzhou. *Archaeology* 1), 3–13.

Wang, Z., Ryves, D. B., Lei, S., Nian, X., Lv, Y., Tang, L., et al. (2018). Middle Holocene Marine Flooding and Human Response in the South Yangtze Coastal Plain, East China. *Quaternary Sci. Rev.* 187, 80–93. doi: 10.1016/j.quascirev.2018.03.001

Wang, K. F., and Zhang, Y. L. (1981). Inferring the Climatic Changes in the Shanghai-Hangzhou Region for More Than 10,000 Years Based on Sporopollen Analysis. *Historical Geography* 1, 6.

Wehausen, R., and Brumsack, H. J. (2002). Astronomical Forcing of the East Asian Monsoon Mirrored by the Composition of Pliocene South China Sea Sediments. *Earth Planet. Sci. Lett.* 201 (3-4), 621–636. doi: 10.1016/S0012-821X(02)00746-X

Wu, X. D., Shen, J., and Wang, Y. (2011). Paleoenvironmental Evolution Since the Holocene as Reflected by Lacustrine Marl Lake Sediments. *Marine Geol. Quaternary Geol.* 31 (4), 8.

Xu, G. L. (2012). *Changes in the Structure and Connectivity of the Taihu Plain and Their Effects on Hydrological Processes* (Nanjing: Nanjing University).

Yang, S. Y., Tang, M., Yim, W. W. S., Zong, Y. Q., Huang, G. Q., Switzer, A. D., et al. (2011). Burial of Organic Carbon in Holocene Sediments of the Zhujiang (Pearl River) and Changjiang (Yangtze River) Estuaries. *Marine Chem.* 123 (1-4), 1–10. doi: 10.1016/j.marchem.2010.07.001

Yang, T., Zhang, J., and Shi, W. (2002). The Characteristics of Tidal Current Distribution in Zhapu Section of the Hangzhou Bay. *Donghai Mar. Sci.* 20 (4), 1–7. . doi: 10.3969/j.issn.1001-909X.2002.04.001

Yan, Z. M., Lu, X. X., and Zheng, G. A. (1959). Problems of Comprehensive Utilization of Soil and Water Resources in the Hangjia Lake Area. *Acta Geographica Sin.* 04), 299–312.

Yao, Y., Yang, H., Liu, W., Li, X., and Chen, Y. (2015). Hydrological Changes of the Past 1400 Years Recorded in δd of Sedimentary N-Alkanes From Poyang Lake, Southeastern China. *Holocene* 25, 1068–1075. doi: 10.1177/0959683615576231

Yi, S., Saito, Y., Oshima, H., Zhou, Y., and Wei, H. (2003). Holocene Environmental History Inferred From Pollen Assemblages in the Huanghe (Yellow River) Delta, China: Climatic Change and Human Impact. *Quaternary Sci. Rev.* 22, 609–628. doi: 10.1016/S0277-3791(02)00086-0

Yi, S., Saito, Y., and Yang, D. Y. (2006). Palynological Evidence for Holocene Environmental Change in the Changjiang (Yangtze River) Delta, China. *Palaeogeography Palaeoclimatol. Palaeoecol.* 241, 103–117. doi: 10.1016/j.palaeo.2006.06.016

Yi, S., Saito, Y., Zhao, Q. H., and Wang, P. X. (2003). Vegetation and Climate Changes in the Changjiang (Yangtze River) Delta, China, During the Past

13,000 Years Inferred From Pollen Records. *Quaternary Sci. Rev.* 22, 1501–1519. doi: 10.1016/S0277-3791(03)00080-5

Zeng, X., Li, B., Feng, F., Liu, X., and Zhou, T. (2011). East China Summer Rainfall During ENSO Decaying Years Simulated by a Regional Climate Model. *Atmos. Oceanic Sci. Lett.* 2011 (4), 91–97. . doi: 10.1080/16742834.2011.11446908

Zhang, Y. L. (2005). Study on the Late Quaternary Spore Powder and Paleoenvironment in Dianshan Lake Area. *J. Tongji University: Natural Sci. Edition* 33 (2), 6. doi: 10.3321/j.issn:0253-374X.2005.02.024

Zhang, Z. H., Leduc, G., and Sachs, J. P. (2014). El Niño's Evolution During the Holocene Revealed by a Biomarker Rain Gauge in the Galápagos Islands. *Earth Planet. Sci. Lett.* 404, 420–434. doi: 10.1016/j.epsl.2014.07.013

Zheng, Y. H., Li, Q. Y., Wang, Z. Z., Naafs, B. D. A., Yu, X. F., and Pancost, R. D. (2015). Peatland GDGT Records of Holocene Climatic and Biogeochemical Responses to the Asian Monsoon. *Organic Geochemistry* 87, 86–95. doi: 10.1016/j.orggeochem.2015.07.012

Zhuang, Y., Ding, P., and French, C. (2014). Water Management and Agricultural Intensification of Rice Farming at the Late-Neolithic Site of Maoshan, Lower Yangtze River, China. *Holocene* 24, 531–545. doi: 10.1177/0959683614522310

Zhu, Z., Feinberg, J. M., Xie, S., Bourne, M. D., Huang, C., and Hu, C. (2017). Holocene ENSO-Related Cyclic Storms Recorded by Magnetic Minerals in Speleothems of Central China. *Proc. Natl. Acad. Sci.* 114 (5), 852–857. doi: 10.1073/pnas.1610930114

Zong, Y., Chen, Z., Innes, J. B., Chen, C., Wang, Z., and Wang, H. (2007). Fire and Flood Management of Coastal Swamp Enabled First Rice Paddy Cultivation in East China. *Nature* 449 (7161), 459–462. doi: 10.1038/nature06135

Zong, Y., Wang, Z., Innes, J., and Chen, Z. (2012). Holocene Environmental Change and Neolithic Rice Agriculture in the Lower Yangtze Region of China: A Review. *Holocene* 22 (6), 623–635. doi: 10.1177/0959683611409775

**Conflict of Interest:** The authors declare that the research was conducted in the absence of any commercial or financial relationships that could be construed as a potential conflict of interest.

**Publisher's Note:** All claims expressed in this article are solely those of the authors and do not necessarily represent those of their affiliated organizations, or those of the publisher, the editors and the reviewers. Any product that may be evaluated in this article, or claim that may be made by its manufacturer, is not guaranteed or endorsed by the publisher.

frontiers | Frontiers in Marine Science

TYPE Original Research
PUBLISHED 26 July 2022
DOI 10.3389/fmars.2022.937616



OPEN ACCESS

EDITED BY
Joseph Carlin,
California State University, Fullerton, United States

REVIEWED BY
Jiantao Cao,
Tongji University, China
Qiang Xie,
Chinese Academy of Sciences (CAS), China

*CORRESPONDENCE
Gang Li
gangli@scsio.ac.cn

SPECIALTY SECTION
This article was submitted to Coastal Ocean Processes, a section of the journal Frontiers in Marine Science

RECEIVED 06 May 2022
ACCEPTED 29 June 2022
PUBLISHED 26 July 2022

CITATION
Li G, Miao L and Yan W (2022) Holocene evolution of the shelf mud deposits in the north-western South China Sea. *Front. Mar. Sci.* 9:937616. doi: 10.3389/fmars.2022.937616



# Holocene evolution of the shelf mud deposits in the north-western South China Sea

Gang Li[1,2]*, Li Miao[1,2] and Wen Yan[3]

[1]Southern Marine Science and Engineering Guangdong Laboratory (Guangzhou), Guangzhou, China, [2]Key Laboratory of Ocean and Marginal Sea Geology, South China Sea Institute of Oceanology, Innovation Academy of South China Sea Ecology and Environmental Engineering, Chinese Academy of Sciences, Guangzhou, China, [3]University of Chinese Academy of Sciences, Beijing, China

Marine mud deposits contain rich information on past interactions between riverine sediment fluxes and marine processes. Massive mud deposits attached to a major river from South China, the Pearl River, are distributed on the north-western shelf of the South China Sea. This study examines the evolution history using cores penetrating through Holocene strata and deciphers its response to the river system, sea-level change, monsoon variations, human activities, etc. Geochemical and sedimentological data constrained by robust radiocarbon data show the difference in the evolution of mud deposits in shallow waters and on the middle shelf. Muddy wedges in shallow waters along the coast have formed since 7 ka BP, when modern current systems were established during the middle Holocene sea-level highstand. However, wide-spread muddy deposits in the middle shelf initiated after 3 ka BP which are associated with enhanced sediment fluxes and strengthened winter monsoon. Human activities on recent millennia have play a significant role in influencing the mud deposition on the north-west shelf of the South China Sea, as evidenced by the enrichment of heavy metals in marine sediments.

KEYWORDS

**shelf muddy sediments, sea-level changes, Pearl River, northern South China Sea, human activity**

## Introduction

Mud deposits are widely distributed on the continental shelf of the world and are an important archive of past environmental changes (Nizou et al., 2010; Bassetti et al., 2016). Mud successions on the shelf provide very high-resolution records of oceanic circulations and climate changes (Wang et al., 2014). However, sedimentary records of shelf deposits

are rarely continuous over a long period because the formation is influenced by complex interactions such as sea-level conditions, sediment supply, transport and accumulation processes, and shelf morphology (see the thorough reviews by Gao and Collins, 2014; Hanebuth et al., 2015). To fully understand these sedimentary records, it is necessary to obtain knowledge about the process–product relationships of mud deposits on the shelf.

As coastal rivers in China carry enormous amounts of sediment into the continental margin, this massive sedimentation is responsible for the occurrence of the widest continental shelves on earth (Wang, 1999). Most of the fine-grained sediments from rivers are trapped on the wide shelf and build various mud deposits in different water depths. Two types of muddy depositional systems were identified, i.e., isolated eddy muddy bodies on the shelf and coast-attached muddy zones (Gao and Collins, 2014; Li et al., 2014). Isolated eddy mud deposits are generally present in calm hydrodynamic environments on the middle and outer shelf and are associated with shelf currents favorable for fine-grained sediment transport and deposition (Li et al., 2014). Mud deposits found on the middle and outer shelf were mostly formed during the transgression period (Park et al., 2000). Coastal mud deposits on the inner shelf are mostly attached to big rivers, such as the Shandong Peninsula muddy belt in the northern Yellow Sea (Liu et al., 2009) and the Zhe-Min mud belt in the East China Sea (Liu et al., 2007). As the distal sink of river-discharged suspended sediments, the formation and evolution of coastal mud deposits is closely correlated with the evolution of river systems (Liu et al., 2007; Gao and Collins, 2014; Gao et al., 2015; Xu et al., 2012). The sea-level change also plays a significant role on the formation of coastal mud deposits and most initiated after the attainment of the high sea-level stand (Liu et al., 2007; Li et al., 2014). Provenance studies on coastal mud deposits in the East China Sea revealed the role of coastal currents associated with the East Asian monsoon (Chen et al., 2017). Intensive human activities were also proposed to be a potential cause of the increased sedimentation rates of coastal mud wedges during the late Holocene (Xu et al., 2012).

In the north-western South China Sea (SCS), an extensive mud belt attached to the Pear River estuary has an area of more than 8,000 km$^2$ on the continental shelf (Figure 1A). Liu et al. (2009) and Ge et al. (2014) compiled an isopach map of the Holocene strata on the inner shelf using high-resolution Chirp acoustic profiles. Huang et al. (2018) dated the thick coastal mud wedge in the north-west SCS. However, grain-size analyses on multiple short cores by Liu et al. (2014) and Gao et al. (2015) showed that most mud deposits on the north-west SCS shelf had a thickness of less than 1 m. However, cores penetrating the whole Holocene sequence have not been reported on the north-western SCS shelf. The developmental history of mud depositional systems on this continental shelf has not been well studied.

This study addresses an issue about the developmental history of mud deposits on the northwest SCS shelf by combining previous core records and one new core penetrating Holocene strata. Based on new geochemical and sedimentological data sets, the purpose of this study is to 1) reveal the developmental history of the shelf mud depositional system in the north-western SCS; 2) decipher the formation of shelf mud and its response to the riverine sediment supply, sea-level change, and human activities using robust age constraints.

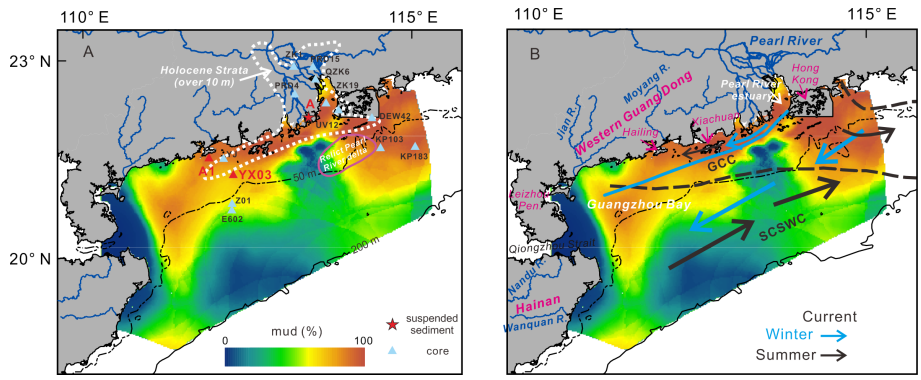


FIGURE 1
The study area and core sites: **(A)** location of new cores (red triangle) and some reference cores (blue triangle) in this study. Grain size data of suspended sediments from the Pearl River was measured by Zheng et al. (2017) at the station **(A)** Dotted lines circle the zones with thick Holocene deposits (>10 m) according to Ge et al. (2014). The relict delta of the Pearl River was mapped by Bao (1995). **(B)** Current systems and freshwater plumes in summer and winter on the northern shelf of South China Sea according to Ding et al. (2017) and Su (2004). GCC, Guangdong coastal current; SCSWC, South China Sea warm current.

# Marine settings

The northern continental shelf of the South China Sea has a width of around 200 km and the study area is located from the Pearl River estuary to the east of Hainan Island (Figure 1A). Fluvial sediments are supplied by the Pearl River and other small rivers in the western Guangdong Province and from Hainan Island. The Pearl River annually carries about 80 million tons of suspended sediments to the sea before extensive dam construction (Wang, 1985). The combined sediment fluxes by small rivers are about 3 million tons, including the Moyang River, Jian River and Nandu River (Wang, 2007).

The northern SCS shelf is influenced by the East Asian Monsoon. The north-easterly winds prevail in the winter while the south-westerly winds dominate during the summer. Seasonally reversing monsoon winds play a dominant role in controlling oceanic circulation (Hu et al., 2000; Su, 2004). The Guangdong coastal current (GCC) mainly flows westward in winter and is forced by the north-eastly winds. In summer, the GCC still flows westward along the coast in the north-western SCS, which is driven by fresh-water buoyancy from the Pearl River plume (Bao et al., 2005; Ding et al., 2017) (Figure 1B). On the outer shelf, a stable warm current, i.e., the South China Sea warm current (SCSWC), flows north-eastward along the shelf break during the winter but it spreads over most parts of the continental shelf during the summer (Su, 2004) (Figure 1B).

The highest sediment flux from rivers occurs in summer, taking the form of a suspended sediment plume. Most fine-grained particles from the Pearl River settle out of suspension within the estuary where seawater mixes with freshwater (Wang, 1985). Suspended sediments escaping from the Pearl River estuary are mainly transported alongshore towards the west by the GCC (Wang, 2007). Because the west GCC has a relatively stable speed of over 10 $cms^{-1}$, fine-grained suspended sediments from the Pearl River can be transported alongshore over a long distance before settling down to the seabed (Gao et al., 2015).

In summer, southerly to south-westerly waves have an average height of 0.5–2.5 m in this study area. In the winter, north-easterly waves have an average height of 0.5–4.0 m. High waves are mainly produced by typhoons, which occur during summer and autumn and have a maximum height of over 10 m (Wang, 2007). Typhoon waves in this study area can cause the re-suspension of sea-bottom sediments on the shelf, even on the outer shelf (Xiao et al., 2013; Zhou, 2014).

# Materials and methods

## Seabed coring

One gravity core (A1) with a length of 1.74 m was retrieved in 2008 on the coastal mud wedge, south of Hailing Island (111.9°E, 21.55°N; 16 m water depth). One core (YX03) was obtained in 2013 at a water depth of 35.4 m in muddy zones on the middle shelf (112.27°E, 21.29°N). The total length is 29.6 m, and the upper 2.75 m is the Holocene sediments studied in this paper.

## Geochemical measurements

To capture the variability of elemental composition of the core YX03, high-resolution XRF measurements (at a 0.5-cm interval) for Al, K, Ti, Ca, Sr, and Fe were performed on core halves at the South China Sea Institute of Oceanology *via* the Geotek Multi-Sensor Core Logger (MSCL). The core surfaces were first flattened and covered with a thin (4 μm) ultralene film to avoid contamination of the prism. Two modes of 10 kV with no filter and 40 kV with a silver filter were used for the analysis with a rhodium X-ray tube. The sample was flushed with helium to prevent partial or complete absorption of the emitted soft radiation from the samples by air. A count time of 30 s was set for each mode. To avoid an overprint of the background signal and the influence of pore-water in core sediments, the element-element ratios or the ratios of a single element against the sum of all element intensities (expressed as "element/sum") are used. Data from some segments with uneven surfaces was excluded.

For further measurements of the core YX03, discrete samples for geochemical and grain-size analyses were taken at the intervals of 10 cm and 1 cm, respectively. The gravity core of A1 was sub-sampled at an interval of 5 cm. For geochemical analyses, approximately 2-gram sediments were dried in a 45°C oven and crushed into powder. Major and trace elements are determined using ICP-OES (Agilent 720) and ICP-MS (Bruker Aurora M90) at the Institute of Geochemistry, following the measurement method by Qi et al. (2000). Data quality was guaranteed using one andesite standard (AMH-1) and one slate standard (OU-6) with a relative error of less than 5%.

## Grain-size analysis

To analyze the grain size of terrigenous fractions, biogenic compounds are removed. Samples were treated with a 10% hydrogen peroxide solution under a heated water bath at 60 °C for 12 h to remove organic matters, and acidified with a 20% acetic acid solution at room temperature for 24 h to remove biogenic carbonates. The measurement was performed using a Mastersizer 2000 laser diffraction analyzer.

## End-member modeling of grain-size data

Numerical unmixing of grain size distribution data into constituent components, known as end-member analysis

(EMA), can yield valuable information on sediment transport processes, sedimentary environments, and sediment origin (Prins et al., 2000; Tjallingii et al., 2008). To correlate the core records to modern sedimentary environments and identify potential sources, we decomposed all grain-size data in this study using a newly developed GUI software called AnalySize (Paterson and Heslop, 2015; Figure 2).

## Chronology

The Holocene stratigraphy of cores YX03 and A1 was constrained by nine $^{14}$C-accelerator mass-spectrometric ($^{14}$C-AMS) dates (Table 1), which were measured on mixed foraminifers and bivalve mollusks. All $^{14}$C-AMS dates are calibrated to the calendar year before present using the calibration program Calib 7.0.4 (Reimer et al., 2013), and the additional regional reservoir age of −128 ± 40 is corrected for dates on marine biogenic carbonate shells (Southon et al., 2002).

# Results

## Lithology and stratigraphy

The Holocene sediments in core YX03 are 2.75 m thick and overlie an erosional surface separating from the Pleistocene mud with a grayish green. The $\delta^{13}$C values of organic carbon in the Pleistocene mud range between −25‰ and −27‰, suggesting it might have been deposited in a lacustrine environment. In the lower section (Section I: 60–275 cm), most sediments are dark gray silty sand with abundant shell fragments, and the mud content is higher in the middle part (145–195 cm). Sediments in section II above 60 cm are brown silt, with very poor sorting and high water content. Shell debris and foraminifera could be seen in the upper 60 cm of core YX03. The core of A1 in offshore waters, south of Hailing Island, mainly consists of yellowish brown silt with variable sand content. In the lower section (50–174 cm), sand is mostly higher than 15%. In section II above 50 cm, sediments are silt-dominated. Compared with the YX03, shell fragments are rare in core A1.

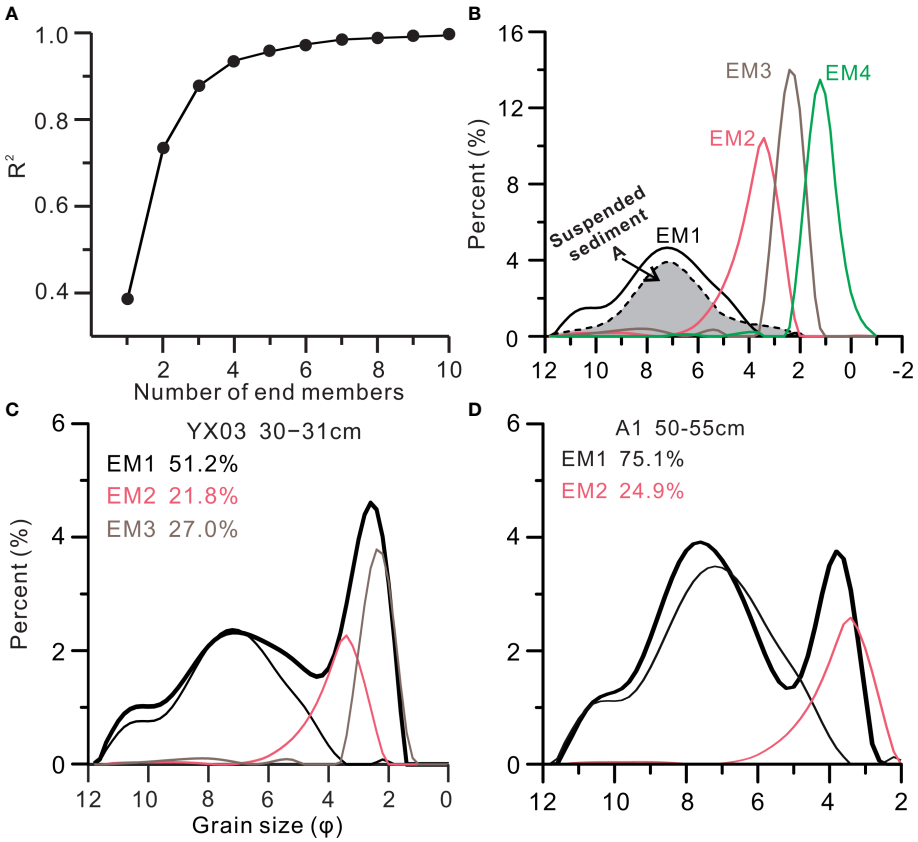


FIGURE 2
Correlation plots between the correlation coefficient (R2) and number of end-member **(A)**. **(B)** grain-size distribution of four end members. EM1 and suspended sediments from modern Pearl River (Zheng et al., 2017) have similar grain-size curves. **(C, D)** representive grain size distribution of samples from cores YX03 and A1 and the results of end-member analysis.

TABLE 1 $^{14}$C-AMS dates of cores YX03 and A1.

| Core | Lab ID | Depth (cm) | Dating materials | $^{14}$C age(BP) | Calibrated age (cal BP) |
|---|---|---|---|---|---|
| YX03 | Beta497641 | 7–8 | Mixed forams | 2,210 ± 30 | 1,958 + 62–72 |
| | Beta495116 | 29–30 | Mixed forams | 2,490 ± 30 | 2,301 + 52–61 |
| | Beta483269 | 60–65 | Bivalve shells | 2,790 ± 30 | 2,700 + 55–49 |
| | Beta375097 | 78–85 | *Tapes literatus* | 6,600 ± 30 | 7,312 + 53–59 |
| | Beta375098 | 152–160 | *Meretrix* spp. | 7,630 ± 30 | 8,289 + 58–58 |
| | Beta483271 | 257–265 | Bivalve shells | 7,670 ± 30 | 8,321 + 56–60 |
| | Beta375099 | 297–304 | Organic sediments | 27,200 ± 180 | 31,152 + 115–117 |
| A1 | Beta495117 | 0–5 | Mixed forams | 1,900 ± 30 | 1,597 + 64–65 |
| | Beta495118 | 60–65 | Mixed forams | 3,030 ± 30 | 2,946 + 69–81 |

Table 1 lists AMS$^{14}$C dates on mollusk and foraminiferal shells obtained from cores YX03 and A1. Organic materials from greenish lacustrine mud in core YX03 below 275 cm were dated to 39.5–31.2 ka BP, suggesting that the grayish mud accumulated during the Pleistocene at low sea levels. Basal Holocene deposits in core YX03 are estimated at 8,400 BP based on dates on bivalve mollusk shells. Six dates in the Holocene section show a large jump in $^{14}$C ages from 7,300 BP at 80 cm to 2,700 BP at 60 cm. Section I of core YX03 was estimated to be between 8,300 BP and 7,300 BP. The upper section above 60 cm has a stable accumulation rate of ~70 cm/ka during the last 2,700 years. One $^{14}$C date (1,960 BP) at the top suggests some younger sediments were lost during the rotary drilling (Table 1). In the core A1, the topmost was dated to be 1,600 BP and the fine-grained upper section (II) developed after 3 ka BP.

## Grain size and end-member modeling results

The mean grain size of core YX03 varies from 4 φ to 6 φ, with an average of 4.8 φ. A clear change in grain-size fractions could be found at 60 cm, showing an obvious fine upward trend. In section I, the sand content is greater than 48% and the clay is lower than 10%. In section II, the sand, silt, and clay content are 39%, 51%, and 10%, respectively. Sediments in core YX03 exhibit very poor sorting and have multiple modes in grain-size distributions. Two distinct modes were present at 2.5 φ and 7.1 φ (Figure 2C). A secondary mode on the fine side at 10.5 φ is also clear in most grain-size curves. Another secondary mode at 5.2 φ could be found in some samples.

In core A1, the mean grain size is 6.7 φ on average, and the sorting coefficient is greater than 2. Silt is dominant in this core with an average content of 70%. In the upper section, the average sand content is less than 7%. In the lower section, sand increases to 18% and the clay content is around 14%. Three modes at 3.7 φ, 7.3 φ, and 10.1 φ are present in the grain-size distributions (Figure 2D). The mode at 7.3 φ is stably present in most samples. However, the mode at 3.7 φ is more prominent below 50 cm.

All grain-size data from the two cores and surface sediments is input into the nonparametric AnalySize to calculate end members. As shown in Figure 2A, the mean coefficient of determination ($R^2$) increases as the number of end members (n) increases. We determined four end members according to the inflection point in the $R^2$-n curve, which reproduced 94% of the dataset variance The first component (EM1) mainly consists of silt and clay with two modes at 7.1 φ and 10.1 φ. The other three components are sand-dominated. EM2, EM3, and EM4 have three modes at 3.3 φ, 2.3 φ, and 1.1 φ, respectively (Figure 2C).

On the north-western shelf of SCS, EM1 exists in most surface samples, and muddy sediments have a higher abundance (Figure 3A). The proportion of EM1 is over 90% in the Pearl River estuary. The very-fine sand component, EM2, has an average proportion of 17%. Offshore sediments south of the Jian River mouth have the highest content of EM2 (30%–40%) (Figure 3B). EM2 is the main component of surface sediments on the shelf west of Hailing Island. Coarse deposits surrounding the Hailan Island and the Leizhou Peninsula have the highest contents of EM3 (Figure 3C) and EM4. Relict sandy deposits on the eastern middle shelf, including the paleo-Pearl River delta, have high proportions of EM3 and EM4 (~20%).

Core YX03 consists mainly of three end-members: EM1, EM2, and EM3. The EM1 varies between 20% and 70% (an average of ~42%), with higher content in section II (Figure 4). The highest proportion of EM1 was found between 20 cm and 45 cm. Another end member, EM3, is also distinct in this core with an average proportion of ~35%. The variation in the proportion of EM3 is anti-phase with the EM1, showing a lower value in section II. Core A1 mainly includes two end members, EM1 and EM2 (Figure 5). The proportion of EM1 is highest between 5 cm and 50 cm, with a value of over 80%.

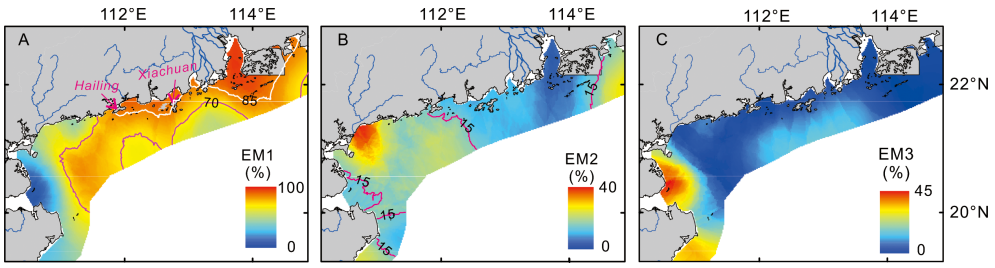


FIGURE 3
The distribution maps of three grain-size end-members (A: EM1; B: EM2; C: EM3) of surface sediments are shown on the north-western South China Sea shelf. Two solid lines in Figure 3A label the EM1 content of 85% and 70%. The purple solid lines in Figure 3B represents the EM2 content of 15%.

## Geochemical compositions

From the comparison of the two elemental datasets of core YX03, the ratios of log(Zr/Al), Al/Sum, and log(K/Al) derived by the XRF core scanner have high correlations with the corresponding ratios by ICP-OES. The Zr/Al ratio and the Al content record the fining upward at 2,700 BP (Figure 4). In section I, high-resolution scanned data detect some coarse beds with a high Zr/Al ratios and low Al contents, such as at 164–181 cm, 130–135 cm, and 120–123 cm. The K/Al ratio in section I, with an average of 0.35, is higher than that in section II. The K/Al ratio is mostly less than 0.31 in section II, and it rapidly decreases at 70–55 cm. The Ti/Nb ratio in core YX03 is an average of 236 in section I, with large fluctuations. However, it shows a decreasing trend from 70 cm to the core top. The Cu/Al and Pb/Al ratios have an average of $3.6 \times 10^{-4}$ and $5.4 \times 10^{-4}$ and no obvious trends are found in these two ratios.

In core A1, the Zr/Al ratio and Al content correlate well with the grain-size variation. Fine sediments in section II have a higher Al content but a lower Zr concentration. The K/Al ratio

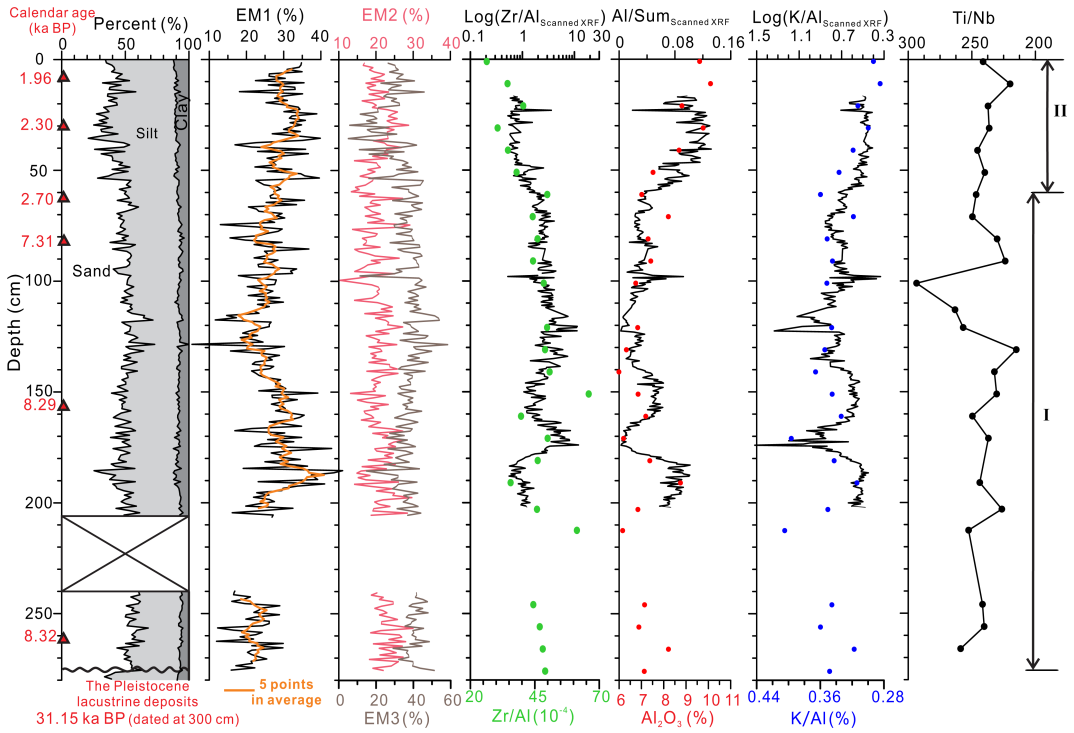


FIGURE 4
Sedimentary compositions and elemental proxies of core YX03. Elemental results of discrete samples were shown by solid dots on down-core elemental profiles collected by the XRF scanner. Red triangles on the depth scale mark $^{14}$C dating samples. Sub-segments are labeled on the right side.

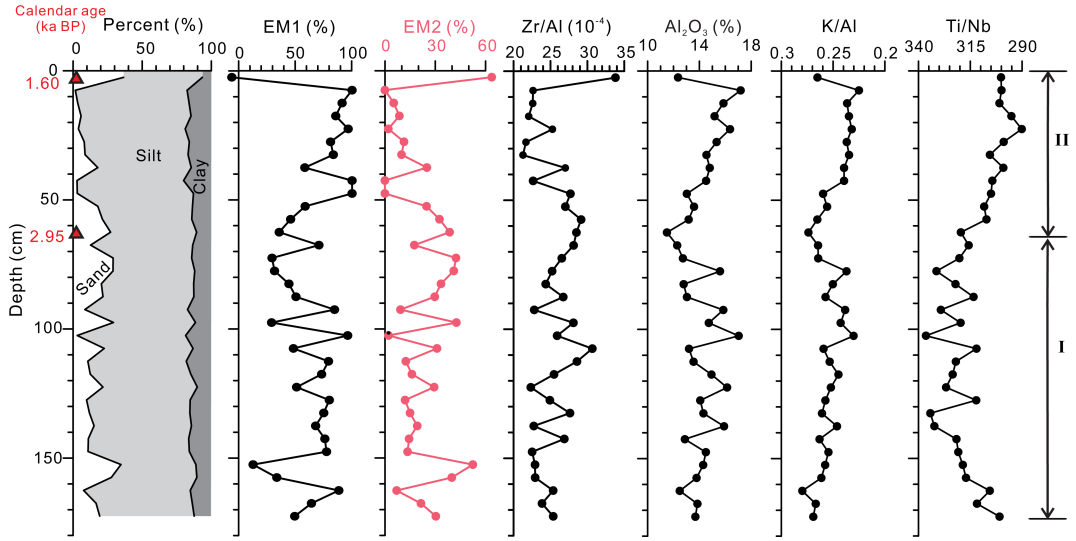


FIGURE 5
Sediment compositions and elemental proxies of core A1. Red triangles on the depth scale marked $^{14}C$ dates. Sub-segments were labelled on the right side.

decreased at 60 cm. The change in geochemical composition could be found in the Ti/Nb ratio, with a lower value in section II. The change in the Ti/Nb ratio was dated to 2.95 ka BP. The Cu/Al ratio shows the lowest value between 75 cm and 30 cm, and sediments above and below this segment have higher values. The highest Pb/Al ratio is present in the top 20 cm.

# Discussion

## Postglacial transgression and shelf sedimentation

Core YX03 on the north-western SCS shelf contains two depositional units with distinct sedimentary textures and chemical compositions. Section I was poorly sorted and sand-dominated (Figure 4). Radiocarbon dates of 8,300–7,300 BP suggest this sand bed was deposited during the middle Holocene. According to a recent report on relative sea-level changes in the northern SCS (Xiong et al., 2018), sea level rose from approximately −5 m to the present position during this period (Figure 6C). The paleo-coastline has retreated to the present shoreline since 8 ka BP, according to recent compiled paleo-geographic maps by Wei et al. (2016) and Yao et al. (2009). Combining the water depth at the coring site and sea-level positions, a paleo-water depth of 30–35 m is estimated when this transgressive sand bed accumulated between 8,300 and 7,300 years of BP. Similar transgressive sandy deposits overlying the Pleistocene terrestrial mud were also found on the middle and outer shelf of the northern SCS (Yim et al., 2006; Xiao et al., 2013; Xiong et al., 2018). These transgressive sands are inferred to be deposited in the inner and middle shelf environments (Figures 6A, B). Foraminifera analyses by Yim et al. (2006) found a high percentage of shallow-water benthonic species, such as *Ammonia beccarii* var., *Elphidium advenum*, and *A. annectens* in these transgressive sands.

Radiocarbon dates show a wide range of age inversions in transgressive sandy deposits in the south of the Pearl River Estuary, suggesting extensive reworking occurred (Yim et al., 2006; Waxi et al., 2016) (Figure 6A). In the north-western SCS, the Holocene sediments on the shelf, such as in cores YX03 and E602, mainly consist of transgressive sands (Figures 1A, 6B). Xiao et al. (2013) conducted a detailed analysis on grain size of E602 and pointed out that transgressive sands were reworked by high frequent tropical storms. The narrow range of $^{14}C$ dates in transgressive sands from cores YX03 and E602 suggests they were not associated with the rapid accumulation but were produced by repeated reworking. Radiocarbon dates with narrow age ranges were also reported from transgressive sands on other continental shelves (Schimanski and Stattegger, 2005; Hong et al., 2019) and some subaqueous deltas (Wang et al., 2010). The youngest dates within these transgressive sands in cores YX03 and E602 might represent the most recent disturbances by storms on the north-western SCS shelf. Radiocarbon dates from transgressive sands in core E602 on the outer shelf are older than those in cores YX03 and YJ on the inner and middle shelf (Figure 6B). The decrease in the ages of transgressive sands records the landward migration of storm-reworking zones during the Holocene. With the sea level rising, the influence of storms decreased in deep waters and mud

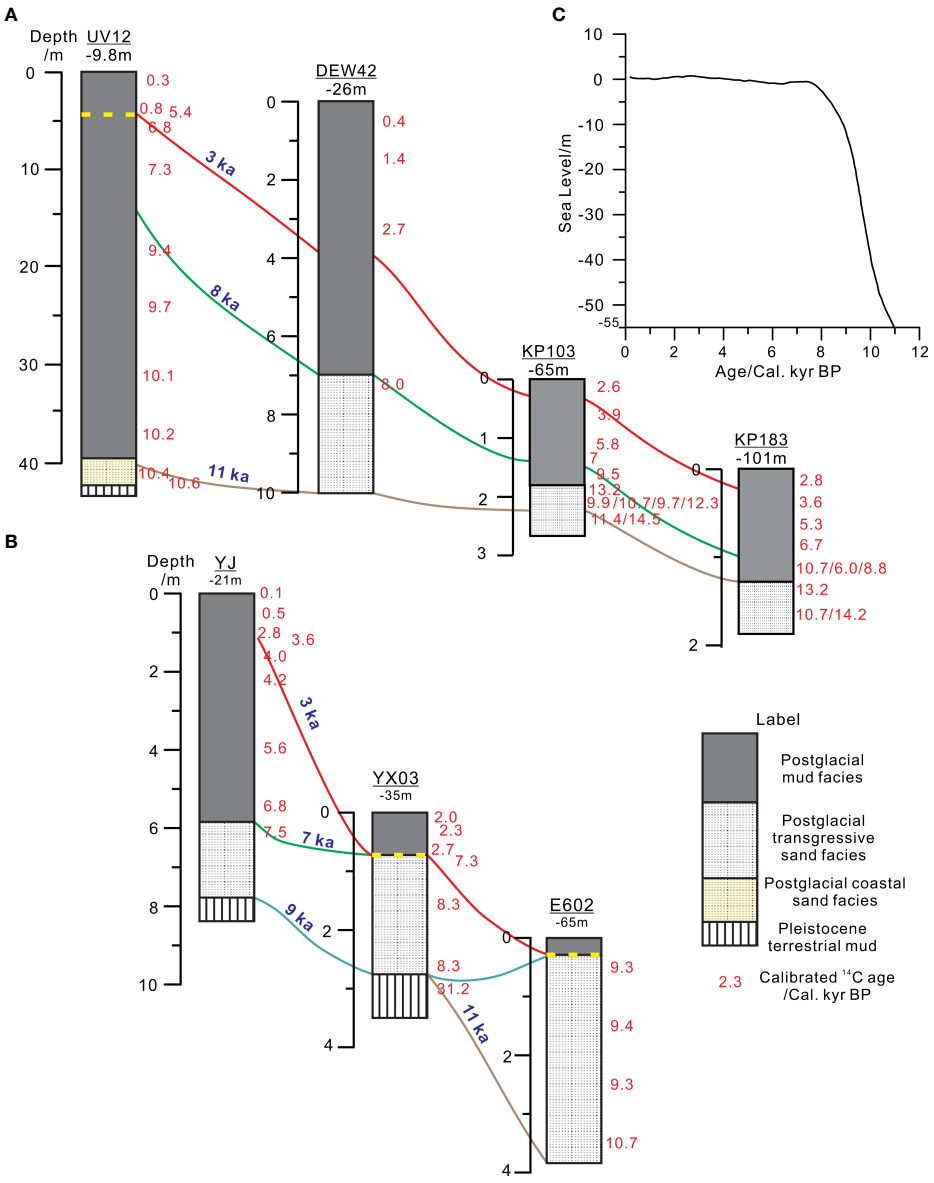


FIGURE 6
Two cross sections of Holocene sedimentary sequence on the north-western SCS shelf (**(A)** in the east; **(B)** in the west). **(C)** Sea-level changes since 11 ka BP according to Xiong et al. (2018). Reference cores were published by Xiao et al. (2013); Huang et al. (2018); Xiong et al. (2018) and Yim et al. (2006). The location of cores can be found in Figure 1A.

sediments subsequently accumulated. In the northern SCS, massive transgressive sands are directly exposed on the present seafloor. Mud sediments were only found in the subaqueous delta of the Pearl River (Yim et al., 2006; Ge et al., 2014) and in shallow waters along the western Guangdong coast (Liu et al., 2009; Xiong et al., 2018). Mud zones on the northwestern SCS shelf mostly have a thickness of less than 1 m (Figure 6B). Even in the uppermost mud deposits, the two coarse end members have high proportions. It indicates that high waves during the most energetic storms can remobilize the underlying transgressive sands and mix them with fine-grained sediments.

In summary, the Holocene sedimentation rates are low in most areas of the northwest SCS shelf, less than 30 cm/ka in most areas except 1–3 m/ka in some shallow waters. The high sedimentation rate along the western Guangdong coast is associated with the influence of the Pearl River. High proportions of transgressive deposits in the Holocene strata reflect the sediment starvation on this shelf due to rising sea

levels. With the rising sea level on a low gradient shelf, sediment supply was vastly reduced due to the increasing distance to river mouths. Under these conditions, marine processes, such as storms and tide currents, heavily reworked and homogenized the Holocene deposits. This is reflected by inconsistent $^{14}C$ dates in Holocene deposits. Origin studies on surface sediments in the same area also highlighted that recycled sediments accounted for a great proportion (Li et al., 2015; Li et al., 2016). Most Holocene sediments on the northern SCS shelf are intensive reworked sediments or palimpsest sediments, according to Swift et al. (1971).

## Expansion of muddy zones on the shelf

On the continental shelf of the north-western SCS, the coast-attached muddy belt has a vast area of 8,000 $km^2$. Using shallow seismic profiles, Liu et al. (2009) and Ge et al. (2014) developed the first isopach map of the Holocene sediments on the northwest SCS shelf. According to seismic stratigraphy, this muddy wedge along the western Guangdong coast (Figure 1A) ends at around Hailing Island, and the Holocene thickness is estimated to be more than 10 m. Huang et al. (2018) retrieved a long core on the distal muddy wedge offshore Hailing Island (YJ at 21 m), and the Holocene stratum is 7.8 m thick (Figure 6B). According to stratigraphic records of core YX03 in this study and other cores reported by Yim et al. (2006), the Holocene deposits on this shelf are less than 5 m thick (mostly less than 3 m) in waters deeper than 30 m (Figures 6A,B). Moreover, the Holocene deposits only contain a very thin muddy carpet, as recorded by core YX03 (Figure 4) and other cores reported by Gao et al. (2015) and Liu et al. (2014).

The grain-size component of EM1 has a similar distribution curve to suspension sediments of the Pearl River, suggesting that EM1 represents fine-grained sediments from this large river (Figure 2B). A previous geochemical study on surface sediments on the northwest SCS shelf found that the Ti/Nb ratio was independent of the sorting process and the grain-size effect (Li et al., 2016). Bulk fluvial sediments from the Pearl River are characterized by a lower Ti/Nb ratio because of a large number of weathered sediments from granitic rocks. In core A1 near the coast, the increase in the relative proportion of EM1 at 60 cm is accompanied by a decrease in the Ti/Nb value, indicating that the fining of sediments is contributed by the Pearl River. In the nearby core YJ, muddy sediments above 5.8 m were mostly projected into the zone of the Pearl River source on a La-Th-Sc ternary diagram (Huang, 2018). Although the EM1 in the core YX03 is not as dominant as in the two coastal cores, the increase in this end member and subtle decrease in Ti/Nb ratio could also be observed in upper mud sediments (Figure 4). According to geochemical evidence, the muddy deposition on the north-western shelf of SCS is closely related to fine-grained sediments from the Pearl River.

However, chronological records show a difference in the evolution history of mud deposits on the middle shelf and in shallow waters in the north-western SCS. Radiocarbon ages from core YJ (Huang et al., 2018) indicated the muddy wedge occurred in offshore waters much earlier than other muddy deposits on the middle shelf (Figure 6B). The base of muddy deposits in YJ was dated at around 7 ka BP (Huang et al., 2018). On the middle shelf, the accumulation of mud sediments started later than 3 ka BP according to this study. Moreover, a hiatus of more than 4,000 years between shelf muddy deposits and transgressive sands in core YX03 was also observed in core E602 in the west (Xiao et al., 2013; Figure 1). Mud sediment (site Z01, which is about 10 km away from the E602 (Figure 1A)) was dated younger than 350 years using the $^{210}Pb$ method (Liu et al., 2014), but transgressive sands were dated older than 9,300 BP by $^{14}C$ ages (Xiao et al., 2013).

The review by Hanebuth et al. (2015) summarized three main initiation phases in the evolution of mud depocenters from different shelf settings at around 14 ka, 9.5–6.5 ka, and 2 ka. From previous records on the northern SCS shelf, mud belts on the outer shelf south of the Pearl River were initiated at around 10 ka BP during the transgression (Yim et al., 2006; Figure 6A). The YJ record in offshore waters along the western Guangdong Province indicates the coastal mud wedge formed after 7ka BP when modern current systems were established (Huang et al., 2018; Figure 6B). The reconstructed salinity using diatoms suggests that freshwater plumes out of the Pearl River mouth have been present since 7ka BP (Zong et al., 2006; Zong et al., 2012). A process-oriented experimental study indicated that freshwater discharge is one of the important factors inducing the formation of westward coastal currents in northern SCS (Ding et al., 2017).

However, most of the mud deposits on the middle shelf did not appear in the north-western SCS until 3 ka BP. The expansion of mud deposition from offshore waters to the middle and outer shelf has been suggested to be associated with the evolution of the Pearl River delta (Gao et al., 2015). According to Wei et al. (2016), the widespread marine inundation produced a large embayment at the mouth of the paleo-Pearl River when the sea-level rose to the present height at around 7 ka BP. Most of the fluvial sediments from the Pearl River were trapped within the paleo-estuary between 7 ka and 2 ka BP (Zong et al., 2009; Wei et al., 2016). Stratigraphic hiatuses found in the deltaic area were commonly dated between ca. 7 ka and 3 ka BP (e.g., Wei et al., 2016; Xiong et al., 2018; Chen et al., 2019) (Figures 7A, B). The hiatus found in cores YX03 and E602 on the western continental shelf is chronologically correlated with those in the Pearl River delta (Figure 7C). They reflect the sediment starvation prevailing in the outer plaeo-Pearl River estuary and on the middle shelf during this period. However, the sedimentation rate in core YJ in western offshore waters shows a significant increase during 7–3 ka BP (Figure 7D). The geochemical compositions of mud deposits in this core point

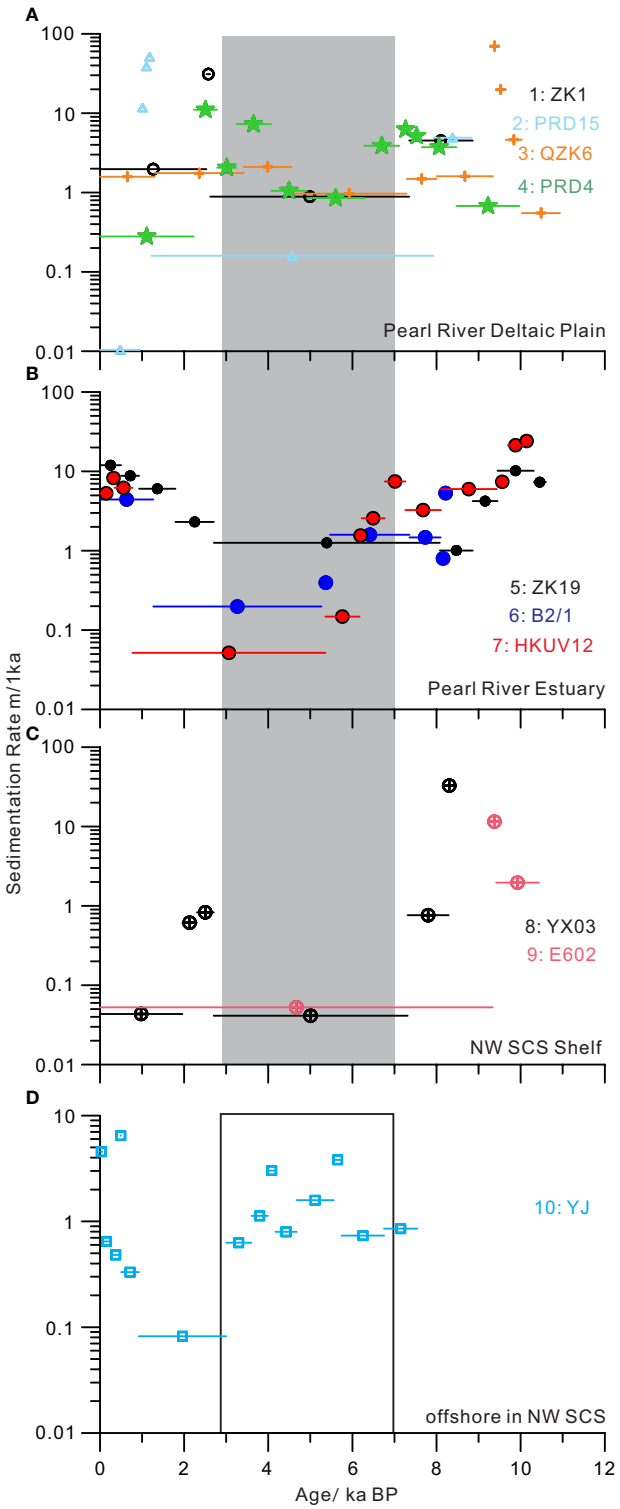


FIGURE 7
Sedimentation rates of marine deposits on the north-western SCS shelf during the past 12 ka BP. See Figure 1A for the locations of cores. Note that between ~3 and 7 ka BP the accumulation rates were low at the Pearl River delta and on the middle-and-outer SCS shelf. The low sedimentation rate during this period was not found in offshore waters. Reference cores were published by Yim et al. (2006); Hu et al. (2013); Xiao et al. (2013); Wei et al. (2016); Huang et al. (2018); Xiong et al. (2018); Chen et al. (2019) and Zong et al. (2012).

to the source of the Pearl River during this period (Huang, 2018). Widespread hiatuses in the outer estuary of the Pearl River and on the northwest SCS shelf denied a large amount of fine-grained sediment directly supplied by this big river during 7–3 cal ka BP. However, a large paleo-delta of the Pearl River was found in water depths of 30–60 m on the northern SCS shelf (Bao, 1995) (Figure 1A). This paleo-delta with an area of 4,000 $km^2$ was heavily reworked and relict coarse sands and gravels lay on the present sea floor (Zhong et al., 2017). Fine-grained sediments reworked from this paleo-delta might have fed the inner-shelf sedimentation through the westward coastal currents during 7–3 ka BP.

After 3 ka BP, the increased sediment discharge of the Pearl River promoted the rapid progradation of its delta (Zong et al., 2009; Wei et al., 2016). Wei et al. (2016) estimated that sediment fluxes in the Pearl River have accelerated to 50 million tons $a^{-1}$ since 2 ka BP, from less than 30 million tons $a^{-1}$ before. The increase in sediment flux in recent millennia was widely thought to be related to human activities (e.g., Zong et al., 2009; Wei et al., 2016) because plenty of evidence, such as diatom, pollen, estuarine $\delta^{13}C$ and stalagmite $\delta^{18}O$ indicated a weakened summer monsoon in South China (Cheng et al., 2018; Dykoski et al., 2005; Yu et al., 2011) (Figure 8A). According to the comparison of charcoal fluxes with previous peak interglacial periods in northern SCS, Cheng et al. (2018) concluded that human activities through land-use modifications completely altered the natural vegetation trend after 5–6 ka BP during the Holocene. Pollen studies widely found the rising concentration of fern spores and Poaceae in deltaic and lacustrine deposits in South China after 4–2 ka BP, suggesting human-induced deforestation and intensified agricultural activity (Zheng and Li, 2000; Wang et al., 2007; Zhao et al., 2009). In addition, significant enrichment of heavy metals in shelf sediments is also thought to be mainly associated with the intensified human

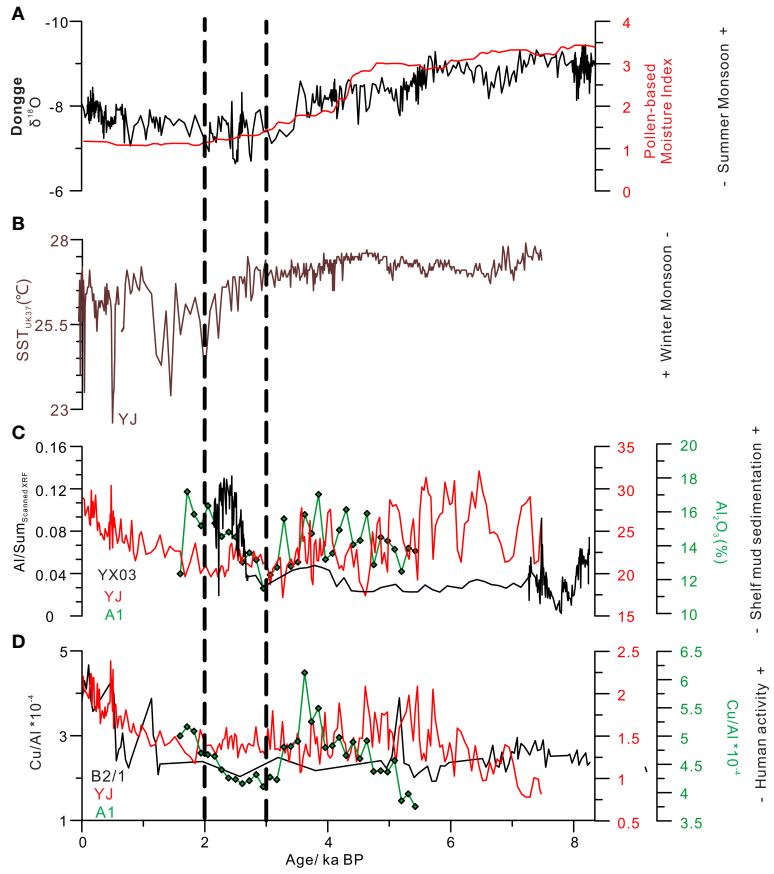


FIGURE 8
Comparison between proxy data of East Asian monsoon, shelf mud sedimentation, and human activities in the northern South China Sea in the past 8ka BP. **(A)** stalagmite $\delta^{18}O$ record from Dongge Cave (Dykoski et al., 2005); moisture index based on pollen (Zhao et al., 2009); **(B)** the strength of winter monsoon recorded by alkenone sea surface temperature of core YJ in the northwest SCS Zhang et al. (2019). **(C)** Al concentrations from cores YX03, YJ (Huang et al., 2008) and A1, recording the initiation of shelf muddy sedimentation; **(D)** The Cu/Al ratio in the Pearl River estuary (Hu et al., 2013) and on the western SCS shelf (Huang et al., 2018 and this study), showing the enhanced anthropologic activities in recent 2000 years.

activities around the northern SCS. Xu et al. (2017) recorded obvious increases in Cu, Cd, and Pb after 4 ka BP in two cores southeast of Hainan Island. The abundance of heavy metals in sediments, such as Cu and Pb, was observed to substantially increase in the Pearl River delta (Hu et al., 2013) and in cores YJ (Huang et al., 2018) and A1 (this study) near the western Guangdong coast, reflecting the expansion of mining and metal-working activities after 2 ka BP (Figure 8D). These enhanced agricultural and mining activities caused soil erosion and increased sediment fluxes of the Pearl River to a certain degree. In addition, land reclamation and dyke construction on the deltaic plain accelerated the shoreline advance of the Pearl River delta (Zong et al., 2009) and promoted sediment delivery to the shelf (Figure 9). Although there are some differences in chronology between different records around the studied area, the predominance of human activities has been significant in recent millennia. The increased fine-grained sediments escaping from the pleo-Pearl River estuary might have initiated the wide mud deposition on the western SCS shelf. Moreover, the enhanced winter monsoon after 3 ka BP might also strengthen the westward Guangdong Coastal Current and promote the transport of fine-grained sediments to the western SCS shelf. The enhanced winter monsoon has caused a significant decrease in the sea surface temperature of coastal waters in the northern SCS (Zhang et al., 2019).

As summarized by Hanebuth et al. (2015), shelf mud deposition mostly took place during the middle Holocene sea-level highstand when fine sediments were available, such as from some big rivers. Distal fine sediments from the Yellow River were transported out of Bohai and built thick muddy clinoforms south of the Shandong Peninsula during 9.5–6.5 ka BP (Liu et al., 2009). The Zhe-Min mud belt on the inner shelf of East China Sea initiated as early as 11 ka BP but rapidly aggraded after 8–7 ka BP when large amounts of fine-grained sediments escaped out of the Yangtze River delta (Liu et al., 2007; Xu et al., 2012; Li et al., 2014). In the eastern Yellow Sea, mud patches were present in the southwest of Cheju Island after 7.4 ka BP due to massive sediment supply by the Yangtze and Yellow rivers (Yoo et al., 2002). Compared with these mud depocenters, fine-grained sediments escaping out of the Pearl River estuary were limited before 3 ka BP, so only small mud patches were present in offshore waters along the western Guangdong coast (Figure 9). The expansion of mud zones occurred after 3 ka BP on the shelf of the northwest SCS. Similarly, the high accumulation rate of the mud wedge after 2 ka BP was found on the inner shelf of the East China Sea (Xu et al., 2012). Hanebuth et al. (2015) pointed out that the expansion and accelerated sedimentation of mud depocenters occurred worldwide after 2 ka BP. Although natural processes, such as coastal current systems (Xu et al., 2012) and winter monsoon (this study), were suggested playing the role in the expansion of mud depocenters on the continental shelf, human activities, including vegetation destruction and deltaic reclamation, have been agreed on the significant influence on marine mud sedimentation (Lesueur et al., 1996; Huang et al., 2018).

## Conclusion

Mud deposits occupy a vast area of 8,000 km$^2$ on the north-western shelf of the South China Sea and consist of muddy wedges in shallow waters and wide-spread muddy belts on the

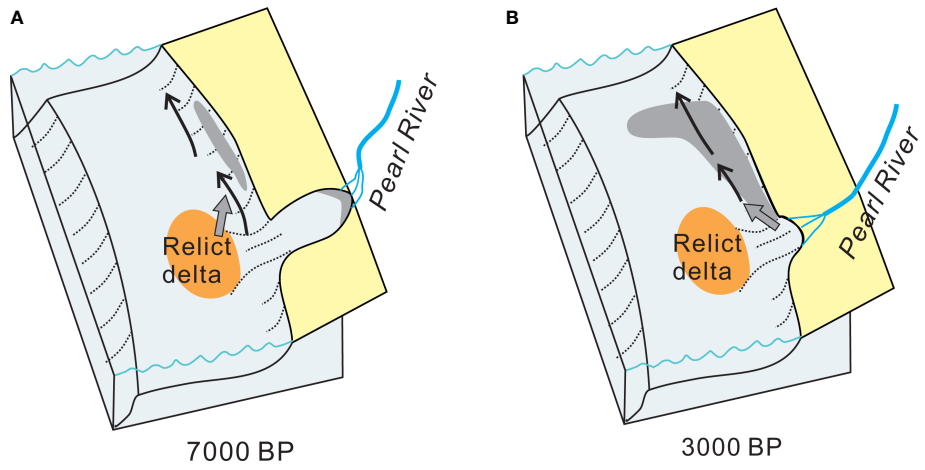


FIGURE 9
Schematic diagrams show the configurations of shelf muddy sedimentation in north-western South China Sea. **(A)** small muddy wedges have been present in shallow waters since 7 ka BP which were fed by reworked sediments from the relict delta of Pearl River. **(B)** wide-spread muddy zones on the middle shelf initiated after 3 ka BP when the paleo-embayment has been filled.

middle shelf. The Holocene evolution of this mud depositional system was reconstructed by combing sedimentary records from cores in shallow waters (Huang et al., 2018) and on the middle shelf. Mud depositional systems in the north-western SCS developed above postglacial transgressive sands which were intensively reworked by frequent storms. Mud wedges in shallow waters along the western coast, which have a thickness of more than 5 m, have formed since 7 ka BP when the sea-level rose to the present position. However, wide-spread mud belts on the shelf initiated after 3 ka BP and thin mud deposits were accumulated with a thickness of less than 1 m. The expansion of mud deposits in the western SCS shelf was associated with the evolution of the Pearl River delta and the enhanced winter monsoon. The enhanced sediment flux of the Pearl River and the acceleration of deltaic progradation caused more delivery of fine-grained sediments to the shelf after 3 ka BP. Enhanced human activities overwhelmed the monsoon in their influence on the evolution of mud deposition on the north-western SCS shelf in recent millennia.

## Data availability statement

The raw data supporting the conclusions of this article will be made available by the authors, without undue reservation.

## Author contributions

GL and WY conceptualized the study. LM carried out elemental analyses of discrete samples from core A1 and GL finished other analyses, including core scanning and grain-size measurements. GL prepared the original draft of the manuscript with contributions from LM and WY. All authors listed have made a substantial, direct, and intellectual contribution to the work and approved it for publication.

## Funding

The study was supported by the Key Special Project for Introduced Talents Team of Southern Marine Science and Engineering, Guangdong Laboratory (Guangzhou) (GML2019ZD0206), the National Natural Science Foundation of China (42176079 and 41976062), the National Key R&D Program of China (2021YFC3100600) and the Youth Innovation Promotion Association of the Chinese Academy of Sciences.

## Conflict of interest

The authors declare that the research was conducted in the absence of any commercial or financial relationships that could be construed as a potential conflict of interest.

## Publisher's note

All claims expressed in this article are solely those of the authors and do not necessarily represent those of their affiliated organizations, or those of the publisher, the editors and the reviewers. Any product that may be evaluated in this article, or claim that may be made by its manufacturer, is not guaranteed or endorsed by the publisher.

## References

Bao, C. W. (1995). Paleo-valleys and paleo-deltas on the continental shelf south of the pearl river (in Chinese with English abstract). *Mari. Geol. Quat. Geol.* 15 (2), 25–36

Bao, X. W., Hou, Y.J., Chen, C. S., Chen, F., and Shi, M.C. (2005). Analysis of characteristics and mechanism of current system on the west coast of Guangdong of China in summer. *Acta Oceanol. Sin.* 24 (4), 1–9.

Bassetti, M.-A., Berné, S., Sicre, M.-A., Dennielou, B., Alonso, Y., Buscail, R., et al. (2016). Holocene Hydrological changes in the rhône river (NW Mediterranean) as recorded in the marine mud belt. *Clim. Past.* 12 (7), 1539–1553. doi: 10.5194/cp-12-1539-2016

Chen, J., Ma, J., Xu, K., Liu, Y., Cao, W., Wei, T., et al (2017). Provenance discrimination of the clay sediment in the western Taiwan strait and its implication for coastal current variability during the late-Holocene. *Holocene* 27 (1), 110–21. doi: 10.1177/0959683616652706

Chen, H., Wang, J., Khan, N. S., Waxi, L., Wu, J., Zhai, Y., et al. (2019). Early and late Holocene paleoenvironmental reconstruction of the pearl river estuary, south China Sea using foraminiferal assemblages and stable carbon isotopes. *Estuar. Coast. Shelf. S.* 222, 112–125. doi: 10.1016/j.ecss.2019.04.002

Cheng, Z., Weng, C., Steinke, S., and Mohtadi, M.. (2018). Anthropogenic modification of vegetated landscapes in southern China from 6,000 years ago. *Nat. Geosci.* 11 (12), 939–943. doi: 10.1038/s41561-018-0250-1

Ding, Y., Bao, X., Yao, Z., Zhang, C., Wan, K., Bao, M., et al. (2017). A modeling study of the characteristics and mechanism of the westward coastal current during summer in the northwestern south China Sea. *Ocean. Sci. J.* 52 (1), 11–30. doi: 10.1007/s12601-017-0011-x

Dykoski, C. A., Edwards, R. L., Cheng, H., Yuan, D., Cai, Y., Zhang, M., et al. (2005). A high-resolution, absolute-dated Holocene and deglacial Asian monsoon record from dongge cave, China. *Earth. Planet. Sci. Lett.* 233 (1), 71–86. doi: 10.1016/j.epsl.2005.01.036

Gao, S., and Collins, M. B. (2014). Holocene Sedimentary systems on continental shelves. *Mar. Geol.* 352, 268–294. doi: 10.1016/j.margeo.2014.03.021

Gao, S., Liu, Y., Yang, Y., Liu, P. J., Zhang, Y., and Wang, Y. P. (2015). Evolution status of the distal mud deposit associated with the pearl river, northern south China Sea continental shelf. *J. Asian Earth Sci.* 114, 562–573. doi: 10.1016/j.jseaes.2015.07.024

Ge, Q., Liu, J. P., Xue, Z., and Chu, F. (2014). Dispersal of the zhujiang river (Pearl river) derived sediment in the Holocene. *Acta Oceanol. Sin.* 33 (8), 1–9. doi: 10.1007/s13131-014-0407-8

Hanebuth, T. J. J., Lantzsch, H., and Nizou, J. (2015). Mud depocenters on continental shelves–appearance, initiation times, and growth dynamics. *Geo-Mar. Lett.* 35 (6), 487–503. doi: 10.1007/s00367-015-0422-6

Hong, S.-H., Chang, T. S., Lee, G.-S., Kim, J. C., Choi, J., and Yoo, D.-G. (2019). Late pleistocene-Holocene sedimentary facies and evolution of the jeju strait shelf, southwest Korea. *Quat. Int.* 519, 156–169. doi: 10.1016/j.quaint.2019.04.014

Huang, C. (2018). *Holocene Climate change and human activity from an archive of continental shelf sediments in the northern south China Sea (in Chinese with English abstract)* (Doctor of Philosophy), University of Chinese Academy of Sciences, Guangzhou, CN, Guangzhou Institute of Geochemistry).

Huang, C., Zeng, T., Ye, F., Xie, L., Wang, Z., Wei, G., et al. (2018). Natural and anthropogenic impacts on environmental changes over the past 7500 years based on the multi-proxy study of shelf sediments in the northern south China Sea. *Quat. Sci. Rev.* 197, 35–48. doi: 10.1016/j.quascirev.2018.08.005

Hu, D., Clift, P. D., Böning, P., Hannigan, R., Hillier, S., Blusztajn, J., et al. (2013). Holocene Evolution in weathering and erosion patterns in the pearl river delta. *Geochem. Geophy. Geosy.* 14 (7), 2349–2368. doi: 10.1002/ggge.20166

Hu, J., Kawamura, H., Hong, H., and Qi, Y.. (2000). A Review on the Currents in the South China Sea: Seasonal Circulation, South China Sea Warm Current and Kuroshio Intrusion. *J. Oceanogr* 56, 607–624. doi: 10.1023/A:1011117531252

Lesueur, P., Tastet, J. P., and Marambat, L. (1996). Shelf mud fields formation within historical times: examples from offshore the gironde estuary. France. *Cont. Shelf. Res.* 16 (14), 1849–1870. doi: 10.1016/0278-4343(96)00013-1

Li, G., Li, P., Liu, Y., Qiao, L., Ma, Y., Xu, J., et al. (2014). Sedimentary system response to the global sea level change in the East China seas since the last glacial maximum. *Earth-Sci. Rev.* 139, 390–405. doi: 10.1016/j.earscirev.2014.09.007

Li, G., Yan, W., and Zhong, L. (2016). Element geochemistry of offshore sediments in the northwestern south China Sea and the dispersal of pearl river sediments. *Prog. Oceanogr.* 141, 17–29. doi: 10.1016/j.pocean.2015.11.005

Li, G., Yan, W., Zhong, L., Xia, Z., and Wang, S. (2015). Provenance of heavy mineral deposits on the northwestern shelf of the south China Sea, evidence from single-mineral chemistry. *Mar. Geol.* 363, 112–124. doi: 10.1016/j.margeo.2015.01.015

Liu, Y., Gao, S., Wang, Y. P., Yang, Y., Long, J., Zhang, Y., et al. (2014). Distal mud deposits associated with the pearl river over the northwestern continental shelf of the south China Sea. *Mari. Geol.* 347, 43–57. doi: 10.1016/j.margeo.2013.10.012

Liu, J. P., Xue, Z., Ross, K., Wang, H. J., Yang, Z. S., Li, A. C., et al. (2009). Fate of sediments delivered to the sea by Asian large rivers: Long-distance transport and formation of remote alongshore clinothems. *Sediment. Rec.* 7 (4), 4–9. doi: 10.2110/sedred.2009.4.4

Liu, J. P., Xu, K. H., Li, A. C., Milliman, J. D., Velozzi, D. M., Xiao, S. B., et al. (2007). Flux and fate of Yangtze river sediment delivered to the East China Sea. *Geomorphology* 85 (3-4), 208–224. doi: 10.1016/j.geomorph.2006.03.023

Nizou, J., Hanebuth, T. J. J., Heslop, D., Schwenk, T., Palamenghi, L., Stuut, J.-B., et al. (2010). The Senegal river mud belt: A high-resolution archive of paleoclimatic change and coastal evolution. *Mari. Geol.* 278 (1), 150–164. doi: 10.1016/j.margeo.2010.10.002

Park, S.-C., Lee, H.-H., Han, H.-S., Lee, G.-H., Kim, D.-C., and Yoo, D.-G. (2000). Evolution of late quaternary mud deposits and recent sediment budget in the southeastern yellow Sea. *Mari. Geol.* 170 (3), 271–288. doi: 10.1016/S0025-3227(00)00099-2

Paterson, G. A., and Heslop, D. (2015). New methods for unmixing sediment grain size data. *Geochem. Geophy. Geosy.* 16 (12), 4494–4506. doi: 10.1002/2015gc006070

Prins, M. A., Postma, G., and Weltje, G. J. (2000). Controls on terrigenous sediment supply to the Arabian Sea during the late quaternary: the makran continental slope. *Mari. Geol.* 169 (3), 351–371. doi: 10.1016/S0025-3227(00)00087-6

Qi, L., Hu, J., and Gregoire, D. C. (2000). Determination of trace elements in granites by inductively coupled plasma mass spectrometry. *Talanta* 51 (3), 507–513. doi: 10.1016/S0039-9140(99)00318-5

Reimer, P. J., Bard, E., Bayliss, A., Beck, J. W., Blackwell, P. G., Ramsey, C. B., et al. (2013). IntCal13 and Marine13 radiocarbon age calibration curves 0–50,000 years cal BP. *Radiocarbon* 55 (4), 1869–1887. doi: 10.2458/azu_js_rc.55.16947

Schimanski, A., and Stattegger, K. (2005). Deglacial and Holocene evolution of the Vietnam shelf: stratigraphy, sediments and sea-level change. *Mari. Geol.* 214 (4), 365–387. doi: 10.1016/j.margeo.2004.11.001

Southon, J., Kashgarian, M., Fontugne, M., Metivier, B., and Yim, W. W.-S. (2002). Marine reservoir corrections for the Indian ocean and southeast Asia. *Radiocarbon* 44 (1), 167–180. doi: 10.1017/s0033822200064778

Su, J. (2004). Overview of the south China Sea circulation and its influence on the coastal physical oceanography outside the pearl river estuary. *Cont. Shelf. Res.* 24 (16), 1745–1760. doi: 10.1016/j.csr.2004.06.005

Swift, D. J. P., Stanley, D. J., and Curray, J. R. (1971). Relict sediments on continental shelves: A reconsideration. *Geol. J.* 79 (3), 322–346. doi: 10.1086/627629

Tjallingii, R., Claussen, M., Stuut, J.-B. W., Fohlmeister, J., Jahn, A., Bickert, T., et al. (2008). Coherent high- and low-latitude control of the northwest African hydrological balance. *Nat. Geosci.* 1, 670. doi: 10.1038/ngeo289

Wang, W. J. (1985). Sedimentation and sedimentary facies of the pearl river mouth (in Chinese with English abstract). *Acta Sed. Sin.* 3 (2), 129–140.

Wang, P. (1999). Response of Western pacific marginal seas to glacial cycles: paleoceanographic and sedimentological features. *Mari. Geol.* 156 (1–4), 5–39. doi: 10.1016/s0025-3227(98)00172-8

Wang, W. J. (2007). *Study on the coastal geomorphological sedimentation of the south China Sea (in Chinese with English abstract)* (Guangzhou, China: Guangdong Economy Publishing House).

Wang, S., Lü, H., Liu, J., and Negendank, J. F. W. (2007). The early Holocene optimum inferred from a high-resolution pollen record of huguangyan maar lake in southern China. *Sci. Bull.* 52 (20), 2829–2836. doi: 10.1007/s11434-007-0419-2

Wang, Z., Xu, H., Zhan, Q., Saito, Y., He, Z., Xie, J., et al. (2010). Lithological and palynological evidence of late quaternary depositional environments in the subaqueous Yangtze delta, China. *Quat. Res.* 73 (3), 550–562. doi: 10.1016/j.yqres.2009.11.001

Wang, K., Zheng, H., Tada, R., Irino, T., Zheng, Y., Saito, K., et al. (2014). Millennial-scale East Asian summer monsoon variability recorded in grain size and provenance of mud belt sediments on the inner shelf of the East China Sea during mid-to late Holocene. *Quat. Int.* 349, 79–89. doi: 10.1016/j.quaint.2014.09.014

Waxi, L., Wang, J. H., Chen, H. X., Wu, J. X., and Tao, H. (2016). Elemental records of the core ZK19 in the lindingyang bay of the pearl river estuary and the paleoenvironmental implications (in Chinese with English abstract). *Trop. Geogr.* 36 (3), 343–354.

Wei, X., Wu, C., Ni, P., and Mo, W. (2016). Holocene Delta evolution and sediment flux of the pearl river, southern China. *J. Quaternary. Sci.* 31 (5), 484–494. doi: 10.1002/jqs.2873

Xiao, S., Li, R., and Chen, M. (2013). Detecting sedimentary cycles using autocorrelation of grain size. *Sci. Rep-UK.* 3, 1653. doi: 10.1038/srep01653

Xiong, H., Zong, Y., Qian, P., Huang, G., and Fu, S. (2018). Holocene Sea-level history of the northern coast of south China Sea. *Quat. Sci. Rev.* 194, 12–26. doi: 10.1016/j.quascirev.2018.06.022

Xu, F. J., Hu, B. Q., Dou, Y. G., Song, Z. J., Liu, X. T., Yuan, S. Q., et al. (2017). Prehistoric heavy metal pollution on the continental shelf off hainan island, south China Sea: from natural to anthropogenic impacts around 4.0 kyr BP. *Holocene* 28 (3), 455–463. doi: 10.1177/0959683617729445

Xu, K., Li, A., Liu, J. P., Milliman, J. D., Yang, Z., Liu, C.-S., et al. (2012). Provenance, structure, and formation of the mud wedge along inner continental shelf of the East China Sea: A synthesis of the Yangtze dispersal system. *Mari. Geol.* 291–294, 176–191. doi: 10.1016/j.margeo.2011.06.003

Yao, Y., Harff, J., Meyer, M., and Zhan, W. (2009). Reconstruction of paleocoastlines for the northwestern south China Sea since the last glacial maximum. *Sci. China Earth Sci.* 52 (8), 1127–1136. doi: 10.1007/s11430-009-0098-8

Yim, W. W. S., Huang, G., Fontugne, M. R., Hale, R. E., Paterne, M., Pirazzoli, P. A., et al. (2006). Postglacial sea-level changes in the northern south China Sea continental shelf: Evidence for a post-8200 calendar yr BP meltwater pulse. *Quat. Int.* 145–146, 55–67. doi: 10.1016/j.quaint.2005.07.005

Yoo, D. G., Lee, C. W., Kim, S. P., Jin, J. H., Kim, J. K., and Han, H. C. (2002). Late quaternary transgressive and highstand systems tracts in the northern East China Sea mid-shelf. *Mar. Geol.* 187 (3-4), 313–328. doi: 10.1016/S0025-3227(02)00384-5

Yu, F., Zong, Y., Lloyd, J. M., Leng, M. J., Switzer, A. D., Yim, W. W. S., et al. (2011). Mid-Holocene variability of the East Asian monsoon based on bulk organic $\delta^{13}C$ and C/N records from the pearl river estuary, southern China. *Holocene* 22 (6), 705–715. doi: 10.1177/0959683611417740

Zhang, Y., Zhu, K., Huang, C., Kong, D., He, Y., Wang, H., et al. (2019). Asian Winter monsoon imprint on Holocene SST changes at the northern coast of the south China Sea. *Geophys. Res. Lett.* 46 (22), 13363–13370. doi: 10.1029/2019GL085617

Zhao, Y., Yu, Z., Chen, F., Zhang, J., and Yang, B. (2009). Vegetation response to Holocene climate change in monsoon-influenced region of China. *Earth-Sci. Rev.* 97 (1), 242–256. doi: 10.1016/j.earscirev.2009.10.007

Zheng, B. X., He, J., Yao, H. Y., and Li, J. F. (2017). Grain-size distribution of suspended load and bed sediments in modaomen estuary of pearl river during flood season and implications for sediment exchange processes (in Chinese with English abstract). *J. Sediment. Res.* 42 (2), 9–15.

Zheng, Z., and Li, Q. (2000). Vegetation, climate, and Sea level in the past 55,000 years, hanjiang delta, southeastern China. *Quat. Res.* 53 (3), 330–340. doi: 10.1006/qres.1999.2126

Zhong, Y., Chen, Z., Li, L., Liu, J., Li, G., Zheng, X., et al. (2017). Bottom water hydrodynamic provinces and transport patterns of the northern south China Sea: Evidence from grain size of the terrigenous sediments. *Cont. Shelf. Res.* 140, 11–26. doi: 10.1016/j.csr.2017.01.023

Zhou, Q. K. (2014). *Numerical research on evolution character of submarine sand waves in the northern south China Sea (in Chinese with English abstract).(Master)* , First Institute of Oceanography,State Oceanic Administration, Qingdao, CN, First Institute of Oceanography).

Zong, Y., Huang, G., Switzer, A. D., Yu, F., and Yim, W. W. S. (2009). An evolutionary model for the Holocene formation of the pearl river delta, China. *Holocene* 19 (1), 129–142. doi: 10.1177/0959683608098957

Zong, Y., Lloyd, J. M., Leng, M. J., Yim, W. W. S., and Huang, G. (2006). Reconstruction of Holocene monsoon history from the pearl river estuary, southern China, using diatoms and carbon isotope ratios. *Holocene* 16 (2), 251–263. doi: 10.1191/0959683606hl911rp

Zong, Y., Yu, F., Huang, G., Lloyd, J. M., and Yim, W. W. S. (2012). The history of water salinity in the pearl river estuary, China, during the late quaternary. *Earth Surf. Proc. Land.* 35 (10), 1221–1233. doi: 10.1002/esp.2030

frontiers | Frontiers in Marine Science

TYPE Original Research
PUBLISHED 28 July 2022
DOI 10.3389/fmars.2022.911880



OPEN ACCESS

EDITED BY
Guan-hong Lee,
Inha University, South Korea

REVIEWED BY
Aoi Sugimoto,
Japan Fisheries Research and Education Agency (FRA), Japan
Lino Vieira De Oliveira Costa,
University of Lisbon, Portugal

*CORRESPONDENCE
Ling Cao
caoling@sjtu.edu.cn

SPECIALTY SECTION
This article was submitted to Marine Affairs and Policy, a section of the journal Frontiers in Marine Science

RECEIVED 03 April 2022
ACCEPTED 06 July 2022
PUBLISHED 28 July 2022

CITATION
Zeng X, Liang J, Zeng J, Chen M, Zeng C, Mazur M, Li S, Zhou Z, Ding W, Ding P and Cao L (2022) Evaluating the effectiveness of three national marine protected areas in the Yangtze River Delta, China. *Front. Mar. Sci.* 9:911880. doi: 10.3389/fmars.2022.911880



# Evaluating the effectiveness of three national marine protected areas in the Yangtze River Delta, China

Xu Zeng[1,2], Jun Liang[3], Jiangning Zeng[2], Mingyang Chen[1], Cong Zeng[1], Makenzie Mazur[4], Shenghui Li[1], Zengjie Zhou[5], Wei Ding[6], Peng Ding[7] and Ling Cao[1]*

[1]School of Oceanography, Shanghai Jiao Tong University, Shanghai, China, [2]Key Laboratory of Marine Ecosystem Dynamics, Second Institute of Oceanography, Ministry of Natural Resources, Hangzhou, China, [3]Fisheries Resources and Ecology Laboratory, Zhejiang Marine Fisheries Research Institute, Zhoushan, China, [4]Fisheries Ecology Lab, Gulf of Maine Research Institute, Portland, ME, United States, [5]Special Marine Protected Area Division, Shengsi Ma'an Special Marine Protected Area Administration Bureau, Shengsi, China, [6]Marine Division, Putuo District Ocean and Fisheries Bureau, Zhoushan, China, [7]Xiangshan Jiushan Islands National Nature Reserve, Xiangshan Natural Resources and Planning Bureau, Xiangshan, China

China's coastal areas face serious environmental degradation as a consequence of large-scale economic development. To balance environmental sustainability with economic development, China is currently implementing a strategy of 'eco-civilization', with marine protected areas (MPAs) expected to be one approach to achieving sustainable marine ecosystems. Since the 1990s, China has established over 270 MPAs, but their effectiveness remains unknown, particularly in the Yangtze River Delta. This study modified pre-existing frameworks to evaluate the effectiveness of three national MPAs in the Yangtze River Delta. The modified framework includes conservation outcomes and their potential drivers. Drivers consist of – attributes species or ecosystems within the MPA, attributes of the MPA, institutional design principles, and participation. Five scenarios were proposed based on score combinations of the four drivers: proactive, well designed, well governed, interactive, and learning. All three MPAs achieved a satisfactory level of outcomes and most of the drivers for all three MPAs achieved a satisfactory level. Two of the MPAs were categorized into the learning scenario, and the third into the well-designed scenario, indicating that there is still room to improve institutional design principles and public participation. We suggest developing cost and benefit indicators to more deeply understand proportionality among stakeholders. In addition, the role of participation should be clarified and promoted. We recommend regular environmental performance monitoring and assessment to identify problems and optimize management.

KEYWORDS

**effectiveness, framework, drivers, environmental performances, management scenarios**

## Introduction

The Earth's oceans are affected by human activities, and over 40% of the marine environment currently faces multiple pressures, including overfishing, climate change, and ocean- and land-based stressors (Halpern et al., 2015). This situation is more pronounced in the coastal areas of developing countries, such as China (McCook et al., 2018). China's coastal areas are of high ecological and socio-economic importance. The country's 18,000 km coastline has four large marine ecosystems (LMEs) – the Yellow Sea, the East China Sea, the Kuroshio Current, and the South China Sea (Qiu et al., 2009). Together, they are home to about 12,000 marine species (Huang, 1994). Marine resources make an important contribution to China's economic development in the areas of fishing, maritime shipping, and oil and gas exploration. In 2019, China's marine economy generated over 8,900-billion-yuan, accounting for 9% of the total GDP (Ministry of Natural Resources (MNR), 2020). Given the importance of China's coastal areas for economic development and the environmental pressures these areas face, effective management to ensure sustainable development is required.

To balance environmental sustainability with economic development, China is currently implementing a strategy of 'eco-civilization'. This strategy calls for the inclusion of environmental protection in the nation's economic, social, cultural, and political systems and establish a long-term mechanism of environmental protection in which stakeholders (the public, businesses, and government officials) can actively participate (United Nations Environment Programme (UNEP), 2016). In the marine environment, this strategy involves "improving the capacity of marine resource exploitation, developing the marine economy, protecting the ecological environment, resolutely safeguarding national marine rights and interests, developing the maritime power" (Xinhua, 2012). Marine protected areas (MPAs) have been adopted as a tool in China's drive towards 'eco-civilization', to conserve biodiversity and the environment. China has two broad categories of MPA: marine nature reserves (MNR), in which extractive activities are highly restricted, and special marine protected areas (SMPA), including marine parks, in which multiple resource use is allowed. According to the importance of their protection targets, MPAs are designated at national and local level (Qiu, 2010). In recent decades, there has been remarkable expansion in the establishment of MPAs, with an increase of 4% annually (Hu et al., 2020). By the end of 2020, there were 271 designated MPAs (106 national MPAs and 165 local MPAs), covering 4.1% of the sea area under China's jurisdiction (Zhao, 2018). Although there is a trend toward increasing the number and coverage of China's MPAs, their effectiveness has not yet been proven. A preliminary assessment found that only 27% of MPAs met three of five success criteria (no-take, enforced, old, large, and isolated) (Hu et al., 2020), which is much lower than the 59% for MPAs globally (Edgar et al., 2014). In addition, many MPAs are unmanaged "paper parks" lacking management administration and funding (Li and Fluharty, 2017). Further research on the effectiveness of China's MPAs is required to improve their conservation outcomes.

The Yangtze River Delta is located near the East China Sea. It supports a population of 225 million people and contributes about one-quarter of China's GDP (Wei, 2020). The region is a strategic location for the sustainable development of China's 'eco-civilization'. At the end of 2020, 34 MPAs had been implemented in the coastal areas of the Yangtze River Delta, of which 41% are MNRs and 59% are SMPAs. These are important environmental management tools. However, the coastal areas of the Yangtze River Delta face a lot of pressure. At present, the total length of continental natural coastline in the Yangtze River Delta is 96,344 km, accounting for 31.2% of China's total coastline (Chen et al., 2018; Wang et al., 2019). Due to the erosion and rapid development, the natural coastline in the Yangtze River Delta is losing (Wang et al., 2019). Besides, the ecosystem health of the Yangtze River Delta is under pressure. According to a 2019 communique on the state of China's marine ecology and environment, the northern Jiangsu shoal (located in the Yangtze River Delta) and the Yangtze Estuary are sub-healthy and Hangzhou Bay is unhealthy (Ministry of Ecology and Environment (MoEE), 2020). In 2019, the Central Committee of the Communist Party of China and the State Council issued the *Outline of the integrated regional development of the Yangtze River Delta*, detailing ongoing social and economic development in the area. To guarantee the sustainable development of the Yangtze River Delta, there is an urgent need to enhance the effectiveness of marine environmental management tools, especially MPAs, which are crucial for the implementation of China's 'eco-civilization' strategy.

Promoting the effectiveness of MPAs is a global requirement. A management effectiveness evaluation (MEE), defined as "the assessment of how well the protected area is being managed – primarily the extent to which it is protecting values and achieving goals and objectives" (Hockings et al., 2006), is an efficient approach to improving the effectiveness of MPAs by identifying the status of management actions, detecting management strengths and weaknesses, and providing information for adaptive management. MEEs have been applied to 60% of MPAs globally (Laffoley et al., 2019), but only a few have been conducted in China (Song et al., 2018).

The first MEE framework for protected areas was developed by the International Union for the Conservation of Nature-World Commission on Protected Areas (IUCN-WCPA). It comprises six key management elements – context, planning, inputs, process, outputs, and outcomes (Hockings et al., 2016). Based on this framework, more than 50 MEE methodologies have been developed (Leverington et al., 2010). The two most relevant frameworks for MPAs are the Marine Score-Card (Staub and Hatziolos, 2004) and How is your MPA doing? (HIYMPAD) (Pomeroy et al., 2005). The former is adapted from

the Management Effectiveness Tracking Tool (METT) (Stolton et al., 2003), which is used to evaluate the progress of management in individual protected areas over time. The latter evaluates the biophysical, socioeconomic, and governance of individual MPAs.

Included in MPA MEE frameworks are evaluations of ecological (e.g., fish density) and socio-economic (e.g., typical income of fishers) outcomes. Recently, researchers have suggested that more attention should be given to the drivers likely to lead to successful MPA outcomes so that management actions and the rational allocation of resources can be prioritized (Bennett and Dearden, 2014). Several evaluations focusing on the potential drivers of MPA outcomes have been conducted at global and regional scales, and enforcement, participation, species attributes, capacity shortfalls, and size of the no-take area have been identified as the main factors impacting MPA outcomes (Ban et al., 2017; Gill et al., 2017; Hargreaves-Allen et al., 2017). The selection of potential drivers is key to these evaluations. An evaluation by Ban et al. (2017) identified four key potential drivers (attributes of the species or ecosystem within the MPA, attributes of the MPA, institutional design principles, and participation) for large MPA outcomes. These drivers were identified based on the management of marine resources, the design and management of small-scale MPAs, and the management of common-pool resources. This framework has a solid theoretical basis and can systematically investigate the social, ecological, and governance characteristics of an MPA using both qualitative and quantitative approaches. It has successfully been tested on 12 large MPAs. Using this framework to evaluate the effectiveness of MPAs will help to more deeply understand the social, ecological, and governance mechanisms that contribute to a range of conservation outcomes.

According to Ban et al (2017) framework, fisheries, ecosystem health (trends in the condition of ecosystem health proxies, such as changes in coral cover), and the wellbeing of fishers were selected as outcomes. In practice, environmental performance should be evaluated within the MPA. It has been demonstrated that even no-take areas can be threatened by toxic chemical contamination, such as persistent organic pollutants (POPs) and trace metals originating from surface runoff, partially treated effluent, freshwater discharge from polluted rivers, and/or contaminated atmospheric deposition (Campanella et al., 2001; Terlizzi et al., 2004). Given that most of China's MPAs are near urban areas and are continuously influenced by anthropogenic activities such as industrial wastewater discharge (Lu et al., 2020), marine organisms inhabiting such MPAs are at risk. In addition, protecting the ecological environment is a common objective for all of China's MPAs based on the Rules of Marine Nature Reserves and the Rule of Special Marine Protected Areas (SOA, 1995; SOA, 2010). Therefore, an evaluation that includes environmental performance is necessary for the sustainability of China's MPAs.

In this study, we assessed the effectiveness of MPAs in the Yangtze River Delta, taking three national MPAs as a case study. For this purpose, we modified Ban et al (2017) framework and environmental evaluation. We analyzed the key potential drivers for MPA outcomes and designed five possible scenarios, with priority given various aspects, each of which has consequences on the MPA's social and ecological systems. The evaluation results offer recommendations and lessons on the sustainability and success of MPAs in the Yangtze River Delta, and provide guidance for the evaluation of MPAs elsewhere in China and in other developing countries.

## Description of the case study sites

Three national MPAs in the Yangtze River Delta were evaluated (Figure 1). They were Shengsi National Marine Park, Putuo National Marine Park, and Jiushan Archipelago Marine Ecological National Nature Reserve (Figure 2). These three cases were chosen because they are national marine protected areas, and the resources and ecosystems within them have significant marine ecological conservation, ecotourism, and exploitation values. The state has invested them more than local MPAs, and people are highly concerned about them. Therefore, there is high interest in whether they are effectively managed and protect the marine ecosystems or not. Besides, these three cases include marine nature reserves and special marine protected area (including marine park), ensuring that all types of MPAs in the Yangtze River Delta can be covered. Furthermore, the three cases are different in time of establishment, primary objectives and size, which allows for better validation of the suitability of the framework we developed.

### Shengsi National Marine Park (Shengsi)

Shengsi National Marine Park is located in Ma'an archipelago. It covers an area of 549 $km^2$ and contains 136 islands. It provides good nursery and suitable habitat for many species (Wang et al., 2012) and is home to 96 fish species, 19 shrimp species, 15 crab species, 118 sea algae species, as well as various mollusks and shellfish. Moreover, it has 64 items of listed cultural heritage, including fish food culture, mussel culture, and Shengsi fishing songs (Second Institute of Oceanography (SIO), 2013).

Ma'an archipelago was designated as Shengsi Ma'an SMPA in 2005. Its protection objectives are marine living resources, unique natural island landforms, and intertidal wetlands. The management administration for this SMPA is Shengsi Ma'an Special Marine Protected Area Administration Bureau. The *Shengsi Marine Fishing Management Interim Measures (Trial)* and *Rules for the Implementation of the Interim Measures for the Management of Reef Resources in Shengsi Ma'an Archipelago* were issued for the management of this MPA in 2011 and 2012, respectively. In 2015, this SMPA was designated as Shengsi

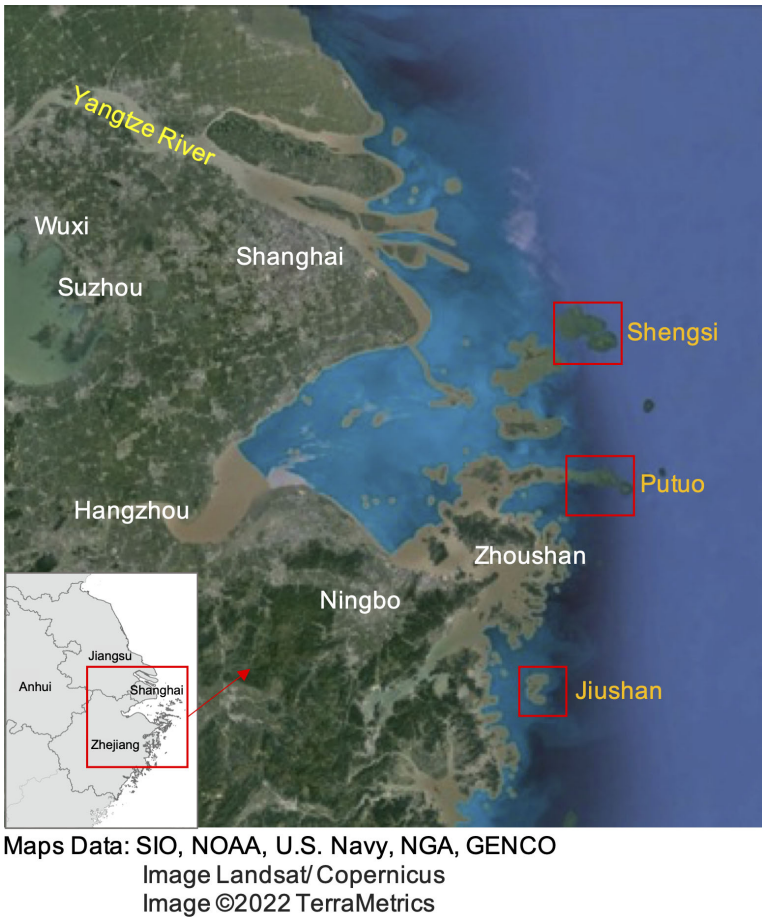


FIGURE 1
The Yangtze River Delta (in the bottom left corner, including Shanghai, Jiangsu, Anhui, Zhejiang) and the locations of Shengsi National Marine Park (Shengsi), Putuo National Marine Park (Putuo), and Jiushan Archipelago Marine Ecological National Nature Reserve (Jiushan).

National Marine Park, with management administration consistent with the previous bureau. However, zones within the marine park were changed into major protected zone, moderate utilization zone, and ecological resources restoration zone (Figure 2). Meanwhile, three management rules issued by the Zhoushan government guide the management of the marine park. These are the *Regulations of National Marine Special Marine Protected Area in Zhoushan*, the *Interim Measures for Marine Fishing in Zhoushan National Special Marine Protected Area*, and the *Interim Measures for Shellfish and Algae Fishing in Zhoushan National Special Marine Protected Area*.

## Putuo National Marine Park (Putuo)

Putuo National Marine Park is located in Zhongjieshan archipelago. It covers an area of 218.4 km$^2$ and contains 151 islands. Mainland runoff and surface current generated by the Yangtze River estuary make this area abundant in nutrients, and it is the site of the Zhongjieshan fishing ground. The marine park is home to more than 35 fish species, 11 shrimp species, and 12 crab species (SIO, 2016). In addition, natural resources include mountains, sea, islands, reefs. The area experiences abundant sunshine and fog and is well-known as a tourist and sea fishing resort. A survey of Asian Fishing Federation experts named Putuo National Marine Park's black sea bream (*Acanthopagrus schlegelii*) the best in the Western Pacific (SIO, 2016). This SMPA aims to protect fish, bird, reefs, and shellfish. Putuo Zhongjieshan Archipelago Special Marine Protected Area Administration Bureau is responsible for the daily management of the park. In 2008, the *Rules for the Implementation of Zhejiang Putuo Zhongjie Mountain Archipelage Special Marine Protected Area* were issued for the management of the SMPA. In 2017, this SMPA was approved as Putuo National Marine Park. Its primary protection objective and management administration are consistent with those of the

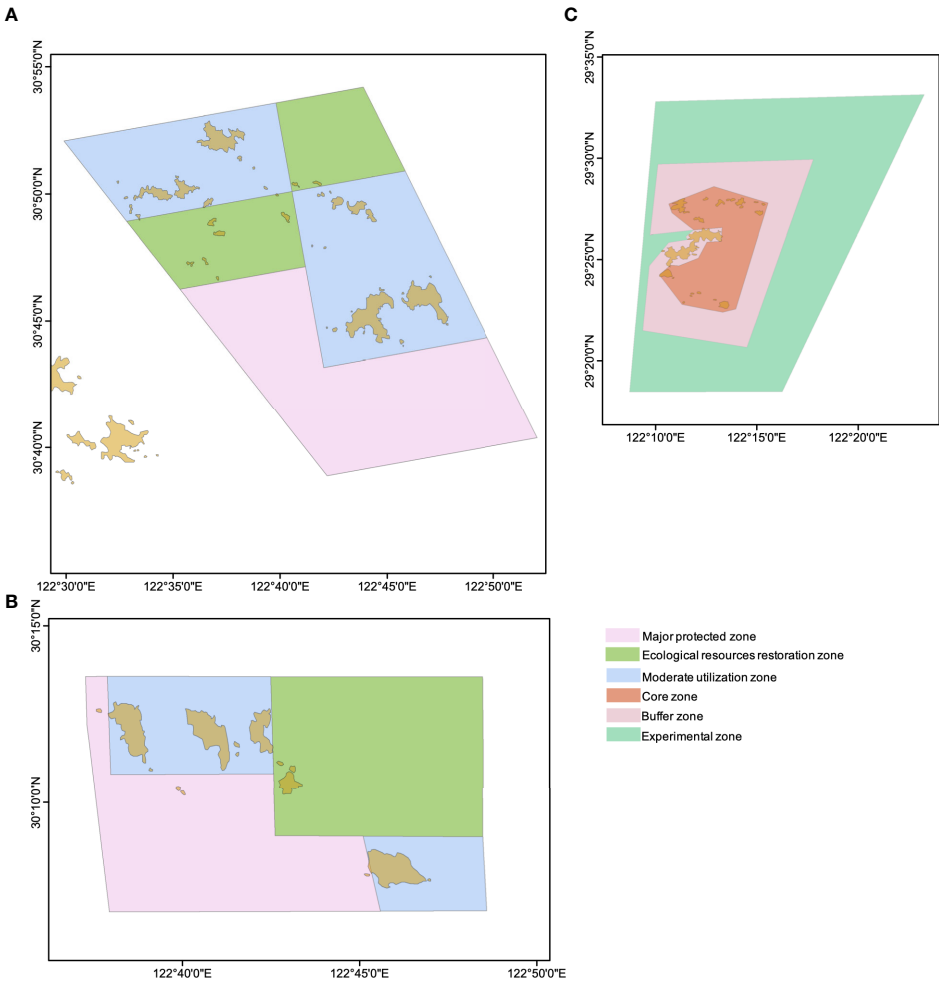


FIGURE 2
Zones in Shengsi National Marine Park **(A)**, Putuo National Marine Park **(B)**, and Jiushan Archipelago Marine Ecological National Nature Reserve **(C)**.

former SMPA. This marine park consists of three zones – major protected zone, moderate utilization zone, and ecological resources restoration zone (Figure 2). It is managed by the *Regulations of National Marine Special Marine Protected Area in Zhoushan*, *Interim Measures for Marine Fishing in Zhoushan National Special Marine Protected Area*, and *Interim Measures for Shellfish and Algae Fishing in Zhoushan National Special Marine Protected Area*.

## Jiushan Archipelago Marine Ecological National Nature Reserve (Jiushan)

Jiushan Archipelago Marine Ecological National Nature Reserve covers an area of 484.8 km$^2$ and is an important seabird breeding site and migratory bird resting point. It has 108 bird species (Ningbo MEMC, 2012), including the Chinese crested tern (*Thalasseus bernsteini*) which is under special protection. Jiushan archipelago also contains suitable habitat for the migration, mating, and reproduction for various marine organisms. It is home to 62 fish species, 49 crustacean species, and more than 30 other species (Ningbo MEMC, 2012). In addition, it is home to the finless porpoise (*Neophocaena asiaeorientalis*) and a variety of waterfowl, making it an excellent place for bird watching, island fishing, and sightseeing.

Jiushan Archipelago was designated as a provincial nature reserve in 2003. It aims to protect the large yellow croaker (*Larimichthys crocea*), cuttlefish (*Sepiella maindroni de rochebrune*), the finless porpoise (*Neophocaena asiaeorientalis*), and the Chinese crested tern (*Thalasseus bernsteini*). Jiushan Archipelago Provincial Ecological Nature Reserve Administration Bureau was established to manage this reserve. In 2006, the *Regulations of Jiushan Archipelago Marine Ecological Nature Reserve* were issued for the management of

this MNR. In 2011, this provincial MNR was approved as a national MNR. Its primary protection objectives are consistent with those of the former provincial MNR, but management administration has changed to Jiushan Archipelago National Marine Ecological Nature Reserve Administration Bureau. The *Regulations of Jiushan Archipelago Marine Ecological Nature Reserve, Ningbo City* were revised in 2017 to manage this MNR. There are three zones (Figure 2) within this reserve – the core zone, in which all extraction activities are forbidden, the buffer zone, in which non-destructive scientific research, teaching practice, and specimen collection activities are allowed, and the experimental zone, in which appropriate development activities are allowed if approved by the management authority.

# Methodology

In this study, we first reviewed literature on methods for evaluating the management effectiveness of MPAs, including the Marine Effectiveness Tracking Tool (METT), the Marine Score-Card, and How is your MPA doing? (HIYMPAD) (Pomeroy et al., 2005), in addition to other frameworks (Bennett and Dearden, 2014; Ban et al., 2017). Given the purpose of this assessment and the common objectives of China's MPAs, we chose the framework that focuses on outcomes and the drivers of those outcomes, and we added additional indicators for biological and environmental performance.

## Modification of the evaluation framework

The modified evaluation framework is adapted from Ban et al. (2017), which was originally used to assess the social and ecological effectiveness of large marine protected areas. This framework focuses on four key aspects that may drive the social and ecological outcomes of an MPA: 1) attributes of the species or ecosystem within the MPA, 2) attributes of the MPA, 3) institutional design principles, and 4) participation, with a total of 32 indicators (Table 1). Two additional outcome indicators (fisher's income and fisheries) were selected for our modified framework.

The three MPAs are located in important fishing grounds and the conservation objectives of all three include fish species protection. Therefore, fisheries reflect the biological indicator of conservation effectiveness. Fish density, the average fish biomass per survey within an MPA, was used to represent fisheries because it is common practice to evaluate all species within an MPA. In addition, species richness (the number of species) here is used as a proxy of the fish diversity indicating the ecological impacts of MPAs at the community level (Gaston et al., 2008). Therefore, we added the fish diversity to evaluate the ecological outcome of the three MPAs. To assess fish density and fish diversity, we compared current data with data from before the establishment of the MPA, and the greater the increase, the higher the score. The pre-establishment data were obtained from the baseline trawl survey in the planning report, and the post-establishment data were obtained from the trawl survey within the MPA in recent 5 years (Han et al., 2019; unpublished data provided by Liang). These surveys were all in accordance with the Marine Survey Specification (GBT 12763.6-2007) (Standards Press of China, 2007). The fish density data were standardized by the swept area method for comparison (Zhan, 1995). The scores corresponding to the options of fish density and diversity are listed in Table A.1.

Given the urgent need to evaluate the environment performance of MPAs in the Yangtze River Delta, we added the environmental performance indicators of biophysical property, heavy metals, nutrients, and oil, all of which focus on different aspects of seawater quality and are commonly included in environment assessments (Xu et al., 2015). We measured these indicators by comparing their category level changes before and after the establishment of each MPA according to the Seawater Quality Standard of China (GB 3097-1997). There are four seawater quality indicators levels (I, II, III, IV) and each is defined within this standard. The higher the category level, the worse the seawater quality. For biophysical property, heavy metals, and nutrients, we adopted the highest category level from all indicators to represent their category level, because each one includes multiple indicators. Using the highest level guaranteed that our assessment was conducted with the utmost care. For oil, we directly compared the category level before and after the construction of each MPA. The detailed assessment method for environmental performance is defined below:

$$EP_i = \frac{Max(Category\ \ level_i)\_after}{Max(Category\ \ level_i)\_\ \ before} \quad (1)$$

Where $EP_i$ is the environmental performance, and $i$ is one aspect of environmental performances. A category level increase after the establishment of the MPA, the $EP_i$ scored 0, a consistent or higher than category level I after the establishment of the MPA scored 1, a decreased and higher than category level I after the establishment of the MPA scored 2, and a decreased or constant category level I after the establishment of the MPA scored 3.

In total, we identified 39 indicators to assess the effectiveness of MPAs in the Yangtze River Delta. Each was rated on a scale of 0 to 3, with 0 being the least favorable situation and 3 being the optimum situation. The definition and options of each indicator, and outcomes raw data are shown in Table A.1. We calculated the average scores for each type of potential driver, outcome, and environmental performance. The average scores were classified into four levels: (1) [0, 0.5), unsatisfactory; (2) [0.5, 1.5), slightly satisfactory; (3) [1.5, 2.5), satisfactory; (4) [2.5, 3], highly satisfactory.

TABLE 1 Evaluation indicators and data resources for assessing Shengsi, Putuo, and Jiushan; bold indicates newly added indicators.

| Type of indicator | Indicators | Data resource |
|---|---|---|
| Attributes of the species or ecosystem within the MPA | Commons mobility | MPA planning report |
| | Commons productivity | MPA planning report |
| | Ecological resilience | MPA planning report |
| | Resource market value | MPA planning report |
| | Distance to market | MPA planning report |
| Attributes of the MPA | No take area | MPA planning report |
| | Age | MPA planning report |
| | Snapshot age | MPA management plan |
| | Size | MPA planning report |
| | Efficient enforcement | MPA manager |
| | Isolated | MPA planning report |
| | Comprehensive, adequate, representative principles | MPA planning report |
| Institutional design principles | Stakeholder boundary clarity | MPA planning report |
| | Stakeholder boundary fuzziness | MPA planning report |
| | Commons boundaries | MPA planning report |
| | Commons boundary negotiability | MPA manager |
| | Outsider exclusion | MPA manager |
| | Social-ecological fit | MPA planning report |
| | Cost and benefit proportionality | MPA manager |
| | Participation in rule making | MPA planning report/MPA manager |
| | Self-monitoring | MPA planning report/MPA manager |
| | Environmental monitoring | MPA planning report/MPA manager |
| | Self-sanctions | MPA planning report/MPA manager |
| | External recognition | MPA planning report/MPA manager |
| | Multiple levels | MPA planning report/MPA manager |
| | Compliance | MPA manager |
| | Conflict resolution | MPA manager |
| Participation | Participation in rule making | MPA planning report/MPA manager |
| | Participation in protected area siting | MPA planning report |
| | Participation in protected area zoning | MPA planning report |
| | Participation in environmental monitoring | MPA manager |
| | Participation in social monitoring (enforcement) | MPA manager |
| Outcomes | **Fish diversity** | MPA monitoring report |
| | Fish density | MPA monitoring report |
| | Income | Local statistical yearbook |
| | **Biophysical property** | MPA monitoring report |
| | **Heavy metals** | MPA monitoring report |
| | **Nutrients** | MPA monitoring report |
| | **Oil** | MPA monitoring report |
| Total number = | 39 | |

Bold indicators represent the newly added indicators in this study.

## Data collection

Five types of data sources were used for evaluation (Table 1): (1) local statistical yearbooks (Putuo Statistics, 2019; Shengsi Statistics, 2019), (2) MPA management plans (Standing Committee of Ningbo Municipal People's Congress, 2017; Standing Committee of Zhoushan People's Congress, 2017), (3) MPA managers, (4) MPA monitoring reports (Ningbo Marine Environmental Monitoring Center (Ningbo MEMC), 2005), and (5) MPA planning reports (Ningbo MEMC, 2012; Second Institute of Oceanography (SIO), 2013; SIO, 2016). Six managers in total, each with a minimum of three years' management experience, were interviewed regarding indicators that could not be assessed using other data sources.

## Definition of five scenarios

We used the possible average score (rounded up to the nearest whole number) of all indicators to represent the unique score for each type of potential driver. There were different combinations, because the average score for each type of driver varied from 1 to 3. The attributes of the species or ecosystem within the MPA cannot be changed through management after an MPA has been designated. Therefore, we focused our analysis on MPA attributes, institutional design principles, and participation. We proposed five possible scenarios, each of which gives priority to one or other aspect (Figure 3).

This method aims to analyze and predict reality. Alternative (five options) and comparable scenarios are used. This is a tool to understand the potential and limits of management. The average score of each aspect that defines these scenarios can change over time and are, therefore, images of present, future and/or ideal situations (Nygrén, 2019). In addition, we could identify whether certain aspect changes cause significant changes to the scenario. It is also possible to see if certain specific changes (in any indicator) cause significant changes in the general model. We defined these five scenarios as: proactive, well designed, well governed, interactive, and learning.

# Results

## Differences in outcomes between the selected MPAs

Overall, Shengsi, Putuo, and Jiushan had satisfactory outcome levels (Figure 4). Shengsi had the highest average score (2) and Jiushan had the second highest (1.7). In terms of each aspect of conservation effectiveness, both fish diversity and density in Shengsi increased after the park was established, while Putuo and Jiushan only experienced increases in fish density, and the fish density of Jiushan increased more than that of Putuo (Table 2). The income of fishers increased after the establishment of the Shengsi and Putuo, while Jiushan scored 0 for this indicator. According to our assessment, the environmental performances of Shengsi and Putuo reached a satisfactory level, and that of Jiushan was at a highly satisfactory level (Figure 4).

## Assessment of drivers in the selected MPAs

We evaluated four key aspects that may impact outcomes: 1) attributes of species or ecosystems within the MPA, 2) attributes of the MPA, 3) institutional design principles, and 4) participation. Shengsi had the highest total score of these potential drivers (69), Putuo ranked second (66), and Jiushan ranked lowest (64). We also calculated the average score of each key aspect for each MPA (Figure 4). According to the score level settings in section 3.1, the effectiveness of Shengsi corresponding to the four key aspects was satisfactory. The attributes of species or ecosystems in Putuo was slightly satisfactory, and the other three aspects were satisfactory. The attributes of Jiushan were highly satisfactory, and the other three aspects were satisfactory.

Attributes of species or ecosystems within the MPA got the lowest average score of the four key aspects (Figure 4). All three MPAs obtained low scores for ecological resilience and distance to market (Table 2). Of the three MPAs, only Jiushan achieved a highly satisfactory level for MPA attributes (Figure 4), mainly due to its high score for no take area (Table 2). All three MPAs

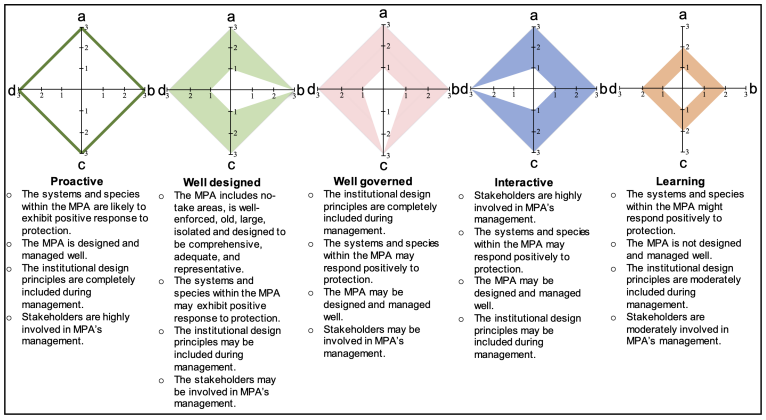


FIGURE 3
Scenario names, definitions, and figures; "a" represents the attributes of the species or ecosystem within the MPA, "b" represents the attributes of the MPA, "c" represents the institutional design principles, and "d" represents participation.

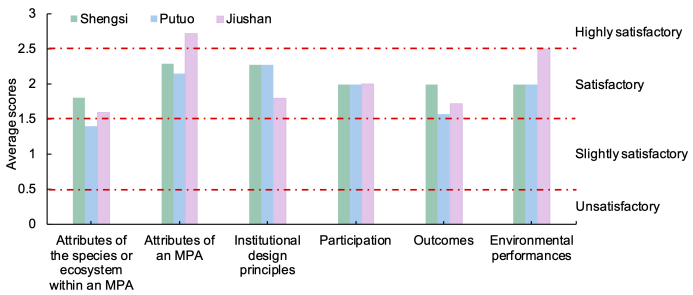


FIGURE 4
The average scores of potential drivers, outcomes and environmental performance within outcomes for the three MPAs in the Yangtze River Delta. The dashed red lines mark score levels; [0, 0.5) = unsatisfactory, [0.5, 1.5) = slightly satisfactory, [1.5, 2.5) = satisfactory [2.5, 3] = highly satisfactory.

scored 0 in the proportionality of their institutional design principles (Table 2). Participation in rule making, protected area siting, zoning, and environmental and social monitoring scored 2 in all three MPAs, indicating that actor groups are moderately involved in MPA management processes (Table 2).

## Scenario evaluation

Shengsi and Putuo scored an average of 1.8 and 1.4, respectively, for attributes of species or ecosystems and 2.3 and 2.1, respectively, attributes of the MPA. They each scored 2.3 for institutional design principles and 2 for participation (Figure 4). The rounding-off method was applied to these average scores. According to scenario definitions, Shengsi and Putuo are currently being managed according to a learning scenario (Figure 5). Jiushan, meanwhile, scored 1.6 for attributes of species or ecosystems, 2.7 for attributes of the MPA, 1.8 for institutional design principles, and 2 for participation and was, thus, identified as a well-designed scenario (Figure 5).

# Discussion

## Applicability of the modified framework

Effectiveness evaluation is to understand the current state of management and to identify problems in management, and thus improve the outcomes of MPAs. A good assessment framework should focus on the management aspects that potentially drive outcomes. In addition, the assessment of effectiveness should also correspond to the objectives of MPAs. The modified framework in this study focuses on those indicators that potentially drive outcomes. These indicators were also successfully applied to assess 12 large marine protected areas and they were found to correlate significantly with indicators of the ecological and economic effectiveness of large marine protected areas (Ban et al., 2017). When we applied these governance indicators to assess three MPAs, we found that data for evaluating these indicators were easily accessible through MPA managers, planning reports, and management plans. According to the Rules of Marine Nature Reserves and the Rule of Special Marine Protected Areas, the common objectives of China's MPAs are to conserve biodiversity, protect the environment, protect ecosystems and their functions within MPAs, and maintain ecosystem services. The indicators of outcomes developed by this study fully covered these aspects (Table 1), which ensures the appropriateness of the assessment.

One advantage of the modified framework is the reliability of the assessment of outcomes. Unlike many frameworks that assess outcomes qualitatively (Stolton et al., 2003; Staub and Hatziolos, 2004; State Oceanic Administration of China (SOA), 2015; Ban et al., 2017), our evaluation of outcomes is based on raw data (Table A.1). On the other hand, our assessment uses a scoring method for the final evaluation of each indicator, which avoids the issue that data from different sources are not easily comparable, or the results of different MPA assessments are hard to be compared. Due to our selection of indicators is derived from existing frameworks, the evaluation results also allow us to complement the global MPA assessment database and contribute to the global scientific study of MPAs. Although there were eight indicators in this framework that were evaluated by the manager's data, they represent only 25% of the total number of indicators. They are from attributes of the MPA, institutional design principles, and participation (Table 1). The qualitative assessment of such management indicators by managers is reliable, and this approach has been used in many studies (Ban et al., 2017; Gill et al., 2017; Hargreaves-Allen et al., 2017). In our study, we interviewed two managers with more than three years of management experience for each MPA to ensure the reliability of the assessment. The assessments of species and ecological attributes within the MPA and outcomes are all derived from MPA monitoring reports or local statistical yearbooks, and these indicators account for

TABLE 2 Evaluation results for Shengsi, Putuo, and Jiushan; bold indicates newly added indicators, *italic* indicates environmental performances indicators.

| Type of indicators | Indicators | Shengsi | Putuo | Jiushan |
|---|---|---|---|---|
| Attributes of the species or ecosystem within the MPA | Commons mobility | 3 | 2 | 3 |
| | Commons productivity | 2 | 1 | 1 |
| | Ecological resilience | 1 | 1 | 1 |
| | Resource market value | 2 | 2 | 2 |
| | Distance to market | 1 | 1 | 1 |
| Attributes of the MPA | No take area | 0 | 0 | 3 |
| | Age | 3 | 3 | 3 |
| | Snapshot age | 2 | 1 | 2 |
| | Size | 3 | 2 | 3 |
| | Efficient enforcement | 2 | 3 | 2 |
| | Isolated | 3 | 3 | 3 |
| | Comprehensive, adequate, representative principles | 3 | 3 | 3 |
| Institutional design principles | Stakeholder boundary clarity | 2 | 2 | 2 |
| | Stakeholder boundary fuzziness | 3 | 3 | 3 |
| | Commons boundaries | 3 | 3 | 3 |
| | Commons boundary negotiability | 1 | 1 | 1 |
| | Outsider exclusion | 2 | 1 | 2 |
| | Social-ecological fit | 3 | 3 | 3 |
| | Proportionality | 0 | 0 | 0 |
| | Participation in rule making | 2 | 2 | 2 |
| | Self-monitoring | 3 | 3 | 0 |
| | Environmental monitoring | 2 | 2 | 2 |
| | Self-sanctions | 3 | 3 | 2 |
| | External recognition | 3 | 3 | 3 |
| | Multiple levels | 2 | 2 | 2 |
| | Compliance | 2 | 3 | 2 |
| | Conflict resolution | 3 | 3 | 0 |
| Participation | Participation in rule making | 2 | 2 | 2 |
| | Participation in protected area siting | 2 | 2 | 2 |
| | Participation in protected area zoning | 2 | 2 | 2 |
| | Participation in environmental monitoring | 2 | 2 | 2 |
| | Participation in social monitoring (enforcement) | 2 | 2 | 2 |
| Outcomes | **Fish diversity** | 1 | 0 | 0 |
| | Fish density | 2 | 1 | 2 |
| | Income | 3 | 2 | 0 |
| | ***Biophysical property*** | 3 | 1 | 3 |
| | ***Heavy metals*** | 1 | 3 | 3 |
| | ***Nutrients*** | 1 | 1 | 1 |
| | ***Oil*** | 3 | 3 | 3 |

The darker the color, the higher the score.
The shade of green indicates the level of the score.

75% of the total number of indicators. Therefore, the results of our assessments can truly reflect the effectiveness of MPA management and conservation.

However, we recognize that the quality of the evaluation data requires further improvement, and particularly the data sources for assessing outcomes. Ideally, a before-after-control-impact (BACI) method should be used when designing MPA monitoring, to provide data that more accurately reflects the impacts of the MPA (Mascia et al., 2017). This method requires baseline surveys and post-establishment surveys at MPAs and control areas with contexts (social and ecological) similar to MPAs. By comparing the differences in data before and after MPAs with the differences in data before and after the control areas, it is possible to determine whether the differences are due to MPAs or natural variations. However, in China, data derived from BACI monitoring is often lacking. We recommend that the

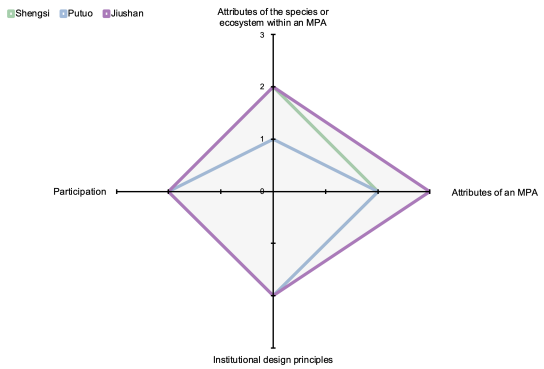


FIGURE 5
Evaluation of the management of Shengsi, Putuo, and Jiushan MPAs.

BACI method should be applied to future MPA monitoring in China, and particularly in the case of newly established MPAs.

## Outcomes

The results of our assessment for outcomes showed that MPAs with a higher average outcome score were associated with higher average scores for two types of potential drivers: 1) attributes of species or ecosystems within the MPA and 2) attributes of the MPA (Figure 4). Existing studies have highlighted the importance of the attributes of species or ecosystems within an MPA; species or systems that are more productive, resilient, less mobile, sheltered from major markets, and have high market value are more likely to exhibit positive responses to protection (Claudet et al., 2010; Collette et al., 2011). An MPA that is no-take, well-enforced, old (>10 years), large (>100 $km^2$), and isolated is more likely to be ecologically effective (Edgar et al., 2014). In addition, MPAs or MPA networks that are comprehensively, adequately, and representatively designed (CAR principles) are also more effective (Margules and Pressey, 2000). Due to limited cases in this study, it is hard to identify the specific indicators that drive outcomes. We recommend strengthening MPA assessment China, and the results will help to compare the effectiveness of different MPA types, identify specific drivers, and promote adaptive management.

The fish diversity and density evaluation results vary between three MPAs after they were established (Table 2). Changes in these two indicators were influenced by a combination of biophysical context, management status, and human activity (Fidler et al., 2021). Future research should establish a long-term MPA monitoring system that includes these three aspects and quantitatively analyzes their effects on biological outcomes. Such studies can reveal mechanisms for ensuring the ecological effectiveness of MPAs and provide evidence-based recommendations for MPA adaptive management.

The income of fishers increased after the establishment of the Shengsi and Putuo MPAs, while Jiushan only scored 0 for this indicator. This is because there are no fishermen living in Jiushan after its establishment. In general, the improvement in fisher's income is beneficial to the enforcement of management actions, as it allows fishers to perceive the benefits brought by the MPA in the places where they carry out their activities. However, caution must be exercised, as this study did not involve an in-depth analysis of fisher's income sources and, therefore, how much of this income increase is related to the MPAs is unknown. Future evaluations could remedy this limitation.

According to our assessment, the environmental performances of Jiushan are better than Shengsi and Putuo (Figure 4). Jiushan is an MNR, which means that tourism and development activities are restricted and it is uninhabited by humans. Therefore, its environmental performance is higher and its seawater quality is better. Shengsi scored low for heavy metals and nutrients (Table 2), implying that concentrations of these two indicators did not decrease after the establishment of the MPA. Two likely reasons for this are: 1) nutrients carried by the Yangtze River and sewage outlets and 2) aquaculture practiced within Shengsi Marine Park. Putuo also had low scores in some environmental indicators (Table 2). Decreased chemical oxygen demand (COD) concentration results in Putuo resulted in a low biophysical properties score, and aquaculture, municiple discharge (e.g., from wastewater treatment plants), fishing companies, and run-off from the Yangtze River caused low COD and increased nutrient concentration (Zhu and Fang, 2014). Differences in environmental performance between the MNR (Jiushan) and the SMPAs (Shengsi and Putuo) suggest that the effectiveness of environmental protection is influenced by management type and human pressures. Given that approximately 41% of China's MPAs are SMPAs, and most are affected by human activities, we recommend more regular monitoring to assess environment performance and to identify problems and optimize management.

## Potential drivers for outcomes

For the attributes of the species or ecosystem within the MPA, the systems within the three MPAs had low resilience to expected threats, suggesting that it will take a long time for the systems within these MPAs to recover from human disturbance. In addition, low scores for distance to market suggests that they are close to the closest markets (10–100 km), which might negatively affect their conservation outcomes. Research conducted in the Indo-Pacific found that reef fish density decreases with decreasing distance from market (Cinner and McClanahan, 2006). A shorter distance leads to lower fish transportation and preservation costs (Claudet et al., 2010),

provides incentives and stable prices to continuously exploit fish resources (Scales et al., 2006), and leads to break-down of common resource management. We recommend that future MPA design and evaluation incorporate ecological resilience and distance to market as potential effects on ecological outcomes.

Jiushan achieved a highly satisfactory level for MPA attributes (Figure 4), mainly due to its high score for no take area (Table 2). As an MNR (corresponding to IUCN Ia), extractive activities are highly limited in Jiushan. Although no-take MPAs are more effective than multiple-use MPAs in general, the establishment of no-take MPAs faces obstacles in developing countries because of high living-dependence on marine resources (Sciberras et al., 2013). Multiple-use MPAs are proposed as an alternative tool. Currently, around 40% of China's MPAs are multiple-use, with more being established. The conservation effectiveness of these multi-use MPAs can be improved through the prompt development of management plans and efficient enforcement of regulations (Table 2).

Although the three MPAs were satisfactory in their institutional design principles and participation (Figure 4), there remains some room for improvement. All three MPAs scored 0 in the proportionality of their institutional design principles (Table 2), as the proportion of costs incurred by stakeholders to the benefits received was unknown. Chinese MPA planning reports include government budgets and social-economic benefit forecasts, that do not include exact amounts or beneficiaries. Given this information, we were unable to determine whether costs and benefits were proportionately distributed among stakeholders. Thus, we recommend developing MPA cost and benefit indicators so that proportionality can be better understood and monitored. In addition, Jiushan scored 0 for self-monitoring because it is uninhabited by humans. The communities of Shengsi and Putuo, meanwhile, monitored each other's common resource behaviors. Self-monitoring is a valuable marine conservation tool, as it helps to detect illegal activities in a timely manner, improves compliance with management rules, and reduces enforcement costs. Given the importance of self-monitoring, we suggest that it is promoted in MPAs where actor groups are present.

Public were moderately participate in rule making, protected area siting, zoning, and environmental and social monitoring in all three MPAs (Table 2). In all three MPAs, preparatory groups shared plans with the municipal governments where these MPAs are located, and local government responses to rulemaking, siting, and zoning were taken into account. In Shengsi and Putuo, surveys were conducted with local communities and business employees regarding siting and perceptions of the MPAs. However, participation can be further improved. We recommend that the government increases stakeholder awareness of the importance of participation and participation mechanisms should be more clearly defined in management plans.

## Scenario evaluation

The scenarios evaluation demonstrates that MNRs and SMPAs are managed by different scenarios, indicating that this method can successfully reveal the management characteristics of MPAs. The MNR evaluated in this study falls under the well governed scenario. This management scenario of MPA includes no-take areas, is well-enforced, old, large, isolated and designed to be comprehensive, adequate, and representative. However, it is not perfect in terms of attributes of the species or ecosystem within the MPA, institutional design principles, and public participation (Figure 5). For example, the commons productivity, ecological resilience, and the distance to market of Jiushan were not scored with high level, and it did not perform well in terms of proportionality, self-monitoring, and conflict resolution within institutional design principles. We can combine this method with the results of specific indicator scores to identify certain areas for improvement.

The SMPAs (Shengsi and Putuo) belong to the learning scenario. MPAs under this scenario are not perfect in terms of 1) attributes of the species or ecosystem within the MPA, 2) attributes of the MPA, 3) institutional design principles, and 4) participation. Aspects that should be improved including the establishment of no-take zones and proportionality assessment indicators. Setting no-take zones in multiple use MPAs can make them effective fisheries management tools (Zupan et al., 2018). The highest protection level zone within China's SMPAs is major protected zone, but there are no clear rules for restricting fishing in this zone. In the future, the zoning design of SMPAs may consider upgrading the management of major protected zone to restrict fishing within them, so that its possible spillover effects can enhance the conservation effectiveness of adjacent zones.

# Conclusions and recommendations

The establishment and management of MPAs in the Yangtze River Delta is very important for the implementation of China's 'eco-civilization'. Assessing whether MPAs are effective can promote and improve adaptive management. This study modified a comprehensive framework to evaluate outcomes with potential drivers for MPAs in the Yangtze River Delta. The framework was successfully applied to three national MPAs. The evaluation results show that Shengsi ranked first for four key aspects and Jiushan ranked lowest. The three MPAs achieved almost satisfactory levels for each key aspect. However, the attributes of species or ecosystems in Putuo achieved a slightly satisfactory level, due to poor ecological resilience and proximity to markets. The three MPAs achieved satisfactory levels in outcomes, and higher average scores for outcomes associated

with attributes of species or ecosystems and attributes of the MPAs. The SMPAs (Shengsi and Putuo) achieved satisfactory levels for environmental performance, while the MNA (Jiushan) achieved a highly satisfactory level. In general, Shengsi and Putuo are managed according to a learning model and Jiushan is managed according to a well-designed model.

To improve the effectiveness of MPAs in the Yangtze River Delta, we recommend that attributes of species or ecosystems and attributes of MPAs are attached great importance, in particular with regard to the ecological resilience of species or ecosystems and the distance between MPAs and markets. Although all three MPAs achieved satisfactory levels for institutional design principles and participation, there is room for improvement, particularly with regard to proportionality. We suggest that developing cost and benefit indicators for monitoring MPAs will deepen understanding of their proportionality. In addition, public awareness of participation needs to be promoted and the process of participation should be clarified in MPA management plans. Regarding the improvement of environmental performance, we recommend conducting regular monitoring and assessment to identify problems and optimize management.

This study evaluated three MPAs and, therefore, could not quantitatively analyze the specific indicators that affect outcomes. However, the results provide information for adaptive management and design of future MPAs. We recommend using this framework to evaluate more MPAs using statistical methods to identify specific outcome drivers.

## Data availability statement

The raw data supporting the conclusions of this article will be made available by the authors, without undue reservation.

## Author contributions

This paper is a joint work of all authors. All authors have participated fully and are responsible for the work. All authors have given their consent to the submission. This paper is an original submission and has not been submitted elsewhere. No other manuscript contains the same, similar or related information as presented here.

## Acknowledgments

We are thankful for the financial support of National Science Foundation of China (Grant #: 42142018 to LC), the Oceanic Interdisciplinary Program of Shanghai Jiao Tong University (SL2021PT101 to LC), Shanghai Frontiers Science Center of Polar Science (SCOPS) (to LC), the East China Sea Environmental Monitoring Center of State Oceanic Administration (MEMRT202112 to LC), and the David and Lucile Packard Foundation (to LC). We would also like to acknowledge the Key Laboratory of Marine Ecosystem Dynamics, Second Institute of Oceanography, Ministry of Natural Resources (Grant #: MED202002 to XZ) for financial support. We are grateful to Shengsi Ma'an Special Marine Protected Area Administration Bureau, Putuo Zhongjie Archipelago Special Marine Protected Area Administration Bureau, Jiushan Archipelago Provincial/National Marine Ecological Nature Reserve Administration Bureau for their assistance in our data collection. We also thank Mr. Li Da, a staff member of Jiushan MNR Administration Bureau, for his assistance.

## Conflict of interest

The authors declare that the research was conducted in the absence of any commercial or financial relationships that could be construed as a potential conflict of interest.

## Publisher's note



## Supplementary material

The Supplementary Material for this article can be found online at: https://www.frontiersin.org/articles/10.3389/fmars.2022.911880/full#supplementary-material

## References

Ban, N. C., Davies, T. E., Aguilera, S. E., Brooks, C., Cox, M., Epstein, G., et al. (2017). Social and ecological effectiveness of large marine protected areas. *Glob Environ. Change* 43, 82–91. doi: 10.1016/j.gloenvcha.2017.01.003

Bennett, N. J., and Dearden, P. (2014). From measuring outcomes to providing inputs: Governance management and local development for more effective marine protected areas. *Mar. Pol.* 50, 96–110. doi: 10.1016/j.marpol.2014.05.005

Campanella, L., Conti, M., Cubadda, F., and Sucapane, C. (2001). Trace metals in seagrass algae and molluscs from an uncontaminated area in the Mediterranean. *Environ. pollut.* 111, 117–126. doi: 10.1016/S0269-7491(99)00327-9

Chen, W., Zhang, D., Cui, D., Lv, L., Xie, W., Shi, S., et al. (2018). Monitoring spatial and temporal changes in the continental coastline and the intertidal zone in jiangsu province. *China Acta Geographica Sin.* 7, 1365–1380. doi: 10.11821/dlxb201807014

Cinner, J., and McClanahan, T. (2006). Socioeconomic factors that lead to overfishing in small-scale coral reef fisheries of Papua new Guinea. *Environ. Conserv.* 33, 73–80. doi: 10.1017/S0376892906002748

Claudet, J., Osenberg, C., Domenici, P., Badalamenti, F., Milazzo, M., Falcón, J. M., et al. (2010). Marine reserves: fish life history and ecological traits matter. *Ecol. Appl.* 20, 830–839. doi: 10.1890/08-2131.1

Collette, B., Carpenter, K., Polidoro, B., Juan-Jordá, M., Boustany, A., Die, D. J., et al. (2011). High value and long life: double jeopardy for tunas and billfishes. *Science* 333, 291–292. doi: 10.1126/science.1208730

Edgar, G. J., Stuart-Smith, R. D., Willis, T. J., Kininmonth, S., Baker, S. C., Banks, S., et al. (2014). Global conservation outcomes depend on marine protected areas with five key features. *Nature* 506, 216–220. doi: 10.1038/nature13022

Fidler, R. Y., Andradi-Brown, D. A., Pada, D., Hidayat, N. I., Ahmadia, G. N., and Harborne, A. R. (2021). The importance of biophysical context in understanding marine protected area outcomes for coral reef fish populations. *Coral Reefs* 40, 791–805. doi: 10.1007/s00338-021-02085-y

Gaston, K. J., Jackson, S. F., Cantu-Salazar, L., and Cruz-Piñón, G. (2008). The ecological performance of protected areas. *Annu. Rev. Ecol. Evol. Syst.* 39, 93–113. doi: 10.1146/annurev.ecolsys.39.110707.173529

Gill, D. A., Mascia, M. B., Ahmadia, G. N., Glew, L., Lester, S. E., Barnes, M., et al. (2017). Capacity shortfalls hinder the performance of marine protected areas globally. *Nature* 543, 665–669. doi: 10.1038/nature21708

Halpern, B. S., Frazier, M., Potapenko, J., Casey, K. S., Koenig, K., Longo, C., et al. (2015). Spatial and temporal changes in cumulative human impacts on the world's ocean. *Nat. Commun.* 6 (1), 1–7. doi: 10.1038/ncomms8615

Han, X., Zhang, S., Wang, Z., Wang, K., Lin, J., and Deng, M. (2019). Fish community structure and its relationship with environmental factors in the ma'an archipelago and its eastern waters. *J. Fisheries China* v.43, 79–93. doi: 10.11964/jfc.20180211197

Hargreaves-Allen, V. A., Mourato, S., and Milnergulland, E. J. (2017). Drivers of coral reef marine protected area performance. *PloS One* 12 6, e0179394. doi: 10.1371/journal.pone.0179394

Hockings, M., Stolton, S., Leverington, F., Dudley, N., and Courrau, J.. (2006). *Evaluating effectiveness: a framework for assessing management effectiveness of protected areas. 2nd Edn.* Switzerland and Cambridge, UK: IUCN, Gland.

Huang, Z. (1994). *Marine species and its distribution in China* (Beijing: Marine Publishing House).

Hu, W., Liu, J., Ma, Z., Wang, Y., Zhang, D., Yu, W., et al. (2020). China's marine protected area system: Evolution challenges and new prospects. *Mar. Pol.* 115, 103780. doi: 10.1016/j.marpol.2019.103780

Laffoley, D., Baxter, J. M., Day, J. C., Wenzel, L., Bueno, P., and Zischka, K. (2019). ""Marine protected areas,"," in *World seas: An environmental evaluation*. Ed. S. Charles (Amsterdam Academic Press), 549–569. doi: 10.1016/B978-0-12-805052-1.09989-7

Leverington, F., Costa, K. L., Pavese, H., Lisle, A., and Hockings, M. (2010). A global analysis of protected area management effectiveness. *Environ. Manag* 46, 685–698. doi: 10.1007/s00267-010-9564-5

Li, Y., and Fluharty, D. L. (2017). Marine protected area networks in China: Challenges and prospects. *Mar. Policy* 85, 8–16. doi: 10.1016/j.marpol.2017.08.001

Lu, L., He, J., and Zeng, G. (2020). Decoupling of economic growth and industrial wastewater discharges from an innovation-driven perspective: Taking the Yangtze river delta urban agglomeration as an example. *Areal Res. Dev.* 39, 7. doi: 10.3969/j.issn.1003-2363.2020.05.028

Margules, C. R., and Pressey, R. L. (2000). Systematic conservation planning. *Nature* 405, 243–253. doi: 10.1038/35012251

Mascia, M. B., Fox, H. E., Glew, L., Ahmadia, G. N., Agrawal, A., Barnes, M., et al. (2017). A novel framework for analyzing conservation impacts: evaluation, theory, and marine protected areas. *Ann. Ny Acad. Sci.* 1399, 93–115. doi: 10.1111/nyas.13428

McCook, L. J., Lian, J., Lei, X., Chen, Z., Xue, G., Ang, P., et al. (2018). Marine protected areas in southern China: Upgrading conservation effectiveness in the 'eco-civilization' era. *Aquat Conserv.* 29, 33–43. doi: 10.1002/aqc.3067

Ministry of Ecology and Environment (MoEE) (2020). *Bulletin on the state of china's marine ecological environment in 2018* (Beijing).

Ministry of Natural Resources (MNR) (2020). *2019 China marine economic statistics bulletin* (Beijing).

Ningbo Marine Environmental Monitoring Center (Ningbo MEMC) (2005). *Scientific monitoring report of zhongjieshan islands special marine protection area* (Zhejiang).

Ningbo MEMC (2012). *Plan for national nature reserve of xiangshan jiushan archipelago* (Zhejiang).

Nygrén, N. A. (2019). Scenario workshops as a tool for participatory planning in a case of lake management. *Futures* 107, 29–44. doi: 10.1016/j.futures.2018.10.004

Pomeroy, R. S., Watson, L. M., Parks, J. E., and Cid, G. A. (2005). How is your MPA doing? a methodology for evaluating the management effectiveness of marine protected areas. *Ocean Coast. Manage* 48, 485–502. doi: 10.1016/j.ocecoaman.2005.05.004

Putuo Statistics (2019). *A brief analysis of urban and rural residents' income in putuo district in 2019* (Zhejiang).

Qiu, W. (2010). *Governing marine protected areas (MPAs) in China: Towards the repositioning of the central state and the empowerment of local communities. [dissertation/doctoral's thesis]. [UCL]* (University College London).

Qiu, W., Wang, B., Jones, P. J. S., and Axmacher, J. C. (2009). Challenges in developing china's marine protected area system. *Mar. Pol.* 33, 599–605. doi: 10.1016/j.marpol.2008.12.005

Scales, H., Balmford, A., Liu, M., Sadovy, Y., and Manica, A. (2006). Keeping bandits at bay? *Science* 313, 612–614. doi: 10.1126/science.313.5787.612c

Sciberras, M., Jenkins, S. R., Kaiser, M. J., Hawkins, S. J., and Pullin, A. S. (2013). Evaluating the biological effectiveness of fully and partially protected marine areas. *Environ. Evid* 2, 1–31. doi: 10.1186/2047-2382-2-4

Second Institute of Oceanography (SIO) (2013). *Report of the shengsi national marine park in zhejiang* (Hangzhou:Zhejiang).

Shengsi Statistics (2019). *2019 shengsi county national economic and social development statistical bulletin* (Zhejiang).

SIO (2016). *Report of putuo national marine park* (Hangzhou:Zhejiang).

SOA (1995). *Rules of marine nature reserves* (Beijing).

SOA (2010). *Rule of special marine protected areas* (Beijing).

Song, R., Yao, J., Wu, K., Zhang, X., Lü, Z., Zhu, Z., et al. (2018). Evaluation of the effectiveness of marine protected areas: Methodologies and progress. *Biodiversity Sci.* 26 (3), 286–294. doi: 10.17520/biods.2018005

Standards Press of China (2007). *Specifications for oceanographic SurVey-part 3: Marine meteorological observations* (Beijing).

Standing Committee of Ningbo Municipal People's Congress (2017). *Regulations of jiushan archipelago marine ecological nature reserve, ningbo city* (Zhejiang).

Standing Committee of Zhoushan People's Congress (2017). *Regulations of national marine special marine protected area in zhoushan* (Zhejiang).

State Oceanic Administration of China (SOA) (2015). *Measures for supervision and inspection of national marine protected areas (trial)* (Beijing).

Staub, F., and Hatziolos, M. E. (2004). Score card to assess progress in achieving management effectiveness goals for marine protected areas. *World Bank* 29, 32938.

Stolton, S., Hockings, M., Dudley, N., MacKinnon, K., and Whitten, T. (2003). *Reporting progress at protected area sites* (Washington: The World Bank and WWF). Available at: https://documents1.worldbank.org/curated/en/291981468171569997/pdf/32939a10ENGLIS1InProtectedAreasTool.pdf.

Terlizzi, A., Delos, A., Garaventa, F., Faimali, M., and Geraci, S. (2004). Limited effectiveness of marine protected areas: imposex in *Hexaplex trunculus* (*Gastropoda muricidae*) populations from Italian marine reserves. *Mar. pollut. Bull.* 48, 188–192. doi: 10.1016/j.marpolbul.2003.10.019

United Nations Environment Programme (UNEP) (2016). *Green is gold: the strategy and actions of china's ecological civilization*. Nairobi: United Nations Environment Programme

Wang, Q., Liu, B., and Xiang, H. (2019). Study on comprehensive management and control strategies of natural coastal lines in zhejiang province. *J. Green Sci. Technol.* 8, 21–25.

Wang, Z., Zhang, S., Chen, Q., Xu, Q., and Wang, K. (2012). Fish community ecology in rocky reef habitat of ma'an archipelago. I species composition and diversity. *Biodiversity Sci.* 20, 41–50. doi: 10.3724/SP.J.1003.2012.10168

Wei, L. (2020) *The total GDP accounts for one fourth of the country the Yangtze river delta depends on what? people's daily*. Available at: https://baijiahao.baidu.com/s?id=1673940305900228629&wfr=spider&for=pc (Accessed June 26, 2021).

Xinhua (2012) *Full text of hu jintao's report at the 18th party congress*. Available at: http://news.xinhuanet.com/english/special/18cpcnc/2012-11/17/c_131981259.htm (Accessed November 27, 2021).

Xu, E. G., Leung, K. M., Morton, B., and Lee, J. H. (2015). An integrated environmental risk assessment and management framework for enhancing the sustainability of marine protected areas: The cape d'Aguilar marine reserve case study in Hong Kong. *Sci. Total Environ.* 505, 269–281. doi: 10.1016/j.scitotenv.2014.09.088

Zhan, B. (1995). *Fisheries resources evaluation* (Beijing: China Agriculture Press).

Zhao, J. (2018)It is urgent to strengthen the protection of coastal ecosystem. In: *China Ocean online*. Available at: http://aoc.ouc.edu.cn/04/3a/c9824a197690/pagem.psp (Accessed June 26, 2021).

Zhu, S., and Fang, T. (2014). Nutrients and eutrophication evaluation of waters mariculture zone in zhongjieshan archipelago. *Sci. Tech. Engrg* 14, 164–169. doi: 10.3969/j.issn.1671-1815.2014.04.034

Zupan, M., Fragkopoulou, E., Claudet, J., Erzini, K., Horta e Costa, B., and Gonçalves, E. J. (2018). Marine partially protected areas: drivers of ecological effectiveness. *Front. Ecl Envriron* 16 (7), 381–387. doi: 10.1002/fee.1934

frontiers | Frontiers in Marine Science

TYPE Original Research
PUBLISHED 02 November 2022
DOI 10.3389/fmars.2022.1035501



OPEN ACCESS

EDITED BY
Gangfeng Ma,
Old Dominion University, United States

REVIEWED BY
Jia-Lin Chen,
National Cheng Kung University, Taiwan
Xi Feng,
Hohai University, China

*CORRESPONDENCE
Minwoo Son
mson@cnu.ac.kr

SPECIALTY SECTION
This article was submitted to Coastal Ocean Processes, a section of the journal Frontiers in Marine Science

RECEIVED 02 September 2022
ACCEPTED 10 October 2022
PUBLISHED 02 November 2022

CITATION
Figueroa SM, Son M and Lee G-h (2022) Effect of estuarine dam location and discharge interval on estuarine hydrodynamics, sediment dynamics, and morphodynamics.
*Front. Mar. Sci.* 9:1035501.
doi: 10.3389/fmars.2022.1035501



# Effect of estuarine dam location and discharge interval on estuarine hydrodynamics, sediment dynamics, and morphodynamics

Steven M. Figueroa[1], Minwoo Son[1]* and Guan-hong Lee[2]

[1]Department of Civil Engineering, Chungnam National University, Daejeon, South Korea, [2]Department of Oceanography, Inha University, Incheon, South Korea

The effect of an estuarine dam located near the mouth for a range of estuarine types (strongly stratified, partially mixed, periodically stratified, and well-mixed) has been studied using a numerical model of an idealized estuary. However, the effect of different dam locations and freshwater discharge intervals has not yet been studied. Here, models were run for each estuary type with dam locations specified at $x$ = 20, 55, and 90 km upstream from the mouth, and discharge intervals specified as once every $\Delta t$ = 0.5, 3, and 7 days. The hydrodynamic, sediment dynamic, and morphodynamic results for the pre- and post-dam estuaries were analyzed to understand changes in estuarine processes. It was found that the estuarine dam altered the tide and river forcing in turn altering the stratification, circulation, sediment fluxes, and depths. The estuarine dam location primarily affected the tide-dominated estuaries, and the resonance length was an important length scale affecting the tidal currents and Stokes return flow. When the location was less than the resonance length, the tidal currents and Stokes return flow were most reduced due to the loss of tidal prism, the dead-end channel, and the shift from mixed to standing tides. The discharge interval primarily affected the river-dominated estuaries, and the tidal cycle period was an important time scale. When the interval was greater than the tidal cycle period, notable seaward discharge pulses and freshwater fronts occurred. Dams located near the mouth with large discharge interval differed the most from their pre-dam condition based on the estuarine parameter space. Greater discharge intervals, associated with large discharge magnitudes, resulted in scour and seaward sediment flux in the river-dominated estuaries, and the dam located near the resonance length resulted in the greatest landward tidal pumping sediment flux and deposition in the tide-dominated estuaries.

KEYWORDS

**estuarine dam, resonance, stokes return flow, tidal asymmetry, discharge pulse, estuarine classification, sediment flux mechanisms**

# 1 Introduction

Dams and weirs are barriers that stop or restrict the flow of surface water and are constructed for water supply, flood control, navigability, and hydroelectric power. In this study, dams are defined as structures where freshwater discharge occurs by sluice gates that can be opened and closed and weirs are defined as structures were freshwater discharge occurs by flow over a weir crest. In addition to rivers, dams and weirs are also found in estuaries. Estuarine dams and weirs are similar to their river counterparts, but they also block upstream salt and tide intrusion. This converts a previously saline and tidal body of water into a freshwater body with a controlled water level. This study is primarily concerned with estuarine dams, however estuarine weirs are also considered due to their similar effect on tides.

The prevalence of river dams has increased rapidly since the 1940s (Syvitski and Kettner, 2011), and there has been a similar increase in estuarine dams. Both dams can impact downstream coastal deltas and estuaries. For example, river dams trap sediment in their reservoirs and can result in delta erosion, while estuarine dams alter estuarine processes and can trap sediment in the remnant estuaries (Syvitski et al., 2005; van Proosdij et al., 2009; Milliman and Farnsworth, 2013; Williams et al., 2013; Williams et al., 2014; Figueroa et al., 2020b; van der Spek and Elias, 2021). In terms of hydrodynamics, sediment dynamics, and morphodynamics, changes to deltas and estuaries due to estuarine dams has not been studied as much as river dams and are not well understood.

Understanding the effects of estuarine dams on estuarine hydrodynamics, sediment dynamics, and morphodynamics is difficult due to the wide array of estuarine types and their complex physical processes. This motivated Figueroa et al. (2022) to investigate idealized estuaries *via* numerical modeling. This approach has the benefit of providing high resolution pre- and post-dam data throughout the estuaries which is often not available from field observations. Four estuarine types (strongly stratified, partially mixed, periodically stratified, and well-mixed) were investigated. It was established that estuarine dams can alter the tide and river forcing and in turn change the estuarine classification and sediment flux mechanisms. Also, the pattern of response to the estuarine dam was found to depend on the estuarine type (i.e. strongly stratified vs. well-mixed).

In Figueroa et al. (2022), the model geometry was based on 10 real estuaries with estuarine dams obtained from the literature. Based on these estuaries, an estuarine dam was placed relatively near the mouth at 20 km from the mouth. Further investigation by Figueroa et al. (2022) using an analytical tidal model (Cai et al., 2016) suggested that the results would be sensitive to the distance of the dam from the mouth. At the same time, Figueroa et al. (2022) had prescribed a discharge interval of one discharge per 3 days based on Geum estuary, Korea (Figueroa et al., 2020a, b), where estuarine dam discharge data was available. What effect the estuarine dam discharge interval had on the result was not clear, although it was suggested to be important.

Therefore, two important parameters were identified for further research. These are the distance of the estuarine dam from the estuary mouth (i.e., dam location) and the interval between freshwater discharges (i.e., discharge interval). With respect to dam location, an estuarine dam can be located at the estuarine mouth at $x = 0$ km, in which the entire estuary is eliminated, up to about $x = 1000$ km which corresponds to one of the longest tidal limits known (the Amazon; Hoitink and Jay, 2016). Examples from the literature of estuarine dams and weirs at different locations include in the Sekiya Diversion Channel of the Shinano River, Japan ($x = 0$ km; Tabata and Fukuoka, 2014), Bang Nara, Thailand ($x = 6$ km; Vongvisessomjai et al., 2003), the Loukkos and Sebou, Morroco ($x = 20$ and 62 km, respectively; Haddout and Maslouhi, 2019), the Guadalquivir, Spain ($x = 110$ km; Díez-Minguito et al., 2012), the Elbe, Germany ($x = 142$ km; Li et al., 2014), and the Columbia, USA ($x = 234$ km; Jay et al., 2015). With respect to discharge interval, the interval conceptually can vary from $\Delta t = 0$ days to 365 days or more. These limiting cases correspond to continuous discharge to practically the elimination of discharge to the estuary, respectively. Relatively little information is available about the discharge intervals of estuarine dams. The Columbia estuary receives continuous discharge, but the post-dam estuary has reduced spring freshets and increased winter flows (Kukulka and Jay, 2003). A 20 year record of estuarine dam discharge at Geum estuary, Korea, indicates that the mean summer and winter discharge intervals are $\Delta t = 1.4$ and 3.4 days, respectively (Figure 1A), and the discharge interval can range overall from about $\Delta t = 0 - 26$ days (Figure 1B). On the side of longer discharge intervals, in the Cochin estuary, India, the estuarine dam is closed during the dry season (January – April) and subsequently opened when the river flow increases (Shivaprasad et al., 2013).

There is little existing research on the effect of dam location and discharge interval on estuaries. Zhu et al. (2017) analyzed depositional patterns in the Xinyanggang estuary, China (dam at $x = 10$ km), using a numerical model. Dam locations at $x = 1$ and 6 km and discharge intervals of $\Delta t = 1 - 7$ days were investigated. It was found that longer channels favored enhanced siltation due greater flood-dominance, and more frequent discharge reduced siltation. Schuttelaars et al. (2013) analyzed sediment trapping in the Ems estuary, Germany (weir at $x = 60$ km), using an idealized analytical model. Weir locations between $x = 20 - 100$ km were investigated. It was found that the weir was near resonance and relocating the weir landward away from resonance could reduce the tidal asymmetry and shift the sediment trapping location seaward. Together these two papers established that the estuarine dam location can strongly affect the tidal asymmetry

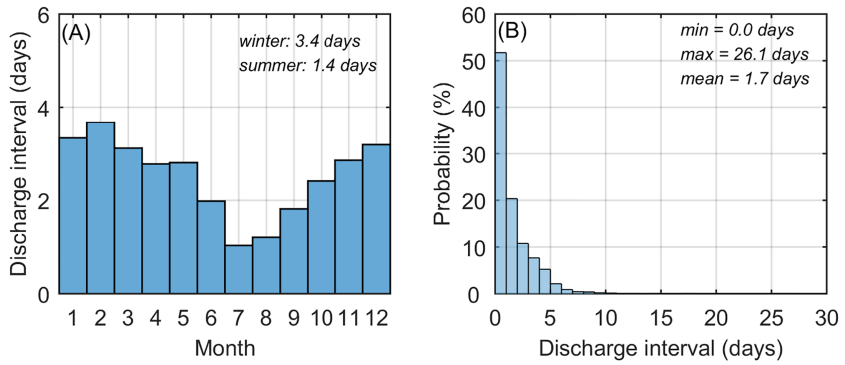


FIGURE 1
Interval between freshwater discharges from Geum River estuarine dam during 1994-2016. **(A)** Long term average discharge interval by month, **(B)** discharge interval probability distribution. Winter is December – February and summer is July – September. Data provided by the Korea Rural Community Corporation.

and sediment trapping. With respect to the discharge interval, Azevedo et al. (2010) analyzed the effect of river discharge patterns in the Douro estuary, Portugal (dam at $x$ = 22 km). It was found that variable discharges were less effective at flushing salt and dispersing contaminants compared to steady discharge. This indicates that the discharge interval can control the estuarine salinity and contaminants in addition to sediment transport reported by Zhu et al. (2017).

As these research studies focused primarily on strongly tidal systems, less research has been conducted on the effect of estuarine dam location in different estuarine types, such as partially mixed or strongly stratified estuaries. Furthermore, the effect of the discharge interval doesn't appear to have been studied for estuarine dams located further than about $x$ = 20 km from the mouth. Therefore, this study was carried out to extend the results of Figueroa et al. (2022), which investigated the effect of an estuarine dam on estuarine types, to include the effect of the estuarine dam location and discharge interval. The overall objective of this study is to understand the effect of estuarine dam location and discharge interval on estuarine processes. Specific research questions are: 1) how does the estuarine dam location affect the tidal processes?, 2) how does the discharge interval affect the river processes?, 3) how do changes in tidal and river processes affect the salinity and estuarine classification?, and 4) how do changes in tidal and river processes affect the sediment transport and estuarine morphology?

To address these research questions, an idealized numerical model of strongly stratified, partially mixed, periodically stratified, and well-mixed estuaries was used. Estuarine dams were placed in the region of the salt intrusion at $x$ = 20, 55, and 90 km, and the discharge interval was varied from the tidal to the spring-neap cycle timescales at $\Delta t$ = 0.5, 3, and 7 days. After evolving for one year, both the pre- and post-dam results were compared based on changes in hydrodynamic, sediment dynamic, and morphodynamic processes. Then trends in the response to the estuarine dam for each estuarine type, dam location, and discharge interval were analyzed.

This paper is organized as follows. Section 2 describes data collection and processing. Section 3 presents the results in order of changes to tide and river processes, salinity related processes and estuarine classification, and sediment flux mechanisms and depth change. Section 4 discusses the interaction of the estuarine dam location and discharge interval with estuarine spatial and temporal scales, the implications of this study for coastal hazards, and the reliability of the idealized estuary model. Finally, Section 5 summarizes the key findings.

# 2 Materials and methods

## 2.1 Data collection

### 2.1.1 Model description

This study used the ocean and sediment transport models of the Coupled-Ocean-Atmosphere-Wave-Sediment Transport (COAWST) modeling system (Warner et al., 2010). The ocean model is the Regional Ocean Modeling System (ROMS) which is a free surface, terrain-following numerical model that solves the three-dimensional Reynolds averaged Navier-Stokes equations using the hydrostatic and Boussinesq approximations (Haidvogel et al., 2008). The sediment transport model is the Community Sediment Transport Modeling System (CSTMS) which computes suspended sediment transport using the advection-diffusion algorithm together with an additional algorithm for vertical settling (Warner et al., 2008; Warner et al., 2010).

### 2.1.2 Model domain

Figure 2 shows the model domain used for scenarios with no estuarine dam and for scenarios with an estuarine dam at $x$ = 20,

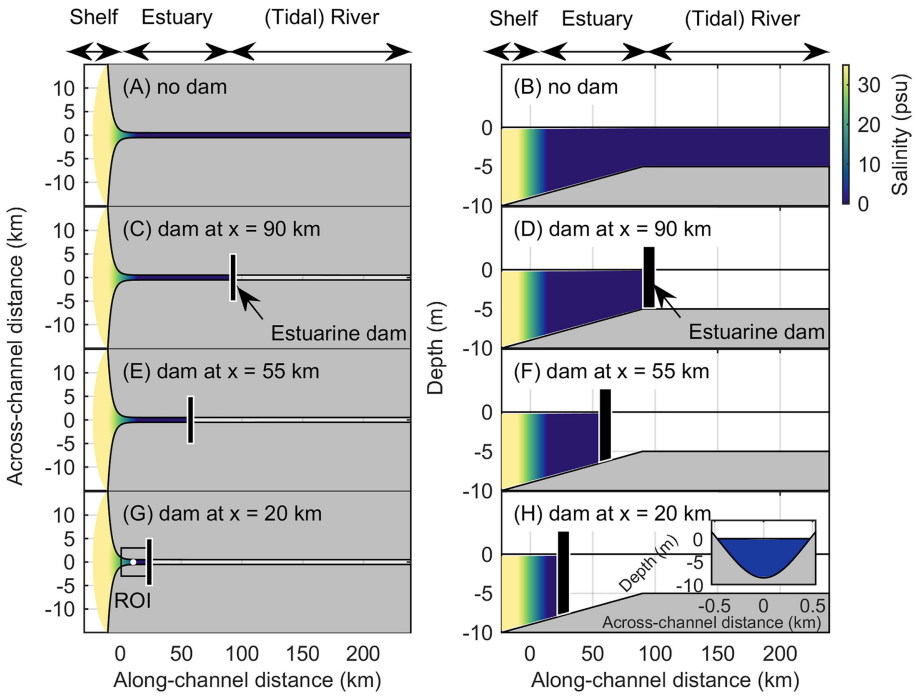


FIGURE 2
Model domain for **(A, B)** no dam, **(C, D)** dam at $x$ = 90 km, **(E, F)** dam at $x$ = 55 km, and **(G, H)** dam at $x$ = 20 km scenarios. Left plots are top-view, right plots are side-view. Salinity and bathymetry are the model initial conditions. An example of a region of interest (ROI) for a post-dam estuary shown in **(G)**. Point is the ROI center and is the location of the across-channel transect shown as an inset in **(H)** and the Figure 6 time series.

55, and 90 km. From the estuary mouth, the pre-dam domain extends 25 km seaward representing a shelf and 250 km landward representing an estuary and tidal river. The idealized estuary is funnel shaped near the mouth but becomes straight 5 km landward of the mouth. The depth decreases linearly and is constant after 90 km from the mouth. The dam location at $x$ = 20 km was based on statistics of real estuaries with estuarine dams (Figueroa et al., 2022). The dam location at $x$ = 90 km was selected as it is the location furthest inland before the depth transition (Figure 2D). The location at $x$ = 55 km was chosen as it is the midpoint between these. The across-channel shape is Gaussian. The pre-dam domain had an along-channel, across-channel, and vertical discretization of 242 × 62 × 20 points. The model was run with a 5 s baroclinic time step, which was divided into 20 barotropic time steps. For each post-dam scenario, the portion of the domain upstream of the estuarine dam was removed.

### 2.1.3 Model setup and boundary conditions

Table 1 lists the sediment properties for the six non-cohesive size classes used. These were divided into two groups: a marine sediment group (sand_1, mud_1, and mud_2) and a fluvial sediment group (sand_2, mud_3, and mud_4), which had the same properties. The model was initialized with only marine sediments well-mixed in the domain bed. Fluvial sediments were discharged from the river and estuarine dam to investigate the mixing of marine and fluvial sediments. During the runs the bed was allowed to evolve, resulting in morphodynamic change. This included intertidal areas which were included by a wetting and drying scheme.

The boundary conditions were closed on the channel banks and river end. The ocean boundary was open and featured a Chapman implicit boundary condition for the free surface and a Flather condition for the 2D momentum. The free surface and 2D momentum boundary conditions on the ocean boundary were chosen such that tidal currents were calculated from the free surface using reduced physics. Radiation and nudging conditions were applied to the salinity and sediment tracers such that they could radiate from the domain at the ocean boundary. The salinity and suspended sediment concentration (SSC) at the ocean boundary were defined as 35 psu and 0 kg $m^{-3}$, respectively.

On the river boundary, a constant river discharge was imposed for the pre-dam cases. For the post-dam cases, the discharge points were relocated to the estuarine dam, and the discharge became episodic to simulate estuarine dam operation. Discharge events from the estuarine dam were limited to 3 hours around mid-ebb tide, when the flow is seaward. During flood

TABLE 1 Sediment properties.

| | sand_1/sand_2 | mud_1/mud_3 | mud_2/mud_4 |
|---|---|---|---|
| Grain size (mm) | 0.125 | 0.062 | 0.031 |
| Density (kg $m^{-3}$) | 2650 | 2650 | 2650 |
| Porosity (%) | 70 | 70 | 70 |
| Critical bed shear stress (N $m^{-2}$) | 0.13 | 0.11 | 0.08 |
| Erosion rate (kg $m^{-2}$ $s^{-1}$) | $5.0 \times 10^{-4}$ | $5.0 \times 10^{-4}$ | $5.0 \times 10^{-4}$ |
| Settling velocity (mm $s^{-1}$) | 11.9 | 3.11 | 0.80 |

Marine sediments (sand_1, mud_1, and mud_2) were initially present in the estuary. Fluvial sediments (sand_2, mud_3, and mud_4) were discharge by the river or estuarine dam.

tides, the sluice gates are closed to block upstream salt intrusion. While dam operation may vary between estuaries with estuarine dams, this operation of discharges only during ebbs or low tides is known to occur in several estuaries including Dutch (Ye, 2006; Nauw, 2014), French (Laffaille et al., 2007; Traini et al., 2015), Chinese (Zhu et al., 2017), and Korean (Shin et al., 2019) estuaries.

### 2.1.4 Model scenarios

Table 2 lists the model scenarios which are organized based on estuarine type, dam location, and discharge interval. The estuarine types are the strongly stratified (hereinafter SS), partially mixed (hereinafter PM), periodically stratified (hereinafter PS), and well-mixed (hereinafter WM) estuaries. The freshwater discharge varied from continuous (no dam) to discrete discharge intervals of $\Delta t$ = 0.5, 3, and 7 days. These discharge intervals were selected to examine the interaction of the freshwater discharge with the tidal and spring-neap cycles. The post-dam freshwater discharge was scaled with the discharge interval to ensure the volume of discharged water over a spring-neap cycle was same for the pre- and post-dam estuaries. This assumes that the reservoir of the estuarine dam is not limited and thus the discharge interval is determined *a priori* (i.e., by a dam operator).

For each estuarine type and discharge interval, the dam location was varied as $x$ = 20, 55, and 90 km. For convenience, hereinafter a scenario is denoted as, for example, $PM_{90}^{0.5}$, where the subscript denotes the dam location and the superscript denotes the discharge interval. The set of scenarios for the partially mixed estuary can then be written as PM, $PM_{20}^{0.5}$, $PM_{20}^{3}$, $PM_{20}^{7}$, $PM_{55}^{0.5}$, $PM_{55}^{3}$, $PM_{55}^{7}$, $PM_{90}^{0.5}$, $PM_{90}^{3}$, $PM_{90}^{7}$, where no super or subscript denotes the pre-dam estuary. Thus, 10 scenarios were implemented for each estuarine type resulting in a total of 40 simulations (4 pre-dam and 36 post-dam). To refer to a group of results, the super and subscripts are written using variables. For example, $PM_{x}^{0.5}$ denotes all partially mixed estuaries with a discharge interval of $\Delta t$ = 0.5 days, and $PM_{90}^{\Delta t}$ denotes all partially mixed estuaries with a dam location of $x$ = 90 km. For convenience, the SS and PM estuaries are also referred to as "river-dominated" end members and the PS and WM estuaries are also referred to as "tide-dominated" end members based on their dominant forcing.

For the pre-dam scenarios, a salinity initialization was implemented followed by a 365-day pre-dam model run. For the post-dam scenarios, the salinity, bed morphology, SSC, and so forth of the pre-dam run were used as the initial condition for the post-dam run and the model was run for an additional 365 days. Data in the estuarine region of the domain and for a selected spring-neap cycle at the end of the runs constitute the dataset of this study. For more information on the model setup and workflow the reader is referred to Figueroa et al. (2022).

## 2.2 Data processing

To understand the effect of dam location and discharge interval on estuarine hydrodynamics, sediment dynamics, and morphodynamics several analysis methods were employed and are described here. Note, for the purpose of this study, key trends

TABLE 2 Model scenarios.

| Estuarine type | Tidal amplitude (m) | | River/estuarine dam freshwater discharge ($m^3$ $s^{-1}$) | | | |
|---|---|---|---|---|---|---|
| | | | pre-dam | post-dam ($x$ = 20, 55, and 90 km) | | |
| | $M_2$ | $S_2$ | continuous | $\Delta t$ = 0.5 day/discharge | $\Delta t$ = 3 day/discharge | $\Delta t$ = 7 day/discharge |
| strongly stratified (SS) | 0.19 | 0.06 | 300 | 1,200 | 7,200 | 16,800 |
| partially mixed (PM) | 0.30 | 0.10 | 40 | 160 | 960 | 2,240 |
| periodically stratified (PS) | 1.50 | 0.50 | 30 | 120 | 720 | 1,680 |
| well-mixed (WM) | 2.25 | 0.75 | 2 | 8 | 48 | 112 |

from these analyses are highlighted using selected model scenarios. For processed data from all model scenarios, the reader is referred to the Supplementary Material.

### 2.2.1 Tide and current amplitude and phase

Tide and current amplitude and phase were extracted along-channel for the principal lunar semidiurnal constituent ($M_2$) for all scenarios using classical tidal harmonic analysis (Pawlowicz et al., 2002). This allowed the analysis of amplification or damping of tides and currents as well as change in the relative phase between current and tide. When interpreting the phase difference, a phase difference of 0° of denotes a progressive wave, a phase difference of 90° of denotes a standing wave, and an intermediate phase difference denotes a mixed wave.

To check the numerical results of change in tidal dynamics, an analytical model of tidal propagation in estuaries with and without an estuarine dam (Cai et al., 2016) was implemented and compared with the numerical results. The analytical model is essentially a function which takes inputs of channel characteristics and tides at the mouth and outputs the along-channel variation of the tidal amplitude, velocity amplitude, and the phase difference between velocity and tide. For simplicity, a straight channel with no tidal flats was specified. The best calibration of the data was found to occur for a Manning-Strickler friction coefficient of $K = 65\ m^{1/3}\ s^{-1}$ and was applied equally to all scenarios.

### 2.2.2 Mean sea level and Eulerian residual current

In addition to higher frequency tidal hydrodynamics, lower frequency sea level and Eulerian residual current were analyzed. In particular the Eulerian residual current has important implications for sediment and morphodynamics. The along-channel variation of mean sea level and Eulerian residual currents were obtained from the model by spring-neap averaging. To better understand the driving processes, two processes were considered. First is the water setup due to freshwater input and the seaward river runoff. The cross-sectionally averaged runoff, $U_R$, was calculated from the model as:

$$U_R = V/A \tag{1}$$

where $V$ is the freshwater discharge and $A$ is the channel cross-sectional area. Second was the landward Stokes drift (a Lagrangian current), Stokes water setup, and the seaward Stokes return flow (an Eulerian current). In strongly tidal estuaries with progressive or mixed tides, a landward Stokes drift is generated due to correlations between the vertical and horizontal tides. The Stokes drift can be approximated by (Uncles and Jordan, 1980; Guo et al., 2014; Moftakhari et al., 2016):

$$U_{stokes} = \frac{1}{2} a v \cos(\varphi)/h \tag{2}$$

where $a$ is the tidal amplitude, $v$ is the velocity amplitude, $\phi$ is the relative phase, and $h$ is the water depth. Over the spring-neap cycle, the landward Stokes drift and seaward Stokes return flow are balanced, and Eq. 2 can be used to estimate the seaward Stokes return flow (Eulerian residual current). The output of $a$, $v$, and $\phi$ from the tidal harmonic analysis for the $M_2$ tidal constituent was used to evaluate Eq. 2 for each scenario.

### 2.2.3 Tidal asymmetry

In addition to the Eulerian residual currents, tidal asymmetry is also an important factor for estuarine sediment and morphodynamics. Guo et al. (2019) reviewed two methods of quantifying tidal asymmetry, namely the harmonic and statistical methods. The harmonic method follows Friedrichs and Aubrey (1988) quantifying the tidal asymmetry via:

$$M_4/M_2 = v_{M4}/v_{M2} \tag{3a}$$

$$2M_2 - M_4 = 2\theta_{M2} - \theta_{M4} \tag{3b}$$

where $M_4$ is the shallow water overtide of the $M_2$ tidal constituent. Eq. 3a is the ratio of the $M_4$ and $M_2$ velocity amplitudes, and its magnitude denotes the magnitude of the tidal asymmetry. Eq. 3b is the phase difference between the $M_2$ and $M_4$ velocity constituents, and it determines the direction of the tidal asymmetry. For $-90° < 2\theta_{M2} - \theta_{M4} < 90°$, the tide is flood-dominant, and for $90° < 2\theta_{M2} - \theta_{M4} < 270°$, the tide is ebb-dominant. For scenarios of this study, the amplitude ratios (Eq. 3a) were averaged over the remnant estuaries and normalized by the corresponding pre-dam values to detect global changes in asymmetry magnitude. The phase difference (Eq. 3b) was also averaged over the remnant estuaries to detect global changes in asymmetry direction. To facilitate comparison between scenarios, the value of the phase difference was set to a binary -1 or +1 to denote either ebb-dominance or flood-dominance, respectively.

The harmonic method works well to understand tidal asymmetry due to distortion of the tidal wave due to frictional interaction with the bottom and intertidal storage. Another form of tidal asymmetry can occur when a tidal current is superimposed on an Eulerian residual current, known as Euler-induced asymmetry (Guo et al., 2014). The harmonic method does not include the Eulerian residual, however the statistical method to quantify tidal asymmetry can. The statistical method follows Nidzieko (2010) and Nidzieko and Ralston (2012) quantifying the tidal asymmetry *via* a velocity skewness parameter, $\gamma_1$, as:

$$\gamma_1 = \frac{\mu_3}{\sigma^3} = \frac{\frac{1}{\tau-1}\sum_{t=1}^{\tau}(v_b)^3}{\left[\frac{1}{\tau-1}\sum_{t=1}^{\tau}(v_b)^2\right]^{\frac{3}{2}}} \tag{4}$$

where $\mu_3$ is the third sample moment, $\sigma$ is the standard deviation, $v_b$ is the bottom current. To investigate the Euler-induced asymmetry, $\mu_3$ and $\sigma$ were taken about zero and not the mean. The bottom current was used as it is important for the sediment transport. The summation is for $\tau$ observations from time $t = 1$ to $t = \tau$. The magnitude of the velocity skewness

indicates the magnitude of tidal asymmetry and the sign indicates the direction ($\gamma_1 < 0$ is ebb-dominant and $\gamma_1 > 0$ is flood-dominant) To facilitate comparison between scenarios, the value of the velocity skewness was also set to a binary -1 or +1 to denote either ebb-dominance or flood-dominance, respectively.

### 2.2.4 Discharge pulse, baroclinic processes, and exchange flow

Discharge of freshwater from an estuarine dam into an estuary results in a seaward propagating pulse of freshwater which decreases in magnitude with distance (Figueroa et al., 2020a; Figueroa et al., 2020b). The pulse speed and range of influence are important factors relevant to salinity and sediment transport. To quantify the high frequency freshwater discharge forcing along-channel (in contrast to low frequency, Section 2.2.2.), time series were selected along-channel, and height of jumps in water level and velocity, associated with the pulse front, were manually extracted.

To better understand the effect of the estuarine dams on the baroclinic hydrodynamics and associated sediment dynamics, spring-neap averaged along-channel salinity and stratification data were collected for each scenario. For the same reason, the following measure for the intensity of the estuarine exchange flow was used based on a similar measure used by Burchard and Hetland (2010):

$$\mu(\langle u \rangle) = \int_0^1 |\langle u(\sigma) \rangle| d\sigma \tag{5}$$

where $\mu$ is referred to here as an exchange flow parameter, $u$ is a spring-neap average velocity profile, and $\sigma$ is the nondimensional sigma depth ($\sigma = z/h$, $z$ is vertical coordinate, $h$, is water depth) ranging from zero at the bed to one at the surface. The parameter $\mu$ calculates the average absolute value of a residual velocity profile. If there was not a residual two-layered circulation, $\mu$ was set to zero.

### 2.2.5 Estuarine parameter space

Previous analyses were directed at understanding changes in tide and river processes caused by an estuarine dam. Such changes in turn may affect the estuarine type which has implications for both the post-dam hydrodynamics and sediment dynamics. To quantify changes in the estuarine type, the estuarine parameter space was used based on the freshwater Froude number, $Fr_f$, and the mixing number, $M$, defined as (Geyer and MacCready, 2014):

$$Fr_f = \frac{U_R}{(\beta g S_{ocean} H)^{\frac{1}{2}}} \tag{6a}$$

$$M^2 = \frac{C_D U_T^2}{\omega N_0 H^2} \tag{6b}$$

where $U_R$ is the cross-sectionally averaged river discharge velocity, $H$ is the cross-sectionally averaged depth, $U_T$ is the amplitude of the cross-sectionally averaged tidal velocity, $N_0 = (\beta g S_{ocean}/H)^{1/2}$ is the buoyancy frequency for maximum bottom-to-top salinity variation in an estuary, $\beta = 7.7 \times 10^{-4}$ psu$^{-1}$ is the coefficient of haline contraction, $S_{ocean}$ = 35 psu is the ocean salinity, $g$ = 9.8 m s$^{-2}$ is the acceleration due to gravity, $C_D$ (taken here as $C_D = 2.5 \times 10^{-3}$) is the drag coefficient, and $\omega = 1.4 \times 10^{-4}$ s$^{-1}$ is the tidal frequency.

Physically, $Fr_f$ is the net velocity of the river flow scaled by the maximum possible frontal propagation speed, and $M$ is the ratio of tidal timescale to the mixing timescale (Geyer and MacCready, 2014). To keep the points within the parameter space for the post-dam estuaries, minimum values of $M$ = 0.22 and $Fr_f = 1.5 \times 10^{-4}$ and a maximum value of $Fr_f$ = 0.9 were specified. Physically, these represent very low currents, very low freshwater discharge, and very high freshwater discharge approaching the maximum baroclinic frontal propagation speed, respectively. It is noted that, in contrast to Figueroa et al. (2022), this study allows $U_T$ to include currents due to the discharge pulse from the estuarine dam, thus permitting the dam discharge to affect $M$.

### 2.2.6 Sediment flux decomposition and bathymetric and surficial sediment change

Changes in hydrodynamics can induce changes in sediment and morphodynamics. Several processes affect both the sediment and morphodynamics. Sediment accumulation and estuarine turbidity maximum (ETM) formation are due to the convergence of tidally averaged, cross-sectionally integrated suspended sediment transport, $A[uc]_A$. To highlight the relevant underlying processes, the sediment fluxes were decomposed following Burchard et al. (2018):

$$\begin{aligned}\langle A[uc]_A \rangle &= \underbrace{W[\langle D[uc]_z \rangle]_y}_{T} \\ &= \underbrace{W[\langle D \rangle \langle [u]_z \rangle \langle [c]_z \rangle]_y}_{T_a} + \underbrace{W\left[\langle D \rangle \langle [u]'_z [c]'_z \rangle\right]_y}_{T_b} \\ &+ \underbrace{W[\langle D \rangle [\langle \tilde{u} \rangle \langle \tilde{c} \rangle]_z]_y}_{T_c} + \underbrace{W\left[\langle D \rangle \left[\langle \tilde{u}' \tilde{c}' \rangle\right]_z\right]_y}_{T_d} \\ &+ \underbrace{W\left[\langle D' [uc]'_z \rangle\right]_y}_{T_e}\end{aligned} \tag{7}$$

where $u$ is the along-channel current velocity, $c$ is the suspended sediment concentration, $D$ is the depth, $W$ is the width, and $A$ is the cross-sectional area. Here, $[\cdot]_y$, $[\cdot]_z$, and $[\cdot]_A$ denote lateral, vertical, and cross-sectional averages, respectively, and $\langle \cdot \rangle$ denotes a tidal average. The prime (') denotes the deviation from a tidal average and a tilde (~) denotes the deviation from a vertical mean. In this way the temporally averaged, cross-sectionally integrated transport was decomposed into five terms, $T_a$ - $T_e$. Each term is associated with a different sediment transport mechanism. $T_a$ is the

transport by averages often due to down-estuary river runoff. $T_b$ is the tidal covariance transport due to tidal pumping. $T_c$ is the vertical covariance of tidal averages transport due to the estuarine exchange flow. $T_d$ is the combined vertical and temporal covariance transport, e.g. suspended sediment is mixed higher up into the water during flood than during ebb by tidal straining. And $T_e$ is the temporal depth covariance transport due to Stokes transport.

The terms were quantified along-channel in both the pre- and post-dam cases to understand the impact of the estuarine dam on the sediment flux mechanisms. As Eq. 7 is exact only for constant depth or averaging in depth-proportional sigma coordinates (Burchard et al., 2018), averaging was done in sigma coordinates. The operations $\langle\cdot\rangle$ for a tidal average and ($'$) for a deviation from a tidal average were computed using Lanczos 36-hour low-pass and high-pass filters, respectively. To facilitate identifying changes between scenarios, $T_a$ - $T_e$ were averaged over representative pre- and post-dam spring-neap cycles, turning them into a function of only along-channel position. To quantify associated changes in the SSC, morphology, bed mud fraction, and bed fluvial sediment fraction, representative width-averaged along-channel transects were obtained from the model for all scenarios.

# 3 Results

## 3.1 Effect of estuarine dam location on tidal processes

The effect of the discharge interval on tidal processes was found to be minor in comparison with the location of the estuarine dam. Therefore, this section uses the post-dam scenarios with the discharge interval $\Delta t$ = 3 days and focuses on the effect of estuarine dam location.

### 3.1.1 Tide and current amplitude and phase

Figure 3 presents numerical and analytical pre- and post-dam along-channel profiles of $M_2$ tidal amplitude, current amplitude, and phase difference between current and tide depending on the estuarine dam location. Considering first the numerical result, the tidal amplitude (Figures 3A1-D1) increased for all post-dam estuaries. In the pre-dam estuaries, the tidal amplitude was constant along-channel for the river-dominated estuaries and decreased landward in the tide-dominated estuaries due to friction. In the post-dam estuaries, the tides increased landward for dam locations $x$ = 20 and 55 km due to reflection of the tidal wave. For dam location $x$ = 90 km, the tidal

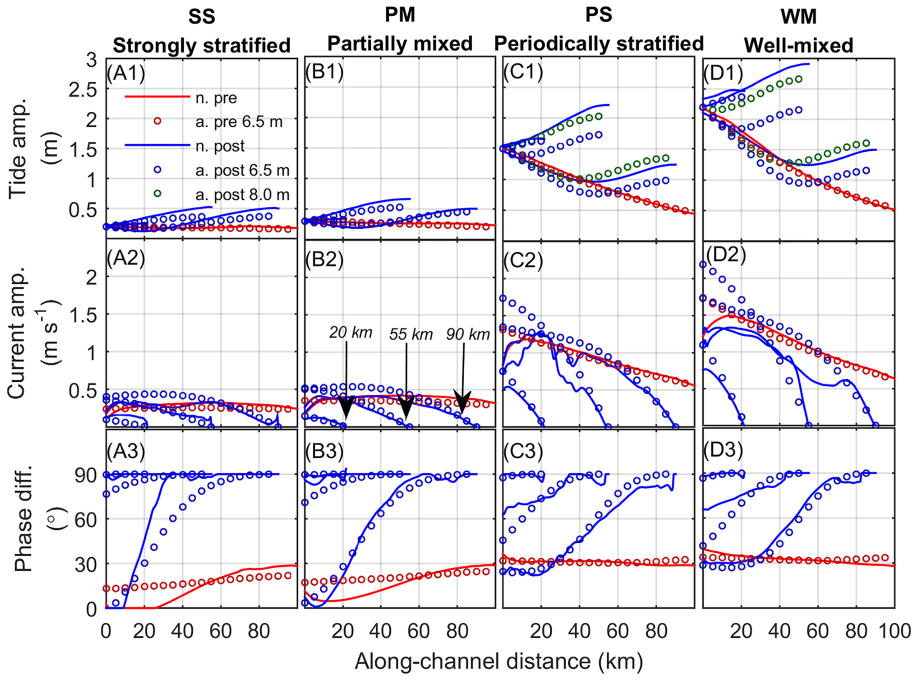


FIGURE 3
Pre- and post-dam along-channel profiles of **(A1-D1)** $M_2$ tidal amplitude (m), **(A2-D2)** $M_2$ current amplitude (m $s^{-1}$), and **(A3-D3)** phase difference between current and tide (°) depending on estuarine dam location (dam at $x$ = 20, 55, and 90 km). Along-channel is distance is from the estuary mouth, positive landward. n. is numerical, a. is analytical, pre is pre-dam, post is post-dam, and 6.5 m and 8.0 m represent the depth at the estuary mouth used in the analytical model. Most analytical models used 6.5 m. All results correspond to scenarios with discharge intervals $\Delta t$ = 3 days.

amplitude near the mouth decreased landward due to friction before increasing near the dam due to reflection. The analytical and numerical results generally matched well. However, it was noted that for the tide-dominated estuaries, post-dam changes in the bathymetry needed to be considered. Thus, without accounting for the post-dam deepening of the mouth from about 6.5 m to 8 m (Section 3.4. below), the post-dam tidal amplitudes were underestimated (Figures 3C1-D1).

Figures 3A1-D1 support numerically that for a given tidal constituent (here $M_2$) a particular dam location can cause maximum tidal amplification due to resonance. For a frictionless, non-convergent estuary, the resonance length is well known to occur when the channel length is a quarter of the tidal wavelength. A simple estimate of the tidal wavelength, $L$, using $L = T\sqrt{gh}$ with tidal period $T$ = 12.4 hr, acceleration due to gravity $g$ = 9.8 m $s^{-2}$, and water depth $h$ = 6.5 m gives $L$ = 360 km and thus a resonance length of $L/4$ = 90 km. This is greater than the resonance length evident in Figure 3D1 where maximum amplification based on the available data occurs near $x$ = 55 km. This is because friction acts to reduce the resonance length. Unfortunately, in the frictional case an explicit analytical solution for the resonance length cannot be found because it requires an iterative procedure (Cai et al., 2016). However, based on the iterative procedure, (Cai et al. 2016; their Figure 7) plotted the resonance length for the frictional case in the estuary shape number ($\gamma$, representing the effect of cross-sectional area convergence) – friction number ($x$, describing the role of the frictional dissipation) space. Using the *WM* estuary as an example, $\gamma$ = 0 (straight channel) and $x$ = 2.5 (moderate to strong friction) and the resonance length is estimated approximately as $L/8$ = 45 km, which is similar to the numerical result. It is noted that the resonance length depends on the tidal amplitude through the friction number, and therefore for a straight channel, smaller tidal amplitudes will have smaller friction numbers, and their resonance lengths will approach the classical $L/4$. This is the case in Figure 3A1 where the resonance length in the microtidal *SS* estuary is likely closer to $L/4$ = 90 km.

The along-channel current amplitude decreased for the post-dam estuaries (Figures 3A2-D2). All post-dam estuaries exhibited currents vanishing at the estuarine dam due to the dead-end channel. The dam location at $x$ = 90 km caused the least change compared to pre-dam conditions, and the dam location at $x$ = 20 km caused the greatest reduction in tidal currents. This was due to the loss of tidal prism near the mouth. For dam locations at $x$ = 55 km in the region of the resonance length, the analytical model predicted larger currents at the mouth. The numerical model did not show these large currents likely due to morphological adjustment (i.e., deepening of the mouth, Section 3.4.).

The pre-dam estuaries had phase differences ranging from $\varphi$ = 0 - 30°, indicating a progressive and mixed wave character. Considering the *WM* estuary as an example, this estuary can be classified following Friedrichs (2010) as a long, intermediate depth, nonconvergent estuary. For this case, the e-folding length of the along-channel tidal amplitude, $L_a$, can be used to analytically estimate the phase difference as $\varphi = \arctan(L_a^{-1}/k)$, where $k$ is the tidal wavenumber. Using data from the *WM* estuary yields a phase difference estimated analytically as $\varphi$ = 40°. This is similar to the numerical result and indicates that the pre-dam estuaries lie between progressive ($\varphi$ = 0°) and diffusive tides ($\varphi$ = 45°).

The post-dam estuaries show a shift to standing wave phase difference ($\varphi$ = 90°) due to wave reflection. Dams located near the mouth ($x$ = 20 km) changed the entire remnant estuary to have a standing wave character. Dams located near the resonance length and landward of the resonance length had progressive or mixed tides at the mouth and standing waves near the estuarine dam ($x$ = 55 and 90 km). The analytical result agreed well with the numerical result. For dam locations beyond the resonance length, the distance from the reflecting end where the reflected wave influences the estuary was given by Friedrichs (2010). The reflected wave should be included for distances less than about $|L_a|/2$, where $|L_a|$ is the absolute value of $L_a$ as predicted by:

$$\frac{L_a^{-1}}{k} = \frac{\omega}{r} - \left(\frac{\omega^2}{r^2} + 1\right)^{1/2} \tag{8}$$

where $r = 8c_D U/3\pi h$ is the friction factor, $c_D$ is the drag coefficient, $U$ is the tidal amplitude, and $h$ is the tidally averaged depth. Taking the *WM* estuary as an example, the distance from the estuarine dam where the reflected wave influences the estuary is found to be about 40 km, which agrees with the model result where the tides transition from a mixed to standing wave character (Figure 3D3).

### 3.1.2 Mean sea level and Eulerian residual current

The pre- and post-dam mean sea levels and Eulerian residual currents were different for the river-dominated estuaries (particularly the *SS* estuary) and the tide-dominated estuaries (*PS* and *WM*; Figure 4). For the river-dominated estuaries, the pre-dam mean sea levels increased landward due to the freshwater discharge (Figures 4A1-B1). For the *PM* estuary, the post-dam mean sea levels were similar, but they increased considerably for the post-dam *SS* estuary because it had the largest input of freshwater volume during a discharge event which was enough to increase the spring-neap averaged sea level. The Eulerian residual currents were seaward (Figures 4A2-B2) and due to river runoff with negligible Stokes return flow (Figures 4A3-B3). The estuarine dam resulted in partially reduced seaward Eulerian currents due to scour of the channel adjacent to the dam (Section 3.4.) and the change from continuous to episodic freshwater discharge. The dam location did not change the overall trend in post-dam mean sea level and Eulerian residual current in the river-dominated estuaries.

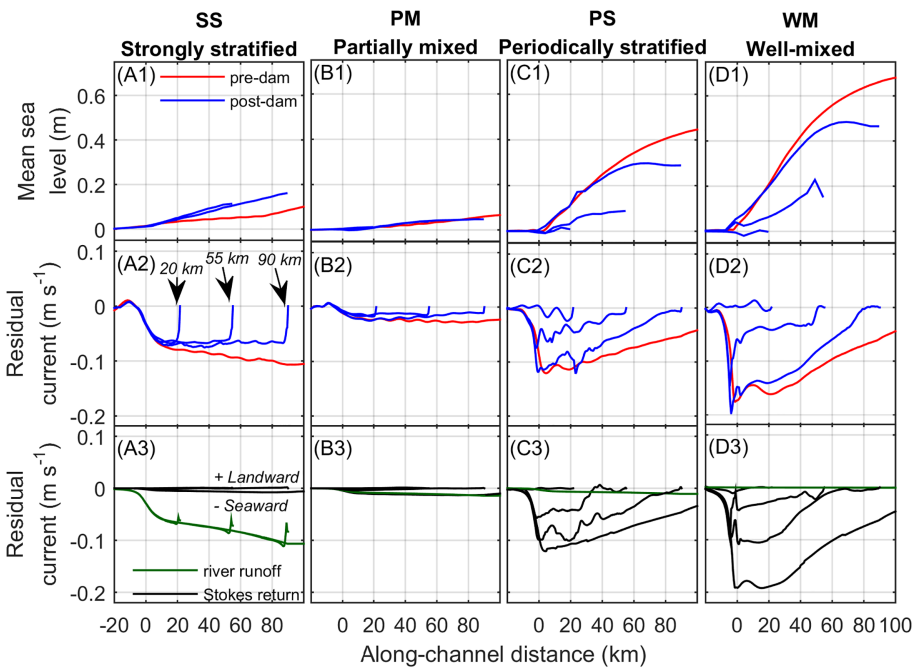


FIGURE 4
Pre-dam and post-dam along-channel profiles of **(A1-D1)** mean sea level (m), **(A2-D2)** cross-sectionally averaged Eulerian residual currents (m $s^{-1}$), and **(A3-D3)** river runoff (m $s^{-1}$) and Stokes return flow (m $s^{-1}$) depending on estuarine dam location (dam at $x$ = 20, 55, and 90 km). Along-channel distance is distance from the estuarine mouth, positive landward. Negative current is seaward. All results correspond to scenarios with discharge intervals $\Delta t$ = 3 days.

For the tide-dominated estuaries, the pre-dam mean sea levels increased landward due to the mixed tides generating a landward Stokes drift and water level setup (Figures 4C1-D1). As the dam location moves toward the mouth, a greater proportion of the estuary experiences standing wave tides, and the landward Stokes drift, Stokes setup (Figures 4C1-D1), and Stokes return flow (Figures 4C2-D2) are reduced. Analytic expressions supported that the Stokes return flow was the main process contributing to the Eulerian residual current and river runoff was negligible (Figures 4C3-D3). Thus, the dam location was found to have a strong effect on the mean sea level and Eulerian residual currents in the tide-dominated estuaries. Furthermore, the effect was greatest for the estuarine dam location near the mouth ($x$ = 20 km). This has important ramifications for the transport of sediment by the Eulerian residual current as well as the Euler-induced tidal asymmetry.

### 3.1.3 Tidal asymmetry

Change in tidal asymmetry for different estuarine types and dam locations is shown in Figure 5. Based on the harmonic method, the magnitude of tidal asymmetry stayed the same or increased for almost all post-dam estuaries (Figure 5A). Relative to the pre-dam tidal asymmetry, the magnitude of the post-dam tidal asymmetry increased the most for the river-dominated estuaries likely due to their pre-dam tides being relatively small, and thus small changes have a relatively larger effect. The dam location near resonance ($x$ = 55 km) caused the least change in tidal asymmetry magnitude whereas the dam location near the mouth ($x$ = 20 km) changed the most. These changes were likely because of differential amplification of the $M_2$ and $M_4$ constituent, changes in mean sea level, and morphologic change. Based on the harmonic method, the tidal asymmetry direction for the river-dominated estuaries was mostly ebb-dominant and for the tide-dominated estuaries was mostly flood-dominant (Figure 5B). This agrees with Friedrichs and Aubrey (1988) who identified that increasing tidal range promotes flood-dominance.

To discuss the tidal asymmetry based on the statistical method and the Euler-induced tidal asymmetry, the bottom Eulerian residual current is shown for reference in Figure 5C. For the pre-dam river-dominated estuaries, the estuarine exchange flow was the main process, and it drove an upstream bottom Eulerian residual current. For the pre-dam tide-dominated estuaries, the Stokes return flow was the main process, and it drove a seaward bottom Eulerian residual current. The post-dam river-dominated estuaries maintained an upstream Eulerian residual current. In the post-dam tide-dominated estuaries, the switch from mixed to more standing wave tides caused the Stokes return flow to be reduced ($PS^3_{90}$, $WM^3_{55}$, $WM^3_{90}$) or replaced by landward exchange flow ($PS^3_{20}$, $P$

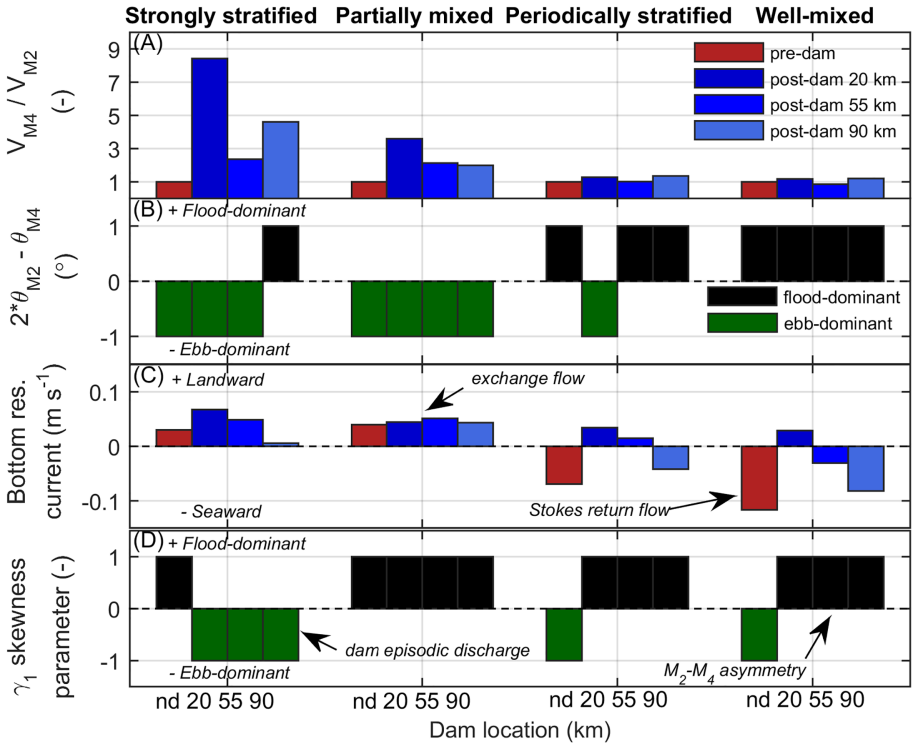


FIGURE 5
Pre- and post-dam tidal asymmetry for different dam locations and estuarine types. **(A)** Ratio of $M_4$ to $M_2$ tidal constituent velocity amplitude ($v_{M4}/v_{M2}$, -) with values normalized to each type's pre-dam case, **(B)** $M_2$ and $M_4$ tidal constituent velocity relative phase difference ($2\theta_{M2} - \theta_{M4}$, °) binned based on dominance, **(C)** bottom residual currents (m $s^{-1}$), and **(D)** bottom velocity skewness parameter ($\gamma_1$, -) with values binned based on dominance. The no dam case is denoted nd. All results correspond to scenarios with discharge intervals $\Delta t$ = 3 days.

$S^3_{55}$, $WM^3_{20}$). Based on the velocity skewness, the tidal asymmetry direction tended to match the bottom Eulerian residual current (indicating Euler-induced asymmetry) with two exceptions. First were $SS^3_{20}$, $SS^3_{55}$, and $SS^3_{90}$ where the velocity skew was dominated by the high frequency freshwater discharge events rather than the low frequency Eulerian residual currents. Second were $PS^3_{90}$, $WM^3_{55}$, and $WM^3_{90}$ where the effect of tidal distortion and interaction of the $M_2$ and $M_4$ constituents was greater than the Euler-induced tidal asymmetry caused by the Stokes return flow. Overall, these results highlight the importance of Euler-induced tidal asymmetry and also the dam episodic discharge in the post-dam *SS* estuary and interaction of the $M_2$ and $M_4$ constituents in the post-dam tide-dominated estuaries.

## 3.2 Effect of estuarine dam discharge interval on river processes

### 3.2.1 Sea surface elevation, current, salinity, and SSC time series

As freshwater discharges are events, time series comparing river- and tide-dominated end members under different discharge intervals is shown in Figure 6. Here, data of $SS^{\Delta t}_{20}$ and $WM^{\Delta t}_{20}$ from the center of the post-dam estuary were selected (center of region of interest, ROI, see Figure 2G).

In the pre-dam *SS* estuary, the discharge was continuous, the tidal range was small, a distinct two-layer circulation occurred, the estuary was strongly stratified, and sediment was resuspended during the spring tides (Figures 6A1-A5). The $SS^{0.5}_{20}$ estuary was overall similar with some change in the surface salinity and bottom resuspension due to discharges during ebb (Figures 6B1-B5). Once the discharge interval exceeded the tidal cycle period, the response was different. The $SS^3_{20}$ estuary had increasingly spaced discharge periods (Figure 6C1). The greater freshwater volume per discharge resulted in a noticeable water level set up, seaward current pulse, freshwater frontal propagation, and greater resuspension of bottom marine sediment and advection of fluvial sediment (Figures 6C2-C5). The $SS^7_{20}$ estuary was similar to the $SS^3_{20}$, but the magnitude of the setup, discharge pulse, freshwater front, and resuspension and advection of marine and fluvial sediment was greater (Figures 6D1-D5). Therefore it can be seen that the discharge interval strongly affects the estuarine dynamics in the river-dominated estuary, particularly if the discharge interval exceeds the tidal cycle period ($\Delta t$ > 0.5 days).

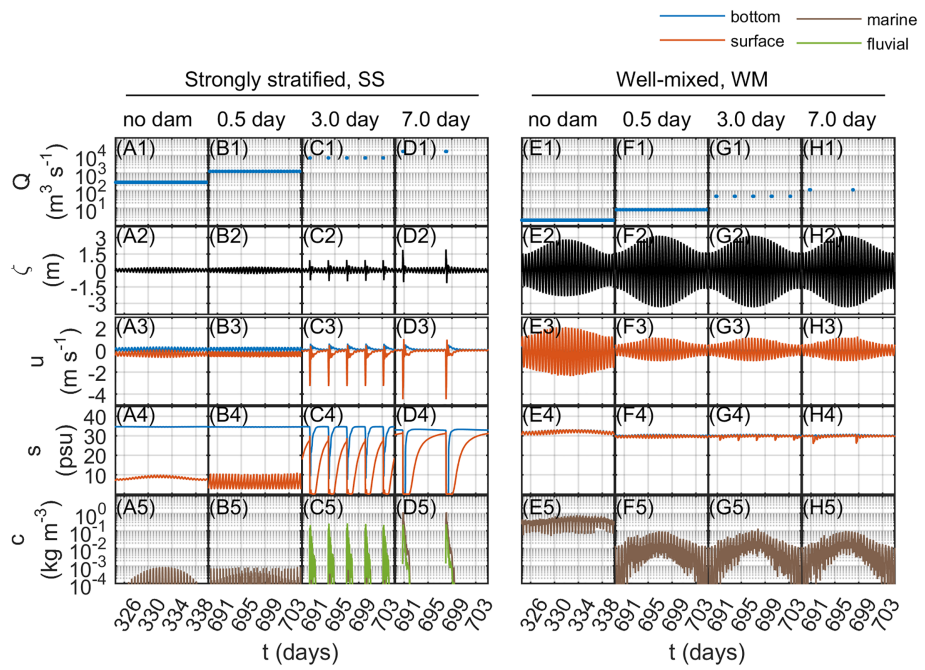


FIGURE 6
Representative time series comparing strongly stratified and well-mixed estuaries under different discharge intervals. **(A1-H1)** Freshwater discharge ($Q$, $m^3\ s^{-1}$), **(A2-H2)** sea surface elevation ($\zeta$, m), **(A3-H3)** bottom and surface along-channel current velocity ($u$, m $s^{-1}$); **(A4-H4)** bottom and surface salinity ($s$, psu), and **(A5-H5)** suspended sediment concentration ($c$, kg $m^{-3}$) versus time ($t$, days). Data are from the center of the region of interest (ROI) for cases with an estuarine dam at $x$ = 20 km. Time is day since initialization with estuarine dam placed on day 365. Positive velocity is landward.

In the pre-dam *WM* estuary, the discharge was continuous, the tidal range was large, the currents were strong, the water column was well-mixed, and the sediment concentrations were relatively high (Figures 6E1-E5). The $WM_{20}^{0.5}$ estuary with discrete discharges showed little change due to the estuarine dam discharge and mostly showed tidal amplification, reduced currents due to the dead-end channel, and reduced SSC due to the reduced currents (Figures 6F1-F5). The $WM_{20}^{3}$ (Figures 6G1-G5) and $WM_{20}^{7}$ (Figures 6H1-H5) similarly did not show the water level setup, discharge pulse, resuspension of bottom marine sediments or advection of fluvial sediments. The primary effect was a relatively weak salinity front followed by periodic stratification of a few psu (not shown in detail). In macrotidal estuaries receiving estuarine dam freshwater discharge, periodic stratification is due to tidal straining of the longitudinal salinity gradient (Figueroa et al., 2019; Figueroa et al., 2020a). Overall, based on both sets of time series, it is found that river-dominated estuaries respond to variations in discharge interval more than tide-dominated estuaries, particularly when the discharge interval exceeds the tidal cycle period.

### 3.2.2 Discharge setup and velocity along-channel profiles

To understand how the discharge forcing varies along channel with dam location and discharge interval, along-channel profiles of discharge setup and velocity are shown in Figure 7. Overall, the discharge setup and velocities were found to depend on dam location, discharge interval, and estuarine type. Due to having the largest freshwater discharge, the post-dam *SS* estuary had the greatest discharge setups and velocities. The longer discharge intervals had greater discharge setup and velocity. The discharge setup ranged from 0.1 m for $SS_{90}^{0.5}$ to 4.5 m for $SS_{90}^{7}$ (Figure 7A1). The velocity magnitude ranged from 1 m $s^{-1}$ for $SS_{90}^{0.5}$ to 3 m $s^{-1}$ for $SS_{90}^{7}$ (Figure 7A2). Dams located further landward (i.e., $SS_{90}^{7}$ vs $SS_{20}^{7}$) had the overall greatest setup due to freshwater discharge into the shallower, landward portion of the channel. On the other hand, dams located further seaward ($SS_{20}^{7}$ vs $SS_{90}^{7}$) generated faster discharge currents due to discharging into deeper water and experienced less dissipation compared to discharges originating further landward.

A similar pattern was observed in the post-dam *PM* estuary. The discharge setup was less, reaching up to 0.5 m ($PM_{90}^{7}$), as was the magnitude of the discharge velocity, reached nearly 1 m $s^{-1}$ ($PM_{90}^{7}$). In the tide-dominated, post-dam *PS* estuary, a significant discharge pulse was generated only for the long discharge interval of $\Delta t$ = 7 days. Also, the pulse dissipated completely before reaching the mouth. In the tide-dominated, post-dam *WM* estuary, the freshwater discharge was the least, and no significant pulse was observed. These results indicate that the river-dominated estuaries are particularly susceptible to discharge pulses, which are greater with increasing discharge

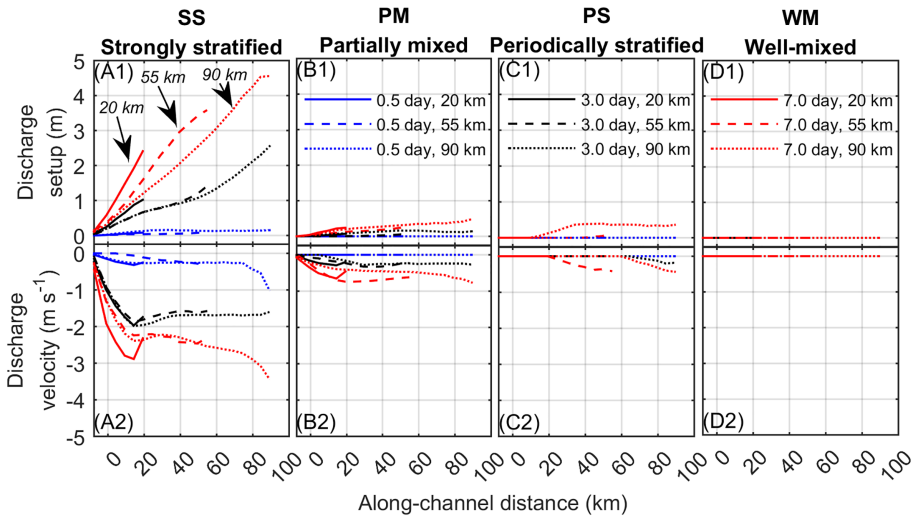


FIGURE 7
Along-channel profiles of **(A1-D1)** discharge setup (m) and **(A2-D2)** velocity (m $s^{-1}$) depending on estuarine type, dam location, and discharge interval. Along-channel distance is distance from the estuarine mouth (positive landward). Negative current is seaward.

interval, and are able to reach the mouth. For tide-dominated estuaries, only the longest discharge interval made a pulse, and it fully dissipated before reaching the mouth.

## 3.3 Effect of tide and river change on salinity, exchange flow, and estuarine classification

### 3.3.1 Salinity, stratification, and the estuarine exchange flow

This section considers changes in salt and baroclinic processes which result from the combined changes to the tide and river forcing. These processes are of interest to gain insight into the effect of the estuarine dam on salt and sediment transport. As data for different discharge intervals were similar, the effect of the dam location is primarily considered.

Along-channel profiles of salinity, stratification, and the estuarine exchange flow parameter for the discharge interval $\Delta t$ = 3 days are shown in Figure 8. For the pre-dam estuaries the salt intrusion increased from the *SS* to *WM* estuary (Figures 8A1-D1). The stratification increased from the *WM* to *SS* estuary (Figures 8A2-D2) as did the exchange flow parameter (Figures 8A3-D3). The exchange flow was greater in the pre-dam *SS* compared to the *PM* estuary because of strong freshwater outflow in the surface layer of the *SS* estuary which is included in the exchange flow parameter, $\mu$.

The estuarine dam located at $x$ = 90 km was near the salt intrusion limit for the *SS*, *PM*, and *PS* estuaries, whereas it was located with the salt intrusion for the *WM* estuary (Figures 8A1-D1). The post-dam river-dominated estuaries tended to get fresher, less stratified, and have decreased exchange flow (Figures 8A1-A3, B1-B3). This was mainly due to the shift from steady two-layer circulation to unsteady freshwater fronts. Greater discharge interval for $SS_x^7$ tended to show higher salinity and stratification and less exchange flow which was due to greater freshwater conveyance, intrusion of salt along the bottom layer during quiescent periods, and discharge unsteadiness. The post-dam tide-dominated estuaries tended to get saltier, more stratified, and have increased exchange flow (Figures 8C1-C3, D1-D3). This was due to the shift from a mixed water column to freshwater pulses conveyed to the shelf primarily along the surface and reduced mixing. The $PM_{20}^3$ and $WM_{20}^3$ estuaries were exceptions for their post-dam salinity change due to differences in stratification and the seaward conveyance of freshwater in the short $x$ = 20 km estuaries.

Overall it was found that the response of the salinity, stratification, and exchange flow are influenced by changes in mixing caused by reduced tidal currents as well as the discharge pulse. Comparing the estuarine types, estuarine dams located further inland affected river-dominated estuaries more by making their inland portions fresh with less exchange flow (Figures 8A1-A3, B1-B3), and estuarine dams located further seaward affected tide-dominated estuaries more by making the mouths more stratified with greater exchange flow (Figures 8C1-C3, D1-D3). Higher discharge interval resulted in similar spatial trends (Figures 8A1-A3). It is likely the discharge interval interacted with a flushing time scale. Thus $SS_{90}^7$ was saltier than $SS_{90}^3$ because the discharge interval was greater than the flushing time scale. This relationship is complex as the flushing

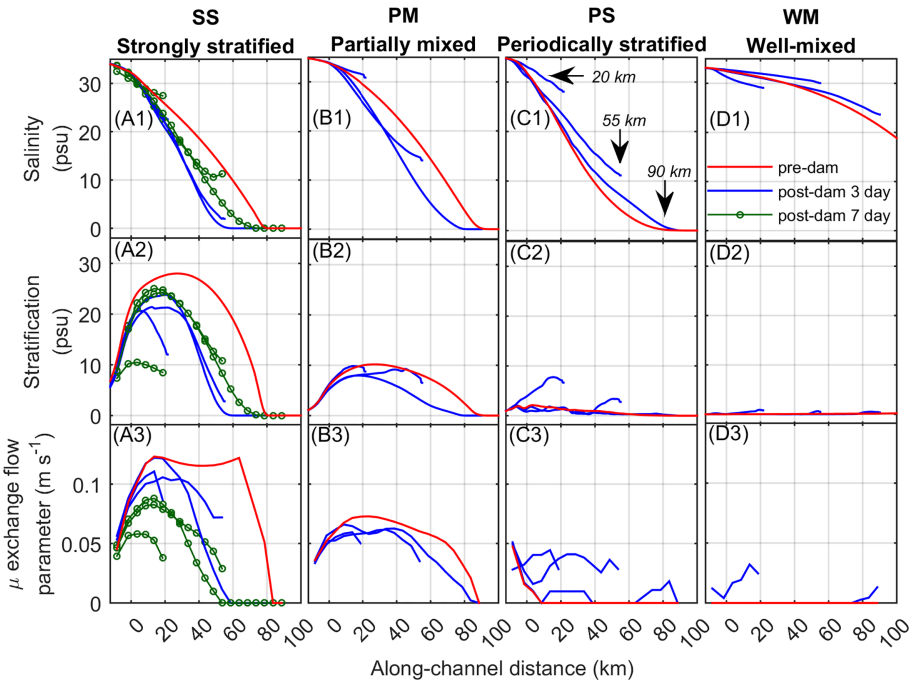


FIGURE 8
Along-channel profiles depending on estuarine type, dam location, and discharge interval of **(A1-D1)** depth-averaged salinity (psu), **(A2-D2)** top-to-bottom salinity stratification (psu), and **(A3-D3)** estuarine circulation parameter $\mu$ (m s$^{-1}$). Along-channel distance is distance from the estuarine mouth (positive landward). Most post-dam data is for discharge interval $\Delta t$ = 3 days. The post-dam data for discharge interval $\Delta t$ = 7 days is shown for the strongly stratified estuary.

time scale is a function of the discharge interval (Azevedo et al., 2010) and reasonably the dam location because of its effect on the estuarine volume and tidal currents.

### 3.3.2 Estuarine parameter space

The change in estuarine classification is shown in Figure 9 with the divisions of the estuarine parameter space into different estuarine types labeled in Figure 9A3 for reference. For the pre-dam estuaries, lower and higher $M$ represent primarily neap and spring tide variation, respectively, and lower and higher $Fr_f$ represent seaward and landward position. The pre-dam estuaries matched their estuarine type (Figure 9, no dam).

Overall, the estuarine dam resulted in significant change in the estuarine type for all the post-dam estuaries due to changes in river and tidal forcing. A key change in the post-dam estuaries was high $Fr_f$ during dam discharge and low $Fr_f$ during no dam discharge (labeled for example in Figure 9A2, D3). During dam discharge, the estuaries tended to shift to the salt wedge and time dependent salt wedge types (Figures 9A1-A3, B2-B3, C2-C3, dam discharge), and during no dam discharge, the estuaries tended to shift to fjord, bay, SIPS, and well-mixed types (Figures 9A1-D3, no dam discharge). The $Fr_f$ at unity or greater during dam discharge for the pre-dam *SS* estuary indicated that the maximum baroclinic frontal propagation speed was at times being replaced by a barotropic propagation speed as salt water was being pushed out of the estuary. Additionally, the post-dam $Fr_f$ increased more for longer discharge periods ($\Delta t$ = 7 days, Figures 9A3-D3) compared to shorter discharge periods ($\Delta t$ = 0.5 days, Figures 9A1-D1).

The mixing number $M$ changed in two ways. First, $M$ was reduced in all cases in the area adjacent to the estuarine dam and in the case of dam location $x$ = 20 km (see, e.g., Figure 9D3). The area adjacent to the dam shows $M$ reducing quickly because of the dead-end channel. The dam location of $x$ = 20 km had the most reduced $M$ because of the dead-end channel and loss of tidal prism. This occurred in all post-dam estuaries but was most noticeable in the tide-dominated estuaries (Figures 9C1-C3, D1-D3, 20 km). Second, $M$ increased adjacent to the estuarine dam during discharges due to the strong discharge currents. This was most apparent in the river-dominated estuaries (see, e.g. Figures 9A1-A3, B1-B3, dam discharge).

Considering the change in $Fr_f$ and $M$ together, it was revealed that the greatest change in estuarine type occurred for dams near the mouth with long discharge intervals ($x$ = 20 km and $\Delta t$ = 7 days). Furthermore, the post-dam river-dominated estuaries varied more than the tide-dominated estuaries due to

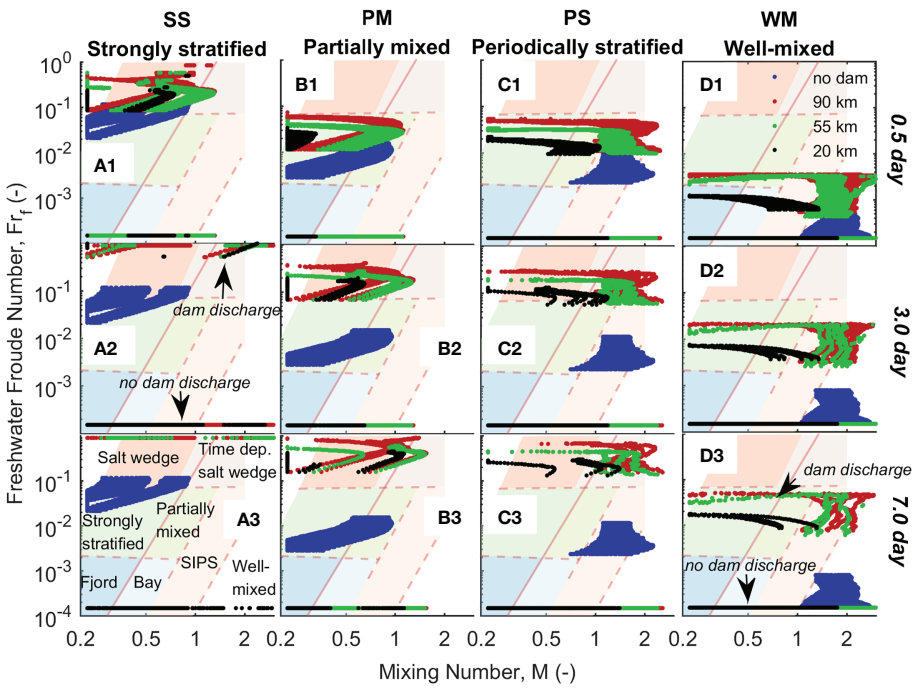


FIGURE 9
Change in estuarine classification for each estuary type depending on estuarine dam location and discharge interval: **(A1-D1)** $\Delta t$ = 0.5 day, **(A2-D2)** $\Delta t$ = 3 day, and **(A3-D3)** $\Delta t$ = 7 day. Minimum values of $M$ = 0.22 and $Fr_f$ = 1.5 × $10^{-4}$ and a maximum value of $Fr_f$ = 0.9 were specified. Physically, these represent very low currents, very low freshwater discharge, and very high freshwater discharge approaching the maximum baroclinic frontal propagation speed, respectively. SIPS is strain-induced periodically stratified estuary, also referred to as a periodically stratified estuary.

the greater range in $Fr_f$, where $SS_x^7$ was an extreme case alternating between, for example, time dependent salt wedge and bay (Figure 9A3).

## 3.4 Effect of tide and river change on sediment flux decomposition and morphology

### 3.4.1 Along-channel depth, mud fraction, fluvial fraction, SSC, and sediment flux

Changes in tide and river due to an estuarine dam can affect the currents, sediment sources, and so forth. Change in aspects of sediment and morphodynamics according to an estuarine dam is shown in Figure 10. As the discharge interval resulted in similar trends, the effect of dam location for cases with $\Delta t$ = 3 days is primarily considered. The effect of the discharge interval on bathymetry and cross-sectionally integrated sediment flux is shown for the post-dam SS estuary (Figures 10A1, A5).

The pre-dam conditions can be summarized as follows. The river-dominated estuaries' depths tended to have less change from the initial condition whereas the tide-dominated estuaries tended to have more because of the Stokes return flow causing a deepening of the mouth and formation of a mouth bar (Figures 10A1-D1). Along the channel the bed was primarily sandy and the shelf was muddy (Figures 10A2-D2). In all cases there was no fluvial sediment reaching the estuary (Figures 10A3-D3). The SSC increased from the river-dominated estuaries to the tide-dominated estuaries (Figures 10A4-D4). And, the magnitude of the sediment flux was increasing from relatively negligible in the river-dominated estuaries to the strongest in the tide-dominated estuaries where the sediment flux was mostly seaward at the mouth due to the Stokes return flow (Figures 10A5-D5).

Similar to the pre-dam estuaries, the post-dam estuaries could be divided into two groups based on their dynamics, the river-dominated and the tide-dominated estuaries, with the *PM* estuary being transitional between the two. The $SS_x^{0.5}$ and $PM_x^3$ showed the formation of bayhead delta deposits due to input of fluvial sediments directly into estuary from the dam, however for longer discharge intervals, the *SS* estuary showed the formation of scour near the dam and deposits further downstream (Figures 10A1-A2). The tide-dominated estuaries with $x$ = 20 km showed relatively little post-dam morphodynamic change, whereas $x$ = 55 and 90 km showed deepening and bar formation at the mouth but also notably deposition adjacent to the dam due to tidal asymmetry. The estuaries became muddier due

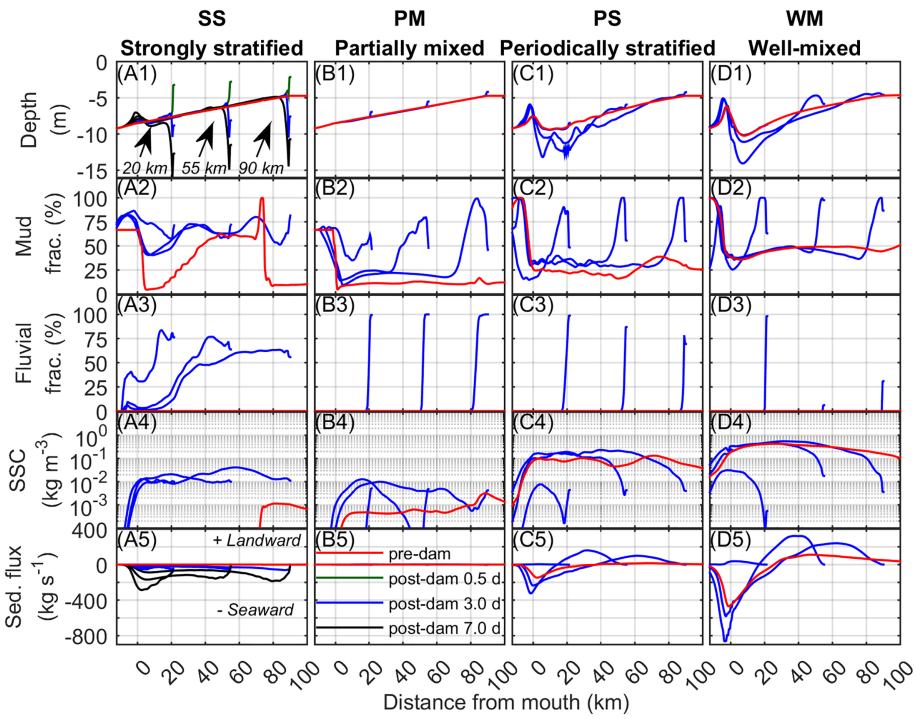


FIGURE 10
Pre-dam and post-dam along-channel profiles depending on estuarine dam location (dam at $x$ = 20, 55, and 90 km) of **(A1-D1)** width-averaged channel depth (m), **(A2-D2)** width-averaged mud fraction (%) on bed surface, **(A3-D3)** width-averaged fluvial sediment fraction (%) on bed surface, **(A4-D4)** depth-averaged suspended sediment concentration along channel thalweg (SSC, kg m$^{-3}$), and **(A5-D5)** cross-sectionally integrated sediment flux (kg s$^{-1}$). Most data correspond to $\Delta t$ = 3 day. In **(A1, A5)** $\Delta t$ = 0.5 and 7 day are also shown. Along-channel distance is distance from the estuarine mouth (positive landward). Negative current is seaward.

to discharge of fluvial mud in the river-dominated estuaries and the deposition of mud from suspension in the tide-dominated estuaries (Figures 10A2-D2). The amount of the fluvial sediment increased in all estuaries near the dam, and throughout the estuaries for the high freshwater discharge post-dam SS estuary (Figures 10A3-D3). The SSC tended to increase for the river-dominated estuaries due to input of sediment and resuspension by discharge pulses, and it tended to decease for the tide-dominated estuaries due to reduction of the tidal currents, particularly for $x$ = 20 km (Figures 10A4-D4). Finally, the relatively small sediment fluxes increased considerably to seaward fluxes in the post-dam *SS* estuary, the fluxes remained low in the post-dam *PM* estuary, and the post-dam tide-dominated estuaries showed a similar pattern as their pre-dam estuaries, yet there was a notable increase in the landward sediment fluxes due to changes in the Stokes return flow and tidal asymmetry (Figures 10A5-D5). Based on these results, it can be seen that the dam location affected the response of the tide-dominated estuaries, and the discharge interval affected the river-dominated estuaries, in particular whether deposition or scour occurred adjacent to the dam. The changes in fluvial sediment and sediment flux directions also indicate that the river-dominated estuaries are primarily receiving sediment from the river boundary whereas the tide-dominated estuaries are primarily receiving sediment from the marine sediments reworked from the estuary and shelf.

### 3.4.2 Sediment flux decomposition

The decomposed sediment fluxes are shown in Figure 11. As different discharge intervals resulted in similar trends, the effect of dam location for cases with $\Delta t$ = 3 days is considered. Overall, the sediment flux mechanisms and their response to the estuarine dam could be divided into the river- and tide-dominated estuaries with the *PM* estuary being transitional between the two.

For the pre-dam *SS* estuary, seaward river runoff ($T_a$) and tidal pumping ($T_b$) by Euler-induced tidal asymmetry were the main mechanisms in the landward tidal river portion, and this led to the two-layered estuary with relatively small sediment fluxes on the seaward side (Figure 11A1). With the estuarine dam, the magnitude of the fluxes increased and $T_a$ and $T_b$ extended throughout the estuary until reaching the shelf (Figures 11A2-A4). As the dam approached the mouth, the importance of seaward tidal pumping increased as did some landward estuarine exchange flow ($T_c$). In this case, the seaward

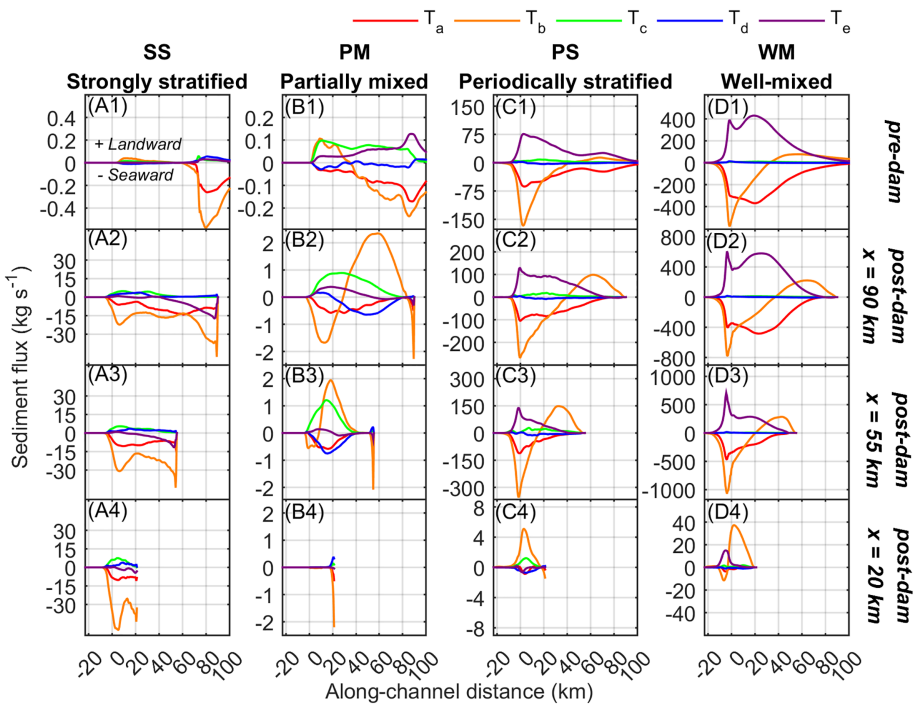


FIGURE 11
Pre- and post-dam spring-neap averaged, cross-sectionally integrated decomposed sediment flux (kg $s^{-1}$) along-channel profiles depending on estuarine type and estuarine dam location for **(A1-D1)** the pre-dam estuaries, **(A2-D2)** dam at x = 90 km, **(A3-D3)** dam at x = 55 km, and **(A4-D4)** dam at x = 20 km for discharge interval $\Delta t$ = 3 days. $T_a$ is the transport by averages due river runoff or Stokes return flow, $T_b$ is tidal pumping, $T_c$ is estuarine exchange flow, $T_d$ is tidal straining, and $T_e$ is Stokes transport. Along-channel distance is distance from the estuarine mouth, positive is landward. Positive sediment flux is landward.

$T_b$ was due to the intratidal discharge pulses instead of the Euler-induced tidal asymmetry which occurred in the tidal river of the pre-dam estuary due to tides interacting with the seaward river runoff.

For the pre-dam *PM* estuary, the tidal straining ($T_d$) and Stokes transport ($T_e$) also made contributions to the sediment flux (Figure 11B1), yet it is noted that $T_d$ was generally found to be negligible in this study. In the pre-dam *PM* estuary, landward $T_c$ and related $T_b$ due to Euler-induced tidal asymmetry occurred near the mouth whereas toward the head seaward $T_a$ and $T_b$ occurred, similar to the pre-dam *SS* estuary. Some landward $T_e$ was present as the tides were of moderate range and mixed. With the estuarine dam at $x$ = 55 and 90 km, two areas could be distinguished (Figures 11B2-B3). First, adjacent to the estuarine dam is a narrow area where the intratidal discharge causes a seaward $T_b$. Second is the broader area of the estuary where $T_a$ and $T_b$ flush some sediment seaward and primarily $T_c$ and associated $T_b$ due to Euler-induced asymmetry bring sediment landward. With $x$ = 20 km, freshwater is conveyed efficiently to the shelf. $T_c$ is reduced, and $T_b$ in the narrow area adjacent to the dam is only active due to discharge pulses while the rest of the estuary is quiescent due to the reduced tidal currents.

The pre-dam tide-dominated estuaries (*PS* and *WM*) were both found to be strongly affected by the Stokes drift ($T_e$), Stokes return flow (here $T_a$), and tidal pumping ($T_b$) due to the Euler-induced tidal asymmetry caused by the interaction of the Stokes return flow Eulerian residual current and the strong tidal currents (Figures 11C1-D1). As discussed in Figueroa et al. (2022), in tide-dominated estuaries with little freshwater input, $T_a$ is better to be thought of as a mean flux due to the Stokes return flow rather than a mean flux due to the river runoff. It is for this reason there is a symmetry between landward $T_e$ and seaward $T_a$ in Figures 11C1-D1. While $T_a$ and $T_e$ approximately balance, the Stokes return flow Eulerian residual current generates the seaward $T_b$ due to the Euler-induced tidal asymmetry. With the estuarine dam at $x$ = 55 and 90 km, the tides become standing near the estuarine dam, resulting in the elimination of Stokes drift there and promotion landward $T_b$ due to landward tidal distortion and interaction of the $M_2$ and $M_4$ constituents. Landward $T_b$ was likely also promoted by the reduction of the Stokes setup and amplification of the tides which would tend to deform the tides more and promote flood-dominance. With $x$ = 20 km, the tides were standing and the Stokes drift was effectively eliminated (Figures 11C4-D4).

Thus, the landward $T_b$ due to tidal deformation dominated with some landward $T_c$ in the $PS^3_{20}$ estuary and some landward $T_e$ over the mouth bar in the $WM^3_{20}$ estuary (Figures 11C4, D4, respectively).

These results indicate that as the estuarine dam location approached the mouth there was a continuous change in the sediment flux mechanisms, including their magnitudes and directions. The river-dominated SS estuary shifted to higher magnitude sediment fluxes which were seaward due to the discharge pulse and could scour sediments. The PM estuary experienced changes in $T_c$ and $T_b$, and when the estuary become very short, the tides were significantly reduced resulting in a shift to a quiescent basin receiving the discharged fluvial sediments. Finally, the tide-dominated estuaries were characterized by the reduction of the Stokes drift due the shift from a mixed to a standing tidal wave. This occurred first adjacent to the estuarine dam, but then came to cover the entire estuary when the estuary became very short. For these parts, $T_b$ was reduced in magnitude but changed direction to landward indicating reworking of the mouth bar and import of marine sediments from the shelf due to tidal distortion and interaction of the $M_2$ and $M_4$ constituents.

# 4 Discussion

## 4.1 Interaction of dam location and discharge interval with estuarine spatial and temporal scales

The overall objective of this study is to understand the effect of estuarine dam location and discharge interval on estuarine processes. It was revealed that the estuarine dam location and discharge interval are important parameters controlling tide and river processes, respectively, and that the estuarine response depends on the estuarine type, broadly river-dominated and tide-dominated estuaries.

In the tide-dominated estuaries, the estuarine dam location was important due to the processes of wave reflection, resonance, the dead-end channel, loss of tidal prism, and shift from progressive and mixed to standing tidal waves. The resonance length was found to be an important length scale determining the estuarine response, and its value (here approximately $L/8$ = 45 km) was noted as being less than the classical value ($L/4$ = 90 km) due to friction. For dams located a distance less than the resonance length from the mouth, the switch from mixed to standing tides reduced the Stokes drift, Stokes setup, Stokes return flow Eulerian residual current, and the seaward tidal pumping due to Euler-induced tidal asymmetry. This resulted in lower mean sea levels, reduced seaward Eulerian residual current, and establishment of landward tidal pumping due to tidal deformation likely supported by the shallower water with amplified tides. For dams located near the resonance length, the mouth was deepened due to the increased currents which resulted in a morphodynamic feedback bringing the currents back to a magnitude similar to the pre-dam condition. The reworking of sediment at the mouth together with the dead-end channel and standing tides near the dam resulted in the greatest deposition near the estuarine dam. For dams located further than the resonance length, the pattern of seaward tidal pumping at the mouth where the tides were mixed resembled the pre-dam estuary, but landward tidal pumping near estuarine dam was prevalent due to the standing tides and flood-dominance due to shallow water tidal deformation.

In addition to the resonance length, the tidal excursion (typically about 14 km; Savenije, 2005) may also be a relevant length scale. This is because in tide-dominated estuaries receiving relatively low discharge, the seaward discharge pulse velocity is not much greater than the ebb current. Thus, the freshwater can travel approximately a tidal excursion before the turn of the tide. Therefore, if the estuarine dam location from the mouth is further than the tidal excursion, more than one tidal cycle is needed for the freshwater to reach the mouth, which can result in discharged fluvial sediments settling and being trapped in the estuary and an inability of the freshwater discharge to resuspend and flush sediments seaward (Figueroa et al., 2020b).

In the river-dominated estuaries, the discharge interval was important due to the processes of discharge water level setup, discharge pulse, exchange flow, freshwater fronts, sediment resuspension, and scour. The tidal cycle period ($T$ = 12.4 hr ≈ 0.5 days) was found to be an important time scale determining the estuarine response to discharge. For a discharge interval equal to the tidal cycle period ($\Delta t$ = 0.5 days, i.e. once every ebb tide), the sea surface elevations, currents, stratification, and sediment resuspension and settling cycles in the post-dam *SS* estuary resembled the pre-dam conditions. For discharge intervals longer than the tidal time scale ($\Delta t$ = 3 and 7 days), the discharge currents were much greater than the pre-dam condition and the *SS* estuary shifted from being a continuously two-layered system to being a time-varying layered system strongly modified by discharge pulses, freshwater fronts, and discharge resuspension. There was also a switch from the deposition of a bayhead delta composed of fluvial sediment adjacent to the estuarine dam to the formation of a scour hole. It can be noted that as the discharge interval scaled with the discharge volume in this study, greater discharge intervals also imply greater ratios of discharge volume to estuarine volume during a discharge event which reasonably is important in determining the pattern of estuarine response, with larger values tending away from the pre-dam behavior.

In addition to the tidal time scale, the flushing time scale is also relevant for the transport of freshwater. For discharge intervals less than the flushing time scale, freshwater may accumulate in the estuary, whereas for discharge intervals greater than the flushing time scale, the estuary will be saltier.

However, defining the flushing time scale is challenging due to its dependence on the discharge interval, dam location, and internal processes.

## 4.2 Implications for coastal hazards

Estuarine dams can provide several societal benefits such as increased freshwater supply for agriculture, stabilized upstream water levels, improved upstream navigability, and often a causeway constructed along the estuarine dam which improves the transportation infrastructure. At the same time, these benefits can be a trade-off with increased risks to coastal hazards such as coastal flooding, coastal erosion, harbor siltation, and water quality issues including eutrophication, algal blooms, and hypoxia. These trade-offs are not limited to the estuary but also include the upstream river and downstream shelf which are also affected by the change in tide and river processes and interruption of the sediment transport pathway.

Estuarine dams can affect coastal flooding in two ways. First, this study indicates that discharge setup and amplification of the tides can be greater than the reduction of the mean sea level by diminished Stokes setup. An example of where this has occurred is the Bang Pakong estuary, Thailand, where unexpected tidal amplification resulted in bank erosion and coastal flooding of saline water (Vongvisessomjai and Srivihok, 2003). Second, this study indicated that for most scenarios fluvial and marine sediments were deposited adjacent to the sluice gates. This can increase the risk of flooding due to the reduced drainage capacity of the river (Zhu et al., 2017; Tilai et al., 2019).

Estuarine dams also have implications for harbor siltation and water quality. For the post-dam tide-dominated estuaries, flood-dominated tidal pumping brought marine sediments reworked from the estuarine mouth or shelf and deposited them in the area with minimum currents. For the post-dam river dominated estuaries, fluvial sediments were deposited as a bay head delta and also scoured sediment were transported seaward, in some cases depositing as a mouth bar. These patterns suggest that the post-dam estuaries are susceptible to siltation and shoaling of the mouth which will require dredging to maintain navigability for any harbor developments. With respect to water quality, most scenarios in this study showed reduced SSC due to reduced currents. Together with nutrient inputs from the watershed, increased water clarity can result in algal blooms (Jeong et al., 2014) which may impact the benthic habitats and fisheries.

Investigation of alternative dam locations and discharge intervals in this study suggests that the estuarine dam always significantly impacts the estuary. Dams located further upstream beyond the resonance length with discharge intervals on the order of the tidal cycle period were found to most resemble the pre-dam estuaries in terms of tidal dynamics, discharge velocity, SSC, sediment fluxes, and depth. However, this dam location and operation, while minimizing the dam impact, limits the ability of the estuarine dam to block the salt intrusion and store freshwater which is in many cases their primary purpose. Nevertheless, while simplified idealized modeling provides a useful tool for understanding patterns in the estuarine response, in practice optimization of the dam location and discharge interval to reduce impacts to a specific estuary will depend the details of the estuary such as the more realistic geometry, forcing, and sediment sources.

## 4.3 Reliability of idealized estuary model

The idealized model appears to aid in understanding first-order impacts of estuarine dams with sluices gates for a range of estuarine types, dam locations, and discharge intervals. However, it should be noted that the estuarine geometry (mouth depth, mouth width, bottom slope, width convergence), estuarine forcing (semidiurnal tides, no waves, no seasonal or interannual discharge variation), and sedimentary aspects (non-cohesive sediment and short morphological time scales) shape the result.

As this study focused primarily on the along-channel dynamics, future research can increase our understanding by evaluating trends in the across-channel, vertical, and temporal dynamics. Furthermore, more research is needed to understand the reservoir. In this study, it is assumed that the inflow is constant and the reservoir is large, so the discharge interval is determined *a priori* by a dam operator. But in general, the upper bound for possible discharge interval is determined by the reservoir volume and freshwater inflow rate. In addition to its effect on the discharge interval, the reservoir is also coupled to the post-dam estuary by influencing the water quality entering the post-dam estuary (Jeong et al., 2014). Over long time scales, the reservoir can fill with sediments and particulate nutrients and then become a source for the downstream estuary (Palinkas et al., 2019). This research would help to better link the reservoir and post-dam estuary sub-environments.

Together with the reservoir, more research can be done on the different gate types. This appears to be important for estuarine dams which are located further upstream or function primarily as hydroelectric plants, weirs and locks. Examples include the Saco Dam on the Saco estuary, Maine (Kelley et al., 2005), the Federal Dam on the Hudson estuary, New York (Ralston et al., 2019), the Conowingo Dam on the Susquehanna estuary, Maryland (Palinkas et al., 2019), and the Franklin Lock and Dam on the Caloosahatchee estuary, Florida (Buzzelli et al., 2014) in the US. These examples fit the definition of an estuarine dam or weir here as they limit the upstream propagation of salt or tides. However, their structure and operation can be different from those applied in this study, with sluice gates discharging during ebb tide, which are found for example in Europe and Asia. This research on different structures and operation should

help to bridge the gap between the effects of estuarine and river dams and weirs on estuaries.

## 5 Conclusions

This study has extended the results of Figueroa et al. (2022) for the effect of an estuarine dam on SS, PM, PS, and WM estuaries to a range of dam locations and discharge intervals. It was confirmed that changes in these parameters resulted in systematic changes in the river and tidal processes which in turn resulted in changes in the estuarine classification, sediment dynamics, and morphodynamics. Some key findings of this research are:

- The dam location primarily impacted the tide-dominated estuaries, and the resonance length was an important length scale. When the dam was seaward of the resonance length, the tidal currents were strongly reduced due to tidal prism loss and the dead-end channel. When the dam was at the resonance length, the morphology adjusted and maintained tidal currents near the mouth, but tidal currents were reduced near the dam due to the dead-end channel. When the dam was landward of the resonance length, the tidal currents were mostly reduced near the dam due to the dead-end channel.
- The discharge interval primarily impacted the river-dominated estuaries, and the tidal cycle was an important time scale. When the discharge interval was less than the tidal cycle period, the estuaries maintained similar salinity and stratification. When the discharge interval was greater than the tidal cycle period, the estuaries began to experience notable seaward discharge pulses and discharge freshwater fronts.
- Dams located near the mouth with large discharge intervals, associated with large discharge magnitudes, differed the most from their pre-dam condition in the estuarine parameter space. Conversely, dams located near the estuary head with small discharge intervals, associated with small discharge magnitudes, differed the least from their pre-dam condition in the estuarine parameter space.
- Dams located near the mouth altered the sediment flux mechanisms the most for all estuaries. The river-dominated estuaries were characterized by a shift from landward flux due to estuarine exchange flow to seaward flux due to river runoff and tidal pumping by the intratidal discharge pulses. The tide-dominated estuaries were characterized by a shift from seaward flux due to Stokes return flow and tidal pumping due to Euler-induced tidal asymmetry to landward flux due to tidal pumping by tidal distortion and $M_2$-$M_4$ interaction in the shallow, macrotidal estuaries.

It is expected this research will be valuable as estuarine dams continue to be constructed (e.g., the Bhadbhut barrage on the Narmada River, India; The Times of India, 2021) and are likely to become more prevalent in the future as sea level rise increases the salt and tidal intrusions, in addition to potentially less river runoff in some areas and dredging to accommodate larger ships (Winterwerp and Wang, 2013; Nienhuis et al., 2018; Nienhuis and van de Wal, 2021).

## Data availability statement

The raw data supporting the conclusions of this article will be made available by the authors, without undue reservation.

## Author contributions

SF, conceptualization, data curation, formal analysis, funding acquisition, investigation, methodology, validation, and visualization. MS, data curation, funding acquisition, investigation, project administration, supervision, and validation. GL, conceptualization, data curation, investigation, methodology, and validation.

## Funding

This research was supported by research fund of Chungnam National University.

## Conflict of interest

The authors declare that the research was conducted in the absence of any commercial or financial relationships that could be construed as a potential conflict of interest.

## Publisher's note



## Supplementary material

The Supplementary Material for this article can be found online at: https://www.frontiersin.org/articles/10.3389/fmars.2022.1035501/full#supplementarymaterial

# References


Azevedo, I. C., Bordalo, A. A., and Duarte, P. M. (2010). Influence of river discharge patterns on the hydrodynamics and potential contaminant dispersion in the douro estuary (Portugal). *Water Res.* 44 (10), 3133–3146. doi: 10.1016/j.watres.2010.03.011

Burchard, H., and Hetland, R. D. (2010). Quantifying the contributions of tidal straining and gravitational circulation to residual circulation in periodically stratified tidal estuaries. *J. Phys. Oceanography* 40 (6), 1243–1262. doi: 10.1175/2010JPO4270.1

Burchard, H., Schuttelaars, H. M., and Ralston, D. K. (2018). Sediment trapping in estuaries. *Annu. Rev. Mar. Sci.* 10, 371–395. doi: 10.1146/annurev-marine-010816-060535

Buzzelli, C., Doering, P. H., Wan, Y., Sun, D., and Fugate, D. (2014). Modeling ecosystem processes with variable freshwater inflow to the caloosahatchee river estuary, southwest florida. i. model development. *Estuarine Coast. Shelf Sci.* 151, 256–271. doi: 10.1016/j.ecss.2014.08.028

Cai, H., Toffolon, M., and Savenije, H. H. (2016). An analytical approach to determining resonance in semi-closed convergent tidal channels. *Coast. Eng. J.* 58 (03), 1650009. doi: 10.1142/S0578563416500091

Díez-Minguito, M., Baquerizo, A., Ortega-Sánchez, M., Navarro, G., and Losada, M. A. (2012). Tide transformation in the guadalquivir estuary (SW Spain) and process-based zonation. *J. Geophysical Res.: Oceans* 117 (C3), C03019. doi: 10.1029/2011JC007344

Figueroa, S. M., Lee, G., Chang, J., and Jung, N. W. (2022). Impact of estuarine dams on the estuarine parameter space and sediment flux decomposition idealized numerical modeling study. *J. Geophysical Res.: Oceans*, 127 (5), e2021JC017829. doi: 10.1029/2021JC017829

Figueroa, S. M., Lee, G., Chang, J., Schieder, N. W., Kim, K., and Kim, S. Y. (2020b). Evaluation of along-channel sediment flux gradients in an anthropocene estuary with an estuarine dam. *Mar. Geol.* 429, 106318. doi: 10.1016/j.margeo.2020.106318

Figueroa, S. M., Lee, G., and Shin, H. J. (2019). The effect of periodic stratification on floc size distribution and its tidal and vertical variability: Geum estuary, south Korea. *Mar. Geol.* 412, 187–198. doi: 10.1016/j.margeo.2019.03.009

Figueroa, S. M., Lee, G., and Shin, H. J. (2020a). Effects of an estuarine dam on sediment flux mechanisms in a shallow, macrotidal estuary. *Estuarine Coast. Shelf Sci.* 238, 106718. doi: 10.1016/j.ecss.2020.106718

Friedrichs, C. T. (2010). Barotropic tides in channelized estuaries. *Contemp. Issues Estuar. Physics* 27, 61. doi: 10.1017/CBO9780511676567.004

Friedrichs, C. T., and Aubrey, D. G. (1988). Non-linear tidal distortion in shallow well-mixed estuaries: a synthesis. *Estuarine Coast. Shelf Sci.* 27 (5), 521–545. doi: 10.1016/0272-7714(88)90082-0

Geyer, W. R., and MacCready, P. (2014). The estuarine circulation. *Annu. Rev. Fluid Mechanics* 46 (1), 175–197. doi: 10.1146/annurev-fluid-010313-141302

Guo, L., Wang, Z. B., Townend, I., and He, Q. (2019). Quantification of tidal asymmetry and its nonstationary variations. *J. Geophysical Res.: Oceans* 124 (1), 773–787. doi: 10.1029/2018JC014372

Guo, L., Van der Wegen, M., Roelvink, J. A., and He, Q. (2014). The role of river flow and tidal asymmetry on 1-D estuarine morphodynamics. *Journal of Geophysical Research: Earth's Surface* 119(11), 2315–34. doi: 10.1002/2014JF003110

Haddout, S., and Maslouhi, A. (2019). Testing analytical tidal propagation models of the one-dimensional hydrodynamic equations in morocco's estuaries. *Int. J. River Basin Management* 17 (3), 353–366. doi: 10.1080/15715124.2018.1546721

Haidvogel, D. B., Arango, H., Budgell, W. P., Cornuelle, B. D., Curchitser, E., Di Lorenzo, E., et al. (2008). Ocean forecasting in terrain-following coordinates: Formulation and skill assessment of the regional ocean modeling system. *J. Comput. Physics* 227 (7), 3595–3624. doi: 10.1016/j.jcp.2007.06.016

Hoitink, A. J. F., and Jay, D. A. (2016). Tidal river dynamics: Implications for deltas. *Rev. Geophysics* 54 (1), 240–272. doi: 10.1002/2015RG000507

Jay, D. A., Leffler, K., Diefenderfer, H. L., and Borde, A. B. (2015). Tidal-fluvial and estuarine processes in the lower Columbia river: I. along-channel water level variations, pacific ocean to Bonneville dam. *Estuaries Coasts* 38 (2), 415–433. doi: 10.1007/s12237-014-9819-0

Jeong, Y. H., Yang, J. S., and Park, K. (2014). Changes in water quality after the construction of an estuary dam in the geum river estuary dam system, Korea. *J. Coast. Res.* 30 (6), 1278–1286. doi: 10.2112/JCOASTRES-D-13-00081.1

Kelley, J. T., Barber, D. C., Belknap, D. F., FitzGerald, D. M., van Heteren, S., Stephen, M., et al. (2005). Sand budgets at geological, historical and contemporary time scales for a developed beach system, saco bay, Maine, USA. *Mar. Geol.* 214 (1–3), 117–142. doi: 10.1016/j.margeo.2004.10.027

Kukulka, T., and Jay, D. A. (2003). Impacts of Columbia river discharge on salmonid habitat: 1. a nonstationary fluvial tide model. *J. Geophysical Res.: Oceans* 108 (C9), 3293. doi: 10.1029/2002JC001382

Laffaille, P., Caraguel, J. M., and Legault, A. (2007). Temporal patterns in the upstream migration of European glass eels (Anguilla anguilla) at the couesnon estuarine dam. *Estuarine Coast. Shelf Sci.* 73 (1-2), 81–90. doi: 10.1016/j.ecss.2006.12.011

Li, M., Ge, J., Kappenberg, J., Much, D., Nino, O., and Chen, Z. (2014). Morphodynamic processes of the Elbe river estuary, Germany: the Coriolis effect, tidal asymmetry and human dredging. *Front. Earth Sci.* 8 (2), 181–189. doi: 10.1007/s11707-013-0418-3

Milliman, J. D., and Farnsworth, K. L. (2013). *River discharge to the coastal ocean: A global synthesis* (Cambridge, Cambridge University Press). doi: 10.1017/CBO9780511781247

Moftakhari, H. R., Jay, D. A., and Talke, S. A. (2016). Estimating river discharge using multiple-tide gauges distributed along a channel. *Journal of Geophysical Research: Oceans* 121(4), 2078–97. doi: 10.1002/2015JC010983

Nauw, J. (2014). "Setup of a 3D hydrodynamic model of the Dutch western wadden Sea," in *NOIZ report*. Den Burg: Royal Netherlands Institute for Sea Research (NOIZ)

Nidzieko, N. J. (2010). Tidal asymmetry in estuaries with mixed semidiurnal/diurnal tides. *J. Geophysical Res.: Oceans* 115 (C8), C08006. doi: 10.1029/2009JC005864

Nidzieko, N. J., and Ralston, D. K. (2012). Tidal asymmetry and velocity skew over tidal flats and shallow channels within a macrotidal river delta. *J. Geophysical Res.: Oceans* 117 (C3), C03001. doi: 10.1029/2011JC007384

Nienhuis, J. H., Hoitink, A. J. F., and Törnqvist, T. E. (2018). Future change to tide-influenced deltas. *Geophysical Res. Lett.* 45 (8), 3499–3507. doi: 10.1029/2018GL077638

Nienhuis, J. H., and van de Wal, R. S. (2021). Projections of global delta land loss from sea-level rise in the 21st century. *Geophysical Res. Lett.* 48 (14), e2021GL093368. doi: 10.1029/2021GL093368

Palinkas, C. M., Testa, J. M., Cornwell, J. C., Li, M., and Sanford, L. P. (2019). Influences of a river dam on delivery and fate of sediments and particulate nutrients to the adjacent estuary: Case study of conowingo dam and Chesapeake bay. *Estuaries Coasts* 42 (8), 2072–2095. doi: 10.1007/s12237-019-00634-x

Pawlowicz, R., Beardsley, B., and Lentz, S. (2002). Classical tidal harmonic analysis including error estimates in MATLAB using T_TIDE. *Comput. Geosci.* 28 (8), 929–937. doi: 10.1016/S0098-3004(02)00013-4

Ralston, D. K., Talke, S., Geyer, W. R., Al-Zubaidi, H. A., and Sommerfield, C. K. (2019). Bigger tides, less flooding: Effects of dredging on barotropic dynamics in a highly modified estuary. *J. Geophysical Res.: Oceans* 124 (1), 96–211. doi: 10.1029/2018JC014313

Savenije, H. H. (2005). *Salinity and tides in alluvial estuaries* (New York: Elsevier). doi: 10.1016/B978-0-444-52107-1.X5000-X

Schuttelaars, H. M., de Jonge, V. N., and Chernetsky, A. (2013). Improving the predictive power when modelling physical effects of human interventions in estuarine systems. *Ocean Coast. Management* 79, 70–82. doi: 10.1016/j.ocecoaman.2012.05.009

Shin, H. J., Lee, G., Kang, K., and Park, K. (2019). Shift of estuarine type in altered estuaries. *Anthropocene Coasts* 2 (1), 145–170. doi: 10.1139/anc-2018-0013

Shivaprasad, A., Vinita, J., Revichandran, C., Manoj, N. T., Srinivas, K., Reny, P. D., et al. (2013). Influence of saltwater barrage on tides, salinity, and chlorophyll a in Cochin estuary, India. *J. Coast. Res.* 29 (6), 1382–1390. doi: 10.2112/JCOASTRES-D-12-00067.1

Syvitski, J. P., Vorosmarty, C. J., Kettner, A. J., and Green, P. (2005). Impact of humans on the flux of terrestrial sediment to the global coastal ocean. *Science* 308 (5720), 376–380. doi: 10.1126/science.1109454

Syvitski, J. P., and Kettner, A. (2011). Sediment flux and the Anthropocene. *Jphilosophical transactions of the royal society a: Mathematical, physical and engineering sciences* 369(1938), 957–975. doi: 10.1098/rsta.2010.0329

Tabata, K., and Fukuoka, S. (2014). "*New computation method for flood flows and bed variations in a low-lying river with complex river systems*," in River Flow. Eds. A. J. Schleiss, J. Cesare De, M. J. Franca and M. Pfister (London: Taylor & Francis Group), 1791–98.

The Times of India (2021) *Bhadbhut barrage to be ready by 2025*. Available at: https://timesofindia.indiatimes.com/city/surat/bhadbhut-barrage-to-be-ready-by-2025/articleshow/85699621.cms (Accessed 25 August 2022).

Tilai, L., Liming, C., Xiangyu, G., and Lei, D. (2019). "Analysis of sediment deposition downstream tidal sluice of estuary," in *International conference on Asian and pacific coasts* (Singapore: Springer), 649–655. doi: 10.1007/978-981-15-0291-0_89

Traini, C., Proust, J. N., Menier, D., and Mathew, M. J. (2015). Distinguishing natural evolution and human impact on estuarine morpho-sedimentary development: A case study from the vilaine estuary, France. *Estuarine Coast. Shelf Sci.* 163, 143–155. doi: 10.1016/j.ecss.2015.06.025

Uncles, R. J., and Jordan, M. B. (1980). A one-dimensional representation ofresidual currents in the Severn estuary and associated observations. *Estuar. Coast. Mar. Sci.* 10 (1), 39–60. doi: 10.1016/S0302-3524(80)80048-X

van der Spek, A. J., and Elias, E. P. (2021). Half a century of morphological change in the haringvliet and grevelingen ebb-tidal deltas (SW netherlands)-impacts of large-scale engineering 1964–2015. *Mar. Geol.* 432, 106404. doi: 10.1016/j.margeo.2020.106404

van Proosdij, D., Milligan, T., Bugden, G., and Butler, K. (2009). A tale of two macro tidal estuaries: differential morphodynamic response of the intertidal zone to causeway construction. *J. Coast. Res.*, SI 56, 772–776. Available at: https://www.jstor.org/stable/25737683.

Vongvisessomjai, S., and Srivihok, P. (2003). The interaction between tide and salinity barriers. *Songklanakarin J. Sci. Technol.* 25 (6), 744. Available at: http://rdo.psu.ac.th/sjst/journal/Sp1-natural-disaster/01042008/No14-06tide_barrier-157-170.pdf.

Vongvisessomjai, S., Weesakul, S., and Srivihok, P. (2003). Water level change by tidal regulator in the bang Nara river. *Songklanakarin J. Sci. Technol.* 25 (6), 757–771. Available at: http://rdo.psu.ac.th/sjst/journal/Sp1-natural-disaster/02042008/No15-07water_BangNara-181-195.pdf.

Warner, J. C., Armstrong, B., He, R., and Zambon, J. B. (2010). Development of a coupled ocean–atmosphere–wave–sediment transport (COAWST) modeling system. *Ocean Modelling* 35 (3), 230–244. doi: 10.1016/j.ocemod.2010.07.010

Warner, J. C., Sherwood, C. R., Signell, R. P., Harris, C. K., and Arango, H. G. (2008). Development of a three-dimensional, regional, coupled wave, current, and sediment-transport model. *Comput. Geosci.* 34 (10), 1284–1306. doi: 10.1016/j.cageo.2008.02.012

Williams, J. R., Dellapenna, T. M., and Lee, G. (2013). Shifts in depositional environments as a natural response to anthropogenic alterations: Nakdong estuary, south Korea. *Mar. Geol.* 343, 47–61. doi: 10.1016/j.margeo.2013.05.010

Williams, J. R., Dellapenna, T. M., Lee, G., and Louchouarn, P. (2014). Sedimentary impacts of anthropogenic alterations on the yeongsan estuary, south Korea. *Mar. Geol.* 357, 256–271. doi: 10.1016/j.margeo.2014.08.004

Winterwerp, J. C., and Wang, Z. B. (2013). Man-induced regime shifts in small estuaries–I: theory. *Ocean Dynamics* 63 (11), 1279–1292. doi: 10.1007/s10236-013-0662-9

Ye, Q. (2006). *Modelling of cohesive sediment transportation, deposition and resuspension in the haringvliet mouth* (Delft, Netherlands: UNESCO-IHE Institute for Water Education).

Zhu, Q., Wang, Y. P., Gao, S., Zhang, J., Li, M., Yang, Y., et al. (2017). Modeling morphological change in anthropogenically controlled estuaries. *Anthropocene* 17, 70–83. doi: 10.1016/j.ancene.2017.03.001

frontiers | Frontiers in Marine Science

TYPE Original Research
PUBLISHED 08 December 2022
DOI 10.3389/fmars.2022.1017434



OPEN ACCESS

EDITED BY
Daidu Fan,
Tongji University, China

REVIEWED BY
Silvia Newell,
Wright State University, United States
Lijun Hou,
East China Normal University, China

*CORRESPONDENCE
Soonmo An
sman@pusan.ac.kr

SPECIALTY SECTION
This article was submitted to Marine Ecosystem Ecology, a section of the journal Frontiers in Marine Science

RECEIVED 12 August 2022
ACCEPTED 17 November 2022
PUBLISHED 08 December 2022

CITATION
Lee J and An S (2022) High ammonium recycling in an anthropogenically altered Yeongsan River Estuary, South Korea. *Front. Mar. Sci.* 9:1017434. doi: 10.3389/fmars.2022.1017434



# High ammonium recycling in an anthropogenically altered Yeongsan River Estuary, South Korea

Jiyoung Lee[1] and Soonmo An[2]*

[1]Marine Environment Research Division, National Institute of Fisheries Science, Busan, South Korea, [2]Division of Earth Environmental System, Pusan National University, Busan, South Korea

Regenerated nitrogen (N) cycling was studied in a turbid and nutrient-rich estuary located in the southeast region of the Yellow Sea (Yeongsan River Estuary; YRE), in order to elucidate the biogeochemical consequences of coastal development. Ammonium regeneration and potential uptake rates were measured from March 2012 to June 2013 using $^{15}N$ tracer techniques. Size fractionation suggested that small-sized bacteria (<0.7 µm), rather than zooplankton, were responsible for most of the ammonium regeneration. Intermittent freshwater discharge events might have prevented stable zooplankton community development and caused the insignificant role of zooplankton in ammonium regeneration. Ammonium regeneration and potential uptake rates were relatively high (0.1–1.2 and 0.2–1.5 µmol $L^{-1}$ $h^{-1}$, respectively), and were highest during summer. Ammonium turnover times were shorter than water residence times throughout the study period. These results indicate that ammonium is actively recycled and is likely to supply enough N required to sustain the high primary productivity observed in the YRE (50%–450%). Reduced turbidity and increased water residence times caused by the construction of an estuarine dam in the YRE have probably resulted in the formation of optimal conditions for the high ammonium regeneration.

KEYWORDS

**Yeongsan River estuary, estuarine dam, nitrogen cycling, ammonium regeneration, isotope dilution experiments, primary productivity**

## Introduction

The Yellow Sea is a shallow marginal sea situated between mainland China and the Korean Peninsula. Increased anthropogenic nitrogen (N) inputs to coastal regions from rivers in China and the Korean Peninsula stimulate eutrophication, trigger the formation of hypoxic zones, and influence the structure and functioning of these coastal ecosystems

(Wei et al., 2007; Zhang et al., 2007; Rabalais et al., 2010; Hyun et al., 2020). However, ecological responses to N inputs in this region have been poorly studied.

The ecological implications of N loading in an estuary depend on the estuary's physical and biogeochemical characteristics (Heip et al., 1995; An and Gardner, 2002; Middelburg and Herman, 2007; Bianchi, 2007). Dissolved inorganic N (DIN) inputs from land, usually in the form of nitrate ($NO_3^-$) are assimilated into particulate organic N (PON) during autochthonous production; some of the PON is recycled into DIN during microbial regeneration, usually in the form of ammonium ($NH_4^+$). The degree of $NO_3^- \rightarrow$ PON $\rightarrow NH_4^+$ conversion may be important for primary productivity because ammonium is the preferred N source for phytoplankton (McCarthy et al., 1977). Many studies have reported that the uptake and turnover rates of ammonium in estuarine environments are higher than those of nitrate (Middelburg and Nieuwenhuize, 2000a; Yuan et al., 2012).

Ammonium regeneration is mainly mediated by bacteria, protozoa and zooplankton. The contribution of bacteria to water column ammonium regeneration differed according to the coastal characteristics such as the temperature, plankton community structure and supply of microbial substates (Gardner et al., 1997; Jochem et al., 2004). For example, Picoplankton (mainly associated with bacteria) contributed significantly to ammonium regeneration during the summer (20-45%), while nanoplankton (mainly associated with ciliates) accounted for 83-88% of the regeneration in winter in the shallow well-mixed water (Maguer et al., 1999). Maguer et al. (1999) suggested that the contribution of picoplankton versus nanoplankton to total ammonium regeneration is regulated by seasonal planktonic community structure. Regenerated ammonium is consumed by processes such as nitrification and assimilation of phytoplankton and heterotrophic bacteria. Photosynthetic ammonium uptake tends to be light-dependent, whereas heterotrophic uptake is largely regulated by the availability of organic substrates (Gardner et al., 2004). The relative importance of ammonium uptake between phytoplankton and heterotrophic bacteria can be demonstrated by light-dark incubations. (Gardner et al., 2004; McCarthy et al., 2009, 2013). In several aquatic systems including Mississippi River plume, Lake Champlain, Western Lake Erie, the light ammonium uptake rates were higher than dark rates suggesting that predominance of photosynthetic uptake (Jochem et al., 2004; McCarthy et al., 2013; Hoffman et al., 2022).

Nutrients and grazing are generally the most important factors controlling phytoplankton productivity and biomass at the ocean surface (Tilman et al., 1982; Armstrong, 1994). However, physical factors, such as light availability, vertical mixing, and freshwater flushing, are also significant (Alpine and Cloern, 1988; Mallin and Paerl, 1992; Sin et al., 1999). The coastal waters of the western Korean Peninsula adjacent to the Yellow Sea are eutrophic; however, algal blooms are relatively rare in the region despite the high nutrient levels (Kim et al., 2013; Park et al., 2013). The rarity of algal blooms may be due to the high turbidity (and low light levels) caused by the high input of suspended solids from rivers and resuspension by the macrotidal (10 m range) regime (Son et al., 2005; Byun et al., 2007). In estuaries with low, rapidly changing light conditions, the N form (nitrate versus ammonium) may be important because nitrate (as an oxidized chemical species) is less likely to be coupled to primary productivity (Middelburg and Nieuwenhuize, 2000a; Yuan et al., 2012).

The Yeongsan River Estuary (YRE) is located in the southeastern Yellow Sea and receives high nutrient loads from a highly populated area (Gwangju; population 1.5 million) and as a result of agricultural practices. A dam was constructed at the mouth of the YRE in 1981 to secure freshwater for agricultural and industrial use (Yim et al., 2018). A large artificial lake was formed, with poor water quality (Lee et al., 2009). The characteristics of the estuary also changed dramatically after the dam construction, which caused reduced water circulation (Cho et al., 2004). The estuary is a tide-dominated, shallow, semi-enclosed bay with intermittent freshwater discharge regulated by dam sluice gates, which affect the physical and biogeochemical characteristics such as current, turbidity, nutrient concentration, and plankton dynamics (2015; Byun et al., 2004; Cho et al., 2009; Sin et al., 2013; Sin and Jeong, 2020).

Like other estuaries adjacent to the Yellow Sea, primary production in the YRE is controlled by physical factors, including vertical mixing, the concentrations of suspended solids, and temperature (Byun et al., 2007). However, the YRE has a higher primary productivity (36–8900 mg C $m^{-2}$ $d^{-1}$; Lee et al., 2011; Sin et al., 2015) than other adjacent estuaries without dams, most likely because turbidity is generally lower due to reduced tidal resuspension near the dam. Summer hypoxia has been reported in the bottom layer of the YRE, which is an unusual finding for a macrotidal estuary (Lim et al., 2006).

This study aims to estimate the ammonium regeneration and potential uptake rates in the YRE by measuring changes in ammonium isotope ratios (Gardner et al., 1995; An et al., 2013) during incubation experiments. An additional goal is to improve the understanding of N recycling in the YRE, where a combination of artificial (high anthropogenic N loads, dam construction) and natural (macrotidal regime, high suspended sediment loads) perturbations co-occur, and to examine how dam construction may alter N cycling in an estuarine system.

# Materials and methods

## Study area

The Yeongsan River (drainage area 3455 $km^2$, length 129 km) is one of the four major rivers in South Korea that flow into the Yellow Sea. An estuarine dam was constructed,

inside the dam, an artificial freshwater lake (the Youngsan Lake) was created. Youngsan Lake has experienced massive sediment accumulation since the dam was constructed (33.6% reduction of the total water storage capacity) (Lee et al., 2009). Restriction of tidal circulation and loading of anthropogenic nutrients and organic compounds from upstream have transformed the area into a eutrophic lake with frequent occurrences of algal blooms and oxygen depletion in the bottom waters (Lee et al., 2009). Outside the dam, a semi-enclosed bay (the YRE) was created. the YRE (2 km wide, 7 km long, average depth 14 m; Figure 1) has a semi-diurnal tidal cycle, with mean spring and neap ranges of approximately 6 and 3 m, respectively. Annual mean precipitation in the region is 1322 mm, and the estuary's annual mean freshwater discharge is approximately 1.5 billion $m^3$. More than half of this precipitation is concentrated in the summer monsoon season (July and August); therefore, freshwater discharge occurs mostly during summer (>80% of annual discharge; Cho et al., 2004). The estuary's vertical temperature and salinity profiles are homogeneous until early June, due to vertical mixing. Thermohaline stratification occurs in summer as a result of increased surface temperatures and warmer freshwater discharges (Cho et al., 2004). This summer stratification is disrupted by heavy freshwater discharges, but redevelops quickly (in approximately two days) after cessation of discharge (Cho et al., 2014).

## Experimental and analytical procedures

Isotope dilution experiments were conducted five times between March 2012 and June 2013 at St. 2 in the YRE (34° 47'21.86", 12626'23.06"; Figure 1) to estimate seasonal variations in ammonium recycling rates. Water samples for incubation experiments were collected 4–7 days after a freshwater discharge: salinities were similar to the outer estuarine bay (Table 1). Isotope dilution experiments were conducted as described in previous studies (Gardner et al., 1997; Jochem et al., 2004; McCarthy et al., 2013). Briefly, surface water samples were collected in Niskin bottles (at a sampling depth of 0.5 m) and spiked with $^{15}NH_4^+$ to achieve a final concentration of 8 μM (98 atom%; $^{15}NH_4Cl$, Sigma-Aldrich). Water Samples were divided into six clear polystyrene culture bottles (75 $cm^2$; SPL Lifesciences). Each experiment was performed in triplicate in light and dark (wrapped in aluminum foil) bottles. The bottles were floated on the surface of the sampling station and incubated for 24 h. Subsamples were collected from each sample after $^{15}NH_4^+$ addition (0 h) and after the incubation intervals. Subsamples were filtered over a 0.2 μm nylon filter (Whatman puradisc syringe filter); the resulting filtrates were collected in 10 ml glass vials (Wheaton) and frozen immediately. In June 2013, ammonium recycling rates were measured in three size fractions (whole fraction,<200 μm,<0.7 μm) to assess the contribution of phytoplankton and zooplankton to ammonium recycling (Jochem et al., 2004). The collected water samples were filtered using a 200 μm stainless steel sieve or Whatman GFF glass-fiber filters (0.7 μm pore size). Each filtrate (<200 μm and<0.7 μm) and unfiltered water sample was then treated according to the procedure described above.

Ammonium isotope ratios and concentrations were measured by high-performance liquid chromatography (HPLC) using a cation-exchange column as described in Gardner et al. (1995), but with a modified procedure using updated HPLC pumps as described in An et al. (2013). Ammonium regeneration and potential uptake rates were calculated from changes in ammonium concentration and isotope ratios over time, using the Blackburn–Caperon model (Blackburn, 1979; Caperon et al., 1979).

In the natural-light incubations in July 2012 and June 2013, ammonium was exhausted by the end of the 24 h incubation period; thus, the uptake and regeneration rates could not be

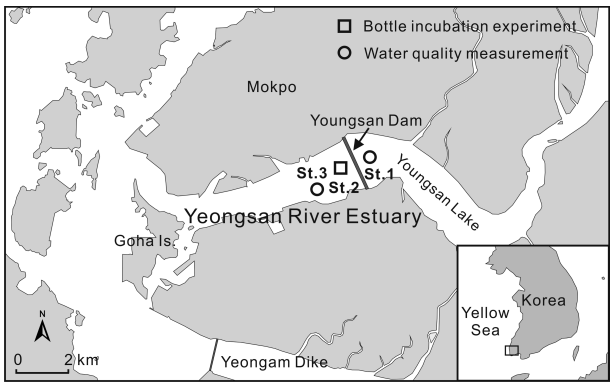


FIGURE 1
Locations of the study sites in the YRE. Water quality data for Sts. 1 and 3 were archived from the National Institute of Environmental Research and the Marine Environment Information System, respectively.

TABLE 1. Seasonal variations in temperature, salinity, ammonium concentration, nitrate + nitrite, ammonium/nitrate + nitrite ratios, dissolved inorganic phosphate (DIP), and DIN:DIP ratio during 2000–2013 obtained from Marine Environment Information System (St. 3) and the sampling periods in the YRE (St. 2).

| Properties | | Seasonal mean and range | | | | Sampling periods | | | | |
|---|---|---|---|---|---|---|---|---|---|---|
| | | Winter(Feb.) | Spring(May) | Summer(Aug.) | Fall(Nov.) | 15 Mar 2012 | 30 Apr 2012 | 30 Jul 2012 | 22 Oct 2012 | 10 Jun 2013 |
| Temperature (℃) | Average(SD) | 5(1) | 16(1) | 27(1) | 16(1) | 7.9 | 12.4 | 25.9 | 19.5 | 18.3 |
| | Range | 4~8 | 14~19 | 24~29 | 13~18 | | | | | |
| Salinity | Average(SD) | 30(2) | 28(6) | 22(8) | 31(2) | 30.0 | 31.1 | 26.9 | 28.4 | 31.2 |
| | Range | 25~32 | 9~33 | 7~29 | 24~33 | | | | | |
| Ammonium (μM) | Average(SD) | 2(2) | 7(12) | 2(2) | 2(2) | 16.6 | 12.2 | 0.3 | 18.0 | 0.7 |
| | Range | 0~6 | 0~41 | 0~7 | 0~7 | | | | | |
| Nitrate+Nitrite (μM) | Average(SD) | 16(10) | 23(28) | 36(40) | 16(6) | 27.0 | 20.9 | 8.3 | 6.2 | 9.9 |
| | Range | 1~36 | 1~95 | 0~119 | 7~33 | | | | | |
| $NH_4^+/(NO_3^-+NO_2^-)$ | Average(SD) | 0.1(0.1) | 1.2(3.5) | 0.4(0.8) | 0.2(0.2) | 0.6 | 0.6 | 0.0 | 2.9 | 0.1 |
| | Range | 0.0~0.3 | 0.0~13.4 | 0.0~2.9 | 0.0~0.6 | | | | | |
| DIP (μM) | Average(SD) | 0.4(0.4) | 0.3(0.2) | 0.7(0.7) | 0.9(0.3) | | | | | |
| | Range | 0.1~1.0 | 0.0~0.7 | 0.0~2.1 | 0.6~1.4 | | | | | |
| DIN:DIP ratio | Average(SD) | 98(79) | 825(1754) | 74(42) | 22(5) | | | | | |
| | Range | 17~230 | 22~4795 | 19~130 | 17~30 | | | | | |

obtained for these samples. However, minimum uptake rates were estimated from the initial ammonium concentrations of these samples and the regeneration rates of the dark incubations.

Sufficient amounts of $^{15}NH_4^+$ were added to the samples to prevent nutrient exhaustion over the incubation period (Gardner et al., 1997; McCarthy et al., 2013). In March, May, and October 2012, the added $^{15}NH_4^+$ was 44%–65% of the ambient levels. In contrast, in July 2012 and June 2013, when ambient ammonium levels were very low, $^{15}NH_4^+$ additions were 1100%–2800% of the ambient levels. The regeneration rates obtained in this study are considered to be the actual rates, as high-level nutrient addition should not affect regeneration rates (Blackburn, 1979), whereas uptake rates are regarded as potential rates (Gardner et al., 1997).

The ammonium and nitrate + nitrite concentrations of collected water samples at St. 2 were determined spectrophotometrically (Strickland and Parsons, 1972; Jones, 1984).

In order to find out the biogeochemical properties of Yeongsan Lake surface water that affects the study area, inorganic nutrient concentration (nitrate plus nitrite, ammonium, dissolved inorganic phosphorus [DIP]) data at St. 1 for 2002–2013 were obtained from the National Institute of Environmental Research (http://water.nier.go.kr) (Figure 2). Physico-chemical data at St. 3 near the survey point were also archived on the Marine Environment Information System (MEIS: http://www.meis.go.kr) website (Table 1). DIP data represented in this study were measured as soluble reactive

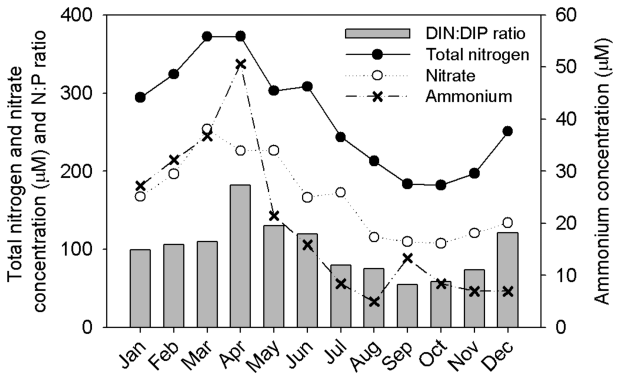


FIGURE 2
Monthly concentration variations in total nitrogen, inorganic nitrogen, and DIN:DIP ratios near the inside of the dam (Yeongsan Lake; St. 1), obtained from the National Institute of Environmental Research (http://water.nier.go.kr).

phosphates (Strickland and Parsons, 1972). t test was conducted to explore the difference between light/dark and size-fraction incubation (whole fraction,<200 μm,<0.7 μm) of the regeneration and uptake rates. Regression analysis was also performed to assess the relationship between temperature with the regeneration and uptake rates. All statistical analyses were carried out using SPSS v20.0.

# Results

During the incubation experiments, DIN concentrations were comparable to seasonal values in the YRE (Table 1). Nitrate + nitrite concentrations were usually high with large fluctuations in surface water throughout the year. On average, seasonal ammonium concentrations were an order of magnitude lower than those of nitrate (Table 1). However, the ammonium concentrations during the study period were usually higher than the seasonal mean value (Table 1). Surface-water nitrate concentrations were generally within the seasonal range obtained by MEIS (St. 3), whereas ammonium concentrations exceeded the seasonal range in spring and fall, and were less than 1 μM in summer (June and July). The average seasonal concentration of DIP was low, not exceeding 1 μM, and nutrient exhaustion was observed in the surface water in spring and summer. The DIN : DIP ratio exceeded the Redfield ratio all year round. The DIN : DIP ratio was highest in spring surface water, averaging 825, and was lowest in the fall, although still higher than the Redfield ratio of 16:1.

To identify the riverine input of nutrients into YRE, the monthly variations in total nitrogen, DIN, and DIN : DIP ratio near the inside of the dam were shown using data from the National Institute of Environmental Research (Figure 2). At St.1, the total and inorganic N concentrations tended to be high in spring (Figure 2). Inorganic N concentrations were high during all seasons, with ammonium and nitrate concentrations of approximately 10 and 100 μM, respectively, even during the summer, when the concentrations were at their lowest. The ratios of nitrate and ammonium to total N were 56%–88% and 2%–14%, respectively. The DIN : DIP ratio (55–182) at St. 1 was higher than the Redfield ratio (Figure 2). We calculated the DIN flux into the estuary through the dam sluice gates based on the DIN concentrations of the Yeongsan Lake and of the freshwater discharge. The DIN flux was 110–682 ton $mon^{-1}$. DIN loading into the surveyed area was highest in summer.

Ammonium uptake rates varied with seasonal temperature and were highest in July 2012 (light uptake versus temperature, $r^2$ = 0.57; dark uptake versus temperature, $r^2$ = 0.59). Ammonium uptake rates were higher in light incubations than in the dark (Figure 3A), although the difference was only statistically significant in July 2012 ($P< 0.001$) and June 2013 ($P< 0.05$). Light enhancement (light uptake − dark uptake)/light uptake) ranged from 47% to 66%. Light uptake was significantly lower in the<0.7 μm fraction than in the whole fraction ($P = 0.008$) in June 2013 (Figure 3A). Uptake in the<0.7 μm fraction was similar in both light and dark incubations; light enhancement was not observed in this size fraction. Potential uptake rates among the size fractions were not significantly different in the dark incubations (Figure 3B).

Identification of seasonal trends of ammonium regeneration over the entire survey period was difficult due to the absence of light data for July 2012 and June 2013. A direct light effect may be insignificant for regeneration because ammonium is mainly regenerated by processes such as dissimilatory bacterial respiration and zooplankton excretion. The dark rate is therefore thought to explain ammonium regeneration by the plankton community in the surveyed area. Ammonium regeneration rates in the dark incubation were 0.1–1.2 μmol $L^{-1}$ $h^{-1}$, with the maximum rate recorded in July 2012 (Figure 4A). Dark regeneration was positively correlated with temperature ($r^2$ = 0.54). Light regeneration rates tended to be higher than dark rates in spring and fall, although this difference was not statistically significant (Figure 4A). Size-fractionated dark regeneration rates (total plankton community,<200 μm, and<0.7 μm size classes) also exhibited no significant differences (Figure 4B).

To assess changes in the turbidity of the surveyed area caused by dam construction, annual mean values of the suspended sediment concentration were compared for the period prior to construction (one year's worth of data; 1976), during construction (1979–1981), and after construction of the dam until 2013 (MEIS, 1997–2013; NFRDA, 1983; Moon et al., 1991). The turbidity of the sampled area decreased after dam construction (Figure 5). Before construction, the annual average suspended sediment concentration of the Mokpo coast was 86.9 mg $l^{-1}$; this decreased by 48% during construction, averaging 45.5 mg $l^{-1}$ (NFRDA, 1983; Moon et al., 1991). After construction, the annual average turbidity range was greatly reduced to 9.9–32.3 mg $l^{-1}$, one-quarter (63%–92% decrease) of pre-construction levels (MEIS, 1997–2013). From 1984 until the present, similar levels have persisted. The range of turbidity variation has also decreased compared to the pre-construction values (Figure 5).

# Discussion

## N:P stoichiometry in the YRE

The surface waters of the study area were rich in nitrate throughout the year, and ammonium was only exhausted in summer (Table 1). The relatively high levels of nitrate in the YRE surface waters appeared to be related to high N loading from upstream areas, which contain farmland, livestock, and large cities (Lee, 2015; Figure 2). The YRE DIN : DIP ratio was higher than the Redfield ratio throughout the year (Table 1). Studies of nutrient-uptake kinetics have suggested that a dissolved N:P ratio of higher than 20–30 indicates a potential P limitation on phytoplankton growth (Goldman et al., 1979; Justic et al., 1995).

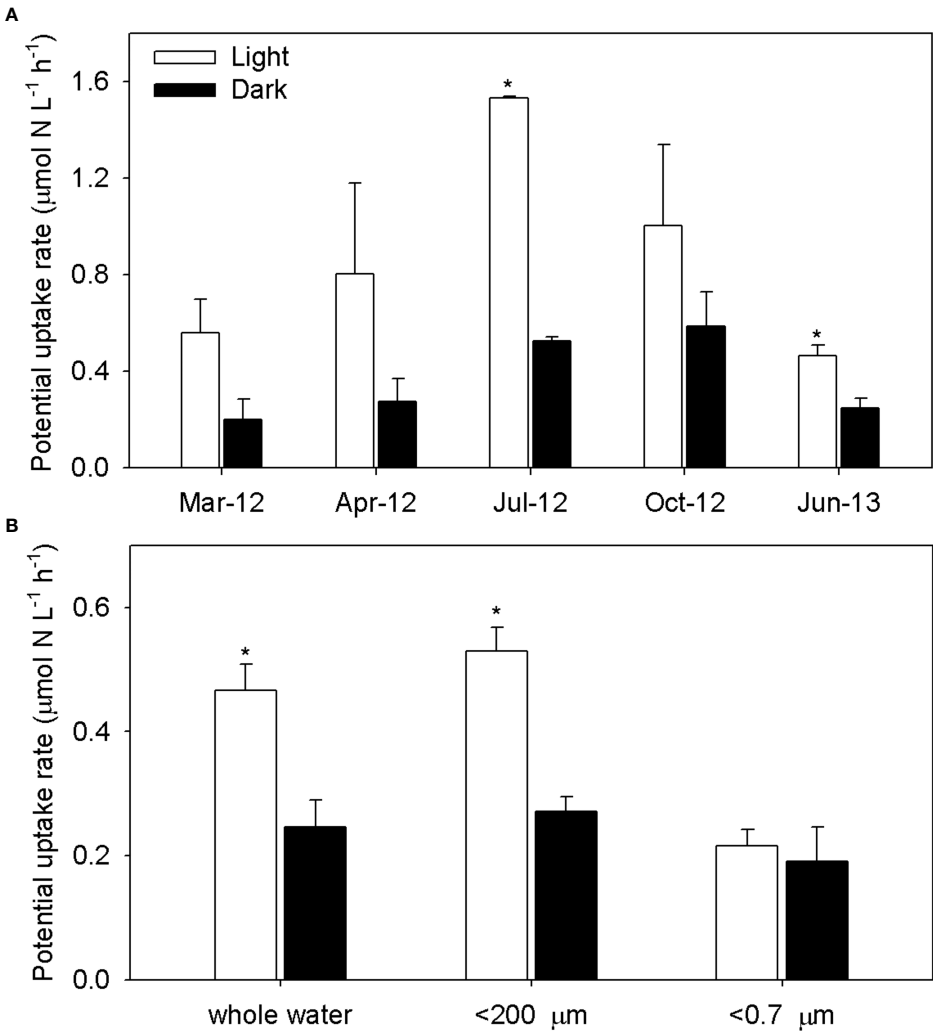


FIGURE 3
Ammonium potential uptake rates for whole-water samples **(A)** and size-fractioned (whole, <200 μm, and <0.7 μm) water samples **(B)** in light and dark treatments in the YRE. The * indicates a minimum value estimated from the initial ammonium concentration and regeneration rates in dark incubations.

Although N is a very important limiting element for primary production in oceanic environments, this is not true for all coastal environments, for example, P limitation (N:P ratio of 200:1) has been reported for the coastal area of the Pearl River Estuary in the South China Sea and North Sea estuaries (Yin et al., 2001; Howarth and Marino, 2006). P limitations in the YRE appear to be the result of enhanced controls on P input from metropolitan areas, coupled with extremely high N input from the agricultural sector (Howarth and Marino, 2006).

However, there is a limit to determining the nutrient limitation only by the N:P ratio in the rapidly changing YRE environment. Which nutrients are limiting or co-limiting factors for phytoplankton growth can change dynamically throughout the year and among years (Fisher et al., 1992; Wu et al., 2017). In a previous study of nutrient limitation in the YRE, although P limitation was predominant estimated through the N:P ratio, bioassay experiments showed that phytoplankton growth was regulated by P inputs from winter to spring, while N played a more dominant controlling role in fall. No nutrient limitation was observed during summer in the YRE (Yoon, 2012; MOF, 2014). In this study, the results of winter with a relatively high N:P ratio and autumn with the lowest values showed similar tendencies to those of Yoon (2012).

The YRE is highly affected by eutrophic freshwater with high N:P ratio discharged from the Youngsan Lake (Figure 2). During the non-discharge period, the N:P ratio and limiting nutrients of phytoplankton can be changed by biogeochemical processes such as recycling of nutrients and sediment-water nutrient

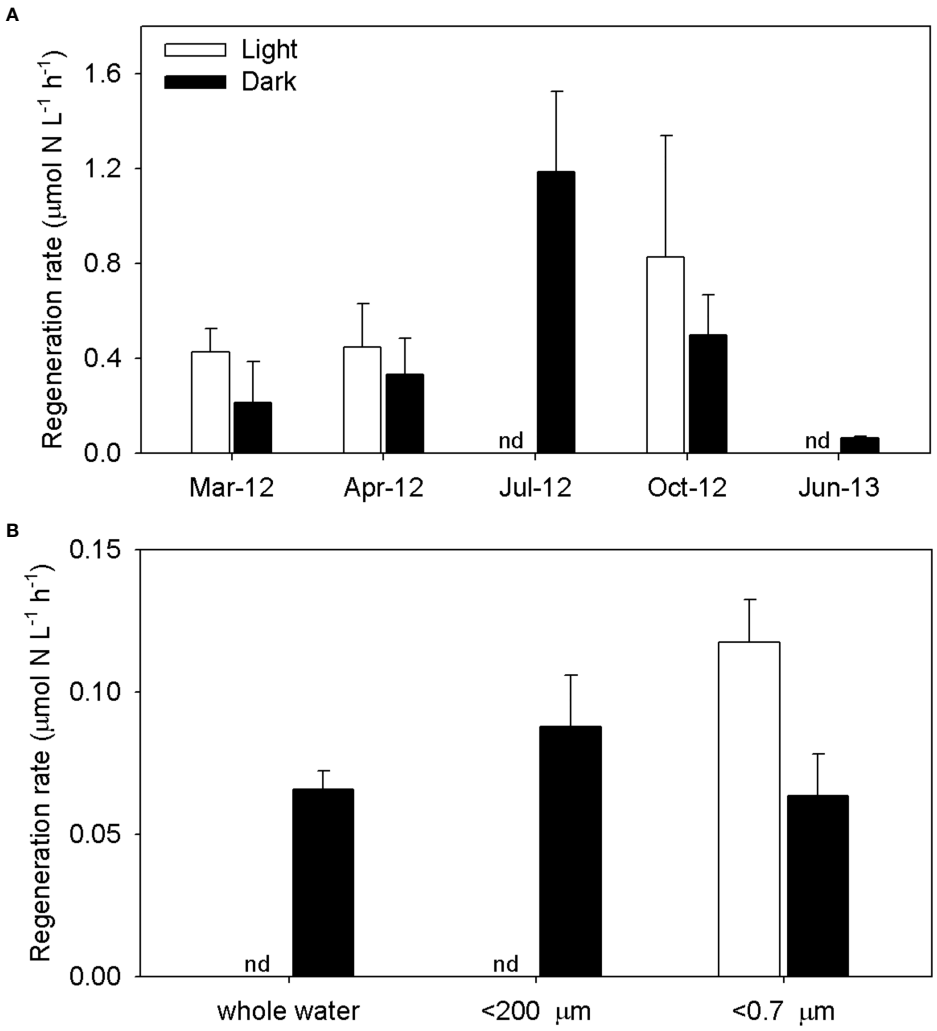


FIGURE 4
Ammonium regeneration rates for whole-water samples **(A)** and size-fractioned (whole, <200 μm, and <0.7 μm) water samples **(B)** in light and dark treatments in the YRE; nd, no data.

exchange within the estuary (Finlay et al., 2013; Wu et al., 2017; Zhou et al., 2022). In this study, active recycling of ammonium in summer can supply sufficient N demand for primary production and is expected to affect the N:P stoichiometry (see the discussion of 'Implications of estuarine dam on ammonium recycling' below). In order to more accurately determine the role of N and P on phytoplankton growth in YRE, further studies are needed in the future, including the biogeochemical processes of N and P.

## Ammonium regeneration in the water column

Although results for natural-light ammonium regeneration by size-fractionated plankton were not obtained, the dark regeneration rates from the size-fraction experiments can provide clues as to which plankton communities mediate ammonium regeneration, as heterotrophic organisms do not generally require light energy for such processes (Wheeler et al., 1989; Gardner et al., 1997). The similarity in dark ammonium regeneration rates between the whole-water and<0.7 μm fractions (Figure 4B) suggests that in early summer, most of the ammonium is regenerated by small bacteria, whereas zooplankton excretion is less important. Similar observations have been reported for the Mississippi River plume (Jochem et al., 2004) and the western English Channel (Maguer et al., 1999). In the Mississippi River plume, no differences were observed between ammonium regeneration rates in whole-water samples and the<2 μm size fraction at several sites along a salinity gradient, indicating that bacterial mineralization was important to the ammonium recycling process (Jochem et al.,

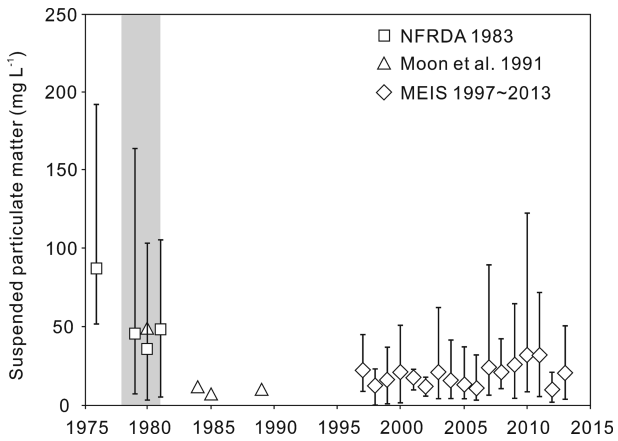


FIGURE 5
Annual mean values and ranges of suspended sediment concentrations for one year prior to (1976), during (1979–1981, shaded area), and after dam construction, until 2013 (MEIS 1997–2013; NFRDA 1983; Moon et al., 1991).

2004). Maguer et al. (1999) reported that picoplankton contribute significantly to ammonium regeneration during summer in the shallow, well-mixed waters of the English Channel. The less significant role of zooplankton in ammonium regeneration may be the result of abrupt freshwater discharges, as sudden changes in salinity and concentration of suspended solids during discharge events may be accompanied by changes in plankton species composition and substantial decreases in zooplankton biomass (Seo, 2008; Sin et al., 2013). Sin et al. (2013) suggested that phytoplankton and zooplankton that accumulate in an estuary during a non-discharge period can be flushed from the estuary by intermittent freshwater discharge events because the freshwater residence time (0.2–2.03 days; Lee and Jun, 2009) is lower than the phytoplankton doubling time (0.56–5.8 days; Sin et al., 2013). Moreover, although the phytoplankton biomass recovers within several days, the zooplankton respond more slowly (MOF, 2014). These intermittent discharges into the YRE, which create an environment that is unsuitable for stable zooplankton populations, may be one reason why ammonium regeneration by zooplankton excretion is not important in this estuary.

Light effects on heterotrophic nutrient regeneration are less obvious than those on autotrophic nutrient uptake (phytoplankton; Wheeler et al., 1989; Gardner et al., 1997). However, previous studies have shown that ammonium regeneration can be enhanced in light incubations (Gardner et al., 1997; James et al., 2011). James et al. (2011) demonstrated that ammonium regeneration in a turbid lake in south Florida was higher in light conditions than in the dark. Differences between light and dark regeneration rates were also observed in the surface waters of the Mississippi River plume, indicating a close coupling between phytoplanktonic production of DON and microbial N recycling processes (Gardner et al., 1997). Slightly higher regeneration rates under natural light incubation were also observed in the present study during spring and fall and support the idea that labile organic nitrogen from phytoplankton was produced more during the day than at night (Figure 4A).

## Ammonium uptake in the water column

The differences between light and dark uptake rates were used to estimate the role of phytoplankton in total ammonium uptake, assuming that the dark ammonium uptake reflects the bacterial contribution to this process. The ammonium uptake in the dark treatment can be considered as the uptake primarily contributed by heterotrophic bacteria, as N uptake by phytoplankton is closely associated with light energy, whereas uptake by heterotrophic bacteria is more correlated with the availability of organic matter (Gardner et al., 2004). Although dark N assimilation by phytoplankton has been reported, this process usually occurs under severe N limitation and is less likely in N-replete systems such as the YRE (Clark et al., 2002; Jochem et al., 2004; Maguer et al., 2011). We also observed that the dark uptake rate for the total plankton community and the light and dark uptake rates for plankton less than 0.7 μm in size were similar (Figure 3B); thus, at least for June 2013, we concluded that the dark uptake was due to small-sized heterotrophic bacteria.

As incubations were performed in surface waters for 24 h, uptake under light conditions reflects the total ammonium uptake for one full day. Therefore, the difference between light and dark (bacterial) uptake can be regarded as the photosynthetic ammonium uptake. The photosynthetic ammonium uptake was usually higher than the bacterial

uptake, although this difference was not statistically significant, except during summer, when photosynthetic uptake was twice as high as bacterial uptake (Figure 3A).

The contribution of phytoplankton and bacteria to ammonium uptake derived from the light/dark uptake differences has been reported in previous studies (Jochem et al., 2004; Gardner et al., 2004; McCarthy et al., 2009; James et al., 2011). McCarthy et al. (2009) demonstrated that there were no differences between light and dark potential uptake rates in Florida Bay. From the results of $^{15}N$ incubations and bacterial abundance, it has been suggested that a substantial fraction of potential ammonium uptake can be ascribed to heterotrophic bacteria. Jochem et al. (2004) have shown that potential ammonium uptake rates in light bottles were higher than those in dark bottles, and the dark uptake as a percentage of total uptake was approximately 40% to 80% in the Mississippi River plume. Gardner et al. (2004) found that the dark uptake rates (attributed mainly to bacteria) during spring in Lake Michigan were ~70% of the natural light uptake rates (bacteria plus phytoplankton) at most lake sites, but only ~30% at river-influenced sites. The results of the present study demonstrated that dark ammonium uptake rates were 34%–53% of natural light uptake rates and were within the range of ratios observed for other estuarine environments, indicating slightly dominant autotrophic consumption of ammonium during most investigation periods (Gardner et al., 2004; Jochem et al., 2004; McCarthy et al., 2009).

## Importance of ammonium regeneration for primary production in the YRE

The ammonium regeneration rates in the YRE were higher than the values previously reported for the Delaware River (Lipschultz et al., 1986), Florida Bay (McCarthy et al., 2009), the West Florida Shelf (Bronk et al., 2014), Copano Bay (Bruesewitz et al., 2015), St. Lucie Estuary (Hampel et al., 2019), a wetland at Lake Erie (Lavrentyev et al., 2004), the Thau lagoon, France (Collos et al., 2003), and the Mississippi River plume (Cotner and Gardner, 1993; Gardner et al., 1997). Our results in the dark treatment were also 22 times higher than those in the Peruvian upwelling system (Fernandez et al., 2009). The maximum value in this study (dark regeneration rate of 1.19 μmole N $L^{-1}$ $h^{-1}$ in July 2012) was comparable to the rates obtained from a coastal mangrove swamp in India (Dham et al., 2002), Lake Okeechobee (Hampel et al., 2019), Yangtze River (Xue et al., 2021a), and lower than those of the subtropical eutrophic Lake Taihu in China (McCarthy et al., 2007; Hampel et al., 2018; Jiang et al., 2019; Xue et al., 2021b). YRE ammonium uptake rates were higher than those observed in other estuaries, including the nitrate-rich Thames Estuary (Middelburg and Nieuwenhuize, 2000b), turbid European tidal estuaries (the Ems, Douro, and Rhine; Middelburg and Nieuwenhuize, 2000a), the West Florida Shelf (Bronk et al., 2014), Copano Bay (Bruesewitz et al., 2015), and Cochin Estuary (Bhavya et al., 2016). However, ammonium uptake rates were similar to those observed for the Mississippi River plume (Gardner et al., 1997), a coastal mangrove swamp in India (Dham et al., 2002), St. Lucie Estuary (Hampel et al., 2019), Yangtze River (Xue et al., 2021a), a Lake Erie wetland (Lavrentyev et al., 2004; Hoffman et al., 2022), and the mesohaline region of the Loire and Scheldt estuary (Middelburg and Nieuwenhuize, 2000a). The ammonium uptake rates were also lower than the values of the Lake Okeechobee (Hampel et al., 2019) and Lake Taihu (Hampel et al., 2018; Jiang et al., 2019). In this study, ammonium regeneration and uptake rates were in a range similar to the values in eutrophic freshwater rather than coastal waters.The ammonium turnover time (ambient concentration divided by uptake rate) in light incubations ranged from 0.01 (July 2012) to 1.24 days (March 2012), even though ammonium was almost depleted in summer. The average residence time of freshwater reported for the YRE ranged from 0.26 (summer wet season) to 2.03 days (fall dry season; Lee and Jun, 2009). Therefore, the ammonium turnover time was shorter than the freshwater residence time, and we can conclude that ammonium recycling actively occurs within this estuary throughout the year. Similarly, it was suggested that the ammonium turnover times reported along a river–estuary continuum in a coastal catchment of the Texas Coastal Bend were lower than water replacement times, supporting high productivity (Bruesewitz et al., 2015). A high rate of ammonium turnover was also reported in Lake Taihu, indicating that may promote cyanobacterial bloom during N-limited season (Xue et al., 2021b).

## Implications of estuarine dam on ammonium recycling

High concentrations of suspended solids in a tidally dominated estuary reduce the euphotic depth and limit primary production (Cloern, 1987; Mallin and Paerl, 1992). Moreover, if the estuarine water residence time is shorter than the cell doubling time of phytoplankton, phytoplankton biomass accumulation is low (Sin et al., 1999; Thomas et al., 2005; Sin et al., 2013). Estuaries and coastal waters located in the southeastern part of the Yellow Sea (including the YRE, Han River, and Geum River) are well-mixed and turbid due to sediment resuspension enhanced by strong macro-tidal currents, with abundant sediment input from land (Lee and Chu, 2001; Byun et al., 2007). Light limits primary production in these systems, but phytoplankton blooms can occur in summer when light conditions temporarily improve, even in turbid estuaries (Wafar et al., 1983; L'Helguen et al., 1996). In the southeastern Yellow Sea, however, because annual precipitation is concentrated during summer, which decreases water residence time (in turn reducing phytoplankton biomass accumulation), phytoplankton blooms are relatively rare, despite the high nutrient levels (Kim et al., 2013; Park et al., 2013). The building of estuarine dams causes physical and biogeochemical

changes to the estuary environment by restricting seawater circulation (Cho et al., 2004; Byun et al., 2007; Gedan et al., 2009). Dam construction weakens tidal currents and generates stagnant areas (Cho et al., 2004; Cho et al., 2014). Mean turbidity in the YRE has decreased to 63%–92% of pre-dam levels (Figure 5), resulting in improved light conditions.

Vigorous ammonium recycling by bacteria and phytoplankton in the YRE may be a combined result of reduced turbidity and increased water residence times due to construction of the estuarine dam. When stratification intensifies during non-discharge periods, ammonium utilization can be enhanced because of favorable light conditions, increased water residence times. This phenomenon—combined with an ammonium turnover time that is shorter than the freshwater residence time, together with high nutrient inputs from inside the dam—can result in phytoplankton blooms (Thomas et al., 2005; Figure 2). In summer, the primary productivity in the YRE was higher (up to 8900 mg C $m^{-2}$ $d^{-1}$, Lee et al., 2011) than that in adjacent estuaries and other estuarine systems (Douro Estuary, Portugal and Westerschelde Estuary, the Netherlands), with similar ranges of suspended solids, nutrients, and flushing times (Kromkamp and Peene, 1995; Middelburg and Nieuwenhuize, 2000a; Azevedo et al., 2006; Middelburg and Herman, 2007). The ammonium demand for primary production, estimated from primary productivity measurements (2,000–8,927 mg C $m^{-2}$ $d^{-1}$ from spring to summer, Lee et al., 2011) and C/N ratios (Redfield ratio), was 302–1,347 mg N $m^{-2}$ $d^{-1}$ in the YRE. In the current study, the estimated ammonium uptake by phytoplankton (assuming a mean euphotic depth of 4 m; Sin et al., 2013) was 710–1350 mg N $m^{-2}$ $d^{-1}$ during the same period. The regeneration of ammonium through active ammonium recycling is likely to supports high phytoplankton production during the spring–summer season in the YRE. Previous studies have suggested that water column N recycling contributes significantly to phytoplankton N demand in aquatic environments (Bronk et al., 2014; Hampel et al., 2018; Jiang et al., 2019; Xue et al., 2021a; Xue et al., 2021b; Xu et al., 2021; Hoffman et al., 2022). In the West Florida Shelf, regenerated ammonium was sufficient to supply the ammonium demand, and supported 85% of the ammonium uptake even during blooms of Karenia brevis (Bronk et al., 2014). Ammonium regeneration in Lake Taihu supported about 60% of potential ammonium demand during summer Microcystis-dominated blooms suggesting the importance of regenerated N cycling for cyanobacterial blooms (Hampel et al., 2018). In studies conducted on Lake Taihu and Lake Erie, extrapolated whole-lake regeneration of ammonium can supply N up to 200% of the external load to the lake, suggesting that internal N cycling plays an important role in supporting high productivity (Hampel et al., 2018; Hoffman et al., 2022). Even though active ammonium recycling was observed within the YRE system, further research is needed on how the altered estuarine structure and function affect the N cycle and primary production such as YRE, including the relative importance of nitrate and ammonium as a source of inorganic N for phytoplankton and primary production.

## Conclusions

This study investigated ammonium regeneration and potential uptake rates an anthropogenically altered YRE using stable-isotope techniques. To the best of our knowledge, this study is the first to examine water column nitrogen recycling in an estuary that has been significantly deformed by dam construction, and has improved our understanding of the impact of man-made structures on the nitrogen cycle. This study showed that high ammonium recycling provides a significant proportion of N to sustain phytoplankton production, suggesting that internal nutrient cycling are important in YRE. The higher contribution of bacteria than zooplankton to ammonium regeneration in this study is likely to be associated with artificial freshwater discharge. In addition, as the environment is changed by dam construction from a highly turbid estuary to semi enclosed bay, decrease in turbidity and increase in residence time were assumed to promote ammonium recycling.

## Data availability statement

The raw data supporting the conclusions of this article will be made available by the authors, without undue reservation.

## Author contributions

JL and SA developed the idea and wrote the manuscript. JL conducted the literature search and analysis. SA provided interpretation of data. Both authors contributed to the article and approved the submitted version.

## Funding

This research was supported by Korea Institute of Marine Science & Technology Promotion(KIMST) funded by the Ministry of Oceans and Fisheries, Korea(20220023). This research was also supported by BK21 School of Earth and Environmental and Environmental systems. This research was also supported by the National Institute of Fisheries Science, Ministry of Oceans and Fisheries, Korea (R2021055).

## Conflict of interest

The authors declare that the research was conducted in the absence of any commercial or financial relationships that could be construed as a potential conflict of interest.

## Publisher's note



## References

Alpine, A. E., and Cloern, J. E. (1988). Phytoplankton growth rates in a light-limited environment, San Francisco bay. *Mar. Ecol. Prog. Ser.* 44, 167–173. doi: 10.3354/meps044167

An, S., and Gardner, W. S. (2002). Dissimilatory nitrate reduction to ammonium (DNRA) as a nitrogen link, versus denitrification as a sink in a shallow estuary (Laguna Madre/Baffin bay, Texas). *Mar. Ecol. Prog. Ser.* 237, 41–50. doi: 10.3354/meps237041

An, S., Lee, J. Y., and Gardner, W. S. (2013). Stable isotope measurement of ammonium using HPLC-RTS (high performance liquid chromatography-retention time shift). *J. Korean Soc Oceanogr.* 18, 47–52. doi: 10.7850/jkso.2013.18.1.47

Armstrong, R. A. (1994). Grazing limitation and nutrient limitation in marine ecosystems: steady state solutions of an ecosystem model with multiple food chains. *Limnol. Oceanogr.* 39, 597–608. doi: 10.4319/lo.1994.39.3.0597

Azevedo, I. C., Duarte, P. M., and Bordalo, A. A. (2006). Pelagic metabolism of the douro estuary (Portugal) - factors controlling primary production. *Estuar. Coast. Shelf S.* 69, 133–146. doi: 10.1016/j.ecss.2006.04.002

Bhavya, P. S., Kumar, S., Gupta, G. V. M., Sudheesh, V., Sudharma, K. V., Varrier, D. S., et al. (2016). Nitrogen uptake dynamics in a tropical eutrophic estuary (Cochin, India) and adjacent coastal waters. *Estuaries Coast.* 39 (1), 54–67. doi: 10.1007/s12237-015-9982-y

Bianchi, T. S. (2007). *Biogeochemistry of estuaries* (New York: Oxford University Press on Demand) 688 pp.

Blackburn, T. H. (1979). Method for measuring rates of $NH_4^+$ turnover in anoxic marine sediments, using a $^{15}N$- $NH_4^+$ dilution technique. *Appl. Environ. Microbiol.* 37, 760–765. doi: 10.1128/aem.37.4.760-765.1979

Bronk, D. A., Killberg-Thoreson, L., Sipler, R. E., Mulholland, M. R., Roberts, Q. N., Bernhardt, P. W., et al. (2014). Nitrogen uptake and regeneration (ammonium regeneration, nitrification and photoproduction) in waters of the West Florida shelf prone to blooms of karenia brevis. *Harmful Algae* 38, 50–62. doi: 10.1016/j.hal.2014.04.007

Bruesewitz, D. A., Gardner, W. S., Mooney, R. F., and Buskey, E. J. (2015). Seasonal water column NH4+ cycling along a semi-arid sub-tropical river–estuary continuum: responses to episodic events and drought conditions. *Ecosystems* 18 (5), 792–812. doi: 10.1007/s10021-015-9863-z

Byun, D. S., Wang, X. H., and Holloway, P. E. (2004). Tidal characteristic adjustment due to dyke and seawall construction in the mokpo coastal zone, Korea. *Estuar. Coast. Shelf S.* 59, 185–196. doi: 10.1016/j.ecss.2003.08.007

Byun, D. S., Wang, X. H., Zavatarelli, M., and Cho, Y. K. (2007). Effects of resuspended sediments and vertical mixing on phytoplankton spring bloom dynamics in a tidal estuarine embayment. *J. Mar. Syst.* 67, 102–118. doi: 10.1016/j.jmarsys.2006.10.003

Caperon, J., Schell, D., Hirota, J., and Laws, E. (1979). Ammonium excretion rates in kaneohe bay, Hawaii, measured by a $^{15}N$ isotope dilution technique. *Mar. Biol.* 54, 33–40. doi: 10.1007/BF00387049

Cho, Y. K., Lee, K. S., and Park, K. Y. (2009). Year-to-year variability of the vertical temperature structure in the youngsan estuary. *Ocean Polar Res.* 31, 239–246. doi: 10.4217/OPR.2009.31.3.239

Cho, Y. K., Park, L. H., Cho, C., Lee, I. T., Park, K. Y., and Oh, C. W. (2004). Multi-layer structure in the youngsan estuary, Korea. *Estuar. Coast. Shelf S.* 61, 325–329. doi: 10.1016/j.ecss.2004.06.003

Cho, C. W., Song, Y. S., Kim, C. K., Kim, T. I., Han, J. S., Woo, S. B., et al. (2014). A modeling study on hypoxia formation in the bottom water of the youngsan river estuary, Korea. *J. Coast. Res.* 31, 920–929. doi: 10.2112/JCOASTRES-D-13-00099.1

Clark, K. R., Flynn, K., and Owens, N. (2002). The large capacity for dark nitrate assimilation in diatoms may overcome nitrate limitation of growth. *New Phytol.* 155, 101–108. doi: 10.1046/j.1469-8137.2002.00435.x

Cloern, J. E. (1987). Turbidity as a control on phytoplankton biomass and productivity in estuaries. *Continent. Shelf Res.* 7 (11-12), 1367–1381. doi: 10.1016/0278-4343(87)90042-2

Collos, Y., Vaquer, A., and Bibent, B. (2003). Response of coastal phytoplankton to ammonium and nitrate pulses: seasonal variations of nitrogen uptake and regeneration. *Aquat. Ecol.* 37, 227–236. doi: 10.1023/A:1025881323812

Cotner, J. B.Jr, and Gardner, W. S. (1993). Heterotrophic bacterial mediation of ammonium and dissolved free amino acid fluxes in the Mississippi river plume. *Mar. Ecol. Prog. Ser.* 93, 75–87. doi: 10.3354/meps093075

Dham, V. V., Heredia, A. M., Wafar, S., and Wafar, M. (2002). Seasonal variations in uptake and *in situ* regeneration of nitrogen in mangrove waters. *Limnol. Oceanogr.* 47, 241–254. doi: 10.4319/lo.2002.47.1.0241

Finlay, J. C., Small, G. E., and Sterner, R. W. (2013). Human influences on nitrogen removal in lakes. *Science* 342 (6155), 247–250. doi: 10.1126/science.1242575

Fernández, C., Farías, L., and Alcaman, M. E. (2009). Primary production and nitrogen regeneration processes in surface waters of the Peruvian upwelling system. *Prog. Oceanogr.* 83, 159–168.

Fisher, T. R., Peele, E. R., Ammerman, J. W., and Harding, L. W.Jr (1992). Nutrient limitation of phytoplankton in Chesapeake bay. *Mar. Ecol. Prog. Ser.* 82, 51–63. doi: 10.3354/meps082051

Gardner, W. S., Bootsma, H. A., Evans, C., and St John, P. A. (1995). Improved chromatographic analysis of $^{15}N$:$^{14}N$ ratios in ammonium or nitrate for isotope addition experiments. *Mar. Chem.* 48, 271–382. doi: 10.1016/0304-4203(94)00060-Q

Gardner, W. S., Cavaletto, J. F., Cotner, J. B., and Johnson, J. M. (1997). Effects of natural light on nitrogen cycling rates in the Mississippi river plume. *Limnol. Oceanogr.* 42, 273–281. doi: 10.4319/lo.1997.42.2.0273

Gardner, W. S., Lavrentyev, P. J., Cavaletto, J. F., McCarthy, M. J., Eadie, B. J., Johengen, T. H., et al. (2004). The distribution and dynamics of nitrogen and microbial plankton in southern lake Michigan during spring transition 1999–2000. *J. Geophys. Res.* 109, 1–16. doi: 10.1029/2002JC001588

Gedan, K. B., Silliman, B. R., and Bertness, M. D. (2009). Centuries of human-driven change in salt marsh ecosystems. *Ann. Rev. Mar. Sci.* 1, 117–141. doi: 10.1146/annurev.marine.010908.163930

Goldman, J. C., McCarthy, J. J., and Peavey, D. G. (1979). Growth rate influence on the chemical composition of phytoplankton in oceanic waters. *Nature* 279, 210–215. doi: 10.1038/279210a0

Hampel, J. J., McCarthy, M. J., Gardner, W. S., Zhang, L., Xu, H., Zhu, G., et al. (2018). Nitrification and ammonium dynamics in taihu lake, China: seasonal competition for ammonium between nitrifiers and cyanobacteria. *Biogeosciences* 15 (3), 733–748. doi: 10.5194/bg-15-733-2018

Hampel, J. J., McCarthy, M. J., Reed, M. H., and Newell, S. E. (2019). Short term effects of hurricane Irma and cyanobacterial blooms on ammonium cycling along a freshwater–estuarine continuum in south Florida. *Front. Mar. Sci.* 6, 640. doi: 10.3389/fmars.2019.00640

Heip, C. H. R., Goosen, N. K., Herman, P. M. J., Kromkamp, J., Middelburg, J. J., and Soetaert, K. (1995). Production and consumption of biological particles in temperate tidal estuaries. *Oceanogr. Mar. Biol. Annu. Rev.* 33, 1–149.

Hoffman, D. K., McCarthy, M. J., Boedecker, A. R., Myers, J. A., and Newell, S. E. (2022). The role of internal nitrogen loading in supporting non-n-fixing harmful cyanobacterial blooms in the water column of a large eutrophic lake. *Limnol. Oceanogr.* 67, 2028–2041. doi: 10.1002/lno.12185

Howarth, R. W., and Marino, R. (2006). Nitrogen as the limiting nutrient for eutrophication in coastal marine ecosystems: Evolving views over three decades. *Limnol. Oceanogr.* 51, 364–376. doi: 10.4319/lo.2006.51.1_part_2.0364

Hyun, J. H., Choi, K. S., Lee, K. S., Lee, S. H., Kim, Y. K., and Kang, C. K. (2020). Climate change and anthropogenic impact around the Korean coastal ecosystems: Korean long-term marine ecological research (K-LTMER). *Estuar. Coast.* 43, 441–448. doi: 10.1007/s12237-020-00711-6

James, R. T., Gardner, W. S., McCarthy, M. J., and Carini, S. A. (2011). Nitrogen dynamics in lake Okeechobee, forms, functions and changes. *Hydrobiologia* 669, 199–212. doi: 10.1007/s10750-011-0683-7

Jiang, X., Zhang, L., Gao, G., Yao, X., Zhao, Z., and Shen, Q. (2019). High rates of ammonium recycling in northwestern lake taihu and adjacent rivers: An important pathway of nutrient supply in a water column. *Environ. pollut.* 252, 1325–1334. doi: 10.1016/j.envpol.2019.06.026

Jochem, F. J., McCarthy, M. J., and Gardner, W. S. (2004). Microbial ammonium cycling in the Mississippi river plume during the drought spring of 2000. *J. Plankton Res.* 26, 1265–1275. doi: 10.1093/plankt/fbh118

Jones, M. N. (1984). Nitrate reduction by shaking with cadmium: alternative to cadmium columns. *Water Res.* 18, 643–646. doi: 10.1016/0043-1354(84)90215-X

Justic, N., Rabalais, N. N., Turner, R. E., and Dortch, Q. (1995). Changes in nutrient structure of river-dominated coastal waters: stoichiometric nutrient balance and its consequences. *Estuar. Coast. Shelf* S. 40, 339–356. doi: 10.1016/S0272-7714(05)80014-9

Kim, T. W., Lee, K. T., Lee, C. K., Jeong, H. D., Suh, Y. S., Lim, W. A., et al. (2013). Interannual nutrient dynamics in Korean coastal waters. *Harmful Algae* 30, S15–S27. doi: 10.1016/j.hal.2013.10.003

Kromkamp, J., and Peene, J. (1995). Possibility of net primary production in the turbid schelde estuary (SW Netherlands). *Mar. Ecol. Prog. Ser.* 121, 249–259. doi: 10.3354/meps121249

Lavrentyev, P. J., McCarthy, M. J., Klarer, D. M., Jochem, F., and Gardner, W. S. (2004). Estuarine microbial food web patterns in a lake Erie coastal wetland. *Microbial. Ecol.* 48, 567–577. doi: 10.1007/s00248-004-0250-0

Lee, J. (2015). The impact of man-made structures on estuarine ecosystems: Nitrogen cycling and halophyte functioning (Busan, Republic of Korea: Pusan National University), 191p.

Lee, Y. G., An, K. G., Ha, P. T., Lee, K. Y., Kang, J. H., Cha, S. M., et al. (2009). Decadal and seasonal scale changes of an artificial lake environment after blocking tidal flows in the yeongsan estuary region, Korea. *Sci. Total Environ.* 407, 6063–6072. doi: 10.1016/j.scitotenv.2009.08.031

Lee, H. J., and Chu, Y. S. (2001). Origin of inner-shelf mud deposit in the southeastern yellow Sea: Huksan mud belt. *J. Sediment Res.* 71, 144–154. doi: 10.1306/040700710144

Lee, K. S., and Jun, S. K. (2009). Material budgets in youngsan river estuary with simple box model. *J. Korean Soc Mar. Environ. Engineer.* 12, 44–53.

Lee, Y. J., Sin, Y. S., Kim, S. H., and Shin, K. H. (2011). Temporal and spatial variations of primary productivity in youngsan river and mokpo coastal areas. *Korean J. Limnol.* 44, 327–336.

L'Helguen, S., Madec, C., and Le Corre, P. (1996). Nitrogen uptake in permanently well-mixed temperate coastal waters. *Estuar. Coast. Shelf* S. 42, 803–818. doi: 10.1006/ecss.1996.0051

Lim, H. S., Diaz, R. J., Hong, J., and Schaffner, L. C. (2006). Hypoxia and benthic community recovery in Korean coastal waters. *Mar. pollut. Bull.* 52, 1517–1526. doi: 10.1016/j.marpolbul.2006.05.013

Lipschultz, F., Wofsey, S. C., and Fox, L. E. (1986). Nitrogen metabolism of the eutrophic Delaware river ecosystem. *Limnol. Oceanogr.* 31, 701–716. doi: 10.4319/lo.1986.31.4.0701

Maguer, J. F., L'Helguen, S., Caradec, J., and Klein, C. (2011). Size-dependent uptake of nitrate and ammonium as a function of light in well-mixed temperate coastal waters. *Cont. Shelf Res.* 31, 1620–1631. doi: 10.1016/j.csr.2011.07.005

Maguer, J. F., L'Helguen, S., Madec, C., and Le Corre, P. (1999). Seasonal patterns of ammonium regeneration from sizefractionated microheterotrophs. *Cont. Shelf Res.* 19, 1755–1770. doi: 10.1016/S0278-4343(99)00037-0

Mallin, M. A., and Paerl, H. W. (1992). Effects of variable irradiance on phytoplankton productivity in shallow estuaries. *Limnol. Oceanogr.* 37, 54–62. doi: 10.4319/lo.1992.37.1.0054

McCarthy, M. J., Gardner, W. S., Lavrentyev, P. J., Jochem, F. J., and Williams, C. J. (2009). Water column nitrogen cycling and microbial plankton in Florida bay. *Contrib. Mar. Sci.* 38, 49–62.

McCarthy, M. J., Gardner, W. S., Lehmann, M. F., and Bird, D. F. (2013). Implications of water column ammonium uptake and regeneration for the nitrogen budget in temperate, eutrophic missisquoi bay, lake Champlain (Canada/USA). *Hydrobiologia* 718, 173–188. doi: 10.1007/s10750-013-1614-6

McCarthy, M. J., Lavrentyev, P. J., Yang, L., Zhang, L., Chen, Y., Qin, B., et al. (2007). Nitrogen dynamics and microbial food web structure during a summer cyanobacterial bloom in a subtropical, shallow, well-mixed, eutrophic lake (Lake taihu, China). *Hydrobiologia* 581, 195–207. doi: 10.1007/s10750-006-0496-2

McCarthy, J. J., Taylor, W. R., and Taft, J. L. (1977). Nitrogenous nutrition of the plankton in the Chesapeake bay. 1. nutrient availability and phytoplankton preferences. *Limnol. Oceanogr.* 22, 996–1011. doi: 10.4319/lo.1977.22.6.0996

Middelburg, J. J., and Herman, P. M. J. (2007). Organic matter processing in tidal estuaries. *Mar. Chem.* 106, 127–147. doi: 10.1016/j.marchem.2006.02.007

Middelburg, J. J., and Nieuwenhuize, J. (2000a). Uptake of dissolved inorganic nitrogen in turbid, tidal estuaries. *Mar. Ecol. Prog. Ser.* 192, 79–88. doi: 10.3354/meps192079

Middelburg, J. J., and Nieuwenhuize, J. (2000b). Nitrogen uptake by heterotrophic bacteria and phytoplankton in the nitrate-rich Thames estuary. *Mar. Ecol. Prog. Ser.* 203, 13–21. doi: 10.3354/meps203013

MOF (2014). *Development of integrated estuarine management system* (Sejong: Ministry of Oceans and Fisheries), 629 p.

Moon, M. H., Cho, J. W., and Lee, M. C. (1991). A variation on the marine environments in the yeongsan river estuary. *Natur. Sci. Res.* 14, 101–115.

NFRDA (1983). *A comprehensive study on marine pollution for the conservation of the Korean coastal ecosystem with respect to culture areas and fishing grounds* (Busan: National fisheries research and development agency), 624. Technical report 58.

Park, J. Y., Jeong, H. J., Yoo, Y. D., and Yoon, E. Y. (2013). Mixotrophic dinoflagellate red tides in Korean waters: Distribution and ecophysiology. *Harmful Algae* 30, S28–S40. doi: 10.1016/j.hal.2013.10.004

Rabalais, N. N., Diaz, R. J., Levin, L. A., Turner, R. E., Gilbert, D., and Zhang, J. (2010). Dynamics and distribution of natural and human-caused hypoxia. *Biogeosciences* 7, 585–619. doi: 10.5194/bg-7-585-2010

Seo, M. H. (2008). *Variation of zooplankton community by Open/Close of yangsan lake dike, Korea* (Gwang Ju: Chonnam National University), 63p.

Sin, Y. S., Hyun, B. K., Jeong, B. K., and Soh, H. Y. (2013). Impacts of eutrophic freshwater inputs on water quality and phytoplankton size structure in a temperate estuary altered by a sea dike. *Mar. Environ. Res.* 85, 54–63. doi: 10.1016/j.marenvres.2013.01.001

Sin, Y., and Jeong, B. (2020). Anthropogenic disturbance of tidal variation in the water properties and phytoplankton community of an estuarine system. *Estuar. Coast.* 43, 547–559. doi: 10.1007/s12237-019-00557-7

Sin, Y., Lee, E., Lee, Y., and Shin, K. H. (2015). The river–estuarine continuum of nutrients and phytoplankton communities in an estuary physically divided by a sea dike. *Estuar. Coast. Shelf S* 163, 279–289. doi: 10.1016/j.ecss.2014.12.028

Sin, Y., Wetzel, R. L., and Anderson, I. C. (1999). Spatial and temporal characteristics of nutrient and phytoplankton dynamics in the York river estuary, Virginia: analyses of long-term data. *Estuaries* 22, 260–275. doi: 10.2307/1352982

Son, S. H., Campbell, J., Dowell, M., Yoo, S., and Noh, J. (2005). Primary production in the yellow Sea determined by ocean color remote sensing. *Mar. Ecol. Prog. Ser.* 303, 91–103. doi: 10.3354/meps303091

Strickland, J. D. H., and Parsons, T. R. (1972). A practical handbook of seawater analysis. *Bull. Fish. Res. Board Canada* 167, 1–310.

Thomas, C. M., Perissinotto, R., and Kibirige, I. (2005). Phytoplankton biomass and size structure in two south African eutrophic, temporarily open / closed estuaries. *Estuar. Coast. Shelf S.* 65, 223–238. doi: 10.1016/j.ecss.2005.05.015

Tilman, D., Kilham, S. S., and Kilman, P. (1982). Phytoplankton community ecology: the role of limiting nutrients. *Annu. Rev. Ecol. Syst.* 13, 349–372. doi: 10.1146/annurev.es.13.110182.002025

Wafar, M. V. M., Le Corre, P., and Birrien, J. L. (1983). Nutrients and primary production in permanently well-mixed temperate coastal waters. *Estuar. Coast. Shelf S.* 17, 431–446. doi: 10.1016/0272-7714(83)90128-2

Wei, H., He, Y., Li, Q., Liu, Z., and Wang, H. (2007). Summer hypoxia adjacent to the changjiang estuary. *J. Mar. Syst.* 67, 292–303. doi: 10.1016/j.jmarsys.2006.04.014

Wheeler, P., Kirchman, D., Landry, M., and Kokkinakis, S. (1989). Diel periodicity in ammonium uptake and regeneration in the oceanic subarctic: implications for interactions in microbial food webs. *Limnol. Oceanogr.* 34, 1025–1033. doi: 10.4319/lo.1989.34.6.1025

Wu, Z., Liu, Y., Liang, Z., Wu, S., and Guo, H. (2017). Internal cycling, not external loading, decides the nutrient limitation in eutrophic lake: A dynamic model with temporal Bayesian hierarchical inference. *Water Res.* 116, 231–240. doi: 10.1016/j.watres.2017.03.039

Xue, J., Yao, X., Zhao, Z., He, C., Shi, Q., and Zhang, L. (2021b). Internal loop sustains cyanobacterial blooms in eutrophic lakes: Evidence from organic nitrogen and ammonium regeneration. *Water Res.* 206, 117724. doi: 10.1016/j.watres.2021.117724

Xue, J., Zhao, Z., Yao, X., Liu, W., and Zhang, L. (2021a). Suspended solids induce increasing microbial ammonium recycling along the river-estuary continuum of the Yangtze river. *Hydrol. Process.* 35 (8), e14345. doi: 10.1002/hyp.14345

Xu, H., McCarthy, M. J., Paerl, H. W., Brookes, J. D., Zhu, G., Hall, N. S., et al. (2021). Contributions of external nutrient loading and internal cycling to cyanobacterial bloom dynamics in lake taihu, China: Implications for nutrient management. *Limnol. Oceanogr.* 66 (4), 1492–1509. doi: 10.1002/lno.11700

Yim, J., Kwon, B.-O., Nam, J., Hwang, J. H., Choi, K., and Khim, J. S. (2018). Analysis of forty years long changes in coastal land use and land cover of the yellow Sea: The gains or losses in ecosystem services. *Environ. pollut.* 241, 74–84. doi: 10.1016/j.envpol.2018.05.058

Yin, K., Qian, D. P. Y., Wu, M. C. S., Chen, J. C., Huang, L. M., Song, X. Y., et al. (2001). Shift from p to n limitation of phytoplankton growth across the pearl river

estuarine plume during summer. *Mar. Ecol. Prog. Ser.* 221, 17–28. doi: 10.3354/meps221017

Yoon, B. B. (2012). A study of nutrient limitation in estuary using bioassay experiment mokpo, republic of Korea (Mokpo: Mokpo Maritime University), 51p.

Yuan, X., Glibert, P. M., Xu, J., Liu, H., Chen, M., Liu, H., et al. (2012). Inorganic and organic nitrogen uptake by phytoplankton and bacteria in Hong Kong waters. *Estuar. Coast.* 35, 325–334. doi: 10.1007/s12237-011-9433-3

Zhang, J., Liu, S. M., Ren, J. L., Wu, Y., and Zhang, G. L. (2007). Nutrient gradients from the eutrophic changjiang (Yangtze river) estuary to the oligotrophic kuroshio waters and re-evaluation of budgets for the East China Sea shelf. *Prog. Oceanogr.* 74, 449–478. doi: 10.1016/j.pocean.2007.04.019

Zhou, J., Han, X., Brookes, J. D., and Qin, B. (2022). High probability of nitrogen and phosphorus co-limitation occurring in eutrophic lakes. *Environ. pollut.* 292, 118276. doi: 10.1016/j.envpol.2021.118276

frontiers | Frontiers in Marine Science

TYPE Original Research
PUBLISHED 19 December 2022
DOI 10.3389/fmars.2022.1002335



OPEN ACCESS

EDITED BY
Guan-hong Lee,
Inha University, South Korea

REVIEWED BY
Abd Mujahid Hamdan,
Ar-Raniry State Islamic University
Banda Aceh, Indonesia
Jinhai Zheng,
Hohai University, China

*CORRESPONDENCE
Xianbin Liu
liuxb_801@163.com

SPECIALTY SECTION
This article was submitted to Coastal Ocean Processes, a section of the journal Frontiers in Marine Science

RECEIVED 25 July 2022
ACCEPTED 06 December 2022
PUBLISHED 19 December 2022

CITATION
Liu X, Chen J, Yue W, Wang Q, Zhan C, Zeng L, Song J, Wang L and Cui B (2022) Tracing the source–sink process of fluvio-clastic materials: Magnetic records of surface sediments in the Yangtze River basin. *Front. Mar. Sci.* 9:1002335. doi: 10.3389/fmars.2022.1002335



# Tracing the source–sink process of fluvio-clastic materials: Magnetic records of surface sediments in the Yangtze River basin

Xianbin Liu[1]*, Jing Chen[2], Wei Yue[3], Qing Wang[1], Chao Zhan[1], Lin Zeng[1], Jian Song[1], Longsheng Wang[1] and Buli Cui[1]

[1]School of Resource and Environmental Engineering, Ludong University, Yantai, China, [2]State Key Laboratory for Estuarine and Coastal Research, East China Normal University, Shanghai, China, [3]School of Geography, Geomatics and Planning, Jiangsu Normal University, Xuzhou, China

In this study, we collected surface sediments from the mainstream and major tributaries of the Yangtze River to systematically analyse their magnetic properties, and discuss the implications for tracing source–sink process of fluvio-clastic materials. Our results showed that the surface sediments from tributaries in the upper basin had a significantly higher content of ferromagnetic minerals and coarser grain sizes than that in the mid-lower basin. The magnetic susceptibility ($\chi_{lf}$) of surface sediments from the mainstream was $34.16*10^{-8}$ $m^3/kg$ at Shigu, rapidly rose to $230.56*10^{-8}$ $m^3/kg$ at Yibin, and then dropped to $68.92*10^{-8}$ $m^3/kg$ at the river mouth. The $\chi_{lf}$ of Yalong River sediments in the upper basin was $276.86*10^{-8} m^3/kg$, considerably higher than that of the sediments from other tributaries, and greatly contribute to the $\chi_{lf}$ of the sediments in the mainstream, reflecting the dominant constraining role of the Emeishan basalts. The distinctive magnetic properties of the upper core sediments from Jianghan basin and the Yangtze delta closely match those of surficial river sediments of the upper Yangtze basin. This may indicate the addition of clastic materials eroded from the upper basin, resulting from the cut-through of the Three Gorges during the evolution of the Yangtze River that occurred in the late Cenozoic. Investigating the magnetic properties of the surface sediments in the Yangtze River basin can provide insights into the source–sink process of clastic materials and environmental changes.

KEYWORDS

**the Yangtze River, magnetic properties, source-sink process, the surface sediments, Emeishan basalts**

# 1 Introduction

Rivers, as the link between land and sea, play a key role in exchanging of global energy and materials. About 15–19*$10^9$ t of clastic materials are transported by rivers from basin to estuaries and marginal seas yearly (Milliman and Meade, 1983; Syvitski et al., 2003; Milliman and Farnsworth, 2011). This source–sink process makes a significant impact on earth surface processes such as soil erosion, shoreline change, and even global biogechemical cycle. (Wang et al., 2011; Wittmann et al., 2016; Li et al., 2017; Jiang et al., 2018; Nel et al., 2018; Park et al., 2021; Ji et al., 2022).

The Yangtze River, with a drainage area up to 1.8 × $10^6$ $km^2$, linking the Tibetan Plateau and the western Pacific marginal seas, is the longest river in Asia. It annually discharges 490×$10^6$ tons sediments into the delta and East China Sea, and dropped sharply to 130×$10^6$ tons due to the construction of the world's largest reservoir– the Three Gorges Dam (Dai and Liu, 2013, Yang et al., 2014; Yang et al., 2015; Dai et al, 2018);. The source to sink transport processes of the Yangtze River sediments have recently attracted great interest on two aspects in terms of time scale (Fan et al., 2012). One is the attempt to decode the impact of human activities in river basin on spatio-temperal variation in sediment delivery processes, especially the industrial and agricultural development, dam construction (Yang et al., 2014; Yang et al., 2015; Dai et al., 2016; Luan et al., 2016; Dai et al., 2018; Yang et al., 2018; Guo et al., 2019; Mei et al., 2021; Yang et al., 2021). The other is to set up the provenance distinguishing models, to achieve robust understanding the evolution of Yangtze River in geological time and its relationship with the gigantic geomorphological changes in East Asia (uplift of the Tibet Plateau, the regional extension throughout eastern China) during the Late Cenozoic, and evolving east Asian monsoon (Yang et al., 2006; Gu et al., 2014; Yue et al., 2016; Liu et al., 2018; Yue et al., 2019; Zhang et al., 2019; Zheng et al., 2019; Yang et al., 2021).

A number of approaches including isotopic geochronology, geochemical compositions, mineral assemblages have been used to trace the source-sink processes of the Yangtze River sediment (Chappell et al., 2006; Yang et al., 2007; He et al., 2013; Zheng et al., 2013; Luo et al., 2014; Li et al., 2016; Yue et al., 2016; Yue et al., 2019; Yang et al., 2021). It is still difficult to fingerprint the discrimination of individual tributaries accurately for huge drainage area, complex tectonics, and various climatic environments (Fan et al., 2012; Yang et al., 2021). Therefore, it still needs to refine the sediment fingerprinting methodology and promote comparison studies between the surface sediments and sedimentary strata.

The magnetic properties of sediments have documented rich information on the environmental evolution (Liu et al., 2012). Previous studies have explored the magnetic properties of the Yangtze River sediments. However, they have primarily focused on local areas in the basin (Zhang et al., 2002; Niu et al., 2008; Zhou et al., 2008; Zhang et al., 2009; Luo et al., 2011; Luo et al., 2013; Pan et al., 2015; Chu et al., 2016). Systematic studies targeting the entire Yangtze River basin are limited. Here, we collected surface sediments from the mainstream and major tributaries of the Yangtze River basin, and systematically analysed their magnetic properties, and further discussed their implications for source-sink progress of sediment transport.

# 2 Background of study area

The Yangtze River basin lies between 90°33′–122°25′ E, 24° 30′–35°45′ N. Geographically, the Yangtze River is approximately 6300 km long, and is divided into the upper, middle, and lower reaches with divisions at Yichang and Hukou. The upper Yangtze River is about 4500 km long, with an elevation above 2000 m and a basin area of roughly 100*$10^4$ $km^2$. The major tributaries joining the mainstream in the upper reaches include the Yalong River, Dadu River, Min River, Tuo River, Jialing River, and Wu River. The middle Yangtze River is about 955 km long, with an elevation of 500–2000 m and a basin area of roughly 63*$10^4$ $km^2$. The main tributaries joining the mainstream in the middle reaches include the Han River, Yuan River, Xiang River, and Gan River. Poyang Lake and Dongting Lake, two major freshwater lakes in China, are also distributed in the middle reaches. The lower Yangtze River is about 938 km long, with an elevation below 500 m and a basin area of roughly 12*$10^4$ $km^2$. No large rivers join the mainstream of the Yangtze River in the lower reaches.

The Yangtze River basin is generally controlled by subtropical monsoon climate. The annual average temperature decreases from east to west. Due to the large area, complex landform, and monsoon climate, the mean annual precipitation varies dramatically throughout the Yangtze River basin. The mean annual precipitation is generally less than 400 mm in the source region and typically 800–1600 mm in the central and eastern parts of the basin.

Multiple types of source rocks are distributed in the upper reaches of the Yangtze River, including large areas of the Paleozoic carbonate rocks, Mesozoic sedimentary and igneous rocks, and scattered metamorphic rocks (Figure 1, Changjiang Water Resources Commission, 1999). The Emeishan basalts are distributed in the upper basin, and their formation is closely related to the volcanic eruption triggered by the intense mantle plume activities in the Permian. The middle and lower Yangtze River basin is mainly distributed with the Paleozoic marine, Mesozoic terrestrial sedimentary rocks, and Quaternary loose sediments of fluvial and lacustrine facies.

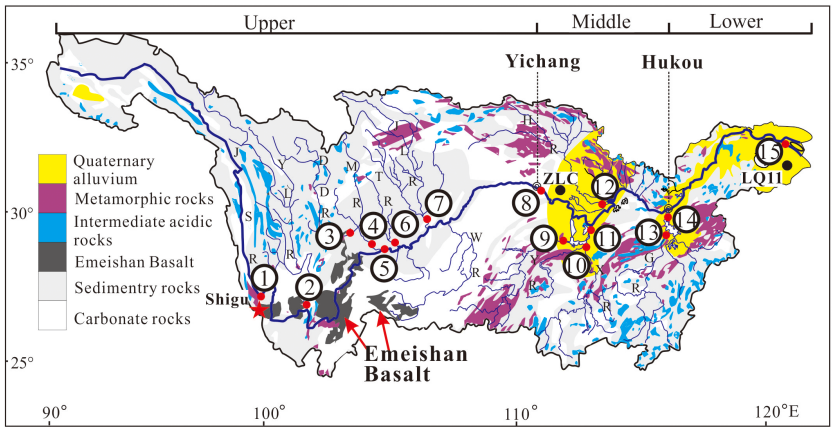


FIGURE 1
Distribution of source rocks in the Yangtze River basin and the sampling sites. 1) the large-scale Emeishan basalt block in the upper Yangtze basin; 2) sampling sites: ① Shigu (26°52′52″N, 99°57′31″E) ② Yalong River (YLR, 26°36′42″N, 101°48′00″E); ③ Dadu River (DDR, 29°33′19″N, 104°43′50″E); ④ Min River (MR, 29°35′28″N, 103°45′54″E); ⑤ Jinsha River (JSR, 26°36′42″N, 101°47′32″E); ⑥ Tuo River (TR, 29°35′39″N, 105°03′25″E); ⑦ Jialing River (JLR, 29°43′30″N, 106°32′08″E); ⑧ Three Gorges (Yichang, 30°40′47″N, 111°16′07″E); ⑨ Yuan River (YR, 29°01′50″N, 111°41′08″E); ⑩ Xiang River (XR, 27°49′27″N, 113°08′43″E); ⑪ Han River (HR, 30°22′53″N, 113°26′55″E); ⑫ Dongting Lake (DTL, 29°22′45″N, 113°05′10″E); ⑬ Gan River (GR, 28°32′28″N, 115°48′43″E); ⑭ Poyang Lake (PYL, 29°43′41″N, 116°11′51″E); ⑮ River Mouth(31°36′19″N, 121°25′26″E); the Emeishan Basalt site (star, 26°35′01″N, 101°38′36″E); 4) Zhoulao Core (ZLC), from the middle Yangtze basin, below the Three Gorges valley (Zhang et al., 2008; 30°02′09″N, 112°59′07″E); the Core LQ11 on the delta (Liu et al., 2018; 31°2′30″N, 121°23′54″E).

# 3 Methodology

Our research team collected mainstream samples in dry season (January 2013) on the floodplain at Shigu, Yibin, Yichang, and the river mouth (Figure 1). The tributary sediments were sampled at the confluences of tributaries and mainstream. To reduce random errors, we collected 2–7 surface sediment samples within a certain area around in each sampling site. A total of 65 samples were obtained from the mainstream and tributaries of the Yangtze River. Since Emeishan basalts are widely exposed in the upper Yangtze River basin, with an area of $30*10^4$ $km^2$, and their magnetic properties are distinct from those of other rock types, we collected one representative sample from the Jianchuan area in the upper basin (Figure 1).

The collected samples were dried in an oven at a low temperature of 30°C for 72 hours in the laboratory, avoiding any mineral changes (Maher, 1986). After the samples were completely dry, any plant roots or other impurities were removed from the sediments by plastic tweezers. Then, the sediments was packed into a non-magnetic plastic sample box (8 $cm^3$ capacity) for further magnetic testing. Low and high frequency susceptibility ($\chi_{lf}$ and $\chi_{lf}$) was measured at 0.47 kHz and 4.7 kHz, respectively, using a Bartington MS2 magnetometer. Each measurement consists of two replications in order to avoid measurement error. The frequency-dependent susceptibility ($\chi_{fd}$%) was calculated as $\chi_{fd}\% = (\chi_{lf} - \chi_{hf})/\chi_{lf}*100$. The anhysteretic remanent magnetization (ARM) was determined using a Dtech2000 alternating field demagnetizer (with a maximum AC magnetic field of 100 mT and a DC magnetic field of 0.04 mT). The remanent magnetization was then measured by a Minispin spinner magnetometer. After obtaining the isothermal remanent magnetization under a 1 T magnetic field using an MMPM10 pulsed-field magnetometer, the samples were rapidly placed into the Minispin spinner magnetometer to measure their remanent magnetization. In this study, the isothermal remanent magnetization obtained under a 1 T magnetic field ($IRM_{1T}$) is defined as saturation isothermal remanent magnetization (SIRM). After obtaining the SIRM, the samples were demagnetized under a 300 mT magnetic field in the opposite direction, and their remanent magnetization was measured again to derive the demagnetization parameters. S-ratio = $-IRM_{-300\ mT}$/SIRM; HIRM (the "hard" IRM) = (SIRM $-$ $IRM_{-300\ mT}$)/2. The representative samples collected were examined using a variable field translational balance (VFTB) to obtain their hysteresis loops and thermomagnetic curves. The magnetic analyses were performed at the State Key Laboratory of Estuarine and Coastal Research, East China Normal University.

# 4 Results

## 4.1 Magnetic properties of surface sediments from the mainstream

The results showed that the $\chi_{lf}$ value of the surface sediments from the mainstream firstly increased and then decreased. The minimum value was 34.16*10-8 m3/kg at Shigu. Then it rapidly rose to $230.56*10^{-8}$ $m^3$/kg at Yibin and slightly decreased to

210.50*10$^{-8}$ m$^3$/kg at Yichang. The value dropped to 68.92*10$^{-8}$ m$^3$/kg at the river mouth (Figure 2). The $\chi_{fd}$% of all surface sediment samples from the mainstream was lower than 3%, indicating magnetic mineral grains in the surface sediments were basically free of superparamagnetic (SP) particles (Thompson and Oldfield, 1986). The variation trend of $\chi_{ARM}$ was similar to those of $\chi_{lf}$ and SIRM. The $\chi_{ARM}/\chi_{lf}$ ratio gradually increased from Shigu through Yibin downstream, reaching the maximum at Yichang. Then, the value slightly decreased at the Yangtze River estuary. In comparison, the $\chi_{ARM}$/SIRM ratio exhibited a continuously increasing trend downstream, implying a gradually decreasing grain size of the magnetic minerals. The S-ratio was above 0.9, indicating the predominance of the low-coercivity ferromagnetic minerals. The HIRM value varied significantly among the sampling sites, the lowest at Shigu and the highest at Yibin (Thompson and Oldfield, 1986; Figure 2).

The variation patterns of the thermomagnetic curves for samples from different sites along the mainstream were relatively similar (Figure 3). The magnetization intensity sharply declined near 585°C and then decreased slightly, indicating a high content of magnetite and small amount of hematite in the samples. The hysteresis loops before and after paramagnetic correction were both narrow, and the closure point of the hysteresis loop after paramagnetic correction occurred at 300 mT, indicating a high abundance of low-coercivity ferromagnetic minerals (Thompson and Oldfield, 1986; Figure 4).

## 4.2 Magnetic properties of surface sediments from the tributaries

The $\chi_{lf}$ values of the surface sediments from the tributaries in the upper Yangtze River basin were generally high. The Yalong River sediments had the highest values, with a mean of 276.86*10$^{-8}$ m$^3$/kg. The Jialing River sediments had the lowest values, with a mean of 55.86*10$^{-8}$ m$^3$/kg (Figure 2). The $\chi_{lf}$ values of the surface sediments from the tributaries in the middle and lower Yangtze River basin were generally low. In which, the Han River sediments had the highest values, with a mean of 80.35*10$^{-8}$ m$^3$/kg. The Gan River sediments had the lowest values, with a mean value of 5.86*10$^{-8}$ m$^3$/kg. The SIRM of the surface sediments from the tributaries exhibited similar variation trends to the $\chi_{lf}$ results. The mean SIRM of the Yalong River sediments was 51908.04*10$^{-5}$ Am$^2$/kg, significantly higher than that of the sediments from the other tributaries. The SIRM of the Gan River sediments was the lowest, with a mean value of only 669.22*10$^{-5}$ Am$^2$/kg. Except for the surface samples from Dongting Lake, the $\chi_{fd}$% of each tributary sample was less

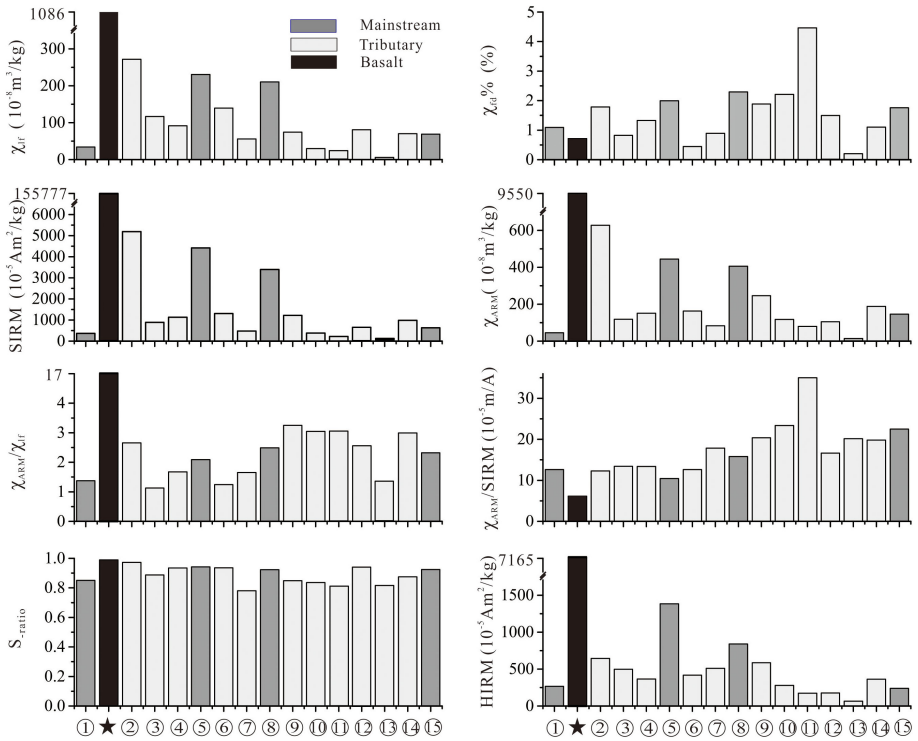


FIGURE 2
Magnetic parameters of the surface sediments from the mainstream and tributaries of the Yangtze River and those of the Emeishan basalts.

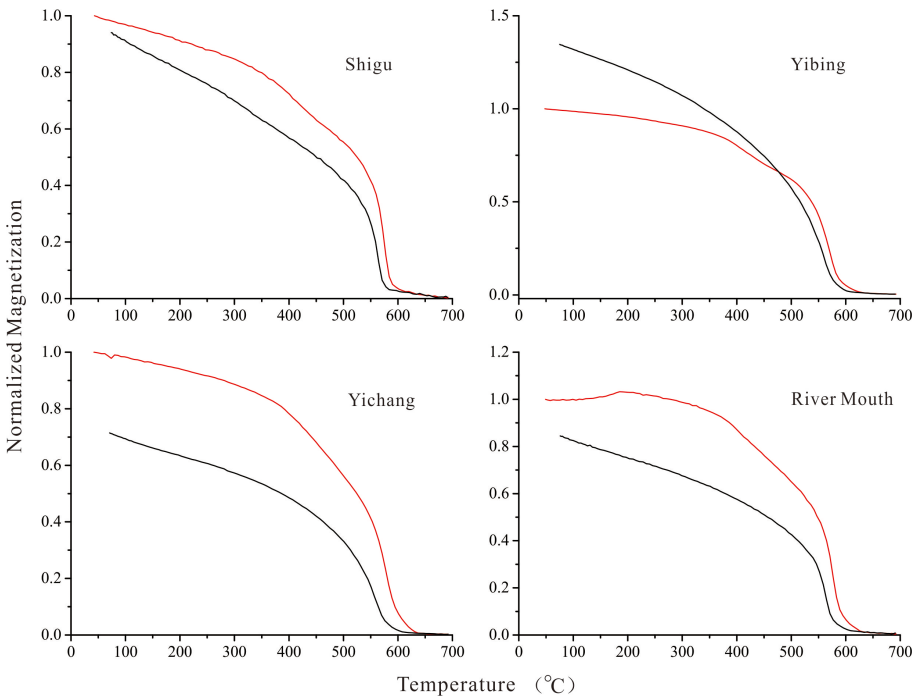


FIGURE 3
Thermomagnetic curves of the surface sediments from the Yangtze River basin (red: heating; black: cooling).

than 3%, indicating that the magnetic mineral grains in the surface sediments from most tributaries were essentially free of SP particles. Except for the Yalong River sediments, the $\chi_{ARM}$ of the surface sediments from each tributary in the upper Yangtze River basin was 83.23–162.79*$10^{-8}$ $m^3$/kg, with minor fluctuations. The $\chi_{ARM}/\chi_{lf}$ and $\chi_{ARM}$/SIRM of most samples from the upper reaches were significantly smaller than those from the middle and lower reaches, indicating that the grain size of magnetic minerals from the tributaries in the upper Yangtze River basin was generally coarser than those from the tributaries in the middle and lower basins. The S-ratio and HIRM of most samples from the tributaries in the upper Yangtze River basin were slightly higher than those from the tributaries in the middle and lower basins.

The thermomagnetic curves of the representative samples generally exhibit similar patterns. The magnetization intensity sharply declined near 585°C and then decreased slightly, indicating a high content of magnetite and small amount of hematite in the samples (Figure 5). The hysteresis loops before and after paramagnetic correction were both narrow, and the closure point of the hysteresis loop after paramagnetic correction occurred at 300 mT, indicating a high abundance of low-coercivity ferromagnetic minerals, such as magnetite (Figure 6). Compared to the hysteresis loops of the other samples, those of the Dongting Lake samples, before and after paramagnetic correction, were distinct, indicating a higher content of paramagnetic minerals in the Dongting Lake sample. Moreover, the hysteresis loop after paramagnetic correction was still not completely closed at 500 mT, implying that the sample also contained certain amounts of high-coercivity magnetic minerals. The magnetization intensity of the samples from the Gan River and Xiang River decreased to a certain extent at 750 mT, indicating a certain amount of diamagnetic minerals in samples.

## 4.3 Magnetic properties of the Emeishan basalt

The magnetic parameters of the Emeishan basalt sample from Jianchuan (Figure 2) are as follows. The $\chi_{lf}$ and SIRM exhibited significantly high values of 1086.73*$10^{-8}$ $m^3$/kg and 155776.63*$10^{-5}$ $Am^2$/kg, respectively. The $\chi_{ARM}/\chi_{lf}$ and $\chi_{ARM}$/SIRM ratios were 9.59 and 6.69*$10^{-5}$ A/m, respectively. The S-ratio of the sample was 0.99, showing the predominance of the low-coercivity ferromagnetic minerals in the magnetic particles.

The thermomagnetic curves of the Emeishan basalt sample (Figure 7) showed the following properties. The magnetization intensity remained roughly constant before reaching 585°C and then dropped sharply near 585°C, indicating a high abundance of representative coarse-grained magnetite. The hysteresis loops before and after paramagnetic correction (Figure 7) almost

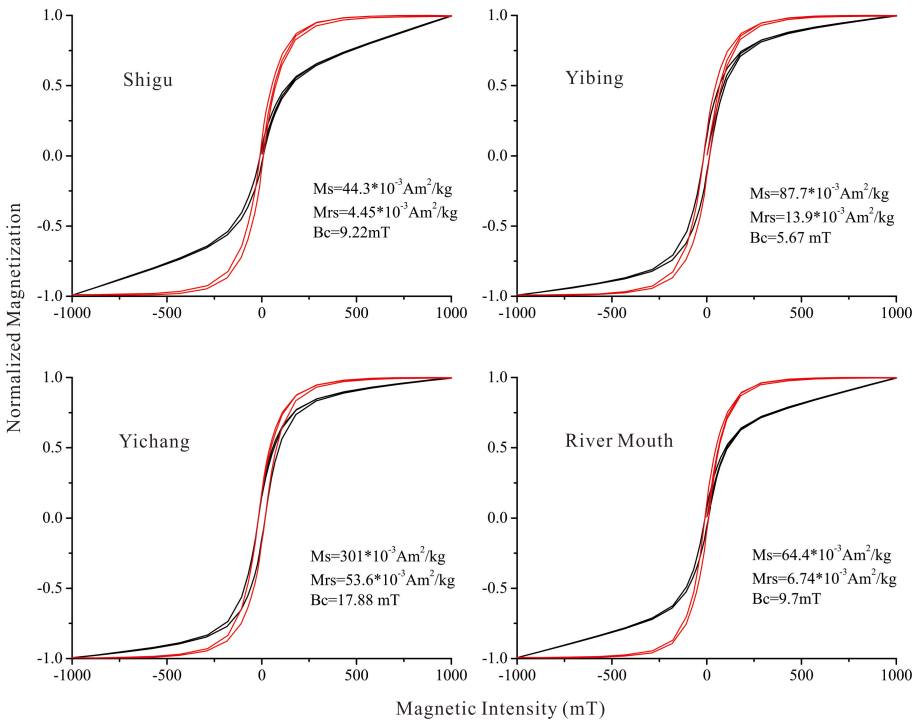


FIGURE 4
Hysteresis loops of the surface sediments from the Yangtze River basin (black: before paramagnetic correction; red: after the correction; Ms, Mrs and Bc in the figures means saturation magnetization, saturation remanent magnetization, and saturation coercivity respectively).

completely overlapped, and the loop of magnetization intensity was completely closed under a magnetic field of 100 mT, implying that low-coercivity magnetic minerals dominate the magnetic particles.

# 5 Discussion

## 5.1 Relationship between magnetic properties of the surface sediments and source rocks in the basin

The fluvial clastic deposits may be subjected to hydrodynamic sorting during the transportation process. The statistical results show that the sediment flux into the sea before the closure of the Three Gorges Dam primarily came from the upper Yangtze River basin (Chen et al., 2001). The heavy mineral assemblages and trace element properties of magnetite in the sediments from the estuary were highly consistent with those in the sediments from the upper basin, which means that the hydrodynamic sorting effect on the minerals was overall not significant (Yue et al., 2016).

Significant differences exist in the magnetic properties of various rocks. The magnetic susceptibility ($\chi_{lf}$) primarily depends on the content of ferromagnetic minerals (Thompson and Oldfield, 1986). The $\chi_{lf}$ of basic and ultrabasic rocks is significantly high, typically greater than $1000*10^{-8}$ $m^3/kg$, and the average of basalts can reach $1800*10^{-8}$ $m^3/kg$. The average $\chi_{lf}$ of granite is $20*10^{-8}$ $m^3/kg$. The $\chi_{lf}$ of metamorphic rocks is generally low, with an average of $5*10^{-8}$ $m^3/kg$ for common gneisses and $1*10^{-8}$ $m^3/kg$ for slates. Sedimentary rocks have the lowest susceptibility overall, generally less than $10*10^{-8}$ $m^3/kg$ (Thompson and Oldfield, 1986).

In the lower Yalong River basin, the outcrops were dominated by Paleozoic carbonate rocks, low-grade metamorphic rocks, and Emeishan basalts (Changjiang Water Resources Commission, 1999). Among the tributaries in the basin, the mean $\chi_{lf}$ of the surface sediments from the Yalong River was $276.86*10^{-8}$ $m^3/kg$, and significantly higher than that of the samples from other tributaries. The $\chi_{lf}$ of the Emeishan basalt sample from Jianchuan was $1086.73*10^{-8}$ $m^3/kg$, indicating that the widely exposed Emeishan basalts have a significant contribution to the $\chi_{lf}$ of the surface sediments in the Yalong River.

The $\chi_{lf}$ of the samples from the tributaries in the middle and lower basin was typically low except Han River. The $\chi_{lf}$ of the Han River sediments was relatively high, with an average of $80.35*10^{-8}$ $m^3/kg$. Quaternary loess deposits are widely distributed in the upper Han River basin. The $\chi_{lf}$ of the loess

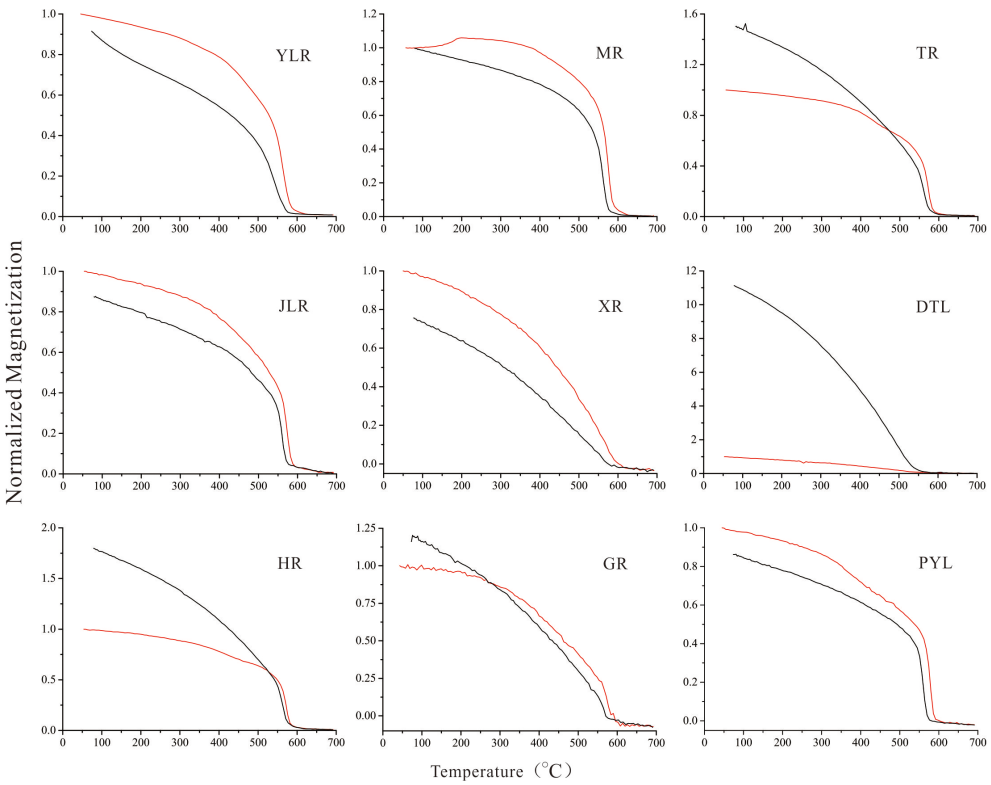


FIGURE 5
Thermomagnetic curves of the surface sediments from the mainstream of the Yangtze River (red: heating; black: cooling).

on the Loess Plateau deposited during glacial periods was primarily 40–60*$10^{-8}$ $m^3$/kg, and the paleosols developed during interglacial periods had a susceptibility in the range of 100–200*$10^{-8}$ $m^3$/kg (Evans and Heller, 2001). The widely distributed Quaternary loess deposits within the upper Han River basin may cause the relatively high $\chi_{lf}$ of the surface sediments in the Han River.

The $\chi_{lf}$ of the surface sediments from the major tributaries in the middle and lower Yangtze River basins, such as the Xiang River, Yuan River, and Gan River, is generally low and roughly related to the types of strata exposed in these tributary basins. The surface sediments in the Dongting Lake were mainly from the Xiangjiang River and Yuanjiang River. The strata exposed in the upper Yuan River basin are primarily sandstones, slates, and the Cretaceous red beds. The Cretaceous red beds, along with a few sandy conglomerates, are widely distributed in the middle and lower basin (Changjiang Water Resources Commission, 1999). The strata exposed in the Xiang River basin are predominantly Carboniferous limestones and Cretaceous red beds. The Gan River basin is widely distributed with pre-Sinian and pre-Devonian metamorphic rocks.

The outcrops in the area from the source of Yangtze River to Shigu were mainly carbonate and clastic rocks, scattered with a few intermediate-acid intrusive and metamorphic rocks, whose $\chi_{lf}$ was generally low, thus leading to the low $\chi_{lf}$ (34.16*$10^{-8}$ $m^3$/kg) of the surface sediments at Shigu. The $\chi_{lf}$ of the surface sediments in the mainstream of the Yangtze River rapidly increased to 230.56*$10^{-8}$ $m^3$/kg at Yibin and slightly decreased to 210.50*$10^{-8}$ $m^3$/kg at Yichang. The $\chi_{lf}$ of the surface sediments from the mainstream at Yibin and Yichang was slightly lower than that of the Yalong River samples but significantly higher than the samples from other tributaries in the upper Yangtze River basin. This means that the Yalong River sediments greatly contribute to the susceptibility value of the sediments in the mainstream. With the addition of the low-susceptibility clastic materials in the middle and lower reaches, the susceptibility of the sediments in the mainstream gradually decreased to 68.92*$10^{-8}$ $m^3$/kg at the river mouth.

## 5.2 The source-sink progress of sediment transport

The Yangtze River originates in the northeast region of the Tibetan Plateau, and flows through three major topographic regions of China before injecting into the East China Sea. A

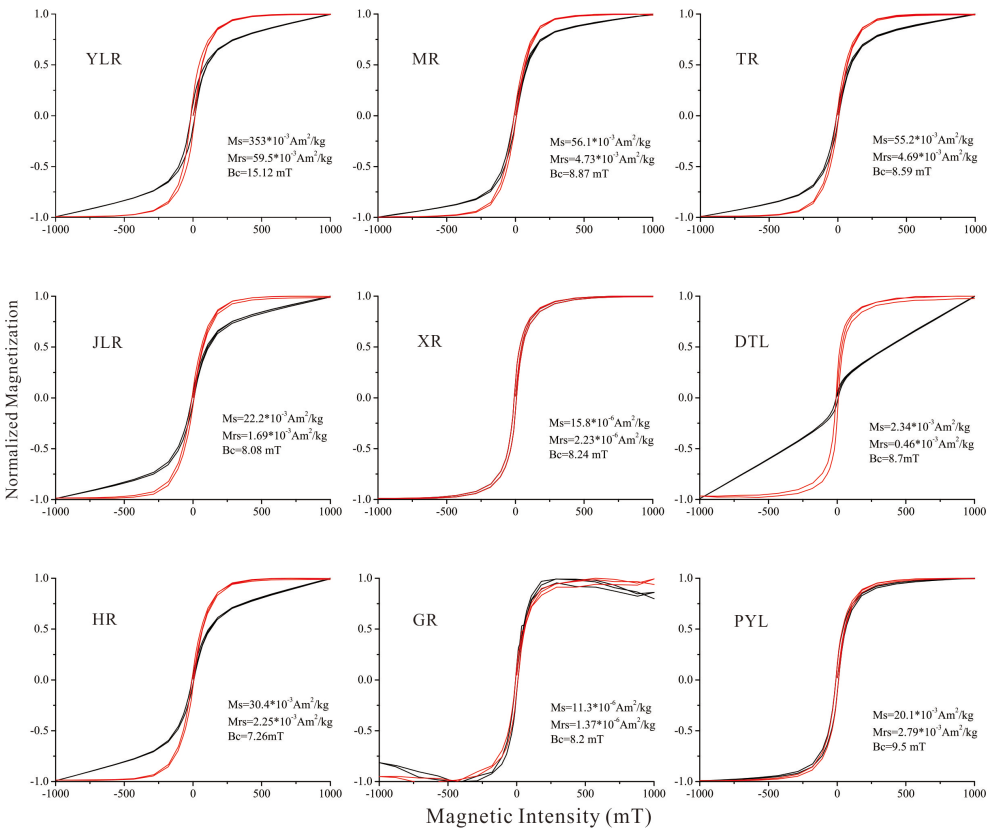


FIGURE 6
Hysteresis loops of the surface sediments from the mainstream of the Yangtze River (black: before paramagnetic correction; red: after the correction).

series of previous studies have demonstrated that the Yangtze River was formed under drastic macro-geomorphological changes in Asia during the Cenozoic such as the uplift of the Tibetan Plateau, continuous subsidence of eastern China (Clark et al., 2004; Fan et al., 2012; Yue et al., 2019). After a series of geomorphological processes such as river capture and headward erosion, a large river roughly 6300 km long was finally shaped.

Most scholars believe that the Huangling anticline in the Three Gorges area was once the drainage divide of the paleo-Yangtze River system and the paleo-Jinsha River system (Clark

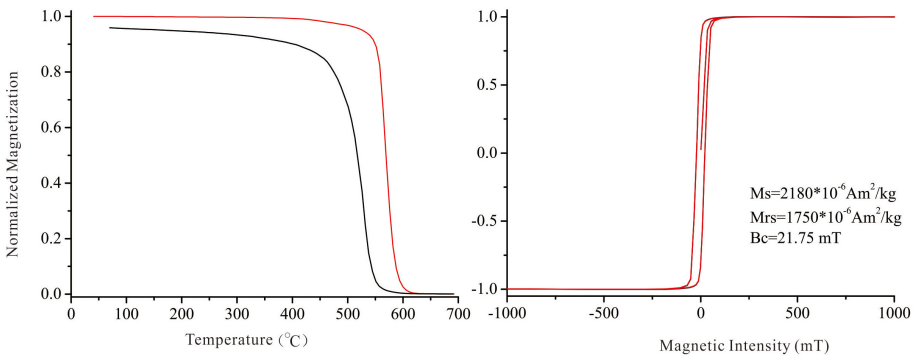


FIGURE 7
Thermomagnetic curves (left) and hysteresis loops (right) of the Emeishan basalt sample.

et al., 2004; Zheng et al., 2013). The paleo-Jinsha river flowed westward through the Sichuan Basin and eventually into the South China Sea. The paleo-Yangtze River was the prototype of the modern Yangtze River, flowing eastward into the sea. After multiple phases of river capture, the flow direction of the paleo-Jinsha River was reversed, thus forming the modern Yangtze River.

After the incision of the Three Gorges, clastic materials from the upper Yangtze River basin first arrived in the Jianghan Basin. Thick sedimentary layers in the Jianghan Basin are ideal research objects for investigating the tectonic movements in the Three Gorges area and the evolution of the Yangtze River. Magnetic analysis of the sediment from the Zhoulao core in the Jianghan Basin has shown that the $\chi_{lf}$ of the sediments significantly increases at the depth of 110 m (Figure 8, Zhang et al., 2008). At the horizons with abrupt changes in magnetic properties, the sediment grains also become coarser, indicating sharply increased hydrodynamic forces during the deposition period. These results are related to the addition of the Emeishan basalt fragments and the clastic sediments from the source region of the modern Yangtze River, which may imply a major reconstruction of the Yangtze River system.

The sediments in the upper Yangtze River basin have a significantly higher content of ferromagnetic minerals than those in the middle and lower basin (Figure 9). During the source–sink transportation process, the materials from the upper basin are mixed with the low $\chi_{lf}$ clastic materials from the middle and lower basin, thus the sediments reaching the estuary are a complex of the mixed clastic materials. The content and grain size magnetic materials in the strata at the Yangtze River delta have consistent variation trends with those in the strata in the Jianghan Basin (Figure 8). The content of the ferromagnetic minerals of the core LQ11 significantly increases at the depth of 110 m (1.2 Ma), and the magnetic mineral grains become coarser at the same time (Liu et al., 2018). The high $\chi_{lf}$ value of the strata at the Yangtze River delta implies that the clastic materials from the upper reaches of the Yangtze River, especially those eroded from the Emeishan basalts, might have reached the estuary, which also means the incision of the Three Gorges and the formation of the modern Yangtze River.

## 6 Conclusions

Our study systematically analyzed the magnetic properties of surface sediments from the mainstream and major tributaries of the Yangtze River basin, tracing the source–sink process of clastic materials. The surface sediments from tributaries in the upper basin had a significantly higher content of ferromagnetic minerals and coarser grain sizes than that in the mid-lower basin. The $\chi_{lf}$ of the Yalong River sediments in the upper basin was $276.86*10^{-8}m^3/kg$, greatly contribute to the $\chi_{lf}$ of the sediments in the mainstream, reflecting the dominant constraining role of the Emeishan basalts. The distinctive

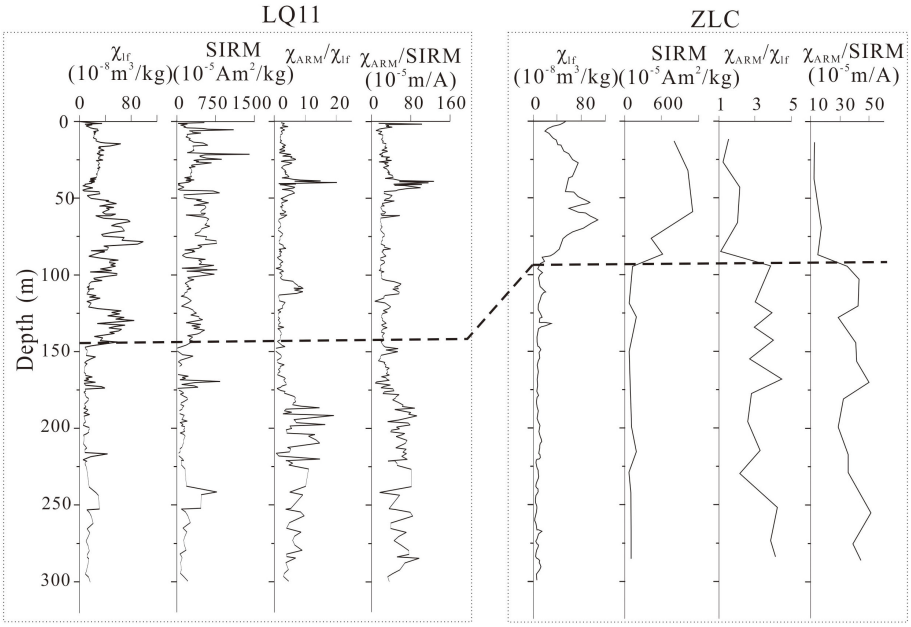


FIGURE 8
Comparison of magnetic parameters of the sediments from the LQ11 borehole at the Yangtze River delta (Liu et al., 2018) and the Zhoulao borehole in the Jianghan Basin (Zhang et al., 2008).

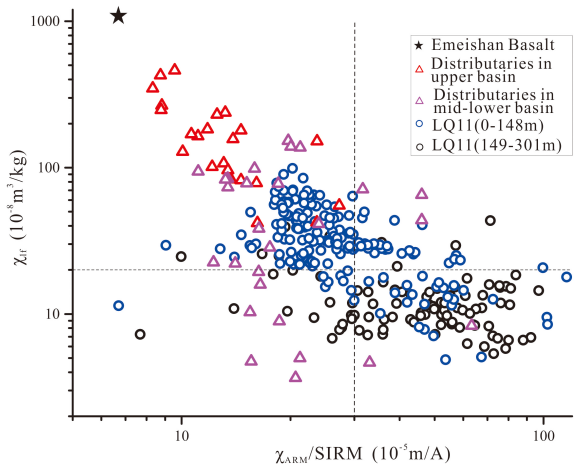


FIGURE 9
Relationship between the magnetic parameters of the sediments from the LQ11 borehole at the Yangtze River delta and the surface sediments from the Yangtze River basin.

magnetic properties of the upper core sediments from major depocenters including Jianghan basin and the Yangtze delta closely match those of surficial river sediments of the upper Yangtze basin. This may indicate the addition of clastic materials eroded from the upper basin, resulting from the cut-through of the Three Gorges during the evolution of the Yangtze River. Investigating the magnetic properties of the surface sediments in the Yangtze River basin can provide insights into the source–sink process of clastic materials and environmental changes.

## Data availability statement

The original contributions presented in the study are included in the article/Supplementary Material, further inquiries can be directed to the corresponding author.

## Author contributions

XL, JC, WY, and QW designed the research. LZ and WY wrote the manuscript, which was edited by all of the co-authors. WY did the fieldwork. XL, LZ, and LW analyzed the magnetic data. QW, CZ, JS, and BC refined the interpretations. All authors contributed to the article and approved the submitted version.

## Funding

This work was supported financially by the National Natural Science Foundation of China (No. 41901102), the National Science Foundation of China-Shandong United (No. U1706220), and the Natural Science Foundation of Shandong Province (No. ZR2019PD013 and ZR2019MD009).

## Conflict of interest

The authors declare that the research was conducted in the absence of any commercial or financial relationships that could be construed as a potential conflict of interest.

## Publisher's note

All claims expressed in this article are solely those of the authors and do not necessarily represent those of their affiliated organizations, or those of the publisher, the editors and the reviewers. Any product that may be evaluated in this article, or claim that may be made by its manufacturer, is not guaranteed or endorsed by the publisher.

## References

Changjiang Water Resources Commission (1999). *Atlas of changjiang river basin* (Beijing: Geological Publishing House), 32–33.

Chappell, J., Zheng, H. B., and Fifield, K. (2006). Yangtse river sediments and erosion rates from source to sink traced with cosmogenic 10Be, sediments from

major rivers[J]. *Palaeogeogr. Palaeoclimatol. Palaeocol.* 241, 79–94. doi: 10.1016/j.palaeo.2006.06.010

Chen, Z. Y., Li, J. F., Shen, H. T., and Wang, Z. H. (2001). Yangtze River of china, historical analysis of discharge variability and sediment flux. *Geomorphology* 41, 77–91. doi: 10.1016/S0169-555X(01)00106-4

Chu, H. M., Zhou, L. M., Huang, J., Gao, B. J., Liu, F., and Zheng, X.M. (2016). Rock magnetic properties of the point bar deposits in the upper mainstream of minjiang river and their origin. *Mar. Geol. Quat. Geol.* 36, 57–66. doi: 10.16562/i.cnki.0256-1492.2016.04.007

Clark, M. K., Schoenbohm, L. M., Royden, L. H., Whipple, K. X., Burchfiel, B. C., Zhang, X., et al. (2004). Surface uplift, tectonics, and erosion of eastern Tibet from large-scale drainage patterns. *Tectonics* 23, TC1006. doi: 10.1029/2002TC001402

Dai, Z. J., Fagherazzi, S., Mei, X. F., Chen, J. Y., and Meng, Y. (2016). Linking the infilling of the north branch in the changjiang (Yangtze) estuary to anthropogenic activities from 1958 to 2013. *Mar. Geol.* 379, 1–12. doi: 10.1016/j.margeo.2016.05.006

Dai, Z. J., and Liu, J. T. (2013). Impacts of large dams on downstream fluvial sedimentation, an example of the three gorges dam (TGD) on the changjiang (Yangtze river). *J. Hydrol.* 480, 10–18. doi: 10.1016/j.jhydrol.2012.12.003

Dai, Z. J., Mei, X. F., Stephen., E., Lou, Y., and Li, W. (2018). Fluvial sediment transfer in the changjiang (Yangtze) river-estuary depositional system. *J. Hydrol.* 566, 719–734. doi: 10.1016/j.jhydrol.2018.09.019

Evans, M. E., and Heller, F. (2001). Magnetism of loess/palaeosol sequences, recent developments. *Earth Sci. Rev.* 54, 129–144. doi: 10.1016/S0012-8252(01)00044-7

Fan, D. D., Wang, Y. Y., and Wu, Y. J. (2012). Advances in provenance studies of changjiang riverine sediments. *Adv. Earth Sci.* 27, 515–552. doi: 10.11867/j.issn.1001-8166.2012.05.0515

Gu, J. W., Chen, J., Sun, Q. L., Wang, Z. H., Wei, Z. X., and Chen, Z. Y. (2014). China's Yangtze delta, geochemical fingerprints reflecting river connection to the sea. *Geomorphology* 227, 166–173. doi: 10.1016/j.geomorph.2014.05.015

Guo, L. C., Su, N., Townend, I., Wang, Z. B., Zhu, C. Y., Zhang, Y. N., et al. (2019). From the headwater to the delta, a synthesis of the basin-scale sediment load regime in the changjiang river. *Earth Sci. Rev.* 197, 102900. doi: 10.1016/j.earscirev.2019.102900

He, M. Y., Zheng, H. B., Huang, X. T., Jia, J. T., and Li, L. (2013). Yangtze River sediments from source to sink traced with clay mineralogy. *J. Asian Earth Sci.* 69, 60–69. doi: 10.1016/j.jseaes.2012.10.001

Jiang, C., Chen, S. L., Pan, S., Fan, Y. S., and Ji, H. Y. (2018). Geomorphic evolution of the yellow river delta, quantification of basin-scale natural and anthropogenic impacts. *Catena* 163, 361–377. doi: 10.1016/j.catena.2017.12.041

Ji, H. Y., Chen, S. L., Pan, S., Xu, C. L., Tian, Y. Y., Li, P., et al. (2022). Fluvial sediment source to sink transfer at the yellow river delta, quantifications, causes, and environmental impacts. *J. Hydrol.* 608, 127622. doi: 10.1016/j.jhydrol.2022.127622

Li, X., Liu, J. P., Saito, Y., and Nguyen, V. L. (2017). Recent evolution of the Mekong delta and the impacts of dams. *Earth Sci. Rev.* 175, 1–17. doi: 10.1016/j.earscirev.2017.10.008

Liu, X. B., Chen, J., Maher, B. A., Zhao, B. C., Yue, W., Sun, Q. L., et al. (2018). Connection of the proto-Yangtze river to the East China Sea traced by sediment magnetic properties. *Geomorphology* 303, 162–171. doi: 10.1016/j.geomorph.2017.11.023

Liu, Q. S., Roberts, A. P., Larrasoaña, J. C., Banerjee, S. K., Guyodo, Y., Tauxe, L., et al. (2012). Environmental magnetism, principles and applications. *Rev. Geophys.* 50, 1–144. doi: 10.1029/2012RG000393

Li, C., Yang, S., Zhao, J. X., Dosseto, A., Bi, L., and Clark, T. R. (2016). The time scale of river sediment source-to-sink processes in East Asia. *Chem. Geolo.* 446, 138–146. doi: 10.1016/j.chemgeo.2016.06.012

Luan, H. L., Ding, P. X., Wang, Z. B., Ge, J. Z., and Yang, S. L. (2016). Decadal morphological evolution of the Yangtze estuary in response to river input changes and estuarine engineering projects. *Geomorphology* 265, 12–23. doi: 10.1016/j.geomorph.2016.04.022

Luo, C., Zheng, H. B., Tada, R., Wu, W. H., Irino, T., Yang, S. Y., et al. (2014). Tracing sr isotopic composition in space and time across the yangtze river basin - sciencedirect. *Chem. Geol.* 388, 59–70. doi: 10.1016/j.chemgeo.2014.09.007

Luo, Y., Zhang, W. G., Liu, Y., and Liu, Y. (2011). Magnetic properties of sediments from the major tributaries of jialing river and their implications for provenance identification. *J. Ocean Univ. China* 2, 99–107. doi: 10.3969/j.issn.1000-5641.2011.02.013

Luo, C., Zheng, Y., Zheng, H. B., Wang, P., He, M. Y., and Wu, W. H. (2013). Magnetic properties of suspended sediment in the Yangtze river and its provenance implications. *Quat. Sci.* 33, 684–696. doi: 10.3969/j.issn.1001-7410.2013.04.06

Maher, B. A. (1986). Characterisation of soils by mineral magnetic measurements, phys. *Earth Planet. Inter.* 42, 76–92. doi: 10.1016/S0031-9201(86)80010-3

Mei, X. F., Dai, Z. J., Stephen, E., Zhang, M., Cai, H. Y., Wang, J., et al. (2021). Landward shifts of the maximum accretion zone in the tidal reach of the changjiang estuary following construction of the three gorges dam. *J. Hydrol.*, 592. doi: 10.1016/j.jhydrol.2020.125789

Milliman, J. D., and Farnsworth, K. L. (2011). *River discharge to the coastal ocean – a global synthesis* (Cambridge: Cambridge University Press).

Milliman, J. D., and Meade, R. H. (1983). World-wide delivery of river sediment to the oceans. *J. Geol.* 91, 1–21. doi: 10.1086/628741

Nel, H. A., Dalu, T., and Wasserman, R. J. (2018). Sinks and sources, assessing microplastic abundance in river sediment and deposit feeders in an austral temperate urban river system. *Sci. Total Environ.* 612, 950–956. doi: 10.1016/j.scitotenv.2017.08.298

Niu, J. L., Yang, Z. S., Li, Y. H., and Qiao., S. Q. (2008). The characteristics of the environmental magnetism in sediment from the river mouth of the changjiang river and the huanghe river and their comparison study. *Mar. Sci.* 32, 23–30. doi: 10.5194/npg-8-1-2001

Pan, D. D., Wang, Z. H., Chen, T., Gao, X. Q., Li, X., and Zhan, Q. (2015). Mineral magnetic characteristics of surficial sediments and their implications for identifying sedimentary environments at the changjiang river mouth. *Acta Oceanol. Sinic.* 37, 101–111. doi: 10.3969/j.issn.0253-4193.2015.05.010

Park, E., Loc, H. H., Lim, J., Herrin, J., and Chitwatkulsiri, D. (2021). Source-to-sink sediment fluxes and budget in the chao phraya river, Thailand, a multi-scale analysis based on the national dataset. *J. Hydrol.* 594, 1-14. doi: 10.1016/j.jhydrol.2020.125643

Syvitski, J., Peckham., S. D., Hilberman., R., and Mulder, T. (2003). Predicting the terrestrial flux of sediment to the global ocean, a planetary perspective. *Sediment. Geol.* 162, 5–24. doi: 10.1016/S0037-0738(03)00232-X

Thompson, R., and Oldfield, F. (1986). *Environmental magnetism* (London: George Allen and Unwin), 1–227.

Wang, H. J., Saito, Y., Bi, N. S., Sun, X., and Yang, Z. S. (2011). Recent changes of sediment flux to the western pacific ocean from major rivers in East and southeast Asia. *Earth Sci. Rev.* 108, 80–100. doi: 10.1016/j.earscirev.2011.06.003

Wittmann, H., Malusà, M. G., Resentini, A., Garzanti, E., and Niedermann, S. (2016). The cosmogenic record of mountain erosion transmitted across a foreland basin, source-to-sink analysis of *in situ* 10Be, 26Al and 21Ne in sediment of the po river catchment[. *Earth. Planet. Sci. Lett.*, 452, 258–271. doi: 10.1016/j.epsl.2016.07.017

Yang, S. Y., Jiang, S. Y., Ling, H. F., Xia, X. P., Sun, M., and Wang, D. J. (2007). Sr-Nd Isotopic compositions of the changjiang sediments, implications for tracing sediment sources. *Sci. China* 50, 1556–1565. doi: 10.1007/s11430-007-0052-6

Yang, S. Y., Li, C. X., and Yokoyama, K. (2006). Elemental compositions and monazite age patterns of core sediments in the changjiang delta, implications for sediment provenance and development history of the changjiang river. *Earth. Planet. Sci. Lett.* 245, 762–776. doi: 10.1016/j.epsl.2006.03.042

Yang, S. L., Milliman, J. D., Xu, K. H., Deng, B., Zhang, X. Y., and Luo, X. X. (2014). Downstream sedimentary and geomorphic impacts of the three gorges dam on the Yangtze river. *Earth Sci. Rev.* 138, 469–486. doi: 10.1016/j.earscirev.2014.07.006

Yang, C. F., Vigier, N., Yang, S. Y., Revel, M., and Bi., L. (2021). Clay Li and Nd isotopes response to hydroclimate changes in the changjiang (Yangtze) basin over the past 14,000 years. *Earth. Planet. Sci. Lett.* 561, 116793. doi: 10.1016/j.epsl.2021.116793

Yang, S. L., Xu, K. H., Milliman, J. D., Yang, H. F., and Wu, C. S. (2015). Decline of Yangtze river water and sediment discharge, impact from natural and anthropogenic changes. *Sci. Rep.* 5, 1-14. doi: 10.1038/srep12581

Yang, H. F., Yang, S. L., Meng, Y., Xu, K. H., Luo.X.X. Wu, C. S., et al. (2018). Recent coarsening of sediments on the southern Yangtze subaqueous delta front, a response to river damming. *Continent. Shelf Res.* 155, 45–51. doi: 10.1016/j.csr.2018.01.012

Yang, H. F., Yang, S. L., Xu, K. H., Milliman, J. D., Wang, H., Yang, Z., et al. (2018). Human impacts on sediment in the Yangtze river, a review and new perspectives. *Glob. Planet. Change* 162, 8–17. doi: 10.1016/j.gloplacha.2018.01.001

Yue, W., Liu, J. T., Zhang, D., Wang, Z. H., Zhao, B. C., Chen, Z. Y., et al. (2016). Magnetite with anomalously high Cr2O3 as a fingerprint to trace upper Yangtze sediments to the sea. *Geomorphology* 268, 4–20. doi: 10.1016/j.geomorph.2016.05.032

Yue, W., Yang, S. Y., Zhao, B. C., Chen, Z. Y., and Chen, J. (2019). Changes in environment and provenance within the changjiang (Yangtze river) delta during pliocene to pleistocene transition. *Mar. Geol.* 416, 105976. doi: 10.1016/j.margeo.2019.105976

Zhang, Y.F., Li, C.A., Wang, Q.L., Chen, L., Ma, Y.F., and Kang, C.G. (2008). Magnetism parameters characteristics of drilling deposits in Jianghan Plain and indication for forming of the Yangtze River Three Gorges. China. *Sci. Bull.* 53, 584–590. doi: doi:10.1007/s11434-008-0111-1

Zhang, J., Wan, S., Clift, P. D., Huang, J., and Zhang, X. (2019). History of yellow river and yangtze river delivering sediment to the yellow sea since 3.5ma, tectonic or climate forcing? *Quat.Sci. Rev.* 216, 74–88. doi: 10.1016/j.quascirev.2019.06.002

Zhang, W. G., Yu, L. Z., and Lu, M. (2002). Relationship between magnetic properties and grain sizes in intertidal sediments of the Yangtze estuary, China. *Sci. China* 32, 783–792. doi: 10.3321/j.issn,1006-9267.2002.09.010

Zheng, H. B., Clift, P. D., Wang, P., Tada, R., Jia, J. T., He, M. Y., et al. (2013). Pre-Miocene birth of the Yangtze river. *Proc. Natl. Acad. Sci. U.S.A.* 110, 7556–7561. doi: 10.1073/pnas.1216241110

Zheng, Y., Yang, S., and Deng, C. (2019). Provenance and climate changes inferred from magnetic properties of the sediments from the lower yangtze river (china) during the last 130 years. *J. Asian Earth Sci.* 175, 128–137. doi: 10.1016/j.jseaes.2019.01.036

Zhou, L. M., Zheng, X. M., Wang, H., Wang, X. Y., Huang, D. F., and Song, L. H. (2008). Magnetic properties of sediments in the middle and lower reaches of the Yangtze river. *J. Ocean Univ. China* 6, 24–31. doi: 10.3969/j.issn.1000-5641.2008.06.004

frontiers | Frontiers in Marine Science

TYPE Original Research
PUBLISHED 20 February 2023
DOI 10.3389/fmars.2023.1107530



OPEN ACCESS

EDITED BY
Tim Rixen,
Leibniz Centre for Tropical Marine Research (LG), Germany

REVIEWED BY
Peter Feldens,
Leibniz Institute for Baltic Sea Research (LG), Germany
Qiliang Sun,
China University of Geosciences Wuhan, China
Jian Hua Gao,
Nanjing University, China

*CORRESPONDENCE
Daidu Fan
ddfan@tongji.edu.cn

SPECIALTY SECTION
This article was submitted to Coastal Ocean Processes, a section of the journal Frontiers in Marine Science

RECEIVED 25 November 2022
ACCEPTED 02 February 2023
PUBLISHED 20 February 2023

CITATION
Song L, Fan D, Su J and Guo X (2023) Controls on shallow gas distribution, migration, and associated geohazards in the Yangtze subaqueous delta and the Hangzhou Bay.
*Front. Mar. Sci.* 10:1107530.
doi: 10.3389/fmars.2023.1107530



# Controls on shallow gas distribution, migration, and associated geohazards in the Yangtze subaqueous delta and the Hangzhou Bay

Lei Song[1], Daidu Fan[1,2]*, Jianfeng Su[1,3] and Xingjie Guo[1,4]

[1]State Key Laboratory of Marine Geology, Tongji University, Shanghai, China, [2]Laboratory of Marine Geology, Qingdao National Laboratory for Marine Science and Technology, Qingdao, China, [3]Zhoushan Field Scientific Observation and Research Station for Marine Geo-hazards, China Geological Survey, Zhoushan, China, [4]Shanghai Institute of Geological Survey, Shanghai, China

Shallow gas is generally extensively distributed in the Holocene muddy sediments and gas seepage has been increasingly reported to induce geohazards in coastal seas, but controls on gas distribution and migration remain elusive. This study explores gas distribution and migration in the Yangtze subaqueous delta and the Hangzhou Bay using high-resolution acoustic profiles and core data. Shallow gas is widely detected by the common presence of acoustic anomalous reflections including enhanced reflection, gas chimney, bright spot, acoustic blanking, and acoustic turbidity. The gas front depth is generally less than 17.5 m, and is meanly shallower in the Hangzhou Bay than in the Yangtze subaqueous delta because of relatively shallower water depth and coarser Holocene sediments in the Hangzhou Bay. Shallow gas is inferred to be a biogenic product, and its distribution is highly contingent on the Holocene stratal thickness and water depth. Active gas migration and seepages are evident, and recently increasing occurrences of gas seepage can be ascribed to global warming and seabed erosion due to sediment deficit. The findings warn us to pay more attention to the positive feedback loops of gas seepages with global warming and seabed erosion for the associated geohazard prediction and reduction, typically in the highly developed coastal regions.

KEYWORDS

**shallow gas, acoustic reflection, gas distribution, seabed instability, Yangtze Delta**

## 1 Introduction

Shallow gas usually refers to the gas accumulated in the sub-bottom sediments within 1,000 m of depth (Fleischer et al., 2001). According to gas formation mechanisms, shallow gas can be divided into biogenic gas and thermogenic gas (Floodgate and Judd, 1992; Ye et al., 2003). Shallow gas is usually a biogenic product in shallow water sediments (Li et al., 2010), of which methane ($CH_4$) is the primary component (Hovland and Judd, 1988; Hu et al., 2012).

The gas can migrate upward from the host sediments to produce seepages, potentially forming pockmarks on the seafloor and gas plumes in the water column (Chen et al., 2017; Chen et al., 2020). If the gas escapes further from seawater into the atmosphere, it should accelerate global warming significantly because $CH_4$ is a greenhouse gas with 20–40 times higher radiative efficiency than $CO_2$ (Letcher, 2019; IPCC, 2021). In the past few decades, the content of $CH_4$ in the atmosphere has been increasing at a rate of approximately 0.5%–1% per year (Rasmussen and Khalil, 1986; IPCC, 2021). Annual global $CH_4$ emission from natural geological sources is estimated at 18–63 Mt, and marine gas leakage contributes 5–10 Mt annually (Etiope and Schwietzke, 2019; Etiope et al., 2019). Approximately 20% of total $CH_4$ emission to the atmosphere is inferred to be sourced from shallow coastal seas, consequently attracting increased research concerns (Fleischer et al., 2001; Jaśniewicz et al., 2019).

Seismic and acoustic explorations have been widely used for investigating gas-related anomalous reflections and mapping gas distribution in sub-bottom sediments (Ye et al., 2003; Hu et al., 2012; Cukur et al., 2013; Schneider von Deimling et al., 2013: Hu et al., 2016; Yang et al., 2019). Because gas-charged sediments can effectively absorb and scatter the energy of sound waves, which rapidly attenuate inner gas-charged sediments along the vertical direction (Hovland and Judd, 1988; Ye et al., 2003; Coughlan et al., 2021; Toker and Tur, 2021; Yang et al., 2022b), stratal structures usually display acoustic anomalous reflections including acoustic turbidity, acoustic blanking, enhanced reflection, bright spot, gas chimney, and pockmark (Ye et al., 2003; Visnovitz et al., 2015; Coughlan et al., 2021; Toker and Tur, 2021). Shallow gas has been surveyed to be widely distributed in coastal zones, such as the Gulf of Mexico, the Baltic Sea, and the East China Sea (Hovland and Judd, 1988; Zhang et al., 2004; Zhang et al., 2008; Lin et al., 2015; Liu et al., 2019; Chen et al., 2020). Abundant organic matter and suitable environmental conditions are conceivably vital for microbial growth to generate biogenic gas (Lin et al., 2015; Feng, 2017). Shallow biogenic gas generally appears when the Holocene sediments reach a certain thickness (García-García et al., 2007; Flury et al., 2016; Chen et al., 2020). However, most of the $CH_4$ produced in shallow sediments can be consumed by anaerobic oxidation of methane (AOM) when $CH_4$ diffuses upwards (Mogollón et al., 2012; Mogollón et al., 2013). It is generally believed that sulfate is the most important electron acceptor in AOM, and the zone where sulfate reduction and AOM occur most strongly is called the sulfate-methane transition zone (SMTZ) (Mogollón et al., 2013; Flury et al., 2016). $CH_4$ produced in organic-rich sediments below the sulfate reduction zone may cause the dissolved $CH_4$ to become oversaturated in pore water, consequently forming gas bubbles that accumulate to produce shallow gas in the sediments (Fleischer et al., 2001).

Shallow gas has been reported to be widely distributed in the post-LGM (last glacial maximum) strata in the Yangtze Delta and the Hangzhou Bay (Li et al., 2008; Hu et al., 2016; Xu et al., 2017; Wang et al., 2018). Thick muddy strata are indicated to be rich in organic matter and formed in an anoxic setting, favoring biogenic gas generation (Lin et al., 2015; Zhang and Lin, 2017). The top border of shallow gas is named the gas front, and its depth generally varies in a wide range from a few meters to tens of meters below the seafloor (Ye et al., 2003; Hu et al., 2016; Wang et al., 2018). Though a few studies have been carried out for acoustic identification and morphological characteristics classification of shallow gas in the Yangtze subaqueous delta and the Hangzhou Bay (Hu et al., 2016; Wang et al., 2018), quantitative analyses of gas distribution and front depth have been little reported. Chen et al. (2020) proposed that the thickness of the Holocene mud wedge is a key factor to determine the front depth of shallow gas, but its internal logic and other factors need additional exploration.

The gas-charged sediments have long been considered marine geologic hazards in terms of several aspects. The shear strength of sub-bottom sediments will be reduced obviously after filling with dissolved $CH_4$, and they are more susceptible to liquefaction under the influence of currents and waves (Sills and Wheeler, 1992; Wang and Liu, 2016; Song et al., 2021). Typically, sediment liquefaction likely occurs during extreme events such as typhoons, producing the collapse of marine constructions (Sumer et al., 2006; Wang et al., 2016; Wang and Liu, 2016; Wang et al., 2019; Wang et al., 2020). Meanwhile, sediment deficit due to dam constructions and other anthropogenic activities has caused severe erosion in the Yangtze subaqueous delta and the Hangzhou Bay (Xie et al., 2013; Guo et al., 2021), which has been accused to activate gas seepages because of thinning low permeability layer above gas-charged sediments (Chen et al., 2020). Considering the shallow burial depth of shallow gas in the study area, the effect of seabed erosion on gas preservation needs further investigation.

Therefore, this study is dedicated to identifying shallow gas-related anomalous acoustic reflections and mapping the gas front depth in the Yangtze subaqueous delta and the northern Hangzhou Bay, where the sedimentation regime has recently shifted from rapid deposition into severe erosion due to sediment deficit (Xie et al., 2013; Guo et al., 2021). Then, acoustic and core data are combined to probe the important influencing factors on gas distribution patterns. Ultimately, potential geological hazards related to recent shallow gas activities will be discussed.

## 2 Study area

The study area consists of the Yangtze subaqueous delta and the Hangzhou Bay (Figure 1). The Yangtze Estuary is influenced by semidiurnal tides, and the average tidal range is 2.6 m with a maximum tidal range of 4.6 m (Fan et al., 2004; Fan et al., 2017). The estuary is influenced more frequently by wind waves and less by swells. The Hangzhou Bay features a funnel shape with a rapid landward increase in tidal ranges (Ni et al., 2003; Xie et al., 2013; Xie et al., 2017). Due to the effect of the Coriolis force, the high tide level on the north shore is much higher than that on the south shore, while the low tide level on the south shore is higher than that on the north shore, resulting in a greater tidal difference between the opposite shores of the Hangzhou Bay (Yang et al., 2011; Luan et al., 2021). The bay is mainly influenced by wind waves, and large waves are induced by typhoons in summer and cold fronts in winter (Liu, 2019).

Deep incised valleys of a few tens of meters were formed at the present Yangtze Delta and the Hangzhou Bay during the LGM when the sea level dropped >130 m below the present sea level (Li et al., 2008; Li et al., 2014; Su et al., 2020). These paleo-incised valleys experienced rapid filling after the post-LGM transgression (Li et al.,

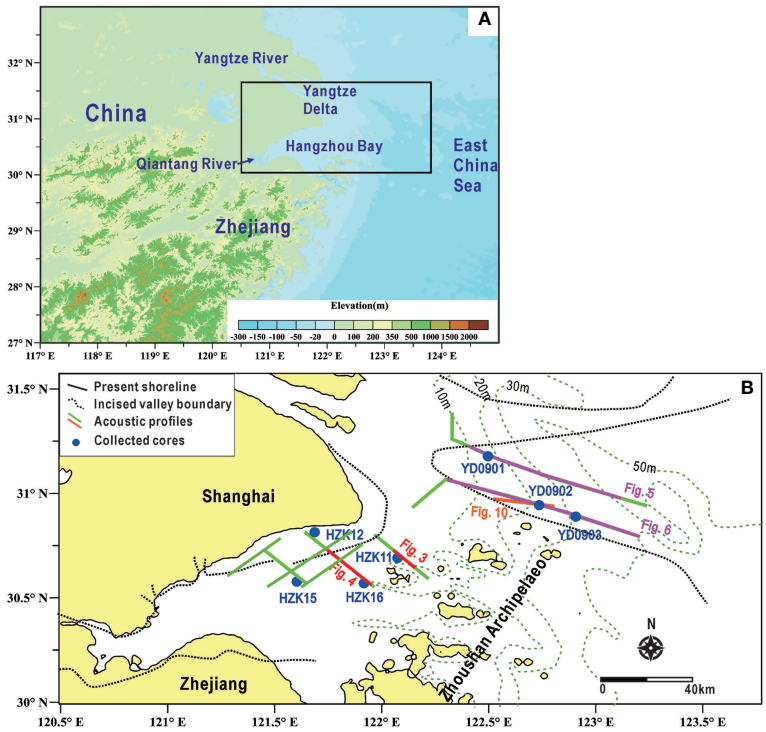


FIGURE 1
Geographical locations of the Yangtze Delta and the Hangzhou Bay **(A)**, and the distribution of shallow acoustic survey profiles and cores **(B)**. Light green dashed lines with numbers denote isobaths in meters.

2008; Zhang et al., 2013a; Lin et al., 2015; Zhang and Lin, 2017; Su et al., 2020). Transgressive surface (TS) is considered as the bottom interface during initial transgression, and maximum flooding surface (MFS) was formed during maximum transgression, occurring at 7.5 ka BP in the present Yangtze Delta area (Li et al., 2014; Su et al., 2017). The transgressive system tract (TST) represents deposition occurring between TS and MFS, and the highstand system tract (HST) is formed above MFS. The HST is further subdivided into early highstand system tract (E-HST) and late highstand system tract (L-HST) using the isochron of 2 kyr BP. Thick Holocene fine-grained sediments bear high TOC content of 0.54%–1.13% (Wang et al., 2012; Zhan et al., 2012), favoring shallow biogenic gas generation (Lin et al., 2010; Zhang et al., 2013a; Lin et al., 2015).

Annual average runoff of the Yangtze River at the Datong gauging station varied insignificantly in the past 60 years (Luan et al., 2021; Yang et al., 2022). However, the suspended sediment discharge has decreased dramatically by approximately 70% after the operation of the Three Gorges Dam (TGD) (Guo et al., 2021). Accordingly, the Yangtze subaqueous delta has shifted from rapid siltation to remarkable erosion, and erosion has recently expanded toward the Hangzhou Bay, which formerly receives a huge sediment supply from the Yangtze Estuary through strong tides (Xie et al., 2013; Xie et al., 2017).

## 3 Data and methods

Two acoustic surveys were carried out in July 2011 and August 2012, respectively. Acoustic profiles in the Yangtze subaqueous delta were collected in 2011 by the EdgeTech 3200XS Sub-Bottom Profiling System with the frequency 0.5–8 kHz at a ship speed of 4–5 kn (Figure 1B). It can penetrate 50 m or more below the seafloor, with a good vertical resolution of 0.12 m. In 2012, the GEO-SPARK2000 Electric Spark System was employed to collect acoustic profiles in the Hangzhou Bay with the frequency 8 kHz at a ship speed of 5 kn, fired at 400-ms intervals with the power of 2,000 J. Theoretically, it can detect the stratigraphic information range of 60 to 70 m below the seafloor. Towing observation operation and differential global positioning system were adopted in two surveys.

SonarWiz 5 software was applied to process all acoustic data (https://chesapeaketech.com/). After gain adjustment, automatic TVG compensation, and filtering technology, all profiles achieve the most effective visualization effect, typically reducing the banding phenomena due to discontinuities at the swath edges. After the interpretation of anomalous acoustic reflections, the gas front was identified and marked in each profile. To calculate the sediment thickness conveniently, the acoustic wave propagation velocity in sediments is set to 1,500 m/s (Chen et al., 2020). The distribution of shallow gas front depths was mapped using DIVA gridding interpolation in professional Ocean Data View software. DIVA, short for data-interpolating variational analysis, is a software tool dedicated to the spatial interpolation of *in situ* oceanographic data on a regular grid in an optimal way (https://www.seadatanet.org/Software/DIVA) (Beckers et al., 2014).

Stratal comparison in the study area was conducted using data from eight cores obtained from published papers (Table 1). Published $^{14}C$ ages were converted into calendar years BP using the Calib Rev. 8.2 program (http://calib.qub.ac.uk/calib/calib.html), and marine

biological samples were calibrated with the Marine20 curve and plant debris or organic-rich sediments with the IntCal20 curve (Stuiver and Reimer, 1993; Su et al., 2020). Meanwhile, the marine radiocarbon reservoir effect ($\Delta R$) of −96 ± 60 yr was adopted here (Southon et al., 2002; Su et al., 2020). After that, the calibrated $^{14}C$ ages under 2σ confidence intervals were selected and took their median ages as the final calibrated ages (Table 2).

# 4 Results

## 4.1 Anomalous acoustic reflections of shallow gas in sediments

Acoustic reflection characteristics of gas-charged sediments are different from gas-free sediments. Gas-charged sediments can significantly absorb and scatter the energy of sound waves, making it difficult to reflect the information of stratal internal structures. Through interpretation and classification of anomalous acoustic reflections in the study area, the anomalies include bright spots, enhanced reflections, gas chimneys, acoustic blanking, acoustic turbidity, phase reversal, and pockmark (Figure 2). Among them, the first five anomalous acoustic reflections were used to identify the presence of shallow gas in the strata.

Bright spots are characterized by strong amplitude reflection at the gas front, featuring the polarity reversal of in-phase axes of normal seismic unit interfaces (Figure 2A). Generally, the extension of bright spots in the study area is less than 1 km, occurring within 10 m below the seafloor. If gas chimneys were found below bright spots, they should be caused by gas migration from the deeper sediments (Figure 2A).

Enhanced reflections show similar strong amplitude characteristics to bright spots, but their extension can be significantly longer than bright spots (Figure 2A). Enhanced reflections can extend more than 10 km in length, showing continuous irregular strong reflections (Figure 3). It is generally believed that enhanced reflections should occur at the topmost gas-charged organic-rich sediments in the sand (Judd and Hovland, 2007). Due to the buoyancy of gas, its upward migration and accumulation should produce the irregular shape of the gas front in the inconsistent sediment lithology and permeability. The depth of enhanced reflections varies greatly from 2 m to more than 10 m below the seafloor (Figures 2A, 3), but is mostly distributed within 10 m.

Formation of the gas chimney is generally thought to be associated with gas migration upwards (Hustoft et al., 2010; Cukur et al., 2013). The gas chimney is characterized as a narrow area of vertical disturbances, where the reflection phase is undular and distorted (main performance is acoustic turbidity) compared with the surrounding horizontal and vertical gas-free sediments (Ye et al., 2003; Cukur et al., 2013; Toker and Tur, 2021) (Figures 2, 4). They serve as gas migration pathways from deep gas-charged sediments upwards. When the gas migrated upwards to reach but not penetrate the seafloor, mound-shaped features could be formed on the seabed (Figures 5, 6). When the gas could penetrate the seabed and escape, the gas plume was observed in the water column (Figure 6). Gas seepages result in the formation of submarine pockmarks. When submarine pockmarks were observed, evidence of gas migration was found in their underlain sediments (Figure 2B).

Acoustic turbidity is characterized by amorphous low-amplitude chaotic reflection, and the phase axis is chaotic and difficult to track (Figures 2B, 5, 6). Acoustic turbidity is commonly observed below enhanced reflections, bright spots, or inside gas chimneys (Figures 2, 5, and 6). As long as the sediment contains 1% of gas content, acoustic turbidity may appear (Fannin, 1980). The extension varies greatly from tens of meters inside gas chimneys to several kilometers below irregularly enhanced reflections (Figures 2A, 3). Acoustic blanking shows phase axis reflection suddenly becoming weak or even disappearing (Figure 2A). For acoustic turbidity and acoustic blanking, the internal structure of the strata is difficult to distinguish. The extension length of acoustic blanking can reach up to tens of kilometers (Figures 5, 6).

Regular gas-related reflections with clear borders can be divided into curtain-shaped, columnar-shaped, and chimney-shaped reflections according to their morphological characteristics (Figure 4). Curtain-shaped reflection having nearly vertical sidewalls refers to the horizontal extension area with a certain width of >1 km, and the gas front is nearly parallel to the bedding with the burial depth of 5–10 m below the seafloor. Columnar-shaped reflection having similar gas front and sidewall structures with the curtain-shaped reflection refers to the gas-bearing disturbance area with a limited horizontal width of 0.5–1.0 km, and the gas front depth is generally not more than 5 m. Compared with curtain-shaped and columnar-shaped reflections, chimney-shaped reflection is characterized by a smaller horizontal extension of <0.5 km and much shallower gas front, which can indicate the stronger upward migration and accumulation of gas.

TABLE 1 Summary information of cores used in this study (see Figure 1B for core locations).

| Core | Water depth (m) | Length (m) | Lon. (E) | Lat. (N) | Source |
|---|---|---|---|---|---|
| HZK11 | −10.8 | 60.8 | 122°04.586’ | 30°41.942’ | Wang et al., 2018 |
| HZK12 | −10.8 | 96.9 | 121°41.300’ | 30°46.198’ | Wang et al., 2018 |
| HZK15 | −13.0 | 53.6 | 121°36.327’ | 30°35.079’ | Wang et al., 2018 |
| HZK16 | −10.0 | 123.0 | 121°55.132’ | 30°34.706’ | Wang et al., 2018 |
| YD0901 | −21.0 | 65.2 | 122°30.011’ | 31°11.029’ | Su et al., 2017 |
| YD0902 | −23.0 | 69.1 | 122°44.348’ | 30°56.999’ | Su et al., 2020 |
| YD0903 | −36.0 | 60.2 | 122°54.550’ | 30°53.905’ | Su et al., 2017 |

TABLE 2 $^{14}C$ age data selected from seven cores in the Yangtze subaqueous delta and the Hangzhou Bay (see Figure 1B for core locations).

| Core ID | Depth (m) | Dating material | $^{14}C$ age (yr BP) | Calibrated age (cal yr BP) | | | Source |
|---|---|---|---|---|---|---|---|
| | | | | 2σ range | Prob. | Median | |
| HZK11 | 2.22 | Bivalve shell | 950 ± 30 | 313–634 | 1 | 474 | Wang et al., 2018 |
| | 6.5 | Gastropod shell | 1,510 ± 30 | 793–1,185 | 1 | 989 | |
| | 9.6 | Gastropod shell | 2,260 ± 30 | 1,588–2,016 | 1 | 1,802 | |
| | 11.1 | Plant material | 8,030 ± 40 | 8,750–9,020 | 0.98 | 8,885 | |
| | 13.03 | Plant material | 8,170 ± 30 | 9,010–9,149 | 0.71 | 9,080 | |
| | 14.58 | Plant material | 8,290 ± 40 | 9,191–9,427 | 0.84 | 9,309 | |
| | 20.5 | Plant material | 8,620 ± 40 | 9,532–9,682 | 1 | 9,607 | |
| HZK15 | 11.2 | Bivalve shell | 7,800 ± 40 | 7,988–8,369 | 1 | 8,179 | Wang et al., 2018 |
| | 11.5 | Bivalve shell | 6,520 ± 40 | 6,690–7,142 | 1 | 6,916 | |
| | 26.7 | Bivalve shell | 8,580 ± 40 | 8,940–9,394 | 1 | 9,167 | |
| | 29.15 | Bivalve shell | 9,330 ± 40 | 9,806–10,313 | 1 | 10,060 | |
| | 32.8 | Bivalve shell | 9,250 ± 40 | 9,709–10,206 | 1 | 9,957 | |
| HZK16 | 9.5 | Bivalve shell | 7,640 ± 30 | 7,824–8,206 | 1 | 8,015 | Wang et al., 2018 |
| | 23.76 | Bivalve shell | 9,140 ± 50 | 9,550–10,103 | 1 | 9,827 | |
| | 27.5 | Bivalve shell | 9,550 ± 50 | 10,156–10,628 | 1 | 10,392 | |
| | 27.82 | Bivalve shell | 9,640 ± 50 | 10,227–10,740 | 1 | 10,484 | |
| | 29.9 | Bivalve shell | 9,800 ± 40 | 10,487–11,049 | 1 | 10,768 | |
| YD0901 | 1.57 | Mollusk shell | 765 ± 30 | 131–492 | 1 | 312 | Su et al., 2017 |
| | 4.01 | Mollusk shell | 790 ± 30 | 151–502 | 1 | 327 | |
| | 7.13 | Mollusk shell | 1,435 ± 30 | 725–1,109 | 1 | 917 | |
| | 7.7 | Mollusk shell | 1,690 ± 30 | 986–1,345 | 1 | 1,166 | |
| | 13.5 | Mollusk shell | 3,085 ± 35 | 2,631–3,054 | 1 | 2,843 | |
| | 14.8 | Mollusk shell | 3,670 ± 35 | 3,327–3,765 | 1 | 3,546 | |
| | 20.78 | Mollusk shell | 5,470 ± 40 | 5,558–5,958 | 1 | 5,758 | |
| | 32.77 | Mollusk shell | 6,310 ± 40 | 6,438–6,887 | 1 | 6,663 | |
| | 33.21 | Mollusk shell | 6,350 ± 40 | 6,484–6,935 | 1 | 6,710 | |
| YD0902 | 8.17 | Snail | 764 ± 36 | 659–731 | 1 | 695 | Ren et al., 2019 |
| | 11.13 | Shell | 1,543 ± 37 | 842–1,238 | 1 | 1,040 | Su et al., 2020 |
| | 14.07 | Shell debris | 2,416 ± 39 | 1,773–2,251 | 1 | 2,012 | |
| | 19.51 | Sediments | 4,703 ± 44 | 5,320–5,427 | 0.56 | 5,374 | |
| | 23.21 | Sediments | 8,791 ± 56 | 9,592–9,963 | 0.83 | 9,778 | |
| | 40.83 | Sediments | 10,325 ± 61 | 11,930–12,474 | 0.98 | 12,202 | |
| YD0903 | 4.45 | Mollusk shell | 2,490 ± 30 | 1,882–2,309 | 1 | 2,096 | Su et al., 2017 |
| | 9.59 | Mollusk shell | 3,200 ± 35 | 1,748–3,175 | 1 | 2,462 | |
| | 18.55 | Mollusk shell | 6,020 ± 40 | 6,153–6,570 | 1 | 6,362 | |
| | 22.04 | Mollusk shell | 7,400 ± 40 | 7,587–7,952 | 1 | 7,770 | |
| | 34.93 | Mollusk shell | 11,350 ± 60 | 12,601–13,007 | 1 | 12,804 | |
| | 47.58 | Mollusk shell | 13,090 ± 83 | 14,603–15,363 | 1 | 14,983 | |

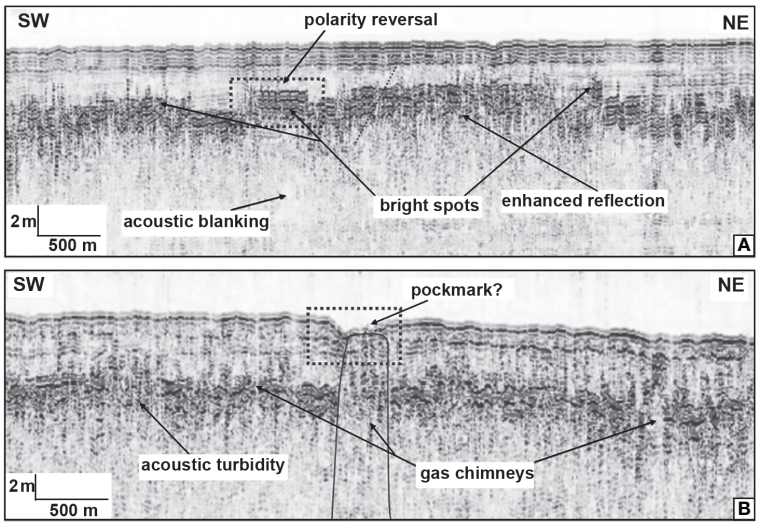


FIGURE 2
Identification and interpretation of main anomalous acoustic reflections in acoustic profiles, such as bright spot, enhanced reflection, polarity reversal, and acoustic blanking **(A)**; gas chimney, pockmark, and acoustic turbidity **(B)**.

## 4.2 Distribution and migration of shallow gas in sediments

The burial depth of the shallow gas front in the study area was mapped according to new sub-bottom acoustic data in this study and those by Chen et al. (2022). Shallow gas is widely distributed in the study area with the gas front depth ranging from 0 to 17.5 m. In comparison, gas front depths varying from 5 to 15 m in the Yangtze subaqueous delta are relatively deeper than those from 2 to 7.5 m in the Hangzhou Bay (Figure 7).

According to acoustic profiles collected in the Yangtze subaqueous delta in 2011 (Figures 5, 6), wide acoustic blanking zones were commonly found below the seafloor. Acoustic turbidity and acoustic basement could be seen between the two acoustic blanking zones (Figure 6). Seaward termination of acoustic blanking zones is present where the Holocene sediment thickness is 14 m (Figure 5) and 23.7 m (Figure 6), respectively. Because the high-altitude paleo-topography interrupts continuous variation of the Holocene sediment thickness, the distribution of acoustic blanking zones is disconnected until the Holocene sediment thickness reaches ~20.7 m (Figure 6). In the southern Yangtze subaqueous delta, gas front depths of two acoustic profiles show their different landward-changing patterns (Figures 5, 6). The gas front depth increases gradually landward along the acoustic profile across core YD0901 (Figure 5), while it increases landward first but ends with a landward decreasing trend along the acoustic profile across cores YD0902 and YD0903 (Figure 6).

In the northern Hangzhou Bay, a series of intermittent narrow acoustic blanking zones and acoustic turbidity zones were found (Figure 4). A few acoustic turbidity zones indicate that gas can migrate upwards from the deeper sediments (Figure 4). In this area, different characteristics of narrow acoustic blanking zones are associated with the gas distribution difference. If the locations of acoustic blanking zones or gas fronts were closely connected to enhanced reflections, they should have a high concentration of shallow gas with a remarkable tendency of upward migration (Figures 3, 4). However, some stratal internal structures can be diagnosed in the weak acoustic blanking zones that are not spatially interwoven with enhanced reflections, thus hinting at a relatively low concentration of shallow gas (Figure 4).

Gas plumes were observed in the water column, and some mounds were found on the seafloor in the Yangtze subaqueous delta (Figures 5, 6). The gas plumes rose ~5 m above the seafloor, and below the seafloor, gas chimney and acoustic turbidity could be

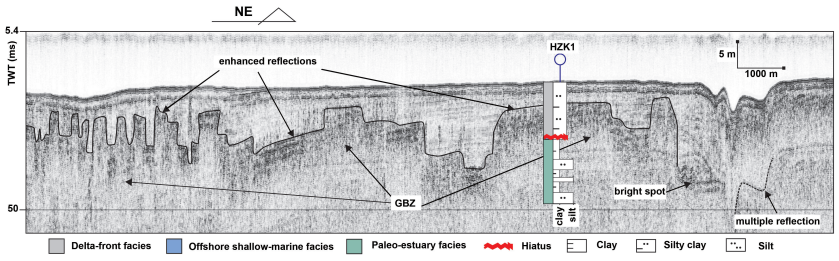


FIGURE 3
A shallow acoustic profile across core HZK11 to show irregular enhanced reflections by the presence of gas in shallow sediments in the Hangzhou Bay. GBZ is short for the gas-bearing zone. See Figure 1B for the locations of the profile and the core.

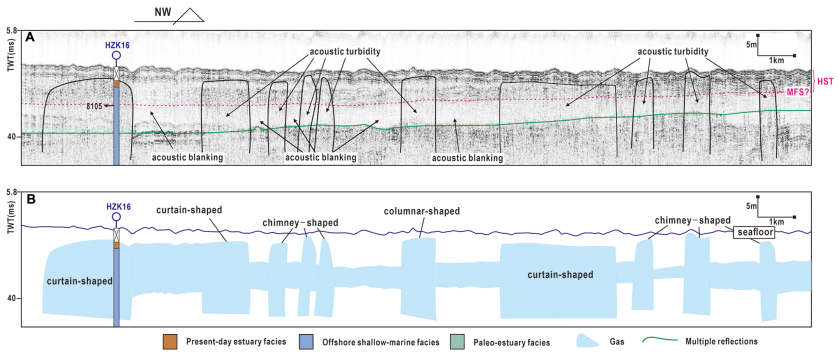


FIGURE 4
A shallow acoustic profile across core HZK16 to show different shapes of abnormal acoustic reflections by the presence of gas in shallow sediments in the Hangzhou Bay **(A)**, and interpretation of the presence of shallow gas in the acoustic profile **(B)**. See Figure 1B for the locations of the profile and the core.

identified (Figure 5). The mounds were approximately 1–2 m high, and their formation was also closely related to gas migration (Figures 5, 6). Pockmarks, with a maximum diameter of ~500 m, were observed in the Jinshan Deep Trough and near Yehuangpan island and Xiaojishan island in the northern Hangzhou Bay, and gas-related acoustic blanking and acoustic turbidity were well developed below the pockmarks. Meanwhile, pockmarks generally are accompanied by enhanced reflections and gas chimneys (Figure 8). The pockmarks with diameters exceeding 20 m were also found in the Yangtze subaqueous delta (Figure 8).

# 5 Discussion

## 5.1 Possible source for shallow gas

Shallow gas can be generated by biogenic (generally $\delta^{13}C_{CH4}$ ~ −110‰−60‰, $\delta D_{CH4}$ <110‰) or thermogenic processes (generally $\delta^{13}C_{CH4}$ >60‰, $\delta D_{CH4}$ >110‰) (Whiticar, 1999; Ye et al., 2003; Feng, 2017). The low $\delta^{13}C$ values and heavy hydrocarbon contents of shallow gas in core sediments retrieved from the Yangtze delta plain (Zhang et al., 2013a; Feng, 2017) and the southern coastal plain of Hangzhou Bay (Yang et al., 2021) indicate its biogenic origin.

In the Yangtze subaqueous delta and the Hangzhou Bay, shallow gas can be detected extensively as shown by acoustic blanking and acoustic turbidity (Figures 4–6). The gas front is distributed in the Holocene sediments of HST and TST, and its burial depth is mostly shallower than 17.5 m (Figure 7). Meanwhile, anomalous acoustic reflections were not observed in the thin Holocene sediments. Thus, the shallow gas is presumed to be biogenic gas within the Holocene deltaic or estuarine sediments.

The generation of shallow biogenic gas requires abundant organic matter in sediments to be used by methanogenic bacteria (Lin et al., 2015; Feng, 2017). The content of total organic carbon (TOC) in cores CJK08, YD0901 (Wang et al., 2012), and ZK9 (Zhan et al., 2012) is generally >0.5%, high enough for the occurrence of microbial

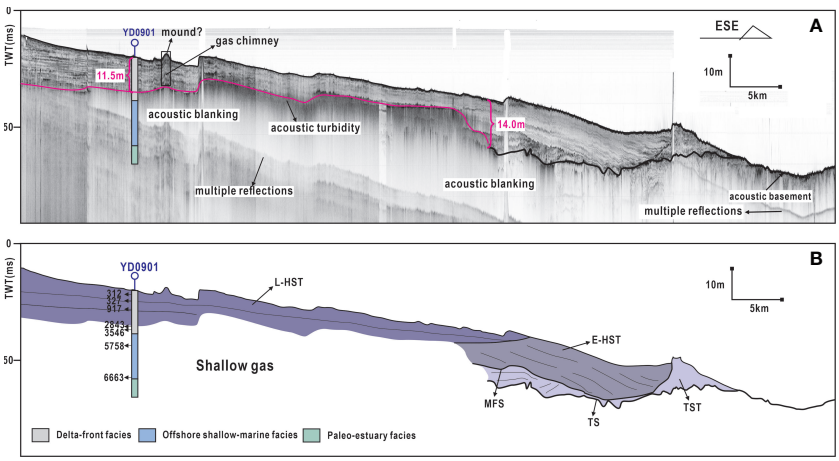


FIGURE 5
A shallow acoustic profile across core YD0901 to show gas-related anomalous reflections in the Yangtze subaqueous delta **(A)**, and interpretation of the profile **(B)**. See Figure 1B for the locations of the profile and the core. The purple line marks the gas front. TS, Transgressive surface; TST, Transgressive system tract; MFS, Maximum flooding surface; E-HST, Early highstand system tract; L-HST, Late highstand system tract.

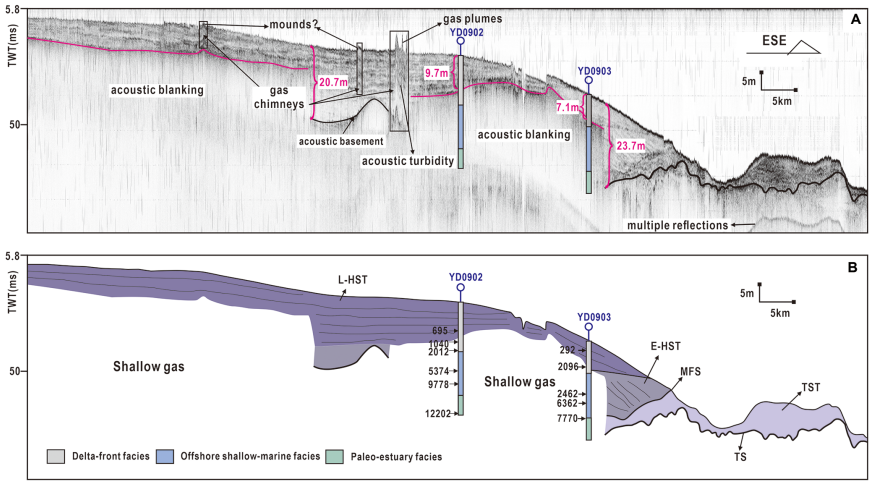


FIGURE 6
A shallow acoustic profile across cores YD0902 and YD0903 to show gas-related anomalous reflections in the Yangtze subaqueous delta **(A)**, and interpretation of the profile **(B)**. See Figure 1B for the locations of the profile and the cores. The purple line marks the gas front. TS, Transgressive surface; TST, Transgressive system tract; MFS, Maximum flooding surface; E-HST, Early highstand system tract; L-HST, Late highstand system tract.

methanogenesis (Rice and Claypool, 1981). In comparison, the upper Holocene sediments in the Yangtze subaqueous delta usually have much higher TOC content (TOC ~ 0.54%–1.13%, Wang et al., 2012; Zhan et al., 2012) than those in the Yangtze delta plain (Zhang et al., 2013b). However, shallow gas is little found in the former strata because therein $CH_4$ production could be mostly consumed by sulfate reduction in marine sediments (Mogollón et al., 2012; Mogollón et al., 2013; Flury et al., 2016). The gas front has often been detected to locate near the bottom boundary of the delta-front facies (Figures 5, 6), indicating that shallow gas should be sourced from the deeper Holocene sediments by upward migration and accumulation in the Yangtze subaqueous delta and the Hangzhou Bay.

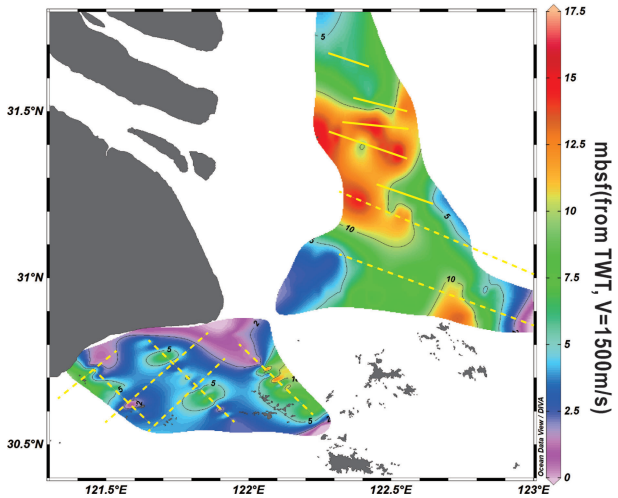


FIGURE 7
The contour map of burial depths of the shallow gas front in the Yangtze subaqueous delta and the Hangzhou Bay. The data of gas front depths in the northern Yangtze subaqueous delta are retrieved from Chen et al. (2022). Dashed yellow lines indicate the acoustic profiles acquired in this study, and solid yellow lines show the acoustic profiles investigated by Chen et al. (2022). Dashed black lines represent the isobaths.

## 5.2 Controlling factors of gas distribution

Shallow gas was usually found in relatively thicker Holocene strata as shown by large-scale distributions of acoustic blanking and acoustic turbidity (Figures 5, 6). It might disappear as the Holocene strata suddenly taper out (Figure 6). Previous studies also concluded that the Holocene stratal thickness plays a key role in controlling shallow gas generation and accumulation (García-García et al., 2007; Flury et al., 2016; Chen et al., 2020). Part of the reason is that thicker fine-grained Holocene sediments with a higher abundance of organic matter tend to generate more $CH_4$, consequently increasing the upward $CH_4$ flux to shift the SMTZ towards the shallow depth (Flury et al., 2016). Moreover, enhanced methanogenesis should produce $CH_4$ supersaturation in sediments to generate $CH_4$ gas bubbles (García-García et al., 2007; Flury et al., 2016), causing its underlying gas-charged strata to not show clear internal stratal structures because of acoustic anomalous reflections.

Increasing water depth may increase the solubility of $CH_4$ in interstitial water, making it more difficult for biogenic $CH_4$ to form gas bubbles in shallow sediments (Ulyanova et al., 2012). This is shown by the acoustic profile across cores YD0902 and YD0903 where shallow gas could be detected in the Holocene strata with its thickness exceeding 20.7 m at the water depth of ~10 m, but the stratal thickness should exceed 23.7 m at the water depth of ~20 m (Figure 6). However, at the water depth of ~20 m along the acoustic profile across core YD0901, shallow gas was observed when the Holocene stratal thickness just exceeded 14.0 m (Figure 5). It is therefore suggested that water depth is an influencing factor but not a single determining factor on the shallow gas distribution in shallow sediments.

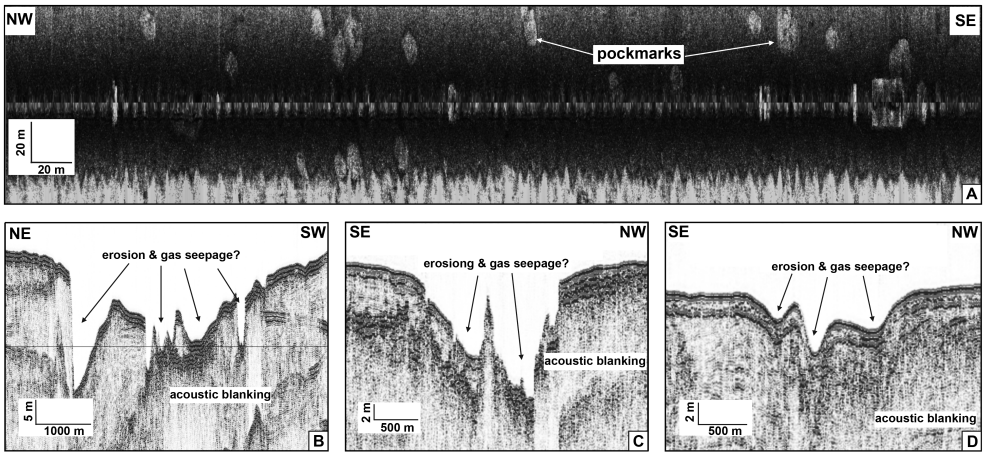


FIGURE 8
Gas-seepage-related structures in the Yangtze subaqueous delta and the Hangzhou Bay: **(A)** pockmarks detected by side-scan sonar (modified from Chen et al., 2022), and **(B–D)** seabed depressions induced by gas seepage activities disclosed by acoustic profiles.

Once the gas is generated, it tends to move upward due to buoyancy. However, upward gas migration requires overcoming the capillary force and the overburden pressure of overlying strata and water mass. Typically, the higher capillary force indicates the lower permeability of the sediment (Lin et al., 2010; Qu et al., 2013; Zhang et al., 2013b). In general, coarse-grained sediments are more beneficial for the gas surpassing capillary forces to migrate upward. The overburden pressure reduces as the water depth and/or the overlying strata thickness decrease. In the Yangtze subaqueous delta, the gas front was usually observed to locate in the delta-front facies (Figures 5, 6), and its burial depth might decrease towards the shallower water zone or the thinner stratal thickness of silt-dominated delta-front facies (Figures 6, 7, 9).

Compared with the Yangtze subaqueous delta, the gas front in the Hangzhou Bay was much shallower as a whole (Figure 7). Firstly, the mean water depth in the Hangzhou Bay is shallower than that in the Yangtze subaqueous delta, potentially leading to lower $CH_4$ solubility for the easier formation of $CH_4$ gas bubbles in the

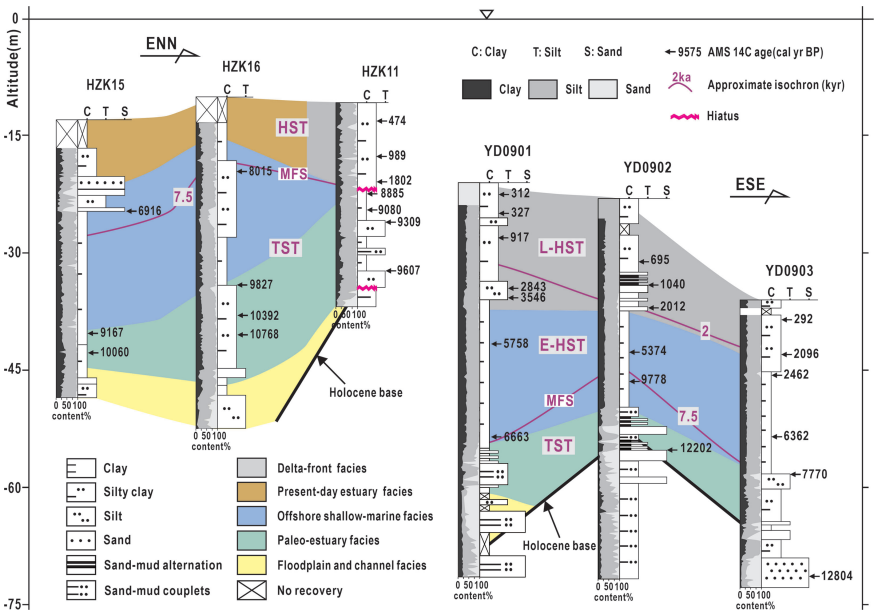


FIGURE 9
Core correlation profiles in the northern Hangzhou Bay and the Yangtze subaqueous delta show detailed information on lithology, sedimentary facies, chronology, and system tracts. The Holocene stratal base at ca. 11.7 ka BP was deduced from $^{14}C$ ages data of cores HZK11, HZK15, and HZK16 (Wang et al., 2018), and cores YD0901, YD0902, and YD0903 (Su et al., 2017; Ren et al., 2019; Su et al., 2020). See Figure 1B for the locations of the cores. TST, Transgressive system tract; MFS, Maximum flooding surface; E-HST, Early highstand system tract; L-HST, Late highstand system tract.

shallower sediments. Then, well-sorted estuarine sediment by intense tidal currents in the northern Hangzhou Bay should increase sediment permeability to ease gas upward migration (Figure 9). Moreover, recently increasing seabed erosion has been extensively observed in the northern Hangzhou Bay due to a sharp decrease in sediment input from the Yangtze River after the TGD construction (Xie et al., 2013; Xie et al., 2017; Guo et al., 2021). The seabed erosion rate in the northern Hangzhou Bay was about −0.4 m/yr during 2010–2014 (Xie et al., 2017), and the total scouring thickness at the Jinshan Deep Trough exceeded 2.4 m during the recent 30 years from 1989 to 2018 (Zhang et al., 2021). The seabed erosion has greatly reduced the thickness of cap sediments above the shallow gas, consequently lessening the overburden pressure of the gas to activate gas seepages in the Hangzhou Bay (Chen et al., 2020).

Gas front depth becoming shallower due to seabed erosion can also be observed in the Yangtze subaqueous delta (Figures 6, 10). According to the acoustic surveys, the gas front depth near YD0902 changed slightly from 9.7 m in July 2011 to 9.4 m in November 2017, which may be related to temperature changes (Martinez-Carreño and Garcia-Gil, 2013). According to the acoustic profiles, the average water depth on the west side was approximately 8.8 m in July 2011, and became 11.6 m in November 2017, indicating a seabed erosion thickness of approximately 2.8 m. Meanwhile, shallow gas front depth became shallow up to 3 m or even more at the inner Yangtze subaqueous delta (Figures 6, 10). A mound was found with its landward occurrence of a shallow acoustic turbidity zone in the seismic profile of 2017, both indicating upward gas migration activities (Figure 10). Meanwhile, the occurrence of huge negative topography at the inner delta front zone in 2017 was considered to be related with recently increasing seabed erosion in the Yangtze subaqueous delta with a water depth of 5–20 m because of sediment deficit (Yang et al., 2011; Chen et al., 2020; Guo et al., 2021).

In summary, gas distribution and accumulation in shallow deltaic/estuarine sediments are primarily determined by the stratal thickness and permeability of the Holocene sediments and water depth (Mogollón et al., 2012; Mogollón et al., 2013; Flury et al., 2016; Chen et al., 2020). Thicker Holocene strata and shallower water depth are favorable for gas generation and accumulation. Overburden pressure and low permeability of sediments above the shallow gas have significant effects on gas migration. Recently, gas migration is highly enhanced by increasing seabed erosion at the inner Yangtze delta front and the northern Hangzhou Bay due to sediment deficit, potentially triggering gas seepage and seabed instability events. Thus, more attention should be paid to this new situation for potential geological hazardous occurrences.

## 5.3 Implications of shallow gas-associated geological hazards

### 5.3.1 Gas seepage

Distinct gas seepage phenomena, such as gas plumes and pockmarks, have been commonly observed in the study area (Figures 5, 6, 8, 10). Gas seepage is closely related to gas migration in sediments. Below the gas plumes and pockmarks, gas chimneys should be visibly observed. The occurrences of mounds on the seabed and gas chimneys below the seafloor show their clear spatial overlap. The mounds are where the gas is trapped below the seabed sediments, conceivably being the initial form of pockmarks (Hovland and Judd, 1988; Koch et al., 2015; Nyman et al., 2020). When the gas pressure exceeds the overburden pressure in shallow sediments because of excessive gas accumulation or seabed erosion, it will cause the seabed sediments to dome upward. Once the accumulation pressure of the gas is high enough within the mounds, the gas will burst into the water column and the companion sediments will be carried away. Afterward, the positive topography of the mound structure should be replaced by the negative topography of pockmark structures (Chen et al., 2017).

The behavior and location of SMTZ are closely linked to the methanogenic efficiency and the gas front depth in shallow sediments. Data of Flury et al. (2016) clearly showed the changes of gas front depths and the SMTZ in gas-charged sediments and gas-free sediments, and the shallowing SMTZ promoted gas generation and accumulation in shallower sediments (Figure 11). Mogollón et al. (2013) also proposed that the gas front depth should take a key role in controlling $CH_4$ and sulfate diffusion fluxes toward the SMTZ. The shallower the gas front depth becomes, the greater the diffusion flux of $CH_4$ is. The latter has the potential to shift the SMTZ upward. In other words, the depth

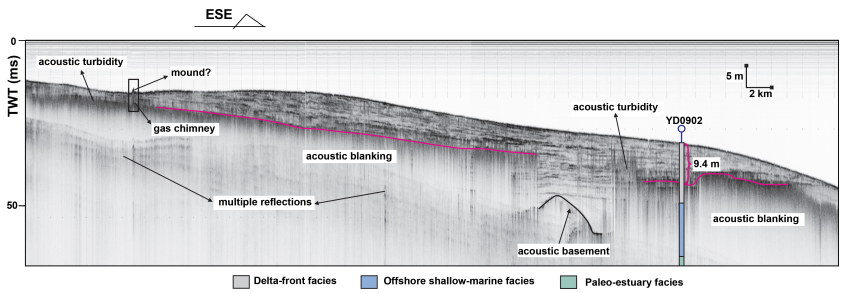


FIGURE 10
A shallow acoustic profile showing gas-related anomalous reflections in the Yangtze subaqueous delta. The purple line marks the gas front. The original acoustic profile was reproduced from Chen et al. (2022).

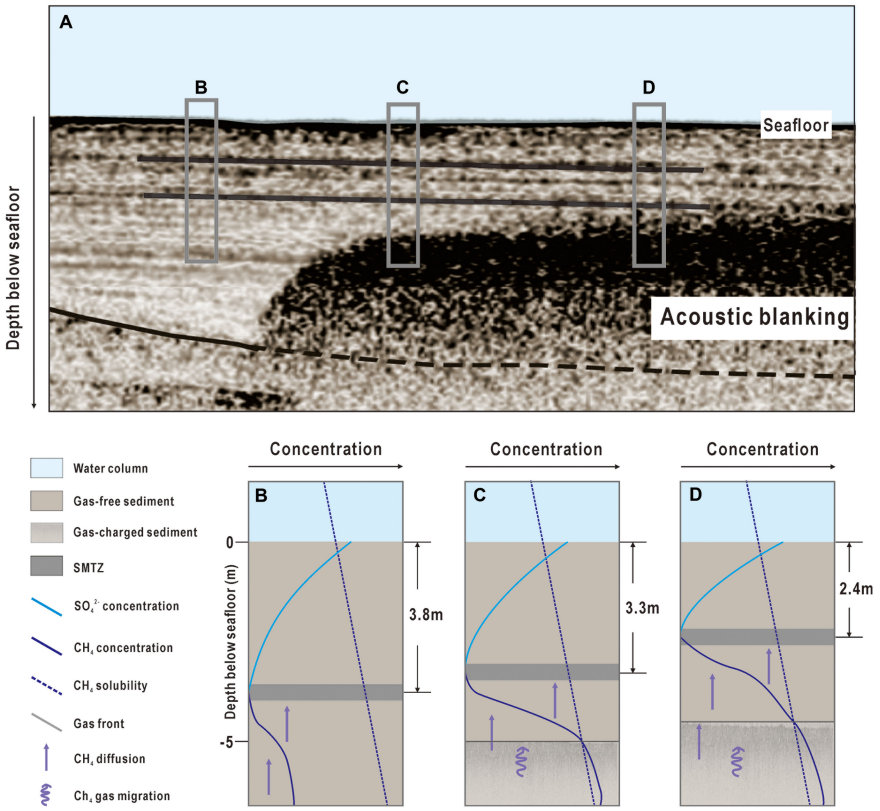


FIGURE 11
The chirp acoustic profile of gas-charged and gas-free sediment intersection area in the Aarhus Bay **(A)**, sulfate (light blue solid line), dissolved $CH_4$ (blue solid line), and $CH_4$ solubility (blue dashed line) profiles in different sediments **(B–D)** (after Flury et al., 2016).

of SMTZ and the gas front depth are closely coupled. As discussed previously, seabed erosion might cause a significant change in both the gas front depths and the SMTZ locations. Since the rapid development of dam projects and soil-water conservation projects in the Yangtze River catchment, the sediment discharge into the estuary has dramatically decreased (Guo et al., 2021; Luan et al., 2021; Yang et al., 2022a). The mean sediment discharge during the first decade after the closure of the Three Gorges Dam in 2003 dropped to a relatively low level (145 Mt $yr^{-1}$), which was only approximately 30% of the value in 1950–1968 (Yang et al., 2021). Shallow water areas between 5 m and 20 m in the Yangtze subaqueous delta and the northern Hangzhou Bay have experienced remarkable erosion (Xie et al., 2013; Guo et al., 2021). From 1989 to 2018, the volume of seabed erosion in the whole Jinshan Deep Trough area was nearly $162.7\times10^6$ $m^3$, and the average erosion thickness exceeded 2.4 m (Zhang et al., 2021). Some pockmarks and mounds were observed in these eroded areas, indicating that the gas migration and seepages responded quickly to the recently increasing seabed erosion (Figure 8).

The gas front depth could fluctuate over different time scales in response to the change in environmental factors, including porewater salinity, sediment temperature, and seafloor hydrostatic pressure (Wever et al., 2006; Diez et al., 2007; Martinez-Carreño and Garcia-Gil, 2013). Over a seasonal scale, Sun et al. (2018) reported that the concentration of $CH_4$ in bottom water in summer and autumn was significantly higher than that in spring and winter in the East China Sea. The seasonal variability of gas front depths and gas seepages was also observed in the Ría de Vigo by means of more gas plumes and shallower gas front depth in summer than in winter (Martinez-Carreño and Garcia-Gil, 2013). This could be explained by the fact that the higher sediment temperature decreases the solubility of $CH_4$ in interstitial water and increases gas pressure in sediments, consequently leading to more $CH_4$ escaping from shallow sediments during the warm season.

Moreover, global warming may trigger more $CH_4$ escaping from marine sediments. $CH_4$ is estimated to be approximately 20–40 times more effective in causing global warming than $CO_2$ (Letcher, 2019; IPCC, 2021). Thus, more caution should be paid to the loop of positive feedback between increasing global warming and more shallow gas seepages from the world's coastal areas.

### 5.3.2 Seabed instability

Marine sediments containing dissolved $CH_4$ can cause a reduction of soil strength, becoming fragile to trigger seabed erosion and seafloor construction subsidence (Huang and Han, 2020; Li, 2020). It is generally believed that the SMTZ depth determines the upper limit of dissolved $CH_4$ diffusion in shallow sediments. The gas front depth was observed to range from 2 to 5 m in

the Hangzhou Bay (Figure 7), suggesting that the dissolved $CH_4$ could even be found in the upper 2-m sub-bottom sediments. As discussed above, the occurrence of seabed erosion will lead to strengthening gas upward migration and shallowing the SMTZ. Continuous erosion due to sediment deficit in the study area should have induced an upward shift of the SMTZ, as indicated by the presence of dissolved $CH_4$ in shallower marine sediments (Wang and Liu, 2016; Song et al., 2021). Meanwhile, shallower sediments containing dissolved $CH_4$ will further enhance seabed erosion. Thus, positive feedback of seabed erosion induced by external factors (e.g., sediment deficit due to river damming projects) and internal factors (e.g., reduced soil strength by the presence of dissolved $CH_4$) could produce severe erosion, gas migration, and seepage events even under small wave conditions (Figure 12A).

The Yangtze Delta and the Hangzhou Bay are subject to storm impacts, including typhoons in summer and cold fronts in winter. Storm waves can cause sediment liquefication and submarine failures due to the sharp increase of pore pressure in water-saturated gassy sediments, leading to geological hazards or even geological disaster events (Figure 12B) (Wang and Liu, 2016; Kramer et al., 2017; Wang et al., 2019; Gupta et al., 2022). In the Hangzhou Bay, the oil and gas pipelines were reported to be destroyed a few times during typhoon events as indicated by newly produced large pockmarks (Cui et al., 2014; Li, 2020). Sometimes, the pipelines can be broken by liquefaction-induced subsidence as shown by the increased burial depth of oil pipeline reaching up to 2 m after the strike of typhoon "SWAN" in the Hangzhou Bay. More frequent and powerful storms are expected in the warming earth; thus, the instability of shallow gas-charged sediments in the highly developed coastal seas deserves more attention to build up early warming capability for hazard and disaster prediction and reduction.

## 6 Conclusion

Shallow gas is explored and has been found to extensively exist in the Holocene muddy sediments in the Yangtze subaqueous delta and the Hangzhou Bay as shown by the common presence of acoustic anomalous reflections including enhanced reflection, gas chimney, bright spot, acoustic blanking, and acoustic turbidity. The gas front depth does not exceed 17.5 m, and it is generally much shallower in the Hangzhou Bay than that in the Yangtze subaqueous delta because the former has, on average, smaller water depth and coarser sediments than the latter. Shallow gas is a biogenic production, and its distribution is primarily determined by the Holocene stratal thickness and water depth. Shallow gas migration is mainly controlled by overburden pressure and sediment permeability. Gas migration and seepage phenomenon (such as gas chimney, mound, pockmark, and gas plumes) are common in the study area, which are clearly enhanced by recently increasing seabed erosion because of sediment deficit. Positive feedback loops of gas migration with global warming and seabed erosion will expose coastal society to more frequent and more intense coastal geological hazards induced by shallow gas seepages. This study improves our understanding of the controlling mechanisms of dynamic changes of shallow gas in coastal seas under internal and external factors, highlighting the urgent requirement to build up early warming capability to monitor and predict shallow gas activities and associated hazards.

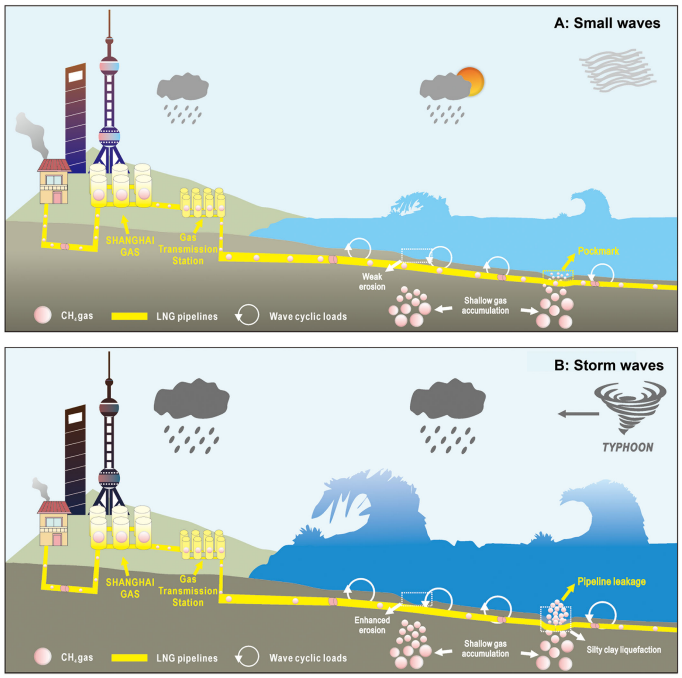


FIGURE 12
Potential geological hazards and disasters induced by the seabed instability of shallow gas-charged sediments in the highly developed coastal seas under small waves **(A)** and storm waves **(B)**.

## Data availability statement

The original contributions presented in the study are included in the article/supplementary material. Further inquiries can be directed to the corresponding author.

## Author contributions

LS collected and analyzed the data and wrote the manuscript. DF conceived the idea, designed the experiments, analyzed the data, and revised the manuscript. JS and XG collected and analyzed the data, and revised the manuscript. All authors contributed to the article and approved the submitted version.

## Funding

This study was supported by the Innovation Program of Shanghai Municipal Education Commission (2021-01-07-00-07-E00093), the National Natural Science Foundation of China (NSFC-41976070 and 42206062), the Open Foundation of Zhoushan Field Scientific Observation and Research Station for Marine Geo-hazards, China Geological Survey (ZSORS-22-11), and the Fundamental Research Funds for the Central Universities (No. ZD-21-202101).

## Conflict of interest

The authors declare that the research was conducted in the absence of any commercial or financial relationships that could be construed as a potential conflict of interest.

## Publisher's note



## References

Beckers, J. M., Barth, A., Troupin, C., and Alvera-Azcárate., A. (2014). Some approximate and efficient methods to assess error fields in spatial gridding with DIVA (Data interpolating variational analysis). *J. Atmospheric Oceanic Technol.* 31, 515–530. doi: 10.1175/JTECH-D-13-00130.1

Chen, Y. F., Deng, B., and Zhang, J. (2020). Shallow gas in the Holocene mud wedge along the inner East China Sea shelf. *Mar. Pet. Geol.* 114, 104233. doi: 10.1016/j.marpetgeo.2020.104233

Chen, Y. F., Deng, B., Zhang, W. G., and Zhang, G. L. (2022). *Required data for paper publication* (Figureshare, v4). doi: 10.6084/m9.Figureshare.14768967.v4

Chen, S. S., Sun, Q. L., Lu, K., Hovland, M., Li, R. H., and Luo, P. (2017). Anomalous depressions in the northern yellow Sea basin: Evidences for their evolution processes. *Mar. Pet. Geol.* 84, 179–194. doi: 10.1016/j.marpetgeo.2017.03.030

Coughlan, M., Roy, S., O'Sullivan, C., Clements, A., O'Toole, R., and Plets, R. (2021). Geological settings and controls of fluid migration and associated seafloor seepage features in the north Irish Sea. *Mar. Pet. Geol.* 123, 104762. doi: 10.1016/j.marpetgeo.2020.104762

Cui, Z. K., Cai, C. L., Shi, J., and Zhang, Y. B. (2014). Geohazard factors and their impact on submarine pipeline safety in the East China Sea. *Mar. Geol. Front.* 30 (01), 48–54.

Cukur, D., Krastel, S., Tomonaga, Y., Çağatay, M. N., and Meydan, A. F. (2013). Seismic evidence of shallow gas from lake van, eastern Turkey. *Mar. Pet. Geol.* 48, 341–353. doi: 10.1016/j.marpetgeo.2013.08.017

Diez, R., García-Gil, S., Durán, R., and Vilas, F. (2007). Gas accumulations and their association with particle size distribution patterns in the ría de arousa seabed (Galicia, NW spain): An application of discriminant analysis. *Geo-Mar. Lett.* 27, 89. doi: 10.1007/s00367-007-0064-4

Etiope, G., Ciotoli, G., Schwietzke, S., and Schoell, M. (2019). Gridded maps of geological methane emissions and their isotopic signature. *Earth Syst. Sci. Data* 11 (1), 1–22. doi: 10.5194/essd-11-1-2019

Etiope, G., and Schwietzke, S. (2019). Global geological methane emissions: An update of top-down and bottom-up estimates. *Elementa-Sci. Anthrop.* 7, 47. doi: 10.1525/elementa.383

Fan, D., Li, C., Wang, D., Wang, P., Archer, A. W., and Greb, S. (2004). Morphology and sedimentation on open-coast intertidal flats of the changjiang delta, China. *J. Coast. Res.* 43, 23–35.

Fan, D., Wu, Y., Zhang, Y., Burr, G., Huo, M., and Li, J. (2017). South flank of the Yangtze delta: Past, present, and future. *Mar. Geol.* 392, 78–93. doi: 10.1016/j.margeo.2017.08.015

Fannin, N. (1980). The use of regional geological surveys in the North Sea and adjacent areas in the recognition of offshore hazards. *Safety in Offshore Drilling: The Role of Gas Surveys*, Kluwer Academic Publishers, Dordrecht.

Feng, X. (2017). Geochemical characterization of shallow Holocene biogenic gas source rocks in the coastal plain of Jiangsu and Zhejiang. *Nanjing University (in Chinese with English abstract).*

Fleischer, P., Orsi, T. H., Richardson, M. D., and Anderson, A. L. (2001). Distribution of free gas in marine sediments: A global overview. *Geo-Mar. Lett.* 21, 103–122. doi: 10.1007/s003670100072

Floodgate, G. D., and Judd, A. G. (1992). The origins of shallow gas. *Cont. Shelf Res.* 12 (10), 1145–1156. doi: 10.1016/0278-4343(92)90075-U

Flury, S., Røy, H., Dale, A. W., Fossing, H., Tóth, Z., Spiess, V., et al. (2016). Controls on subsurface methane fluxes and shallow gas formation in Baltic Sea sediment (Aarhus bay, Denmark). *Geochim. Cosmochim. Acta* 188, 297–309. doi: 10.1016/j.gca.2016.05.037

García-García, A., Orange, D. L., Miserocchi, S., Correggiari, A., Langone, L., Lorenson, T. D., et al. (2007). What controls the distribution of shallow gas in the Western Adriatic Sea? *Cont. Shelf Res.* 27 (3-4), 359–374. doi: 10.1016/j.csr.2006.11.003

Guo, X. J., Yan, X. X., Zheng, S. W., Wang, H. M., and Yin, P. (2021). Characteristics of high-resolution subaqueous micro-topography in the jinshan deep trough and its implications for riverbed deformation, hangzhou bay, China. *Estuar. Coast. Shelf Sci.* 250, 107147. doi: 10.1016/j.ecss.2020.107147

Gupta, S., Schmidt, C., Böttner, C., Rüpke, L., and Hartz, E. H. (2022). Spontaneously exsolved free gas during major storms as an ephemeral gas source for pockmark formation. *Geochem. Geophys. Geosyst.* 23, e2021GC010289. doi: 10.1029/2021GC010289

Hovland, M., and Judd, A. G. (1988). Seabed pockmarks and seepages: Impact on geology, biology and the marine environment. *Graham Trotman*. 244, 590–591. doi: 10.13140/RG.2.1.1414.1286

Hu, X. Q., Gu, Z. F., Zhang, X. H., Zhao, L. H., and Xing, Z. H. (2016). Seismic shape features and distribution of shallow gas in the sea area off the Yangtze river estuary. *Mar. Geol. Quat. Geol.* 36 (01), 151–157.

Hu, Y., Li, H. D., and Xu, J. (2012). Shallow gas accumulation in a small estuary and its implications: A case history from in and around xiamen bay. *Geophys. Res. Lett.* 39, L24605. doi: 10.1029/2012GL054478

Huang, Y., and Han, X. (2020). Features of earthquake-induced seabed liquefaction and mitigation strategies of novel marine structures. *J. Mar. Sci. Eng.* 8 (5), 310. doi: 10.3390/jmse8050310

Hustoft, S., Bünz, S., and Mienert, J. (2010). Three-dimensional seismic analysis of the morphology and spatial distribution of chimneys beneath the nyegga pockmark field, offshore mid-Norway. *Basin Res.* 22, 465–480. doi: 10.1111/j.1365-2117.2010.00486.x

IPCC (2021). *Climate change 2021: The physical science basis: Contribution of working group I to the sixth assessment report of the intergovernmental panel on climate change* (Cambridge: Cambridge University Press).

Jaśniewicz, D., Klusek, Z., Brodecka-Goluch, A., and Bolałek, J. (2019). Acoustic investigations of shallow gas in the southern Baltic Sea (Polish exclusive economic zone): a review. *Geo-Mar Lett.* 39, 1–17. doi: 10.1007/s00367-018-0555-5

Judd, A., and Hovland, M. (2007). *Seabed fluid flow: The impact on geology, biology and the marine environment* (Cambridge University Press), 475.

Koch, S., Berndt, C., Bialas, J., Haeckel, M., Crutchley, G., Papenberg, C., et al. (2015). Gas-controlled seafloor doming. *Geology* 43 (7), 571–574. doi: 10.1130/G36596.1

Kramer, K., Holler, P., and Herbst, G. (2017). Abrupt emergence of a large pockmark field in the German bight, southeastern north Sea. *Sci. Rep.* 7 (1), 5150. doi: 10.1038/s41598-017-05536-1

Letcher, T. M. (2019). Why do we have global warming? *Manage. Glob. Warm.* 1, 3–15. doi: 10.1016/B978-0-12-814104-5.00001-6

Li, X. F. (2020). Damage and repair of subsea pipelines in shallow gas areas. *Oil. Gas. Stor. Transp.* 11, 1310–1315.

Li, P., Du, J., Liu, L. J., Cao, C. X., and Xu, Y. Q. (2010). Distribution characteristics of offshore shallow gas in China. *Chin. J. Geol. Hazards. Prev.* 21 (01), 69–74.

Li, C., Fan, D., Yang, S., and Cai, J. (2008). Characterization and formation of the late quaternary incised valley sequence in the estuarine delta region of China. *J. Paleogeogr.* 10 (1), 87–97. doi: 10.2110/pec.06.85.0141

Li, G. X., Li, P., Liu, Y., Qiao, L. L., Ma, Y. Y., Xu, J. S., et al. (2014). Sedimentary system response to the global sea level change in the East China seas since the last glacial maximum. *Earth-Sci. Rev.* 139, 390–405. doi: 10.1016/j.earscirev.2014.09.007

Lin, C. M., Li, Y. L., Zhuo, H. C., Shurr, G. W., Ridgley, J. L., Zhang, Z. P., et al. (2010). Features and sealing mechanism of shallow biogenic gas in incised valley fills (the qiantang river, eastern china): A case study. *Mar. Pet. Geol.* 27 (4), 909–922. doi: 10.1016/j.marpetgeo.2009.11.006

Lin, C. M., Zhang, X., Xu, Z. Y., Deng, C. W., Yin, Y., and Cheng, Q. Q. (2015). Sedimentary characteristics and accumulation conditions of shallow-biogenic gas for the late quaternary sediments in the changjiang river delta area. *Adv. Earth Sci.* 30 (05), 589–601.

Liu, Y. F. (2019). Recent evolution process and influencing factors of jinshan deep trough in the hangzhou bay. *East China Normal Univ.*

Liu, X. Y., Feng, X. L., Sun, Y. F., Chen, Y. L., Tang, Q. H., Zhou, X. H., et al. (2019). Acoustic and biological characteristics of seafloor depressions in the north yellow Sea basin of China: Active fluid seepage in shallow water seafloor. *Mar. Geol.* 414, 34–46. doi: 10.1016/j.margeo.2019.05.002

Luan, H. L., Ding, P. X., Yang, S. L., and Wang, Z. B. (2021). Accretion-erosion conversion in the subaqueous Yangtze delta in response to fluvial sediment decline. *Geomorphology* 382, 107680. doi: 10.1016/j.geomorph.2021.107680

Martinez-Carreño, N., and Garcia-Gil, S. (2013). The Holocene gas system of the ria de vigo (NW spain): Factors controlling the location of gas accumulations, seeps and pockmarks. *Mar. Geol.* 344, 82–100. doi: 10.1016/j.margeo.2013.07.012

Mogollón, J. M., Dale, A. W., Fossing, H., and Regnier, P. (2012). Timescales for the development of methanogenesis and free gas layers in recently-deposited sediments of arkona basin (Baltic Sea). *Biogeosciences* 9, 1915–1933. doi: 10.5194/bg-9-1915-2012

Mogollón, J. M., Dale, A. W., and Tensen., J. B. (2013). A method for the calculation of anaerobic oxidation of methane rates across regional scales: An example from the belt seas and the sound (North Sea–Baltic Sea transition). *Geo-Mar. Lett.* 33, 299–310. doi: 10.1007/s00367-013-0329-z

Ni, Y. Q., Geng, Z. X., and Zhu, J. Z. (2003). Study on the hydrodynamic characteristics of hangzhou bay. *Hydrodyn. Res. Prog.* 18 (4), 439–445.

Nyman, A., Rinne, H., Salovius-Lauren, S., and Vallius, H. (2020). The distribution and characterization of gas domes in lumparn bay, Åland islands, northern Baltic Sea. *J. Mar. Syst.* 208, 103359. doi: 10.1016/j.jmarsys.2020.103359

Qu, C. W., Zhang, X., Lin, C. M., Chen, S. Y., Li, Y. L., Pan, F., et al. (2013). Characteristics of capillary sealing mechanism of late quaternary shallow biogenic gas in the hangzhou bay area. *Adv. Earth Sci.* 28 (2), 209–220.

Rasmussen, R. A., and Khalil, M. A. (1986). Atmospheric trace gases: Trends and distributions over the last decade. *Science* 232 (4758), 1623–1624. doi: 10.1126/science.232.4758.1623

Ren, F., Fan, D., Wu, Y., and Zhao, Q. (2019). The evolution of hypoxia off the changjiang estuary in the last 3000 years: Evidence from benthic foraminifera and elemental geochemistry. *Mar. Geol.* 417, 106039. doi: 10.1016/j.margeo.2019.106039

Rice, D. D., and Claypool, G. E. (1981). Generation, accumulation, and resource potential of biogenic gas. *AAPG Bulletin.* 65 (1), 5–25. doi: 10.1306/2F919765-16CE-11D7-8645000102C1865D

Schneider von Deimling, J., Weinrebe, W., Tóth, Zs., Fossing, H., Endler, R., Rehder, G., et al. (2013). A low frequency multibeam assessment: Spatial mapping of shallow gas by enhanced penetration and angular response anomaly. *Mar. Pet. Geol.* 44, 217–222. doi: 10.1016/j.marpetgeo.2013.02.013

Sills, G. C., and Wheeler, S. J. (1992). The significance of gas for offshore operations. *Cont. Shelf Res.* 12, 1239–1250. doi: 10.1016/0278-4343(92)90083-V

Song, Y. P., Sun, Y. F., Song, B. H., Dong, L. F., and Du, X. (2021). Comparative study on the liquefaction properties of seabed silt under wave loading in the huanghe river delta. *Acta Oceanol. Sin.* 43 (06), 129–138.

Southon, J., Kashgarian, M., Fontugne, M., Metivier, B., and Yim, W. W. S. (2002). Marine reservoir corrections for the Indian Ocean and southeast Asia. *Radiocarbon* 44, 167–180.

Stuiver, M., and Reimer, P. J. (1993). Extended (super 14) C data base and revised CALIB 3.0 (super 14) C age calibration program. *Radiocarbon* 35 (1), 215–230.

Su, J., Fan, D., Leng, W., Chen, L., and Yin, P. (2017). Postglacial sequence stratigraphy and sedimentary environment evolution of the Yangtze river subaqueous delta. *J. Palaeogeogr.* 19 (03), 541–556.

Su, J., Fan, D., Liu, J., and Wu, Y. (2020). Anatomy of the transgressive depositional system in a sediment-rich tide-dominated estuary: The paleo-Yangtze estuary, China. *Mar. Pet. Geol.* 121, 104588. doi: 10.1016/j.marpetgeo.2020.104588

Sumer, B. M., Truelsen, C., and Fredsøe, J. (2006). Liquefaction around pipelines under waves. *J. Waterw. Port Coast. Ocean Eng.* 132 (4), 266–275. doi: 10.1061/(ASCE)0733-950X(2006)132:4(266)

Sun, M. S., Zhang, G. L., Ma., X., Cao, X. P., Mao, X. Y., Ye, W. W., et al. (2018). Dissolved methane in the East China Sea: Distribution, seasonal variation and emission. *Mar. Chem.* 202, 12–26. doi: 10.1016/j.marchem.2018.03.001

Toker, M., and Tur, H. (2021). Shallow seismic characteristics and distribution of gas in lacustrine sediments at lake erçek, Eastern Anatolia, Turkey, from high–resolution seismic data. *Environ. Earth Sci.* 80, 727. doi: 10.1007/s12665-021-10039-4

Ulyanova, M., Sivkov, V., Kanapatskij, T., Sigalevich, P., and Pimenov, N. (2012). Methane fluxes in the southeastern Baltic Sea. *Geo-Mar Lett.* 32, 535–544. doi: 10.1007/s00367-012-0304-0

Visnovitz, F., Bodnár, T., Tóth, Z., Spiess, V., Kudó, I., Timár, G., et al. (2015). Seismic expressions of shallow gas in the lacustrine deposits of lake balaton, Hungary. *Near Surf Geophys.* 13, 433–446. doi: 10.3997/1873-0604.2015026

Wang, H., and Liu, H. J. (2016). Evaluation of storm wave-induced silty seabed instability and geo-hazards: A case study in the yellow river delta. *Appl. Ocean Res.* 58, 135–145. doi: 10.1016/j.apor.2016.03.013

Wang, H., Liu, H. J., Zhang, M. S., and Wang, X. H. (2016). Wave-induced seepage and its possible contribution to the formation of pockmarks in the huanghe (Yellow) river delta. *Chin. J. Oceanol. Limnol.* 34 (1), 200–211. doi: 10.1007/s00343-015-4245-0

Wang, Z. H., Saito, Y., Zhan, Q., Nian, X. M., Pan, D. D., Wang, L., et al. (2018). Three-dimensional evolution of the Yangtze river mouth, China during the Holocene: Impacts of sea level, climate and human activity. *Earth-Sci. Rev.* 185, 938–955. doi: 10.1016/j.earscirev.2018.08.012

Wang, H., Su, L., Zhang, M. S., and Liu, H. J. (2020). Effects of storm wave-induced liquefaction on lateral deformation of monopile-type offshore wind turbines in silt seabed. *J. Mar. Environ. Eng.* 10 (3), 225–242.

Wang, Y., Yan, X. X., Wang, Z. H., Zhao, B. C., and Zhan, Q. (2019). Shallow seismic facies characteristics of the modern underwater delta of the Yangtze river. *Mar. Geol. Quat. Geol.* 39 (02), 114–122.

Wang, M. J., Zheng, H. B., Yang, S. Y., and Fan, D. D. (2012). Environmental information in subaqueous Yangtze river delta since Holocene. *J. Tongji Univ. (Nat. Sci.)* 40 (03), 473–477.

Wever, T. F., Lühder, R., and Knispel, U. (2006). Potential environmental control of free shallow gas in the seafloor of eckernförde bay, Germany. *Mar. Geol.* 225, 1–4. doi: 10.1016/j.margeo.2005.08.005

Whiticar, M. J. (1999). Carbon and hydrogen isotope systematics of bacterial formation and oxidation of methane. *Chem. Geol.* 161, 291–314. doi: 10.1016/S0009-2541(99)00092-3

Xie, D. F., Pan, C. H., Cao, Y., and Zhang, B. H. (2013). Decadal variations in the erosion/deposition pattern of the hangzhou bay and their mechanism in recent 50a. *Acta Oceanol. Sin.* 35 (04), 121–128.

Xie, D. F., Pan, C. H., Wu, X. G., Gao, S., and Wang, Z. B. (2017). Local human activities overwhelm decreased sediment supply from the changjiang river: Continued rapid accumulation in the hangzhou bay-qiantang estuary system. *Mar. Geol.* 392, 66–77. doi: 10.1016/j.margeo.2017.08.013

Xu, Y. S., Wu, H. N., Shen, J. S., and Zhang, N. (2017). Risk and impacts on the environment of free-phase biogas in quaternary deposits along the coastal region of shanghai. *Ocean Eng.* 137, 129–137. doi: 10.1016/j.oceaneng.2017.03.051

Yang, J. H., Lai, X. H., and Chen, Z. X. (2021). Analysis of submarine pockmarked landforms and their genesis in the waters of Qingbang Island, eastern Zhoushan Islands. *J Appl. Oceanogr.* 40 (02), 251–259.

Yang, X. D., Chun, M. H., Luo, X. Q., and Yao, Z. G. (2022b). Research on application of seismic attribute analysis in identification of subsea shallow gas. *Coast. Eng.* 01), 26–36.

Yang, H. F., Li, B. C., Yang, S. L., Zhang, Z. L., Xu, K. H., Chen, C. P., et al. (2022a). Impacts of large projects on the sediment dynamics and evolution of the hengsha shoal in the Yangtze delta. *Ocean Eng.* 261, 112030. doi: 10.1016/j.oceaneng.2022.112030

Yang, S. L., Milliman, J. D., Li, P., and Xu, K. (2011). 50,000 dams later: Erosion of the Yangtze river and its delta. *Glob. Planet. Change* 75 (1-2), 14–20. doi: 10.1016/j.gloplacha.2010.09.006

Yang, X. D., Yao, Z. G., Chun, M. H., and Luo, X. Q. (2019). Research on detection technology of subsea well mouth. *Coast. Eng.* 38 (03), 232–239.

Ye, Y. C., Chen, J. R., Pan, G. F., and Liu, K. (2003). A study of formation cause, existing characteristics of the shallow gas and its danger to engineering. *Donghai Mar. Sci.* 01), 27–36.

Zhan, Q., Wang, Z., Xie, Y., Xie, J., and He, Z. (2012). Assessing C/N and $\delta^{13}C$ as indicators of Holocene sea level and freshwater discharge changes in the subaqueous Yangtze delta, China. *Holocene* 22, 697–704. doi: 10.1177/0959683611423685

Zhang, X., and Lin, C. M. (2017). Characteristics and accumulation model of the late quaternary shallow biogenic gas in the modern changjiang delta area, eastern China. *Pet. Sci.* 14, 261–275. doi: 10.1007/s12182-017-0157-2

Zhang, X., Lin, C. M., Gao, S., Robert, W. D., Qu, C. W., Yin, Y., et al. (2013a). Sedimentary sequence and distribution pattern of filling in qiantang river incised valley. *J. Paleogeogr.* 15 (06), 839–852.

Zhang, X., Lin, C. M., Li, Y. L., Qu, C. W., and Wang, S. J. (2013b). Sealing mechanism for cap beds of shallow-biogenic gas reservoirs in the qiantang river incised valley, China. *Cont. Shelf Res.* 69, 155–167. doi: 10.1016/j.csr.2013.09.006

Zhang, X. Y., Dai, Z. J., Feng, L. X., and Huang, Z. M. (2021). Study of the erosion-siltation state of the Jinshan deep trough on the north coast of Hangzhou Bay. *Adv Mar. Sci.* 39 (04), 535–547.

Zhang, G. L., Zhang, J., Kang, Y. B., and Liu, S. M. (2004). Distributions and fluxes of methane in the East China Sea and the yellow Sea in spring. *J. Geophys. Res.* 109, C07011. doi: 10.1029/2004JC002268

Zhang, G. L., Zhang, J., Liu, S. M., Ren, J. L., Xu, J., and Zhang, F. (2008). Methane in the changjiang (Yangtze river) estuary and its adjacent marine area: Riverine input, sediment release and atmospheric fluxes. *Biogeochemistry* 91 (1), 71–84. doi: 10.1007/s10533-008-9259-7

frontiers | Frontiers in Marine Science

TYPE Original Research
PUBLISHED 20 February 2023
DOI 10.3389/fmars.2023.1114337



OPEN ACCESS

EDITED BY
Yifei Zhao,
Nanjing Normal University, China

REVIEWED BY
Qiang Yao,
Louisiana State University Agricultural Center, United States
Feifei Wang,
Qingdao Institute of Marine Geology (QIMG), China

*CORRESPONDENCE
Daidu Fan
ddfan@tongji.edu.cn

SPECIALTY SECTION
This article was submitted to Coastal Ocean Processes, a section of the journal Frontiers in Marine Science

RECEIVED 02 December 2022
ACCEPTED 27 January 2023
PUBLISHED 20 February 2023

CITATION
Jiang F, Fan D, Zhao Q, Wu Y, Ren F, Liu Y and Li A (2023) Comparison of alive and dead benthic foraminiferal fauna off the Changjiang Estuary: Understanding water-mass properties and taphonomic processes.
*Front. Mar. Sci.* 10:1114337.
doi: 10.3389/fmars.2023.1114337



# Comparison of alive and dead benthic foraminiferal fauna off the Changjiang Estuary: Understanding water-mass properties and taphonomic processes

Feng Jiang[1], Daidu Fan[1,2]*, Quanhong Zhao[1], Yijing Wu[1], Fahui Ren[1], Yan Liu[3] and Ang Li[1]

[1]State Key Laboratory of Marine Geology, Tongji University, Shanghai, China, [2]Laboratory of Marine Geology, Qingdao National Laboratory for Marine Science and Technology, Qingdao, China, [3]State Key Laboratory of Estuarine and Coastal Research, East China Normal University, Shanghai, China

Benthic foraminifera (BF) are utilized in palaeo-environmental reconstruction based on our understanding of how living individuals respond to environmental variations. However, there is still a lack of empirical insight into how non-environmental factors, such as taphonomic processes, influence the preservations of fossil BF in strata. In this study, we compare the spatial distribution and composition of alive and dead BF fauna in surface sediments to elucidate how well fossil foraminiferal fauna mirror quasi-contemporary alive BF groups indicative of different water masses off a mega-river (Changjiang) estuary, which is characterized by intense and complex river-sea interactions. On-site measurements of bottom water salinity, temperature, and dissolved oxygen were conducted in the summer to determine water mass properties. A same-site comparison of alive (Rose Bengal stained) and dead foraminiferal fauna in surface sediment samples over 73 stations was then carried out. Q-mode Hierarchical clustering analysis was used to differentiate foraminiferal assemblages based on the relative abundance of common species. Three distinct regions with different water-mass properties were identified. The distribution pattern of dead foraminiferal fauna is mainly inherited from alive fauna, while the density and diversity of the dead fauna were found to be higher than those of the alive one. Both alive and dead fauna were clustered into four assemblages. A few common alive species (small-agglutinated and thin-calcareous) were rarely found in dead fauna, and a few common dead species (preferring low temperature and indicating allochthonous sources) were rarely present in alive fauna. The alive foraminiferal abundance and diversity were mainly determined by food resources and environmental properties of salinity and temperature. Alive foraminiferal assemblages were separated by different water masses determined by river-sea interactions off the Changjiang Estuary. The "time-averaging" effect was found to be responsible for the higher density and diversity of the dead fauna. Disintegration of agglutinated tests, dissolution of calcareous tests and selective transportation were observed to contribute to the different species

compositions between the alive and dead fauna. Nevertheless, indicative species-environment relations in alive and taphocoenose fauna were found to be almost homologous among most common species. This suggests that distinct benthic foraminiferal assemblages can be used to effectively differentiate between different water masses in the study coastal seas.

KEYWORDS

benthic foraminifera, coastal seas, surface sediment, shelf circulations, postmortem processes, water mass

## 1 Introduction

Benthic foraminifera (BF) are single-celled organisms that are widely distributed in marginal seas and are often used as a reliable proxy to indicate palaeoceanographic changes due to their high sensitivity to environmental conditions (Schönfeld and Zahn, 2000; Evans et al., 2002; Abrantes et al., 2005; Murray, 2006; Dai et al., 2018; Zhao et al., 2018; Ren et al., 2019; Jiang et al., 2021). This time-tested methodology is also highly dependent on baseline data regarding the response and sensitivity of alive BF to various biological, chemical and physical conditions (Wang et al., 1988; Murray, 2006). To understand how taphocoenose BF (including alive and dead BF) are buried and fossilized, hence, a comparative study between alive and dead benthic foraminiferal fauna in surface sediments is needed to explore the effects of taphonomic processes on the composition and preservation of BF, and whether the fossil BF accurately mirror the quasi-contemporary living faunal groups. Such research has been a focus of interest for paleontologists worldwide for the past few decades (Jorissen and Wittling, 1999; Horton and Murray, 2006; Bouchet et al., 2012; Wang et al., 2016; Stefanoudis et al., 2017; Ye et al., 2021).

Previous studies have demonstrated that water-mass properties, such as bottom-water salinity (BWS), temperature (BWT), dissolved oxygen (DO), food availability, and sediment composition, are essential in determining the living benthic foraminiferal composition (Gupta, 1999; Murray, 2006; Lei et al., 2017; Jernas et al., 2018). Furthermore, taphonomic processes, such as the destruction, dissolution, and transportation of tests have been indicated to alter the living and dead faunas (Gooday and Hughes, 2002; Murray, 2006; Berkeley et al., 2007; Glover et al., 2010; Duros et al., 2012). Thus, further research into these taphonomic processes is essential to accurately interpret BF data and associated paleoenvironmental variations.

Comparative studies between living and dead BF in dynamic estuarine and shelf environments are remarkably rare (Mendes et al., 2013; Goineau et al., 2015). The mega-Changjiang Estuary and broad shelf of the eastern China seas are characterized by complex interactions of different water masses with distinct physical and chemical properties (Su, 1998; Naimie et al., 2001; Yang et al., 2018; Liu et al., 2021), hence, serving as an ideal platform to conduct such comparative study. In the East China Sea (ECS), the quantitative relationship between contemporary benthic foraminiferal distributions in surface sediments and the associated controlling environmental factors have been well discussed, significantly improving our understanding of common BF inhabiting the estuary and shelf (Wang et al., 1988; Zheng, 1988; Zhao et al., 2009; Lei and Li, 2016; Xu et al., 2017; Wang et al., 2018; Guo et al., 2019; Zhang et al., 2020). However, the differences between *in-situ* living and dead BF have so far been little studied. Thus, large data gap exists in the impacts of taphonomic processes on changing the compositions from living to dead foraminiferal fauna.

This study focuses on the Changjiang Estuary and its adjacent coastal sea, which are characterized by notable environmental gradients in terms of oceanographic, biological, and sediment compositions. Except for on-site observations of water-mass properties, analyses of living and dead benthic foraminiferal fauna in surface sediments were conducted in detail to assess their structures (abundance, diversity and species compositions). Multivariate statistical methods were employed to cluster stations into different assemblage types based on species compositions. Comparisons between water-mass and maps of faunal structures were designed to quantify the role of water-mass properties in determining faunal structures. The differences between living and dead faunal structures were used to assess effects of taphonomic processes. Furthermore, relationships among the common species and multiple environmental parameters were established by a linear method of redundance analysis in living and taphocoenose fauna to validate reliability of the marine environmental index.

## 2 Oceanographic and sedimentary settings of the study coastal sea

The study coastal sea is located off the Changjiang Estuary, including the northwestern part of the ECS and the southwestern part of the Yellow Sea (Figure 1A). It is characterized by intense interactions of the Changjiang Diluted Water (CDW), coastal currents and the intrusions of the Kuroshio Current (KC) and its branches, which are strongly affected by seasonal East Asian Monsoon activities. In summer, the southeasterly monsoon wind stress enhances the eastern and northeastern expansion of the CDW, separating the southerly YSCC and the northerly ZFCC (Su, 1998; Naimie et al., 2001; Guan and Fang, 2006). In addition, the warm and salty branched-flows driven by the KC move northwards throughout the year, intruding into the ECS inner shelf at the bottom along the 50 m isobath (Yang et al., 2018). Water masses from diverse sources possess distinct physical and chemical properties, creating a high environmental heterogeneity in the study area.

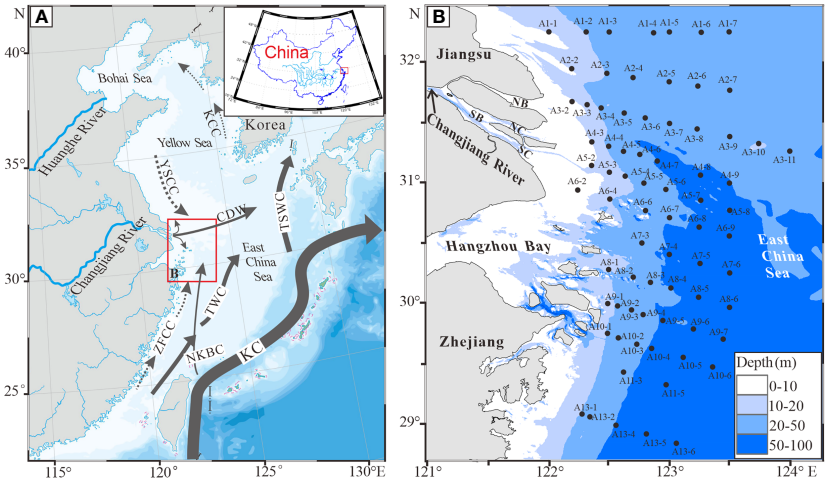


FIGURE 1
Schematic diagram of oceanic circulation patterns in summer in the eastern China seas (after Lee et al., 2002; Su and Yuan, 2005; Guan and Fang, 2006; Yang et al., 2012), and **(B)** distribution of 73 sampling stations off the Changjiang Estuary. Acronyms in **(A)** and their full expressions are KC, Kuroshio Current; NKBC, nearshore Kuroshio branch current; TSWC, Tsushima warm current; TWC, Taiwan warm current; YSCC, Yellow Sea costal current; ZFCC, Zhejiang-Fujian costal current; KCC, Korean coastal current; and CDW, Changjiang diluted water; those in **(B)** are NB, the North Branch; SB, the South Branch; NC, the North Channel; and SC, the South Channel of the Changjiang Estuary.

The complex hydrodynamical conditions and sediment sources result in the patchy distribution of fine-grained mud, coarse-grained sand, and mixed deposits off the Changjiang Estuary. Generally, muddy and sandy depositions prevail respectively in the inner and outer belts off the Changjiang Estuary, while the narrow patch of sand and mud mixture lies in between (Qiao et al., 2017). The sedimentation rates deduced from $^{210}$Pb data generally decrease both eastward and southward from the Changjiang subaqueous delta where a maximum sedimentation rate of >4.0 cm/yr occurs (Gao et al., 2015; Jia et al., 2018).

# 3 Materials and methods

## 3.1 Oceanographic surveys and sediment sampling

A cruise survey was conducted in and off the Changjiang Estuary (Figure 1B) from 6 to 22 July in 2014 on board *R/V* "*Runjiang-1*". Water depth, BWS and BWT were recorded using a CTD (conductivity, temperature and depth; Model: SBE-25, USA). DO in bottom water samples was measured using the Winkler titration method (Dickson, 1994). Seventy-three sediment samples were collected from the water depths of 7.5 m to 67.0 m (Figure 1B using a stainless-steel sediment grab sampler, and the top layers (0-2 cm thick) were taken for grain-size measurements and living and dead benthic foraminiferal analyses.

## 3.2 Grain-size test

Grain-size analysis were conducted on all 73 surface sediment samples. All samples were pretreated with 30% hydrogen peroxide to remove organic matter and then with 10% diluted hydrochloric acid to remove carbonates, followed by repeated washing with de-ionized water and then dispersed in an ultrasonic vibrator for several minutes. The particle-size distribution was measured with a laser-diffraction Beckman Coulter LS230, ranging from 0.375 to 2,000 μm. The calculation of the particle sizes relies on the theory of Folk and Ward (1957).

## 3.3 Benthic foraminiferal analysis

All 73 surface sediment samples for foraminiferal analysis were soaked and thoroughly mixed with a methanol and Rose Bengal solution (1.0 g/L) for the purpose of tinting living individuals to distinguish them from dead ones immediately after collection on board. These samples were dried and weighed, and then were wet-sieved through a 63 μm-sieve in the lab. The coarse fraction (>63 μm) was dried and split, and the split sample was examined completely for foraminiferal compositions. Benthic species were identified and quantified under a stereomicroscope with continuous zooming up to a maximum amplification of 40×. Living specimens were identified by the presence of Rose Bengal-stained protoplasm in their tests, including those that were entirely stained or those with the last one or two chambers been unstained (De Stigter et al., 1998).Taxonomic identification mainly followed the protocol outlined by Zheng (1988); Wang et al. (1988), and Lei and Li (2016).

Faunal abundance (*N*, individuals ind./g dry weight of sediment) and foraminiferal species richness (H′, Shannon-Wiener diversity index based on calculation of equation (1), Shannon, 1984) were calculated for living and dead foraminiferal communities on raw data. Benthic species with relative abundances of >5% in at least three samples were regarded as common species in the study coastal sea (Wang et al., 1988).

$$H' = -\sum_{i=1}^{S} P_i \ln P_i, \quad P_i = proportion \quad of \quad the \quad ith \quad species \quad (1)$$

Additionally, we quantitatively interpreted the living and dead foraminiferal ecology by utilizing multivariate statistical methods based on ordination and classification methods such as Q-mode Hierarchical clustering analysis (HCA) and redundancy analysis (RDA). HCA was used to classify the distribution of foraminiferal groups and subgroups into homogeneous assemblage zones. RDA was applied to quantify the relationships between faunal structures and environmental variables.

# 4 Results

## 4.1 Bottom-water oceanographic conditions and sediment size compositions

The distribution patterns of BWS and BWT featured the elongated bands roughly parallel to the coast (Figures 2A, B). The BWS increased seaward from 13.4 to 34.6, while the BWT decreased eastward from 25.2 °C to18.6 °C. The northern coastal water body off the North Branch (NB) and Jiangsu coast had much higher DO than the coastal water body off the Hangzhou Bay and Zhejiang coast. The latter enclosed a subzone with DO values lower than 4.0 mg/L (Figure 2C). Sandy sediments (>63 μm) occupied the northeastern region known as the Yangtze Shoal and the rest area was covered by silty clay or silt (Figure 2D).

## 4.2 Foraminiferal abundance and species richness

### 4.2.1 Abundance of living and dead BF

The living abundance varied from 0 to 1,845 ind./g (Supporting Information Table S2-Living BF2), with an average of 76 ind./g. The peak abundance (>100 ind./g) occurred at the inner belt off the South Channel (SC) and the Hangzhou Bay (blue to red in Figure 3A). The intermediate abundance (20-100 ind./g) occurred at south of the peak abundance zone, the inner belt off Zhejiang coast (dark purple to blue in Figure 3A). A narrow belt with an abundance between 10 and 20 ind./g extended north-south at the outer band off the Hangzhou Bay and Zhejiang coast (dark purple in Figure 3A). More than a half of all stations had living abundance of less than 10 ind./g, typically located off the NB and Jiangsu coast (light purple in Figure 3A).

The dead abundance ranged between 0 ind./g and 11,586 ind./g, with a mean of 844 ind./g (Supporting Information Table S2-Dead BF2). The peak abundance (>1000 ind./g) occurred at stations off

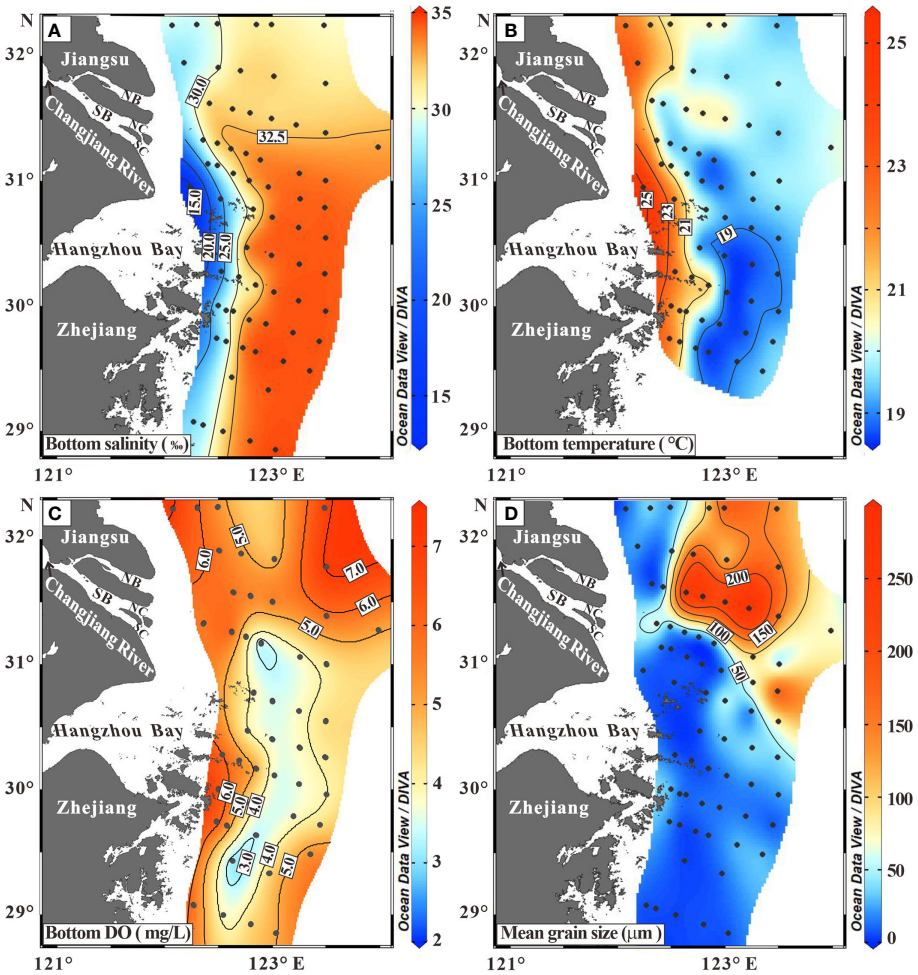


FIGURE 2
Distribution patterns of bottom-water oceanographic indexes including **(A)** salinity (‰), **(B)** temperature (°C), and **(C)** DO (mg/L), and **(D)** mean grain size (μm) of surface sediments. Detailed data are included in Supporting Information Table S1.

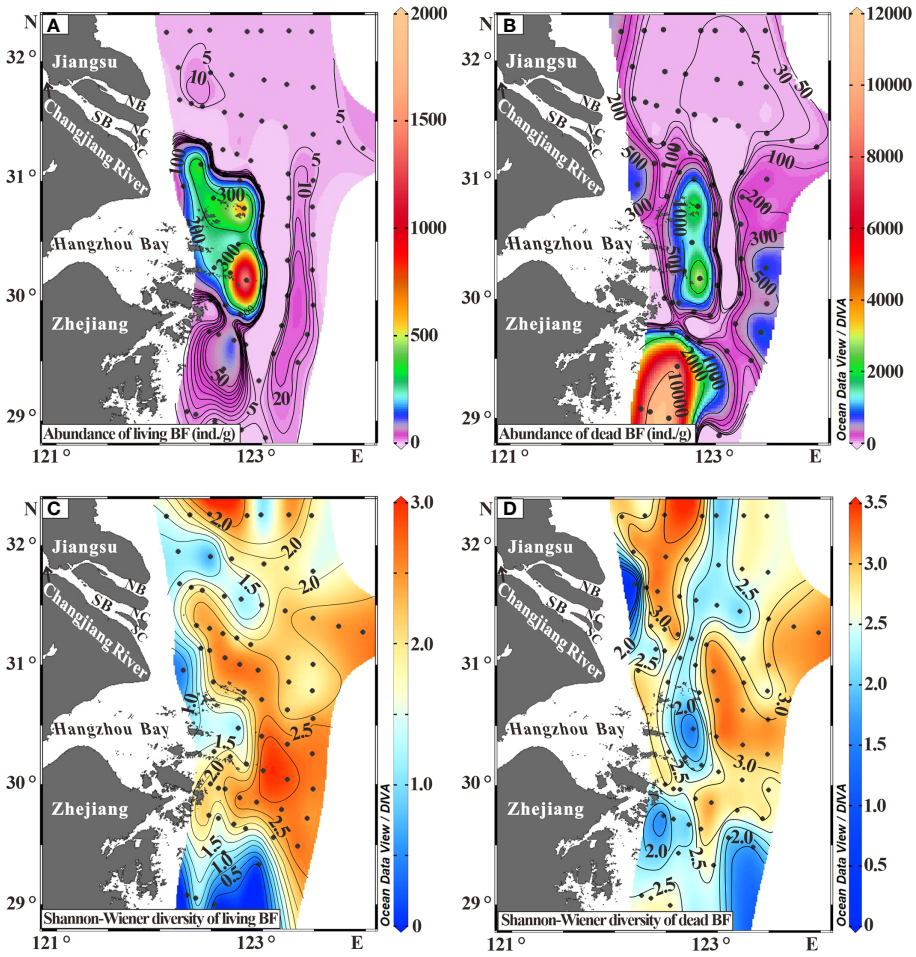


FIGURE 3
Distribution of living and dead benthic foraminiferal abundance **(A, B)**, and distribution of Shannon-Wiener diversity (H′) of living and dead benthic foraminiferal fauna **(C, D)**. Detailed data are included in Supporting Information Table S2.

Zhejiang coast (blue to red in Figure 3B). The intermediate abundance (100-1000 ind./g) occurred in the inner and outer regions off the SC and the Hangzhou Bay (dark purple to green in Figure 3B). The less abundance (<100 ind./g) occurred at coastal zone off the Jiangsu coast and the NB, together with a narrow N-S belt between the inner peak and the outer intermediate abundance belts off the Hangzhou Bay (light purple in Figure 3B).

### 4.2.2 Diversity of living and dead BF

Shannon-Wiener diversity index (H′) for living fauna ranged from 0.5 to 2.9 (Supporting Information Table S2-Living BF2). The southernmost region had the lowest faunal diversity. The inner bands off the Changjiang Estuary and the Hangzhou Bay had a lower diversity (H′<1.5), while their outer counterparts had a relatively higher diversity (H′>1.5) (Figure 3C).

The H′ values of dead fauna had a relatively higher and wider range (0-3.4) (Supporting Information Table S2-Dead BF2) than the living one. Additionally, there were some differences in their spatial patterns (Figures 3C, D). The inner region off the Changjiang Estuary and the region off Zhejiang coast exhibited a relatively lower diversity (H′<2.0, blue in Figure 3D). The remanent area was characterized by two higher H′ (>2.5) bands, which were interspersed with a lower H′ belt (2.0-2.5) (Figure 3D).

## 4.3 Species compositions and spatial partitions of benthic foraminiferal assemblages

### 4.3.1 Clusters analyses and spatial distribution of living assemblages

Living species were identified among 15,158 counts of stained individuals (Supporting Information Table S2-Living BF1). Twenty-three species with an abundance over 5% from at least 3 stations were identified, accounting for 87% of living fauna (Figure 4A). The dominant species include *Verneuilinulla advena* (*V. advena*), *Bolivina striatula* (*B. striatula*) and *Nonionella jacksonensis* (*N. jacksonensis*), which were found in over 50 stations.

The resultant dendrograms of Q-mode HCA based on the 23 common species demonstrate four clusters: FI-a, FI-b, FII and FIII (Figure 4A). Twenty-three stations are organized into Cluster FI-a in terms of the dominance of *N. jacksonensis* (37.2% on average), *Cribrononion subincertum* (*C. subincertum*, 12.1%) and *Verneuilinulla advena* (*V. advena*, 6.6%), and they generally congregate at the inner band off Jiangsu coast and the Changjiang Estuary (Figure 5A). Cluster FI-b includes 10 stations off the SC and the Hangzhou Bay (Figure 5A), with *Florilus atlanticus* (*F. atlanticus*,

17.5%), *Polskiammina asiatica* (*P. asiatica*, 15.5%), *Ammonia pauciloculata* (*A. pauciloculata*, 7.2%), and *N. jacksonensis* (5.2%) being the dominate species (Figure 4A). Cluster FII consists of 16 stations dominated by *Florilus decorus* (*F. decorus*, 24.7%), *A. convexidorsa* (13.1%), *B. striatula* (12.0%), *V. advena* (11.0%), *Ammonia tepida* (*A. tepida*, 10.0%), and *N. jacksonensis* (9.9%) (Figure 4A), which are mainly located at the outer region off Jiangsu coast and the Changjiang Estuary (Figure 5A). Cluster FIII includes 17 stations, with *Ammonia compressiuscula* (*A. compressiuscula*, 27.5%), *F. atlanticus* (7.2%), *Cancris auriculus* (*C. auriculus*, 6.6%), *B. marginata* (4.7%) and *B. robusta* (3.4%) being the dominate species (Figure 4A), and they are mainly located at the outer region off the SC and the Hangzhou Bay (Figure 5A).

### 4.3.2 Clusters analyses and spatial distribution of dead assemblages

The species were identified among 16,075 counts of dead individuals (Supporting Information Table S2, Dead BF1). Twenty-eight species with an abundance over 5% from at least 3 stations were identified, accounting for 80% of dead fauna. (Figure 4B). The dominant species that frequently appeared at over 50 stations are *Bolivina robusta* (*B. robusta*), *Bulimina marginata* (*B. marginata*), *A. tepida*, *A. compressiuscula*, *Elphidium advenum* (*E. advenum*) and *F. atlanticus*.

The resultant dendrograms of Q-mode HCA based on 28 common species distinguish four clusters: FI′-a, FI′-b, FII′ and FIII′ (Figure 4B). Thirty-seven stations are regarded as Cluster FI′-a in terms of the dominance of *Epistominella naraensis* (*E. naraensis*, 10.9%), *B. robusta* (7.7%), *B. marginata* (7.6%), and *F. decorus* (5.8%) (Figure 4B), and they are majorly distributed in the northern half of study coastal sea (Figure 5B). Thirteen stations of Cluster FI′-b, with *F. atlanticus* (14.6%), *N. jacksonensis* (11.8%), and *A. tepida* (8.2%) being the dominate species (Figure 4B), and they are majorly distributed in the inner belts off the SC, the Hangzhou Bay and Zhejiang coast (Figure 5B). Seven stations are classified as Cluster FII′ based on high abundance of *Ammonia ketienziensis* (*A. ketienziensis*, 19.4%), *B. robusta* (11.3%), *E. advenum* (7.8%), *A. compressiuscula* (7.0%) and *Q. seminulangulata* (5.9%) (Figure 4B), which are scattered in the outer belt off Jiangsu coast and the NB (Figure 5B). Another 16 stations are grouped into Cluster FIII′ showing high abundance of *A. compressiuscula* (23.4%), *Quinqueloculina*

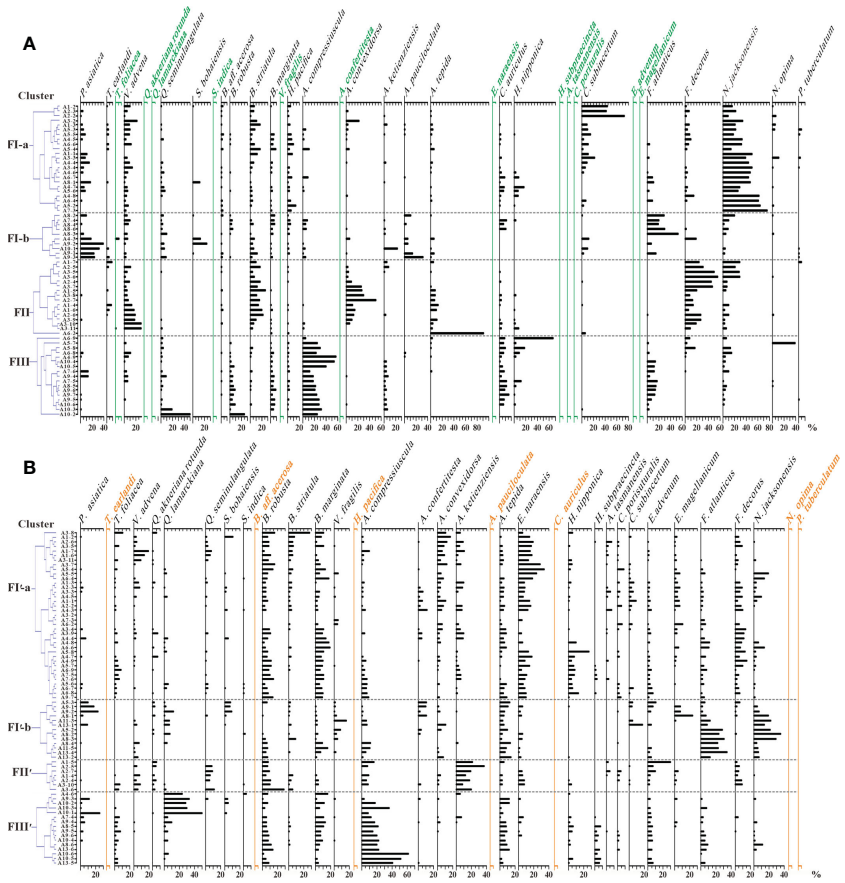


FIGURE 4
Relative abundance (%) of common species of living **(A)** and dead **(B)** benthic foraminiferal fauna. Species shown in black are common for both living and dead fauna, and those in green or orange are common only for dead or living fauna. The dendrograms of Q-mode HCA are plotted in the left to show four clusters of common species: FI-a (FI′-a), FI-b (FI′-b), FII (FII′) and FIII (FIII′) for living and dead fauna in different station groups (see Figure 1B for their locations). Detailed data are included in Supporting Information Table S2-Living BF3 and Dead BF3.

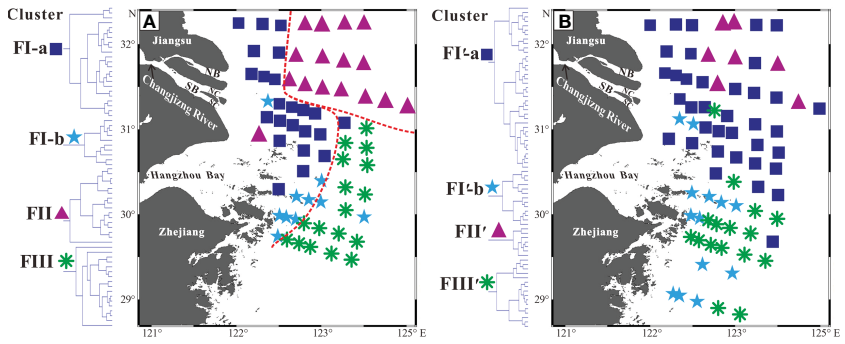


FIGURE 5
Partition maps of living **(A)** and dead **(B)** benthic foraminiferal assemblages. Blue squares, cyan stars, purple deltas, and green asterisks denote Clusters FI-a, FI-b, FII, and FIII in **(A)**, and FI′-a, FI′-b, FII′, and FIII′ in **(B)**. See Figure 4 for the information of different clusters and their associated stations.

*lamarckiana* (*Q. lamarckiana*, 12.5%), *B. marginata* (7.1%), *A. tepida* (6.4%), and *B. robusta* (6.4%) (Figure 4B), and they are mainly present off the southern Hangzhou Bay and the outer belt off Zhejiang coast (Figure 5B).

# 5 Discussion

## 5.1 Effects of intense river-sea interactions on water-mass properties in summer

The dominant hydrodynamic processes in relatively shallow eastern China seas are strongly affected by massive freshwater outflows, tides, monsoon-related waves and currents, and the KC and its branches (Su, 1998; Naimie et al., 2001). Interactions among the above-mentioned factors result in different circulation regimes and water masses that are generally diagnosed by their varied physical properties, especially temperature and salinity (Park and Chu, 2006; Chen, 2009).

In summer, the inner belt of the study coastal sea is generally occupied by the water mass WI of low BWS (15.0-30.0) and high BWT (21.0–25.0°C) (Figures 2A, B, 6), resulting from a mixture of the Changjiang diluted water and alongshore currents (Chen, 2009). For example, the water mass to the south of the Changjiang Estuary is significantly impacted by the southward fresher CDW and the northward ZFCC (Figure 6; Lee et al., 2002; Su and Yuan, 2005; Liu et al., 2021). The NE offshore area (the outer region off Jiangsu coast and the Changjiang Estuary) is prevailed by the water mass WII with high BWS (30.0-32.5) and low BWT (19.0-21.0°C) (Figures 2A, B, 6), receiving interactive effects of the northeastward CDW, the southward YSCC and the northward TWC (Figure 6; Lee et al., 2002; Su and Yuan, 2005; Liu et al., 2021). The SE offshore area (the outer region off the Hangzhou Bay and Zhejiang coast) is occupied by the water mass WIII with high BWS (32.5-34.6), low BWT (ca. 19.0 °C) and relative lower DO (<4.0 mg/L) (Figures 2A–C, 6), resulting from strong intrusion of salty Kuroshio branch currents (Yang et al., 2018). Meanwhile the relative lower DO values in the WIII waters (Figure 2C) could also be driven by water column stratification and organic matter decomposition near the bottom in summer (Li et al., 2002; Zhu et al., 2017; Wang et al., 2021; Zhang et al., 2021).

## 5.2 Impacts of water-mass properties on living benthic foraminiferal distributions

Living individuals are short-lived and highly sensitive to ecological conditions during their growing stage. Marine ecological system is complex and multivariate due to dynamic interactions between environmental factors (salinity, temperature, DO, substrate and food supply) and living organisms (Wang et al., 1988; Murray, 2006).

### 5.2.1 Controlling factors of spatial variations in living abundance and diversity

The considerably high abundance (>100 ind./g) was observed at the inner region off the SC and the Hangzhou Bay (Figure 3A). This region has a low salinity and high temperature (Figures 2A, B), whereas abundant nutrient inputs from the densely-populated river plume and coastal upwelling cause frequent algal bloom (Tseng et al., 2014; Hu and Wang, 2016; Wang et al., 2019). In the marine ecosystems, phytoplankton serves as the main food source for BF (Murray, 2006). Being as the most important and leading environment parameters, food quality and quantity can shape the foraminiferal abundance (Gustafsson and Nordberg, 1999; Contreras-Rosales et al., 2010; Mojtahid et al., 2016; Wang et al., 2016).

The occurrence of lower abundance (0-20 ind./g) at the inner region off Jiangsu coast and the NB (Figure 3A) was mainly ascribed to lower salinity (Figure 2A) (Lei et al., 2017). Moreover, the inner region is characterized by high suspended sediment concentrations, where low transparency of the water mass limits the growth of primary producers consequently lowering the abundance (Li et al., 2020). To the east of 123°E, the lower abundance (Figure 3A) was constrained by nutrient deficits from the river plumes (Wang et al., 2019).

The occurrence of high diversity (H′>1.5) in the outer region of the studied coastal sea was generally coincident with high BWS (30.0-34.6), low BWT (18.6-21.0 °C), and lower DO (2.3-5.0 mg/L) (Figures 2, 3C). Previous studies indicated that the diversity is positively correlated to salinity (Lei et al., 2017) and the normal salinity (33.0) in the ECS provokes foraminiferal diversity (Wang et al., 1988). In addition, a temperature ranging between 18.0 and 24.0°C could promote the growth of various foraminiferal species, but

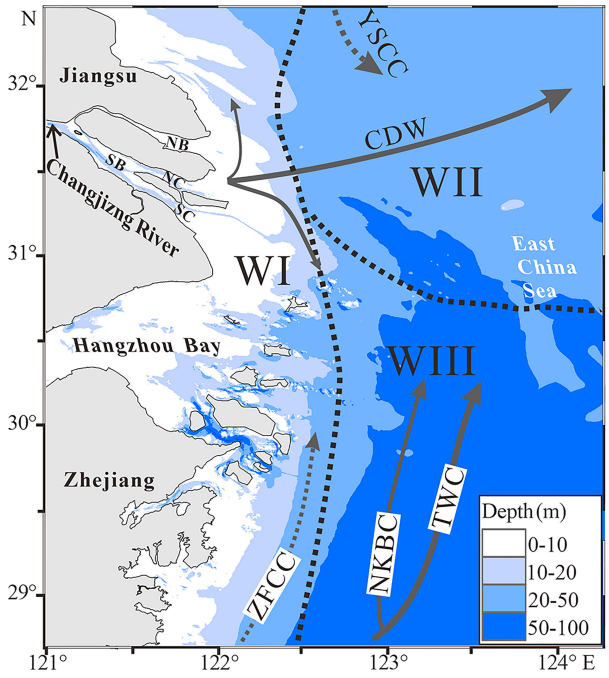


FIGURE 6
General current circulations (Su and Yuan, 2005; Guan and Fang, 2006; Yang et al., 2018) and the distribution of water masses in coastal sea off the Changjiang Estuary in summer. WI: low BWS and high BWT and DO water mass, WII: high BWS and DO and low BWT water mass, and WIII: high BWS and low BWT and DO water mass.

higher temperature may in turn reduce the species richness (Lei et al., 2017). Moreover, the lower DO in the outer region may also play a side-role in promoting higher foraminiferal diversity (Levin et al., 2009).

### 5.2.2 Spatial partitions of living clusters determined by distinct water-mass properties

Four clusters of living common species in the study coastal sea were determined by Q-mode HCA as FI-a, FI-b, FII and FIII (Figure 4A), and their spatial partitions were closely linked to the distribution of three water masses in this area (Figures 5A, 6).

Cluster FI-a (dominated by *N. jacksonensis*, *C. subincertum*, and *V. advena*) and Cluster FI-b (dominated by *F. atlanticus*, *P. asiatica*, *A. pauciloculata* and *N. jacksonensis*) (Figure 4A) enriched with low salinity species were prevalent in the inner belt of the study coastal sea, highly coincident with the distribution of the water mass WI (Figures 5A, 6). Previous studies also indicated that these species are specifically keen to the estuarine water mass with lower salinity and higher temperature and DO (Wang et al., 1988; Lei and Li, 2016). Moreover, the *F. atlanticus* and *A. pauciloculata* were recognized as species being particularly influenced by the ZFCC (Wang et al., 1988). Thus, the Clusters FI-a and FI-b represent assemblages that are unique to the inner estuarine and coastal sea, which are strongly influenced by the CDW and the ZFCC.

Cluster FII consists of species with a large range of salinity tolerance, from *A. convexidorsa*, a low salinity species to *B. striatula*, a high salinity species (Figure 4A), prevailed in the outer region off Jiangsu coast and the Changjiang Estuary. The region was coincident with the distribution of the water mass WII (Figures 5A, 6), where high salinity gradient is produced by the mixture of the YSCC (higher salinity and lower temperature) and the CDW (lower salinity and higher temperature) (Figure 2A, B) (Chen, 2009).

Cluster FIII consisting of species *A. compressiuscula*, *C. auriculus*, *B. marginata*, and *B. robusta* (Figure 4A), was prevalent in the outer region off the Hangzhou Bay and Zhejiang coast (Figure 5A), where the intrusion of the TWC and the NKBC produces the water mass WIII featuring higher salinity, lower temperature and DO (Figures 2A–C, 6). The species *A. compressiuscula* and *C. auriculus* have been recognized to thrive well in high salinity waters, while the species *A. compressiuscula*, *B. marginata* and *B. robusta* could adapt well to a lower DO condition (Wang et al., 1988; Gooday and Jorissed, 2012). Thus, spatial partitions of living assemblages are clearly determined by the distribution of water masses with their distinct oceanographic and ecological properties.

## 5.3 Taphonomic processes changing the benthic foraminiferal abundance and diversity from living to dead fauna

Taphonomic processes change the abundance, diversity and species composition in surface sediments during transition from living to dead faunas in response to sediment accumulation, destruction and transportation (Murray, 2006; Glover et al., 2010).

### 5.3.1 Time-averaging effects on dead abundance and diversity

In general, the abundance and diversity of dead BF are rather higher than those of the living ones. For instance, the dead abundance reached >1000 ind./g in the inner region off the SC and the Hangzhou

Bay, but the living abundance was only ca. 100 ind./g (Figures 3A, B). Meanwhile, distribution patterns of the two faunal abundance and diversity are relatively comparable (Figure 3), denoting their close affiliation. This affiliation has been reported to be common in the Bohai Sea, the northern Yellow Sea and the South China Sea (Li et al., 2014, Li et al., 2021).

The 2-cm thick surface sediment analyzed in this study represents a depositional period from 0.5 to 4.0 years according to the $^{210}$Pb derived sedimentation rates of 0.5-4.0 cm/yr in the study area (Gao et al., 2015; Jia et al., 2018). In contrast, living fauna has much shorter life spans than the depositional period. Thus, it indicates that dead fauna is a burial accumulation of multiple living faunas over a period of time. Such result offers an interpretation for the dissimilarities between living and dead faunas in the surface sediment samples, known as "time-averaging" effect (Murray, 2006; Glover et al., 2010; Kidwell and Tomasovych, 2013). The sedimentation rates in the inner region off Zhejiang coast are much lower (0.5-1.0 cm/yr) than the others (Gao et al., 2015; Jia et al., 2018), hence, a longer time-averaging effect results in a higher dead BF abundance (Figure 3B). In contrast, the lower diversity (a 2.0-2.5 H′ belt) of dead fauna in the central study area (Figure 3D) was likely due to therein higher sedimentation rates (ca. 2.0-3.0 cm/yr) (Gao et al., 2015; Jia et al., 2018).

### 5.3.2 Impacts of postmortem processes (destruction, transport and reburial) on dead species compositions

In addition to abundance and diversity, the difference of species compositions is quite evident between living and dead fauna in the same sample. Such difference is also obvious in the statistics analytic result of common species over the entire study area. Totally, 23 common species in living fauna are less than 28 in dead fauna (Figure 4). The 7 common living species, including *Textularia earlandi* (*T.earlandi*), *Bolivina aff. acerosa* (*B.aff.acerosa*), *Hopkinsina pacifica* (*H. pacifica*), *A. pauciloculata*, *C. auriculus*, *Nonionella opima* (*N. opima*) and *Protelphidium tuberculatum* (*P.tuberculatum*) were rare or not present in dead fauna (Figure 4A). On the contrary, the 12 common species in dead fauna were rare or not present in living fauna, including *Textularia foliacea* (*T. foliacea*), *Quinqueloculina akneriana rotunda* (*Q. akneriana rotunda*), *Q. lamarckiana*, *Spiroloculina indica* (*S. indica*), *Virgulinella fragilis* (*V. fragilis*), *Ammonia confertitesta* (*A. confertitesta*), *E. naraensis*, *Heterolepa subpraecincta* (*H. subpraecincta*), *Cribrononion porisuturalis* (*C. porituralis*), *Astrononion tasmanensis* (*A. tasmanensis*), *E. advenum* and *Elphidium magellanicum* (*E. magellanicum*) (Figure 4B).

The above-mentioned 7 common species are of small (fine-sand size) agglutinated and thin-shell calcitic tests. Agglutinated tests with small amount of organic cement and loosely cemented walls are susceptible to bacterial or chemical decay of organic matter, to be scarcely fossilized in discernable forms (Murray and Alve, 1999; Kuhnt et al., 2000; Murray, 2006; Lei and Li, 2016; Dessandier et al., 2018). Shells of the calcitic species such as *H. pacifica* and *C. auriculus* are very thin and susceptible to destruction and dissolution, leading to a poor preservation (Gooday and Hughes, 2002; Murray, 2006; Duros et al., 2012).

There are a few reasons for why the 12 common species in dead fauna were rare or not present in living fauna. First of all, some species can grow in other seasons besides summer when surface sediments were sampled for this study. For example, *T. foliacea* and *Q. lamarckiana* in dead fauna (Figure 4B) are marked by large tests, indicating a low-temperature (even below 4.0 °C) condition, and BF with calcareous tests such as *S. indica* and *E. naraensis* prefer a water temperature below 17.5 °C (Lei and Li, 2016). These species probably grow in winter and spring before being buried after death. In addition, external sources of dead fauna are expected to be transported by strong currents although living individuals are less likely to be carried away because their reticulopodial network tends to anchor them firmly in the sediments (Goldstein, 1999; Murray, 2006). For instance, *E. advenum* and *E. magellanicum* were reportedly to be a typical coastal species along Jiangsu coast and *A. confertitesta* a typical supratidal species (Wang et al., 1988). Thus, their common presence in the dead fauna (Figure 4B) demonstrates their allochthonous source *via* sediment transport.

## 5.4 Bio-ecological implications of indicative foraminiferal species

RDA analysis was employed to explore potential correlations between indicative foraminiferal species and key environmental factors (BWS, BWT, DO and sediment size) for both living (Figure 7A) and taphocoenose (living + dead) fauna (Figure 7B). As discussed above, living fauna can rapidly respond to environmental conditions, but it needs further investigation to reveal whether species-environmental relationships are consistent between living and taphocoenose fauna or valid for palaeo-environmental reconstruction. In RDA ordination diagrams, longer vectors with smaller angles indicate greater correlation between the BF species and environmental parameters.

There are quite a few common species that show their persistent relationship with certain environmental parameters before and after burial. The relative abundance of *A. compressiuscula* and *H. nipponica* are positively correlated with water depth and BWS in both living and taphocoenose fauna (Figure 7). *A. compressiuscula* is one of the typical species in the middle shelf of the ECS, and *H. nipponica* tends to live in the middle and outer shelf (Wang et al., 1988; Zheng, 1988; Lei and Li, 2016). *C. subincertum*, *S. bohaiensis* and *N. jacksonensis* build an inverse relationship with salinity, and *P. asiatica* ties up with temperature (Figure 7). The two species, *B. robusta* and *B. marginata*, known as the low oxygen foraminiferal species (Gooday and Jorissed, 2012), show a negative correlation to DO (Figure 7). Abiotic factors such as grain size also impact foraminiferal assemblages (Magno et al., 2012). For instance, *A. convexidorsa*, *A. ketienziensis*, *V. advena*, and *F. decorus* prefer sandy setting, while *F. atlanticus* likes clayey seabed (Figure 7). Our results of the RDA explain the same ecological preferences of the same species in the two faunas. This indicates that the environmental signal in living fauna is preserved in the taphocoenose fauna.

There are also some species to show varied relationships with environmental parameters before and after burial (shown in green in Figure 7). *Q. seminulangulata* (stenohaline) in living fauna is

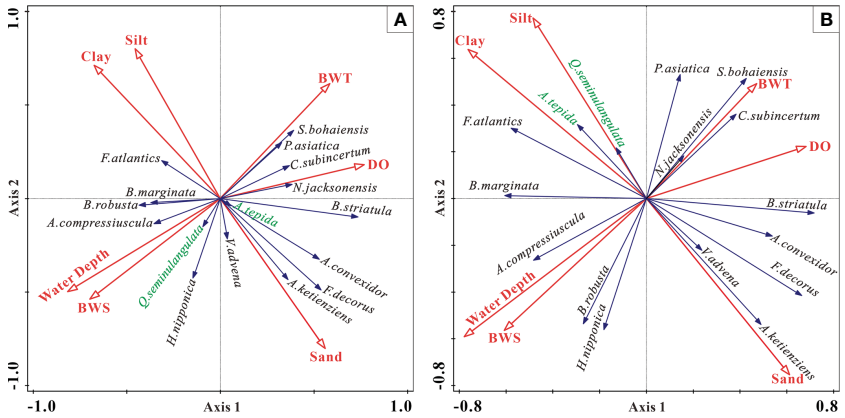


FIGURE 7
RDA ordination diagrams of living benthic foraminiferal fauna **(A)** and taphocoenose benthic foraminiferal fauna **(B)** with key environmental variables (BWS, BWT, DO and sediment size) measured in the summer of 2014.

positively associated with salinity (Figure 7A), but this was not revealed in taphocoenose fauna probably due to reworking process after death (Figure 7B) (Wang et al., 1988; Zheng, 1988; Lei and Li, 2016). *A. tepida*, especially abundant in dead fauna (Figure 4B), shows a little association with other environmental factors except grain size (Figure 7), probably ascribed to its higher capacity of bio-ecological adaptation throughout the year (Debenay et al., 2000), and it prefers living in a sandy setting (Figure 7A), but may be displaced into a muddy setting after death (Figure 7B). The taphocoenose fauna is built up by combined ecological and taphonomic forces over a period of time, hence taphocoenose species provide a time averaged record integrating different seasonal conditions (Glover et al., 2010).

## 6 Conclusion

Collectively, our results have demonstrated that living benthic foraminifera (BF) responds sensitively to water-mass properties but dead benthic foraminiferal fauna can be partly reformed by taphonomic forces over a period of time. Food resources (primary productivity) play a key role in affecting living benthic foraminiferal fauna abundance, and the distribution laws of living diversity and salinity are generally consistent. Furthermore, distinct water masses (WI, WII and WIII) with different properties (BWS, BWT and DO) shaped by river-sea interactions explain well the distribution of four living assemblages (FI-a and FI-b, FII, FIII).

The effects of taphonomic processes on dead faunal structures are revealed through comparison between living and dead faunal indices. Because of the "time-averaging" effect, the dead fauna has higher abundance and diversity than the living fauna, in that the former contains a few species that are not present in the sampling time or location. In addition, the dead fauna may lack certain living species due to their poor preservation ability, such as agglutinated-test species and thin-shell calcitic species.

The taphocoenose fauna is the result of both ecological and taphonomic forces within a given temporal framework. Correlations between the most indicative species and environment variables in both living and taphocoenose fauna remain homologous. Thus, taphocoenose BF in core sediments can be effectively used to reconstruct the past marine environments, although care should be taken with a few species that are prone to heavy taphonomic influences.

## Data availability statement

The original contributions presented in the study are included in the article/Supplementary Material. Further inquiries can be directed to the corresponding author.

## Author contributions

FJ: Conceptualization, Methodology, Validation, Formal analysis, Investigation, Writing-Original Draft, Writing-Review & Editing, Visualization. DF: Conceptualization, Resources, Writing-Review & Editing, Supervision, Project administration, Funding acquisition. QZ: Investigation, Writing-Review & Editing. YW: Investigation, Writing-Review & Editing. FR: Investigation, Writing-Review & Editing. AL: Investigation. YL: Writing-Review & Editing. All authors contributed to the article and approved the submitted version.

## Funding

This research is jointly funded by the Innovation Program of Shanghai Municipal Education Commission (2021-01-07-00-07-E00093), the National Natural Science Foundation of China (NSFC-41976070, 42206052, 41971007), and the Fundamental Research Funds for the Central Universities (No. ZD-21-202101).

## Conflict of interest

The authors declare that the research was conducted in the absence of any commercial or financial relationships that could be construed as a potential conflict of interest.

## Publisher's note



## Supplementary material

The Supplementary Material for this article can be found online at: https://www.frontiersin.org/articles/10.3389/fmars.2023.1114337/full#supplementary-material

SUPPLEMENTARY TABLE 1
The Longitude and Latitude of stations, bottom-water oceanographic conditions (water depth, temperature, salinity and dissolve oxygen) and sediment size compositions.

SUPPLEMENTARY TABLE 2
Dataset of living and dead benthic foraminifera: sheet of Living BF1 is "Living BF species counted of all stations", sheet of Living BF2 is "Abundance and Shannon-Wiener diversity index (H′) of living BF", sheet of Living BF3 is "Relative abundance (%) of common species of living BF", sheet of Dead BF1 is "Dead BF species counted of all stations", sheet of Dead BF2 is "Abundance and Shannon-Wiener diversity index (H′) of dead BF", sheet of Dead BF3 is "Relative abundance (%) of common species of dead BF".

## References

Abrantes, F., Lebreiro, S., Rodrigues, T., Gil, I., Bartels-Jónsdóttir, H., Oliveira, P., et al. (2005). Shallow-marine sediment cores record climate variability and earthquake activity off Lisbon (Portugal) for the last 2000 years. *Quat. Sci. Rev.* 24, 2477–2494. doi: 10.1016/j.quascirev.2004.04.009

Berkeley, A., Perry, C.T., Smithers, S.G., Horton, B.P., and Taylor, K.G. (2007). A review of the ecological and taphonomic controls on foraminiferal assemblage development in intertidal environments. *Earth-Sci. Rev.* 83, 205–230. doi: 10.1016/j.earscirev.2007.04.003

Bouchet, V., Alve, E., Rygg, B., and Telford, R. (2012). Benthic foraminifera provide a promising tool for ecological quality assessment of marine waters. *Ecol. Indic.* 23, 66–75. doi: 10.1016/j.ecolind.2012.03.011

Chen, C. (2009). Chemical and physical fronts in the bohai, yellow and East China seas. *J. Mar. Syst.* 78, 394–410. doi: 10.1016/j.jmarsys.2008.11.016

Contreras-Rosales, L. A., Koho, K. A., Duijnstee, I., Strigter, H., and Epping, E. (2010). Living deep-sea benthic foraminifera from the cap de creus canyon (western mediterranean): Faunal–geochemical interactions. *Deep. Sea. Res. 1 Oceanogr. Res. Pap.* 57, 22–42. doi: 10.1016/j.dsr.2012.01.010

Dai, B., Liu, Y., Sun, Q., Ma, F., Chen, J., and Chen, Z. (2018). Foraminiferal evidence for Holocene environmental transitions in the yaojiang valley, south hangzhou bay, eastern China, and its significance for neolithic occupations. *Mar. Geol.* 404, 15–23. doi: 10.1016/j.margeo.2018.07.001

Debenay, J. P., Guillou, J. J., Redois, F., and Geslin, E. (2000). ""Distribution trends of foraminiferal assemblages in paralic environments: A base for using foraminifera as bioindicators,"," in *Environmental micropaleontology*, vol. 39-67 . Ed. R. E. Martin (New York: Springer US Publication).

Dessandier, P., Bonnin, J., Kim, J., and Racine, C. (2018). Comparison of living and dead benthic foraminifera on the Portuguese margin: Understanding the taphonomical processes. *Mar. Micropaleontol.* 140, 1–16. doi: 10.1016/j.marmicro.2018.01.001

De Stigter, H. C., Jorissen, F. J., and van der Zwaan, G. J. (1998). Bathymetric distribution and microhabitat partitioning of live (Rose Bengal stained) benthic foraminifera along a shelf to deep sea transect in the southern Adriatic Sea. *J. Foraminiferal. Res.* 28, 40–65. doi: 10.1016/S0016-6995(98)80113-7

Dickson, A. G. (1994). *Determination of dissolved oxygen in sea water by winkler titration* (Massachusetts: WOCE Hydrographic Program, Operations and Methods Manual. Woods Hole).

Duros, P., Fontanier, C., De Stigter, H. C., Cesbron, F., Metzger, E., and Jorissen, F. J. (2012). Live and dead benthic foraminiferal faunas from whittard canyon (NE atlantic): focus on taphonomic processes and paleo-environmental applications. *Mar. Micropaleontol.* 94, 25–44. doi: 10.1016/j.marmicro.2012.05.004

Evans, J., Austin, W. E. N., Brew, D. S., Wilkinson, I. P., and Kennedy, H. A. (2002). Holocene Shelf sea evolution offshore northeast England. *Mar. Geol.* 191, 147–164. doi: 10.1016/S0025-3227(02)00529-7

Folk, R. L., and Ward, W. C. (1957). Brazos river bar: A study in the significance of grain size parameters. *J. Sediment. Petrol.* 31, 514–529. doi: 10.1306/74D70646-2B21-11D7-8648000102C1865D

Gao, S., Wang, D., Yang, Y., Zhou, L., Zhao, Y., Gao, W., et al. (2015). Holocene Sedimentary systems on a broad continental shelf with abundant river input: process-product relationships. *Geol. Soc Spec. Publ.* 429, 223–259. doi: 10.1144/SP429.4

Glover, A. G., Gooday, A. J., Bailey, D. M., Billett, D. S. M., Chevaldonne, P., Colaco, A., et al. (2010). Temporal change in deep-sea benthic ecosystems: a review of the evidence from recent time-series studies. *Adv. Mar. Biol.* 58, 1–95. doi: 10.1016/S0065-2881(10)58001-5

Goineau, A., Fontanier, C., Mojtahid, M., Fanget, A.-S., Bassetti, M.-A., Berné, S., et al. (2015). Live-dead comparison of benthic foraminiferal faunas from the rhône prodelta (Gulf of lions, NW mediterranean): Development of a proxy for paleoenvironmental reconstructions. *Mar. Micropaleontol.* 119, 17–33. doi: 10.1016/j.marmicro.2015.07.002

Goldstein, S. T. (1999). ""Foraminifera: a biological overview,"," in *Benthic foraminiferal microhabitats below the sediment-water interface*. Ed. B. K. Sen Gupta (Dordrecht: Kluwer Academic Publishers), 37–56.

Gooday, A. J., and Hughes, J. A. (2002). Foraminifera associated with phytodetritus deposits at a bathyal site in the northern rockall trough (NE atlantic): seasonal contrasts and a comparison of stained and dead assemblages. *Mar. Micropaleontol.* 46, 83–110. doi: 10.1016/S0377-8398(02)00050-6

Gooday, A., and Jorissed, F. (2012). Benthic foraminiferal biogeography: Controls on global distribution patterns in deep-water settings. *Ann. Rev. Mar. Sci.* 4, 237–262. doi: 10.1146/annurev-marine-120709-142737

Guan, B. X., and Fang, G. H. (2006). Winter counter-wind currents off the southeastern China coast: A review. *J. Oceanogr.* 62, 1–24. doi: 10.1007/s10872-006-0028-8

Guo, X., Xu, B., Burnett, W. C., Yu, Z., Yang, S., Huang, X., et al. (2019). A potential proxy for seasonal hypoxia: LA-ICP-MS Mn/Ca ratios in benthic foraminifera from the Yangtze river estuary. *Geochim. Cosmochim. Acta* 245, 290–303. doi: 10.1016/j.gca.2018.11.007

Gupta, B. K. S. (1999). *Modern foraminifera* Vol. 371 p (Dordrecht: Kluwer Acdaemic Publishers).

Gustafsson, M., and Nordberg, K. (1999). Benthic foraminifera and their response to hydrography, periodic hypoxic conditions and primary production in the kolö fjordfjord on the Swedish west coast. *J. Sea. Res.* 41, 163–178. doi: 10.1016/S1385-1101(99)00002-7

Horton, B. P., and Murray, J. W. (2006). Patterns in cumulative increase in live and dead species from foraminiferal time series of cowpen marsh, Tees estuary, UK: implications for sea-level studies. *Mar. Micropaleontol.* 58, 287–315. doi: 10.1016/j.marmicro.2005.10.006

Hu, J., and Wang, X. (2016). Progress on upwelling studies in the China seas. *Rev. Geophysis.* 54, 653–673. doi: 10.1002/2015RG000505

Jernas, P., Klitgaard-Kristensen, D., Husum, K., Koc, N., Tverberg, V., Loubere, P., et al. (2018). Annual changes in Arctic fjord environment and modern benthic foraminiferal fauna: Evidence from kongsfjorden, Svalbard. *Glob. Planet. Change* 163, 119–140. doi: 10.1016/j.gloplacha.2017.11.013

Jia, J., Gao, J., Cai, T., Liu, Y., Yang, Y., Wang, Y., et al. (2018). Sediment accumulation and retention of the changjiang (Yangtze river) subaqueous delta and its distal muds over the last century. *Mar. Geol.* 401, 2–16. doi: 10.1016/j.margeo.2018.04.005

Jiang, F., Wang, Y., Zhao, X., Liu, Y., Chen, J., Sun, Q., et al. (2021). Reconstruction of the Holocene sedimentary–ecological complex in the incised valley of the Yangtze delta, China. *Palaeogeogr. Palaeoclimatol. Palaeoecol.* 571, 11038. doi: 10.1016/j.palaeo.2021.110387

Jorissen, F. J., and Wittling, I. (1999). Ecological evidence from live-dead comparisons of benthic foraminiferal faunas off cape blanc (Northwest Africa). *Palaeogeogr. Palaeoclimatol. Palaeoecol.* 149, 151–170. doi: 10.1016/S0031-0182(98)00198-9

Kidwell, S. M., and Tomasovych, A. (2013). Implications of time-averaged death assemblages for ecology and conservation biology. *Annu. Rev. Ecol. Syst.* 44, 539–563. doi: 10.1146/annurev-ecolsys-110512-135838

Kuhnt, W., Collins, E., and Scott, D. B. (2000). "Deep water agglutinated foraminiferal assemblages across the gulf stream: distribution patterns and taphonomy," in *Proceedings of the fifth international workshop on agglutinated foraminifera* (Grzybowski Foundation Special Publication), 261–298.

Lee, H. J., Jung, K. T., So, J. K., and Chung, J. Y. (2002). A three-dimensional mixed finite-difference galerkin function model for the oceanic circulation in the yellow Sea and the East China Sea in the presence of $M_2$ tide. *Continental. Shelf. Res.* 22, 67–91. doi: 10.1016/S0278-4343(01)00068-1

Lei, Y., and Li, T. (2016). *Atlas of benthic foraminifera from China seas* Vol. 345 (Springer Berlin Heidelberg), p.

Lei, Y., Li, T., Jian, Z., and Nigam, R. (2017). Taxonomy and distribution of benthic foraminifera in an intertidal zone of the yellow Sea, PR China: Correlations with sediment temperature and salinity. *Mar. Micropaleontol.* 133, 1–20. doi: 10.1016/j.marmicro.2017.04.005

Levin, L., Ekau, W., Gooday, A., Jorssen, F., Middelburg, J., Naqvi, S., et al. (2009). Effects of natural and human-induced hypoxia on coastal benthos. *Biogeosciences* 6, 2063–2098. doi: 10.5194/bg-6-2063-2009

Li, T., Cai, G., Zhang, M., Li, S., and Nie, X. (2021). The response of benthic foraminifera to heavy metals and grain sizes: A case study from hainan island, China. *Mar. pollut. Bull.* 167, 112328. doi: 10.1016/j.marpolbul.2021.112328

Li, W., Ge, J., Ding, P., Ma, J., Glibert, P., and Liu, D. (2020). Effects of dual fronts on the spatial pattern of chlorophyll-a concentrations in and off the changjiang river estuary. *Estuaries. Coast.* 44, 1408–1418. doi: 10.1007/s12237-020-00893-z

Li, Z., Liu, D., and Long, H. (2014). Living and dead benthic foraminifera assemblages in the bohai and northern yellow seas: Seasonal distributions and paleoenvironmental implications. *Quat. Int.* 349, 113–126. doi: 10.1016/j.quaint.2014.05.019

Liu, Z., Gan, J., Wu, H., Hu, J., Cai, Z., and Deng, Y. (2021). Advances on coastal and estuarine circulations around the changjiang estuary in the recent decades, (2000-2020). *Front. Mar. Sci.* 8. doi: 10.3389/fmars.2021.615929

Li, D., Zhang, J., Huang, D., Wu, Y., and Liang, J. (2002). Oxygen depletion off the changjiang (Yangtze river) estuary. *Sci. China Ser. D. Earth Sci.* 45, 1137–1146. doi: 10.1360/02yd9110

Magno, M. C., Bergamin, L., Finoia, M. G., Pierfranceschi, G., Venti, F., and Romano, E. (2012). Correlation between textural characteristics of marine sediments and benthic foraminifera in highly anthropogenically-altered coastal areas. *Mar. Geol.* 315, 143–161. doi: 10.1016/j.margeo.2012.04.002

Mendes, I., Dias, J. A., Schöffel, J., Ferreira, Ó., Rosa, F., and Lobo, F. J. (2013). Living, dead and fossil benthic foraminifera on a river dominated shelf (northern gulf of cadiz) and their use for paleoenvironmental reconstruction. *Cont. Shelf. Res.* 68, 91–111. doi: 10.1016/j.csr.2013.08.013

Mojtahid, M., Geslin, E., Coynel, A., Gorse, L., Vella, C., Davranche, A., et al. (2016). Spatial distribution of living (Rose Bengal stained) benthic foraminifera in the Loire estuary (western France). *J. Sea. Res.* 118, 1–16. doi: 10.1016/j.seares.2016.02.003

Murray, J. W. (2006). *Ecology and applications of benthic foraminifera* Vol. 426 (Cambridge: Cambridge University Press), p.

Murray, J. W., and Alve, E. (1999). Natural dissolution of modern shallow water benthic foraminifera: taphonomic effects on the paleoecological record. *Palaeogeogr. Palaeoclimatol. Palaeoecol.* 146, 195–209. doi: 10.1016/S0031-0182(98)00132-1

Naimie, B., Blain, C., and Lynch, D. (2001). Seasonal mean circulation in the yellow Sea-a model-generated climatology. *Cont. Shelf. Res.* 21, 667–695. doi: 10.1016/S0278-4343(00)00102-3

Park, S., and Chu, P. C. (2006). Thermal and haline fronts in the Yellow/East China seas: Surface and subsurface seasonality comparison. *J. Oceanogr.* 62, 617–638. doi: 10.1007/S10872-006-0081-3

Qiao, S., Shi, X., Wang, G., Zhou, L., Hu, B., Hu, L., et al. (2017). Sediment accumulation and budget in the bohai Sea, yellow Sea and East China Sea. *Mar. Geol.* 390, 270–281. doi: 10.1016/j.margeo.2017.06.004

Ren, F., Fan, D., Wu, Y., and Zhao, Q. (2019). The evolution of hypoxia off the changjiang estuary in the last 3000 years: Evidence from benthic foraminifera and elemental geochemistry. *Mar. Geol.* 417, 106039. doi: 10.1016/j.margeo.2019.106039

Schlitzer, R. (2009) *Ocean data view*. Available at: http://odv.awi.de.

Schönfeld, J., and Zahn, R. (2000). Late glacial to Holocene history of the Mediterranean outflow. evidence from benthic foraminiferal assemblages and stable isotopes at the Portuguese margin. *Palaeogeogr. Palaeoclimatol. Palaeoecol.* 59, 85–111. doi: 10.1016/S0031-0182(00)00035-3

Shannon, C. E. (1984). A mathematical theory of communications. *Bell. Syst. Tech. J.* 27, 379–423. doi: 10.1002/j.1538-7305.1948.tb01338.x

Stefanoudis, P., Bett, B., and Gooday, A. (2017). Relationship between 'live' and dead benthic foraminiferal assemblages in the abyssal NE Atlantic. *Deep-Sea. Res. 1* 121, 190–201. doi: 10.1016/j.dsr.2017.01.014

Su, J. (1998). ""Circulation dynamics of the China seas north of 18°N,"," in *The sea*. Eds. A. R. Robinson and K. H. Brink (New York, NY: Wiley), 483–505.

Su, J. L., and Yuan, Y. L. (2005). *Hydrology of Chinese coastal waters* Vol. 367 (Beijing: China Ocean Press), p. (In Chinese).

Tseng, Y. F., Lin, J., Dai, M., and Kao, S. J. (2014). Joint effect of freshwater plume and coastal upwelling on phytoplankton growth off the changjiang river. *Biogeosciences* 11, 409–423. doi: 10.5194/bg-11-409-2014

Wang, S. L., Fan, D., Huang, W. J., Wu, Y., and Su, J. (2021). Hypoxic effects on the radiocarbon in DIC of the ECS subsurface water. *J. Geophys. Res. Oceans.* 126, e2020JC016979. doi: 10.1029/2020JC016979

Wang, F., Gao, M., Liu, J., Pei, S., Li, C., Mei, X., et al. (2016). Distribution and environmental significance of live and dead benthic foraminiferal assemblages in surface sediments of laizhou bay, bohai Sea. *Mar. Micropaleontol.* 123, 1–14. doi: 10.1016/j.marmicro.2015.12.006

Wang, Y., Wu, H., Gao, L., Shen, F., and Liang, X. (2019). Spatial distribution and physical controls of the spring algal blooming off the changjiang river estuary. *Estuaries. Coast.* 42, 1066–1083. doi: 10.1007/s12237-019-00545-x

Wang, F., Yu, Z., Xu, B., Liu, J., Guo, X., and Nan, H. (2018). Nepartak typhoon influenced bottom sediments from the Yangtze river estuary and adjacent East China Sea-foraminiferal evidence. *Geochem. Geophys. Geosyst.* 19, 1046–1063. doi: 10.1002/2017GC007413

Wang, P. X., Zhang, J. J., Zhao, Q. H., Min, Q. B., Bian, Y. H., Zheng, L. F., et al. (1988). *Foraminifera and ostracoda in bottom sediments of the East China Sea* Vol. 438 (Beijing: China Ocean Press), p. (In Chinese with English abstract).

Xu, Z., Liu, S., Xiang, R., and Song, G. (2017). Live benthic foraminifera in the yellow Sea and the East China Sea: vertical distribution, nitrate storage, and potential denitrification. *Mar. Ecol. Prog. Ser.* 571, 65–81. doi: 10.3354/meps12135

Yang, D. Z., Yin, B. S., Chai, F., Feng, X., Xue, H., Gao, G., et al. (2018). The onshore intrusion of kuroshio subsurface water from February to July. *Prog. Oceanogr.* 167, 97–115. doi: 10.1016/j.pocean.2018.08.004

Yang, D. Z., Yin, B. S., Liu, Z. L., Bai, T., Qi, J. F., and Chen, H. Y. (2012). Numerical study on the pattern and origins of kuroshio branches in the bottom water of southern East China Sea in summer. *J. Geophys. Res. Oceans.* 117 (C2), C02014. doi: 10.1029/2011JC007528

Ye, F., Huang, X., Shi, Z., and Chen, B. (2021). The spatial distribution of benthic foraminifera in the pearl river estuary, south China and its environmental significance. *Mar. pollut. Bull.* 173, 113055. doi: 10.1016/j.marpolbul.2021.113055

Zhang, J., Hu, G., Ma, G., Hui, J., Zhang, M., Zhang, Y., et al. (2020). Distribution of benthic foraminifera in the surficial sediments of changjiang distal delta and its environmental implications. *Mar. Geol. Quat. Geol.* 40, 127–138. doi: 10.16562/j.cnki.0256-1492.2019101401. (In Chinese with English abstract).

Zhang, W., Moriarty, J., Wu, H., and Feng, Y. (2021). Response of bottom hypoxia off the changjiang river estuary to multiple factors: A numerical study. *Ocean. Model.* 159, 101751. doi: 10.1016/j.ocemod.2021.101751

Zhao, Q., Jian, Z., Zhang, Z., Cheng, X., Wang, K., and Zhen, H. (2009). Holocene Benthic foraminifera and ostracoda from the shelf mud area of the east China Sea and their paleoenvironmental implication. *Acta Micropalaeontol. Sin.* 26, 117–128. (In Chinese with English abstract). doi: 10.1360/972009-495

Zhao, B., Yan, X., Wang, Z., Shi, Y., Chen, Z., Xie, J., et al. (2018). Sedimentary evolution of the Yangtze river mouth (East China Sea) over the past 19,000 years, with emphasis on the Holocene variations in coastal currents. *Palaeogeogr. Palaeoclimatol. Palaeoecol.* 490, 421–449. doi: 10.1016/j.palaeo.2017.11.023

Zheng, S. Y. (1988). *The agglutinated and porcelaneous foraminifera of the East China Sea* Vol. 337 (Beijing: Science Press), p. (In Chinese).

Zhu, Z., Wu, H., Liu, S., Wu, Y., Huang, D., Zhang, J., et al. (2017). Hypoxia off the changjiang (Yangtze river) estuary and in the adjacent East China Sea: Quantitative approaches to estimating the tidal impact and nutrient regeneration. *Mar. pollut. Bull.* 125, 103–114. doi: 10.1016/j.marpolbul.2017.07.029

frontiers | Frontiers in Marine Science

TYPE Original Research
PUBLISHED 09 May 2023
DOI 10.3389/fmars.2023.1101658



OPEN ACCESS

EDITED BY
Achilleas G. Samaras,
Democritus University of Thrace, Greece

REVIEWED BY
Xiao Wu,
Ocean University of China, China
Jie Wang,
East China Normal University, China

*CORRESPONDENCE
Guan-hong Lee
ghlee@inha.ac.kr

RECEIVED 18 November 2022
ACCEPTED 05 April 2023
PUBLISHED 09 May 2023

CITATION
Chang J, Lee G, Harris CK, Figueroa SM and Jung NW (2023) Relative contribution of the presence of an estuarine dam and land reclamation to sediment dynamics of the Nakdong Estuary.
*Front. Mar. Sci.* 10:1101658.
doi: 10.3389/fmars.2023.1101658



# Relative contribution of the presence of an estuarine dam and land reclamation to sediment dynamics of the Nakdong Estuary

Jongwi Chang[1], Guan-hong Lee[1]*, Courtney K. Harris[2], Steven Miguel Figueroa[3] and Nathalie W. Jung[4]

[1]Department of Oceanography, Inha University, Incheon, Republic of Korea, [2]Virginia Institute of Marine Science, William & Mary, Gloucester Point, VA, United States, [3]Department of Civil Engineering, Chungnam National University, Daejeon, Republic of Korea, [4]Department of Marine and Coastal Environment Science, Texas A&M University at Galveston, Galveston, TX, United States

The Nakdong Estuary of Korea is a dramatic example of an urban estuary that has been heavily developed with the installation of two estuarine dams and approximately 17 km$^2$ of tidal flat reclamation. This study aims to understand the relative contribution of the different physical alterations by implementing four model simulations of the COAWST modeling system: (1) present condition, (2) pre-estuarine dam construction, (3) pre-tidal flat reclamation, (4) both pre-estuarine dam construction and pre-reclamation. In Cases 2 and 4, the model grid was modified to extend the Nakdong estuary upriver about 60 km and remove the estuarine dam. In Cases 3 and 4, the model grid was modified to restore the reclaimed tidal flats. All simulations shared the same initial conditions, boundary conditions, and forcing. Then, the simulation results for current velocity, suspended sediment concentration (SSC), and deposition were used to estimate the relative contribution of each alteration. The results showed that the annual, depth-averaged currents for the pre-estuarine dam (Case 2) were 80% faster than the present condition but were 10% slower for Case 3 (no land reclamation case). Likewise, the depth-averaged SSC was higher by about 25 mg/L in the estuary for Case 2, but it was reduced by about 9 mg/L for Case 3. The increase of velocity and SSC for Case 2 resulted from the removal of the estuarine dam, which changed both the tidal properties (tidal amplitude was reduced by about 40 cm) and estuarine circulation (factor of 5 reductions in the vertical salinity gradient), while the decrease for Case 3 was induced by the reduction in sediment accommodation space (15% of water volume) without a change in the circulation. These results also revealed that the estuarine dam enhanced deposition more than the land reclamation that showed very little change. The changes in current velocity, SSC, and deposition for Case 4 (no dam/reclamation) were very similar to Case 2. Overall, this study suggests that the influence of the estuarine dam was larger than that of the land reclamation in the altered Nakdong Estuary. Moreover, the combination of estuarine alterations acted to enhance the effects. These findings can serve as analogs that can be applied to other estuaries where various human alterations have occurred.

KEYWORDS

**sediment transport mechanism, land reclamation, estuarine dam, relative contribution, the Nakdong Estuary, numerical model**

# 1 Introduction

Estuaries are critical interfaces between rivers and the ocean, offering habitat for important species and acting as effective sediment traps (Guerry et al., 2012; Eidam et al., 2020). Because of their advantageous location at the land-ocean boundary, estuaries have undergone intensive development by humans to increase their utilization over the past centuries. The physical alterations of estuarine development have included land reclamation and dredging, as well as the construction of estuarine dams (French, 2001; Morris and Mitchell, 2013; Wolanksi and Elliott, 2015). Channel dredging has frequently been needed to facilitate ship navigation, and the dredged materials were often used to reclaim tidal flats to secure land for industrial, agricultural, and domestic purposes. Estuarine dams, while not as common as other alterations, have been constructed within the tidal limit to block salt intrusion and regulate freshwater discharge for agricultural, industrial, and domestic use (Williams et al., 2014).

Multiple human alterations have often occurred in a single estuary, each influencing the hydrodynamics and sediment dynamics. Previous studies have tried to characterize the relative influence of each of these combined human alterations. First, the influence of both land reclamation and dredging was revealed in The Ems River Estuary (Germany) which is an estuary that has undergone both alterations. Following those human changes, this estuary has experienced continuous siltation, necessitating additional dredging (de Jonge et al., 2014; van Maren et al., 2015a). The dredging contributed to this siltation by increasing tidal amplitude and reducing hydraulic drag, and then increasing the up-estuary sediment transport (van Maren et al., 2015b). On the other hand, land reclamation led to the reduction of sediment sinks by increasing suspended sediment concentration due to decreased accommodation space (van Maren et al., 2016). Similar processes were found in other European estuaries such as the Seine estuary (France) (Grasso et al., 2018; Grasso and Le Hir, 2019) and the Loire estuary (France) (Walther et al., 2012; Winterwerp and Wang, 2013). Second, dam construction and dredging occurred in the Brisbane River estuary (Australia), resulting in enhanced sediment trapping (Eyre et al., 1998). In other estuaries, it has been found that dam construction increased the trapping capacity of the estuary by reducing the freshwater flow, while dredging contributed to trapping by increasing the volume of the estuarine basin. Third, in the estuary where the dam construction and land reclamation were done, the dam construction reduced the tidal prism. This change reduced seaward transport but increased landward transport and deposition (Zhang et al., 2015; van der Spek and Elias, 2021). Meanwhile, land reclamation enhanced erosion by reducing flood dominance and decreasing landward transport caused by tidal pumping (Cheng et al., 2020). Additionally, both estuarine dam construction and land reclamation can influence wave reworking, causing the migration of sand shoals in front of the estuary (Barusseau et al., 1998; Gao et al., 2012; Jia et al., 2013).

Previous studies suggested that various human alterations have an influence on sediment transport with different intensities and effects depending on where the alterations occurred (Luan et al., 2016; Chu et al., 2022). These studies considered the responses that occurred after human alterations. Furthermore, despite its importance to not only the management of the estuarine environment but also the future restoration of the estuary, there has been no quantitative comparison of the influence of each alteration and the mechanism that caused the changes.

The Nakdong Estuary in South Korea provides a dramatic example of an estuary that has been significantly modified by human activities in its surrounding region, including dam construction and land reclamation. Over the last century, two major estuarine dams were built there to prevent saltwater intrusion. The first was the permanently closed Noksan Dam constructed in 1934 in the West Nakdong Estuary and the second was the Nakdong Estuarine Dam constructed between 1983-1987 in the East Nakdong Estuary to regulate river discharge. Approximately 17 $km^2$ of the estuarine area was also reclaimed to create additional area for agricultural, industrial, and residential uses since 1927. Previous observational studies found that deposition in the West Nakdong Estuary and the East Nakdong Estuary differed significantly after those alterations. Deposition in the West Nakdong Estuary was gradual, at about 2-4 cm/yr, and surficial sediment was muddy; while in the East Nakdong Estuary deposition was rapid at 6 cm/yr and surficial sediment was sandy (Williams et al., 2013). Observations and a modeling study revealed that the East Nakdong Estuary was mostly affected by residual sediment flux convergence by river discharge, resulting in a rapid deposition during flood events, while the West Nakdong Estuary was affected by sediment flux convergence by tides and waves causing gradual deposition (Williams et al., 2015; Chang et al., 2020).

Although these studies have revealed sediment transport patterns that occurred after dam construction and land reclamation in the Nakdong Estuary, the relative contributions of the dam and land reclamation to the sediment transport and the quantitative comparison of sediment transport and morphological change between these alterations were still unclear due to the limitations of observations. Also, no studies have been conducted to understand the change in sediment transport mechanisms in response to those alterations in the Nakdong Estuary. To complement previous studies, this study aimed to quantitatively understand the relative contribution of the dam and land reclamation to increased sedimentation and changes to the sediment transport mechanisms throughout the Nakdong Estuary.

A numerical hydrodynamic and sediment transport model, the Coupled Ocean Atmosphere Wave Sediment Transport (COAWST) modeling system was implemented to achieve the objective by conducting and analyzing four model simulations: (1) present condition, (2) no estuarine dam construction, (3) no tidal flat reclamation, (4) both no estuarine dam construction and no tidal flat reclamation. The specific objectives to be answered by analyzing the model results are: (1) examine the relative intensity of change as a response to the estuarine dam construction and land reclamation by comparing hydrodynamics and sediment dynamics; (2) estimate the changes to sediment transport mechanism for each

alteration by decomposing sediment flux; and (3) investigate the interaction between the dam and land reclamation.

The structure of this paper is as follows. Section 2 introduces the Nakdong Estuary in further detail, while Section 3 describes the four simulations. The model simulation results are presented in Section 4. Then, Section 5 discusses the model results in terms of different impacts of dam construction and land reclamation in sediment transport and mechanisms. Finally, the conclusions of this study are drawn in Section 6.

## 2 Study Site: the Nakdong Estuary

The Nakdong Estuary is the second longest river in Korea with a length of 510 km and a drainage basin area of approximately 23,384 $km^2$ (Figure 1A). The Nakdong River bifurcates into two distributaries 20 km from the estuary mouth. The distributary that splits to the west flows about 22 km to form the West Nakdong and discharges to the offshore through the West Nakdong channel. The eastern distributary flows about 20 km to form the East Nakdong, and due to the Eulsuk Island, it leads to the offshore mainly through the East Eulsuk channel also known as the Main channel, with some split to the West Eulsuk channel (Figure 1B). There are eight sand shoals spread in front of the estuary blocking the external forcing from offshore.

The climate of the Nakdong Estuary is dominated by the East Asian monsoon. The summer climate is characterized by weak southeasterly winds and heavy precipitation, while relatively strong northwesterly winds and small precipitation occur during winter. Because of this monsoonal characteristic, about 68% of the annual precipitation occurs during the summer months between July and September, increasing freshwater discharge from the river (Park and Lee, 2016). The wave climate is also mainly controlled by the East Asian monsoon. Strong waves occur in summer when the wind blows into the estuary and weak waves occur in winter when the wind blows out from the estuary (Yoon et al., 2008). The Nakdong

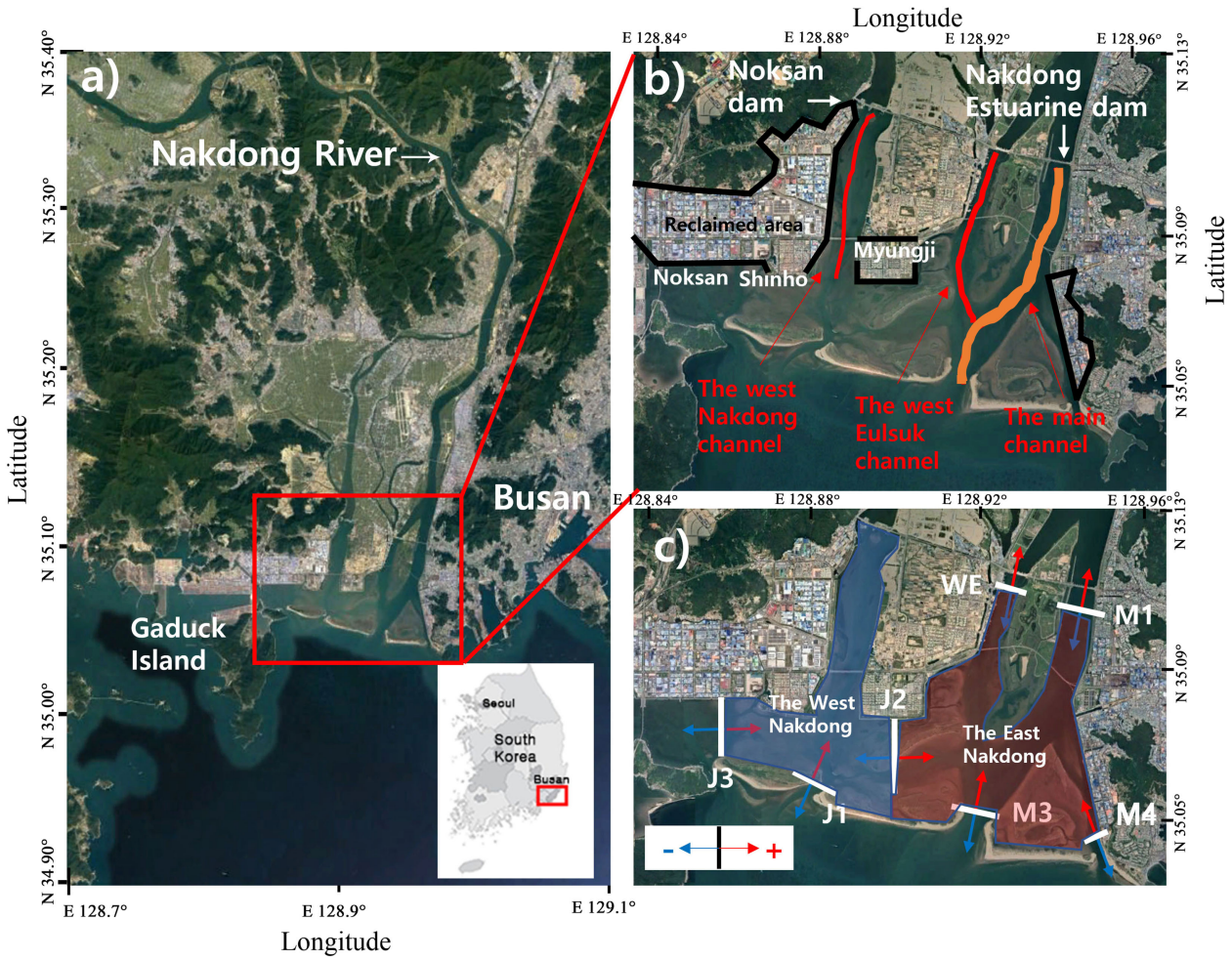


FIGURE 1
Map of Nakdong Estuary with annotation of channels and cross-sections used for analysis. **(A)** Map of South Korea and location of Nakdong Estuary. **(B)** The major anthropogenic structures are referred to as the Noksan Dam, the Nakdong Estuarine Dam, and Noksan, Shinho, and Myungji reclamation. The three channels are referred to as the West Nakdong channel, the west Eulsuk channel, and the main channel following Williams et al. (2013). The main channel was used to reveal the responses of salinity distribution and stratification in Figure 4. **(C)** Cross-sections where the sediment fluxes were calculated. Positive means landward or eastward flux and the negative means seaward or westward flux.

Estuary is classified as a microtidal, semi-diurnal system. The maximum tidal range reaches 1.5 m during a spring tide (Yoon and Lee, 2008).

The Nakdong Estuary has historically served as a habitat and as a resource for humans. The population living near this area increased from 5 million in 1966 to 7 million in 2017 (Kim, 2011). This increase has resulted in continuous development of the estuarine area. Estuarine dam construction and land reclamation are two significant anthropogenic alterations to the Nakdong Estuary within the last century.

Beginning in the 1930s, estuarine dams have been established in the Nakdong estuary to enable agricultural and industrial water usage. The Noksan Dam was the first to be built in 1934 in the West Nakdong River (Figure 1B) to save agricultural water by blocking the freshwater discharge, while the Nakdong Estuarine Dam was built in 1987 in the East Nakdong for agricultural and industrial purposes. The operation of these two estuarine dams showed significant differences, which led to different hydrodynamic environments on both sides of the Nakdong Estuary. The Noksan dam in the West Nakdong was permanently closed to save freshwater and discharged only when the water level inside of the dam was much higher than that of the sea to prevent flooding of farmland. On the other hand, the Nakdong Estuarine Dam in the East Nakdong consists of 10 radial-type main floodgates connected to the main channel to control freshwater discharge, and 5 floodgates connected to the West Eulsuk channel to support the main floodgates. Discharge primarily occurs through the main channel, and discharge through the West Eulsuk channel is only released when a large flood event occurs, such as the huge typhoon period that occurs less than twice a year, to support the main floodgates. During flood conditions, the floodgates are opened from the bottom to release freshwater, and the more the floodgates are opened from the bottom, the larger the amount of water discharged, containing both coarse sediments transported in bedload on the bottom and fine sediments transported in suspended load in the water column. These floodgates remain closed during dry conditions, and only a small amount of freshwater overflows from the top of the gates when the water level becomes higher than the dam gates; this freshwater carries only fine-grained sediment (Shin et al., 2019). As a result of the dam constructions, the West Nakdong became a low-energy regime lacking the influence of river discharge and the waves and tides became a major force to transport the sediment, causing the gradual deposition of surficial fine sediment. On the other hand, the East Nakdong was significantly controlled by river discharge from the Nakdong estuarine dam, causing dramatically rapid deposition during summer flood periods (Williams et al., 2013; Williams et al., 2015; Chang et al., 2020).

The other important human alteration which occurred in the Nakdong Estuary was land reclamation. Substantial areas of tidal flats were lost for industrial development and residential uses. Reclamation began in the 1990s in the Myungji and Noksan districts for developing residential and industrial complexes, respectively. The Myungji reclamation was conducted by solidifying the seaward edge of the island with approximately 3 km of seawalls. The Noksan reclamation was rapidly shifted from tidal flat to land by expanding the Shinho industrial port westward. As a result of reclamation, approximately 17 $km^2$ of tidal flats (13 $km^2$ in West Nakdong and 4 $km^2$ in East Nakdong) had been lost since 1927, straightening the coastline.

# 3 Methodology

A numerical hydrodynamic and sediment transport model, Coupled-Ocean-Atmosphere-Wave-Sediment Transport (COAWST) modelling system was applied to the Nakdong Estuary. In a previous study, COAWST was used to develop a model that reproduced the present-day sediment transport in the Nakdong Estuary and to reveal the mechanisms of sediment transport and morphological change (Chang et al., 2020). Here we expand on the previous study by designing three additional model scenarios to investigate the relative contributions of the estuarine dam and land reclamation to morphological change. In these additional model scenarios, the model configuration was modified to represent the Nakdong Estuary without the dam and/or land reclamation projects. This section provides the details of the designed model scenarios, briefly explains the model settings described more in Chang et al. (2020), and introduces how the model results were analyzed.

## 3.1 Model setup

Four model scenarios were designed and implemented to investigate the relative contributions of dam construction and land reclamation. They included 1) present condition (Case 1: Present), 2) No estuarine dam construction (Case 2: No dam), 3) No-tidal flat reclamation (Case 3: No reclamation), 4) No-estuarine dam and No-reclamation (Case 4: No dam/reclamation).

Case 1 (Present; Figure 2A) represents the present-day condition of the Nakdong Estuary for which results are reported in Chang et al. (2020). For Case 2 (No dam; Figure 2B), the model grid was modified so that the estuarine grid in the main channel was removed, and the Nakdong Estuary was extended upstream by about 60 km to the Nakdong River (Figure 2C). The model grid retained the Noksan dam so that the West Nakdong was still blocked. This was because the Noksan dam has not been discharged to save agricultural water since its construction in 1934, while most human developments occurred in the late 1900s including the land reclamation of a massive tidal flat region and the construction of the Nakdong estuarine dam. The bathymetry of the Nakdong River was based on available bathymetric maps, while the bathymetry of the Nakdong Estuary was the same as in Case 1. The sediment sample data from a previous study was interpolated to derive the sediment fraction on the model's riverbed (Kim et al., 2017). Bed sediment in the Nakdong River was dominated by sand (Figure 3A).

Case 3 (No reclamation) was designed to represent the system in the absence of the tidal flat reclamation projects in the Nakdong Estuary (Figure 2D). The reclaimed tidal flat was removed from the model grid based on the 1971 coastline (Figure 2E). Based on the historical records, about 13.4 $km^2$ of tidal flats in the West Nakdong

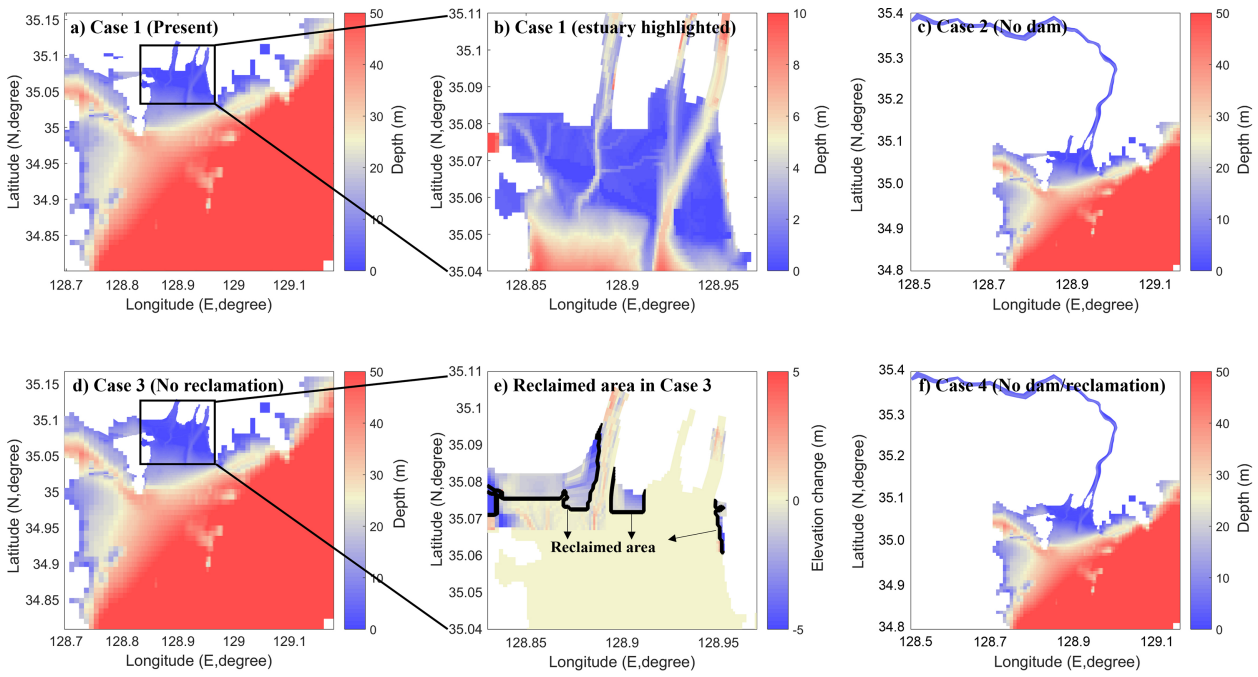


FIGURE 2
Description of the model domain of **(A)** Case 1 (Present), **(B)** The areas where the model results were mainly analyzed. **(C)** Case 2 (No dam) was extended to the Nakdong River without the Nakdong Estuarine dam while the Noksan dam was still closed, **(D)** Case 3 (No reclamation) without land reclamation of about 17 $km^2$, **(E)** The areas where land reclamation occurred compared to Case 1. **(F)** Case 4 (No dam/reclamation) without both dam construction and land reclamation by combining the Case 2 and 3. The color is water depth for each scenario.

and only 3.6 $km^2$ of tidal flats in the East Nakdong were restored in this scenario. The bathymetry of restored areas was recreated based on the bathymetric map from 1971 (Williams et al., 2015). Lacking observations, the sediment fraction in the restored area was obtained by interpolating the nearest sediment size distribution of the surrounding area (Figure 3B). Most of the restored tidal flats showed a similar sediment fraction with similar percentages of clay, silt, and sand.

Case 4 (No dam and no reclamation) was designed to reproduce pristine conditions that lack both the estuarine dam and reclamation (Figure 2F). The bathymetry and sediment fraction of the Nakdong River which was used for Case 2 and those of restored tidal flats for Case 3 were combined to represent hydrodynamic and sediment transport conditions prior to both estuarine dam construction and land reclamation.

The model grid included the Nakdong Estuary and the offshore region, and for Cases 2 and 4 the upstream Nakdong River was also included. The finest horizontal grid resolution was about 70 m in the estuary and grew coarser offshore. The resolution of the vertical grid increased within the estuary (0.1 m) and decreased at the open boundary (11 m). The model scenarios were run to represent sediment transport through one year (January 1 – December 31, 2011), and this period was selected because the observation and model validation was conducted in previous studies (Williams et al., 2015; Chang et al., 2020). All scenarios shared the same forcing including four different types: wind, river discharge, waves, and tides. The river discharge was concentrated during summer and occurred at the upstream river channel for Cases 2 and 4 without the estuarine dam construction, while the discharge was released at the location of the estuarine dam for Cases 1 and 3. The fluvial discharge data observed daily in the Nakdong estuarine dam for 2011 by the Korea Water Resources Corporation was used. The annual mean discharge was about 450 $m^3/s$ and the maximum reached 10,200 $m^3/s$ in July, accounting for 60% of discharge in summer. The sediment discharge increased corresponding to riverRechel discharge and the same amount of sediment was included for each scenario. The waves and tides for the scenarios were propagated from the boundary, sharing the same wave heightRechel and tidal range. All scenarios also shared the sameRechel initial conditions and boundary conditions to isolate the influence of estuarine dam construction and land reclamation. Like Chang et al. (2020), the model accounted for six sediment classes including two fluvial sediment classes (clay, silt) and fourRechel estuarine sediment classes (clay, silt, sand, washload sediment). Cohesive sediment processes such as flocculation and deflocculation were neglected in the sediment transport calculations following Warner et al. (2008).

The model was validated extensively by Chang et al. (2020) and performed reasonably well in reproducing the hydrodynamics and sediment dynamics in the Nakdong Estuary. The in site observation data for 2011 of tide, current velocity, and SSC were utilized to validate the model results (Williams et al., 2015). The model was validated at the point between the inlets and the point located in front of the Nakdong estuarine dam. The correlation coefficient reached about 0.96 for tide, 0.84 for current velocity, and 0.80 for SSC. And the skill value showed >0.91 for tide, >0.83 for current

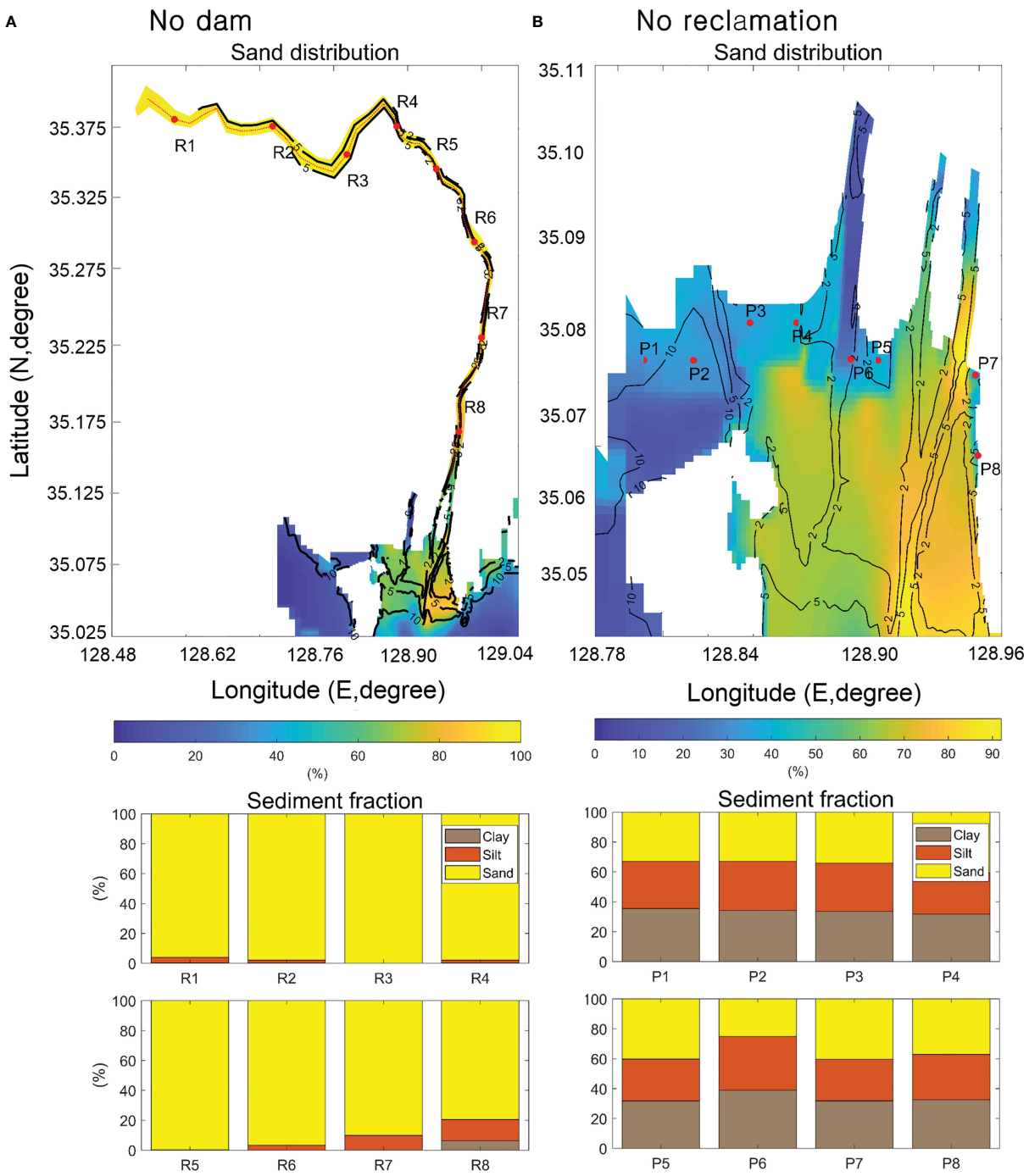


FIGURE 3
Reproduced sediment bed properties. **(A)** sand distribution of no dam scenarios (Cases 2 and 4) (top) and sediment fraction of designated points. **(B)** sand distribution of no reclamation cases (Case 1 and 3) (top) and sediment fraction of designated points. The area of the river added for the no-dam case was dominated by sand and the area of the flats added for the no-reclamation case contained similar fractions of sediment in the bed which were relatively equally distributed.

velocity, and >0.64 for SSC. For more details, readers can refer to Chang et al. (2020).

## 3.2 Model data analysis

The model results were analyzed to quantify the influence of estuarine dam construction and land reclamation on hydrodynamics and sediment transport. The model results from the initial 14 days were excluded from the analysis to allow for the model to stabilize. To quantitatively evaluate the roles of estuarine dam construction and land reclamation, the annual and depth-averaged current velocity and suspended sediment concentration (SSC) were calculated and compared between scenarios (Figure 1B). Sediment flux was calculated as the product of velocity ($u_{(z)}$) and SSC ($c_{(z)}$). This sediment flux was integrated through the cross-

sections representing the boundaries between the East and West Nakdong, offshore, and river (Figure 1C), and then time-integrated to estimate the net sediment transport through boundaries (Scully and Friedrichs, 2007; Sommerfield and Wong, 2011). The bed level change was calculated as the difference between the bed level after one year to that after the model was stabilized (14 days). The deposited sediment mass was also compared to estimate the depositional pattern of each scenario. The sediment mass deposited or eroded from the sediment bed was analyzed using the same procedure with bed level change and integrated spatially.

Another method was applied to compare the processes related to sediment transport and deposition. The water column stability determined by stratification and vertical mixing is an important factor that significantly affects the vertical diffusion of suspended sediment within the water column. The Richardson number (Ri) was calculated to compare water column stability:

$$N^2 = -\frac{g}{\rho}\left(\frac{d\rho}{dz}\right) \quad ,$$

$$Ri = \left(\frac{N}{du/dz}\right)^2 \qquad \text{(Eq. 1)}$$

This number was suggested by Richardson (1920) based on the relative magnitudes of vertical shear (du/dz) and vertical buoyancy frequency (N) where g is gravitational acceleration, $\rho$ is water density, and u is current velocity. Previous studies provide the stability threshold number of 0.25 (Miles, 1961). Ri<0.25 is generally a sufficient condition for instability while Ri>0.25 insures stability. By multiplying the Richardson number by 4 and taking the log, positive values can be interpreted to indicate the presence of stratification, and negative values indicate a well-mixed water column.

To understand the underlying processes driving fluxes, many researchers have applied decompositions of flux (Dyer, 1997; Díez-Minguito et al., 2014; Becherer et al., 2016). This study used more advanced sediment flux decomposition suggested by Burchard et al. (2018), which consists of five components to estimate the relative importance of sediment transport mechanisms for each modeled scenario. The decomposition takes the following form:

$$A[uc]_A = W[D[u]_z[c]_z]_y + W[D[u]'_z[c]'_z]_y + W[D[\tilde{u}\tilde{c}]_z]_y + W[D[\tilde{u}'\tilde{c}']_z]_y + W[D'[uc]'_z]_y \qquad \text{(Eq. 2)}$$

Here, the prime (‘) and a tilde (~) denote the deviation of a tidal average and a vertical mean respectively. The $[]_z$ represents depth-averaged values and < > the tidal-averaged values. Also $[]_y$ represents the lateral-averaged values and $[]_A$ the cross-sectional averaged values. The first term on the right-hand side is called the mean flux and represents the average transport which is usually down-estuary transport driven by river runoff, but can be influenced by other processes such as wind. The second term is referred to as the tidal pumping flux and is calculated as the tidal covariance of tidally averaged transport. This flux represents the depth-averaged sediment transport difference between flood and ebb tides. The third term was referred to as the estuarine circulation flux and represents the vertical covariance of tidally averaged transport. The fourth term was vertical and temporal covariance transport. This flux represents the difference in sediment transport between flood and ebb by tidal straining resulting from the destabilization of the water column. The last term was temporal depth covariance induced by Stokes transport.

The sediment flux decomposition analysis was completed to evaluate how anthropogenic modifications (land reclamation and damming) may have shifted the balance among the sediment flux mechanisms. All the model scenarios applied this decomposition to compare and examine the relative influence of estuarine dam construction and land reclamation on the sediment transport mechanism. For each model scenario, the decomposition was applied to three locations (the main channel, the West Nakdong channel, and the West Eulsuk channel) and during two different modeled events (tide and discharge events).

# 4 Results

## 4.1 Short-term response of stratification and SSC to estuarine alterations

To evaluate the response of estuarine circulation and water column stability to estuarine dam construction and land reclamation, the salinity, Richardson Number, and vertical SSC distribution were compared between scenarios. Figure 4 shows the vertical salinity distributions along the main channel that were averaged over cross-sections and one tidal cycle on July 9, 2011, which represents the typical condition of freshwater discharge. The presence of the estuarine dam significantly influenced the salinity distribution, exhibiting similar distributions of salinity for Cases 1 and 3 (Figures 4B, D). The water column showed strong stratification with a large salinity gradient between the surface and bottom because of freshwater discharge from the estuarine dam. An exception was that the water column was well-mixed in front of the dam where the freshwater discharge occurred from the bottom. On the other hand, Cases 2 and 4 showed higher salinity in the main channel, ranging from 29 to 33 psu (Figures 4C, E). This increased salinity without vertical salinity gradient resulted from enhanced saltwater intrusion in the absence of the estuarine dam as well as enhanced mixing due to the increased current velocity.

Water column stability is determined by the density gradient and current velocity and is an important factor that controls both the vertical mixing and the vertical diffusion of suspended sediment from the bed. Figure 4 also shows the Richardson number, averaged over cross-sections and one tidal cycle, for model scenarios (Cases 1 to 4), and the presence or absence of the estuarine dam played an important role in water column stability. For scenarios with the estuarine dam (Cases 1 and 3), the Richardson number exceeded the critical value of 0.25 throughout the channel, implying that the water was strongly stratified due to the influence of freshwater discharge from the estuarine dam (Figures 4F, H). On the other hand, Cases 2 and 4 showed the Richardson number less than 0.25 in the channel especially in the mid-water column and surface waters, indicating that the layers were well-mixed (Figures 4G, I). This mixing

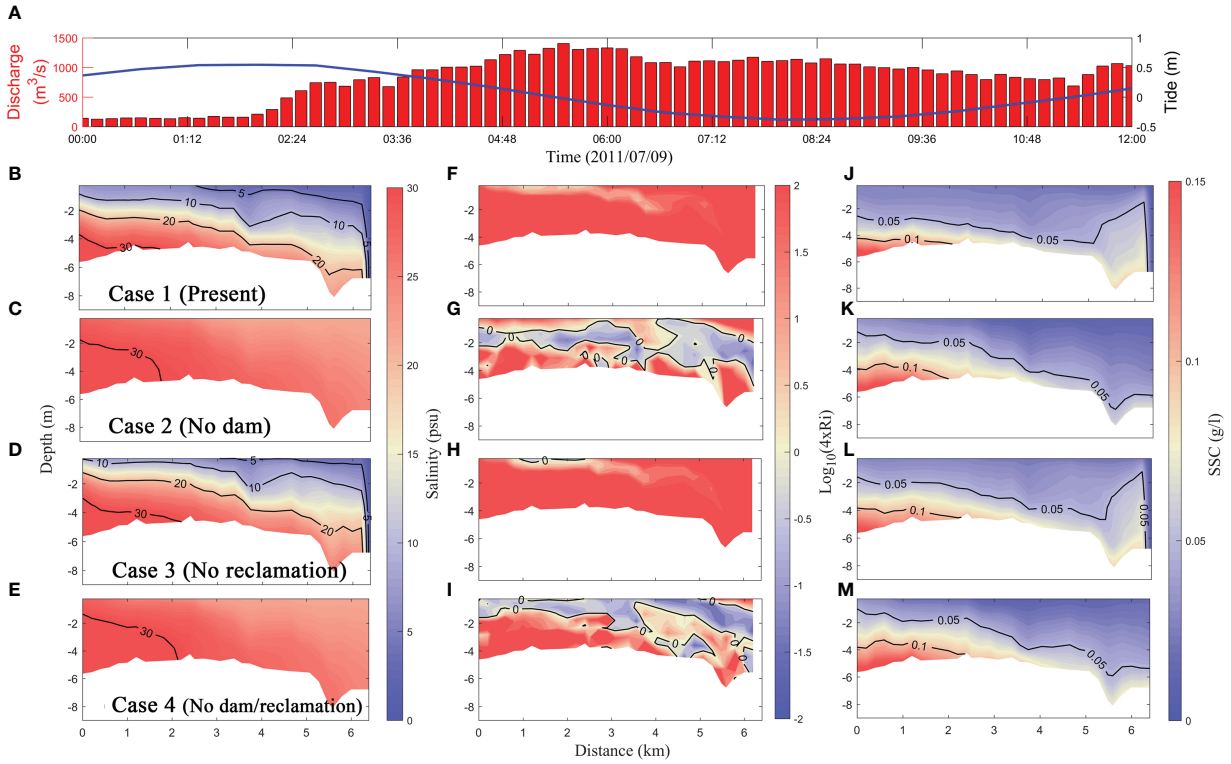


FIGURE 4
The distribution of tidally averaged salinity **(B–E)**, the Richardson Number **(F-I)**, and suspended sediment concentration (SSC) **(J–M)** in the main channel for Case 1 **(B, F, J)**, Case 2 **(C, G, K)**, Case 3 **(D, H, I)** and Case 4 **(E, I, M)**. The results were averaged on July 9, 2011, when there was river discharge corresponding to the annual mean value and mean tidal range **(A)**. The x-axis indicates the distance up the main channel, with 6.5 km being the location of the present-day Nakdong Estuarine Dam. The blue in salinity **(B–E)** and SSC **(F–I)** means low salinity and SSC, while red means high salinity and SSC. The Richardson Number was scaled as ($\log_{10}$(4Ri)) so that positive values indicate stratified conditions, and negative values indicate well-mixed conditions.

resulted from increased saltwater intrusion and faster current velocities in the absence of the estuarine dam.

Figure 4J to 4M show the vertical distribution of SSC in the main channel, averaged over cross-sections and one tidal cycle, for Cases 1 to 4, respectively. The distribution of SSC was also significantly influenced by the estuarine dam construction. The SSC for Cases 1 and 3 was limited to the bottom of the water column due to the stratification (Figures 4J, L). In front of the dam (5-6.5 km), the suspended sediment was diffused to the water surface from the bottom (Figures 4J, L). In contrast, the scenarios without the estuarine dam (Cases 2 and 4) showed slightly higher SSC in the water column owing to the enhanced mixing in the water column (Figures 4K, M).

## 4.2 Hydrodynamics and suspended sediment concentration

The current velocity and suspended sediment concentration were averaged over the depth and a year to quantitively compare the response of the hydrodynamics and sediment dynamics. Figure 5 shows the mean current velocities (arrows) and suspended sediment concentrations (pseudocolor) for 4 scenarios (Cases 1 to 4) and their values for the East and West Nakdong, and the whole estuary are tabulated in Table 1. The estuarine dam had a greater influence on the annual mean current velocity than land reclamation. The overall pattern of currents of Case 2 was similar to that of Case 1, but the magnitude increased from 0.088 m/s for Case 1 to 0.158 m/s for Case 2 (Figure 5B). This significant change in current speed mostly occurred in the East Nakdong, but the current speed remained similar in the West Nakdong. The current speeds for Case 4 were the fastest among the scenarios, but they were only slightly faster than those for Case 2 (Figure 5D; Table 1). It is noted that the velocity turned landward in the West Eulsuk Channel while the seaward velocity increased in the main channel, unlike the current directed seaward in both channels for Case 2. The current velocity for Case 3 didn't change significantly, implying that the land reclamation had a weaker influence than the estuarine dam (Figure 5C; Table 1).

The suspended sediment concentration changed significantly by both the estuarine dam and the land reclamation. The SSC increased from 0.036 kg/m$^3$ for Case 1 to 0.052 kg/m$^3$ (44%) for Case 2 in the entire Nakdong estuary (Figure 5B; Table 1). The concentration on both sides of the Nakdong Estuary increased, though it was higher (88%) in the East Nakdong compared to a slight increase (10%) in the West Nakdong. A greater increase of SSC in the East Nakdong was consistent with the increase in the current velocity that occurred in the East Nakdong for the scenarios

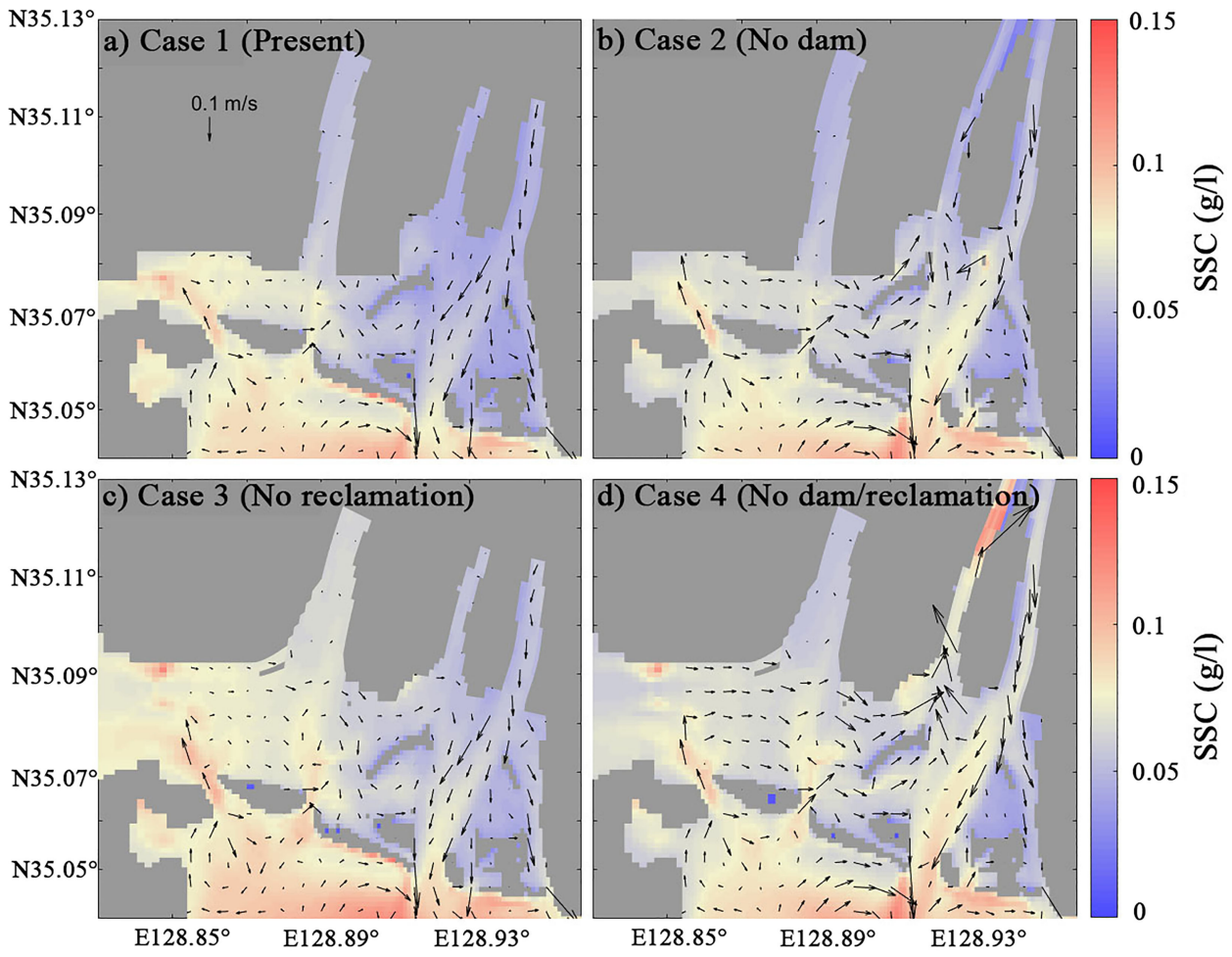


FIGURE 5
Depth-averaged and annual mean velocity (arrows) and suspended sediment concentration (SSC, pseudocolor) depending on the presence of the estuarine dam and land reclamation for **(A)** Case 1, **(B)** Case 2, **(C)** Case 3, and **(D)** Case 4.

without the estuarine dam (Cases 2 and 4). On the other hand, the SSC of the entire estuarine area decreased by 42% from 0.036 to 0.021 kg/m$^3$ for Case 3 (Figure 5C). This decrease in SSC occurred mainly in the West Nakdong (43% from 0.046 to 0.026 kg/m$^3$). The SSC was the most enhanced for Case 4, which was about 10% larger than Case 2 (Figure 5D; Table 1). The increase in SSC occurred in both the East and West Nakdong and the response of SSC corresponded to the enhanced current velocity seen in Case 4.

## 4.3 Sediment flux

The cross-sectionally integrated, time cumulative sediment flux was calculated through the five cross-sectional transects (shown in Figure 1C) to characterize the transport of sediment (Figure 6). The sediment fluxes for M4 and J2 appeared similar to other cross-sections in the East Nakdong and the West Nakdong, respectively, and they were excluded from Figure 6. See the supplementary material for all cross-sections (Figure S1). The sediment flux of M1 in front of the Nakdong estuarine dam was mainly directed seaward about 600 kt at the end of the year for Cases 1-3, but it increased to about 900 kt for Case 4 (Figure 6C). The increase in sediment flux was gradual most of the time, but the large sediment flux occurred during the large discharge events. M3 near the tidal inlet showed similar behavior to M1 but had a reduced magnitude of sediment flux (220 kt for Cases 1-3 and 400 kt for Case 4), indicating the convergence of sediment flux (Figure 6E). The cross-section WE, located in the West Eulsuk channel, exhibited different behavior in sediment flux (Figure 6D). No sediment flux occurred for Cases 1 and 3 because no discharge was allowed through the estuarine dam in the West Eulsuk channel. By removing the estuarine dam (Case 2), WE showed a similar pattern of sediment flux as shown in the East Nakdong, but at a reduced magnitude. On the other hand, the sediment flux was directed landward with the total integrated sediment flux of about 400 kt for Case 4. The change in the sediment flux coincided with the change in currents (Figure 5D). Overall, the removal of the dam appears to have a larger impact than the land reclamation in the East Nakdong estuary.

The cumulative sediment flux for the year was less in the West Nakdong than in the East Nakdong. Since no freshwater discharge was allowed from the estuarine dam in the West Nakdong,

TABLE 1 Comparison of hydrodynamics and sediment dynamics for each case. East and west denote the East Nakdong and West Nakdong estuary, respectively.

| | | current | | SSC | | depositional mass | |
|---|---|---|---|---|---|---|---|
| | | (m/s) | (%) | (kg/m$^3$) | (%) | ($10^8$ kg) | (%) |
| Case 1 | total | 0.09 | 0.0 | 0.04 | 0.0 | 8.30 | 0.0 |
| | east | 0.10 | 0.0 | 0.03 | 0.0 | 5.64 | 0.0 |
| | west | 0.06 | 0.0 | 0.05 | 0.0 | 2.56 | 0.0 |
| Case 2 | total | 0.16 | 79.5 | 0.05 | 44.4 | 1.31 | -84.2 |
| | east | 0.21 | 118.0 | 0.06 | 84.0 | 0.51 | **-91.0** |
| | west | 0.06 | 6.0 | 0.05 | 10.0 | 0.80 | -69.0 |
| Case 3 | total | 0.09 | 2.3 | 0.02 | -41.7 | **8.68** | 4.6 |
| | east | 0.10 | 1.0 | 0.03 | -3.0 | 4.94 | -12.0 |
| | west | 0.06 | 6.0 | 0.03 | -43.0 | 3.74 | 46.0 |
| Case 4 | total | 0.16 | 87.8 | 0.06 | 58.3 | 1.70 | -79.5 |
| | east | **0.22** | **129.0** | **0.06** | **96.0** | 0.97 | -82.0 |
| | west | 0.07 | 11.0 | 0.06 | 21.0 | 0.73 | -72.0 |

SSC is suspended sediment concentration. The percentage represents the change from Case 1.
The bolds are representing the largest value of each component (current, SSC, depositional mass).

sediment was transported into the estuary through the inlet (J1) for all scenarios (Figure 6F). Of the four scenarios, the largest cumulative sediment flux (about 100 kt) occurred for Case 4. Cases 2 and 3 had smaller sediment fluxes about 50 kt and the smallest sediment flux was shown for Case 1. The cross-section at the western boundary of the West Nakdong (J3) had positive sediment flux except for Case 2, implying the gradual inflow of sediment (Figure 6G). Cases 1 and 3 delivered about the same amount of sediment across this transect, while this sediment flux decreased for Case 2 at about 10 kt. Notably, the inflow of sediment was amplified for Case 4, delivering 120 kt across transect J3. The responses of sediment flux in the West Nakdong indicated the influence of both the estuarine dam construction and land reclamation.

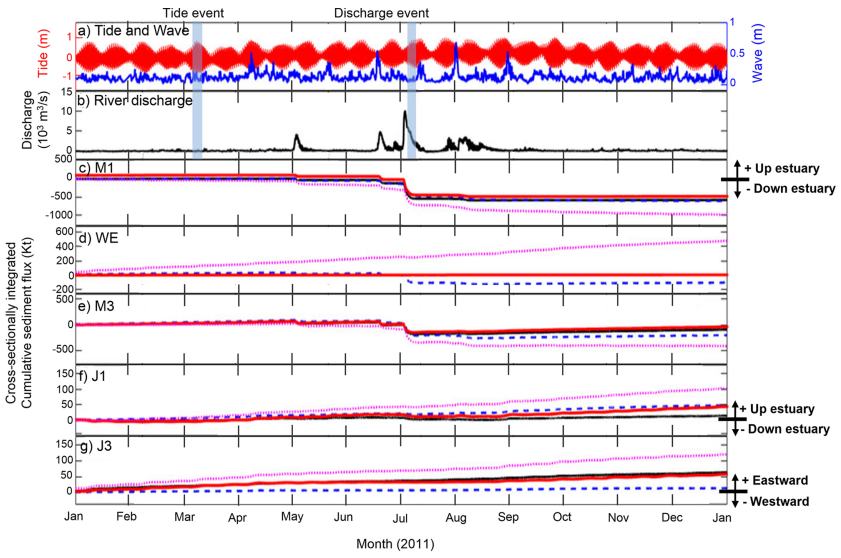


FIGURE 6
Cross-sectionally integrated cumulative sediment flux for estuarine cross-sections. **(A)** Tide range and wave height during 2011. **(B)** River discharge during 2011. Cross-sectionally integrated cumulative sediment fluxes are shown for cross-sections **(C)** M1, **(D)** WE, **(E)** M3, **(F)** J1, and **(G)** J3. For M1, WE, M3, and J1, positive sediment flux is directed up-estuary. For J3, positive sediment flux is directed eastward. The M4 cross-section appeared similar to other cross-sections in the East Nakdong (M1, M3, and WE), and J2 appeared to be similar to J1, so these cross-sections were omitted. For all cases and channels, the reader is referred to the supplementary material (Figure S1).

## 4.4 Bed level change and the fate of river sediment

The presence and absence of the land reclamation and estuarine dam led to changes in hydrodynamics and sediment transport, which then changed depositional patterns. Figure 7 shows the bed level change over a year for all scenarios (Figures 7A–D) and the difference in bed level change between Case 1 and other scenarios (Figures 7E–G). The most significant bed level changes due to both erosion and accretion occurred in the tidal flats and the main channel for Case 1 (Figure 7A). The major bed level change in the West Nakdong resulted mainly from deposition, but the magnitude was smaller. The removal of the estuarine dam (Cases 2 and 4) significantly changed the bed level in the main channel. The overall pattern for Case 2 was similar to that for Case 1 (Figure 7B), but the erosion and accretion were intensified (Figures 7B, E). On the other hand, there was no noticeable change in the bed level in the West Nakdong between Cases 1 and 2. The bed level change due to the land reclamation was less than due to the estuarine dam construction. The patterns for the bed level change were quite similar between Cases 1 and 3 (Figures 7A, C), but different in the tidal inlets in general and most significant in the West Nakdong (Figure 7F). The pattern for the bed level change for Case 4 had combined features for both Cases 2 and 3 (Figure 7D). The resemblance in the main channel between Cases 2 and 4 and in the West Nakdong between Cases 3 and 4 is striking (Figure 7). However, the bed level change in the West Eulsuk channel for Case 4 didn't correspond to any other cases. More erosion with a spatial mean of 15 cm appeared in the West Eulsuk channel for Case 4 in response to the combined effects of the estuarine dam and land reclamation.

These changes in bed level in response to the presence/absence of the dam and land reclamation can be seen in the amount of sediment mass deposited. Table 1 tabulated the net amount of deposited sediment for each scenario in the West Nakdong, East Nakdong, and entire estuary. With the removal of the estuarine dam for Case 2, the decrease in deposited sediment was notable in the East Nakdong, amounting to a 91% reduction compared to Case 1. In the West Nakdong, the reduction also occurred, but it was smaller by 70%. In contrast, about 50% of deposition occurred in the West Nakdong for Case 3, while the East Nakdong estuary underwent a 12% reduction from Case 1. These changes were less significant than the changes for Case 2, reflecting that land reclamation had less impact on the deposition. The sediment mass for Case 4 showed the combined effects of both alterations. The deposited sediment mass decreased by about 80% in the East Nakdong, indicating the effect of the estuarine dam removal. On the other hand, about 70% of the sediment mass decreased in the West Nakdong, representing the restoration of the reclaimed tidal flats (Table 1).

Next, the depositional patterns for the river-derived sediment were analyzed for each model scenario. The percentage of river-derived sediment was calculated for 10 areas (1: Upstream, 1: Estuary, 8: Coastal/shelf) and shown in Figure 8 for each scenario. The washload sediment passed the river section without deposition and the majority of washload sediment (40-57%) settled

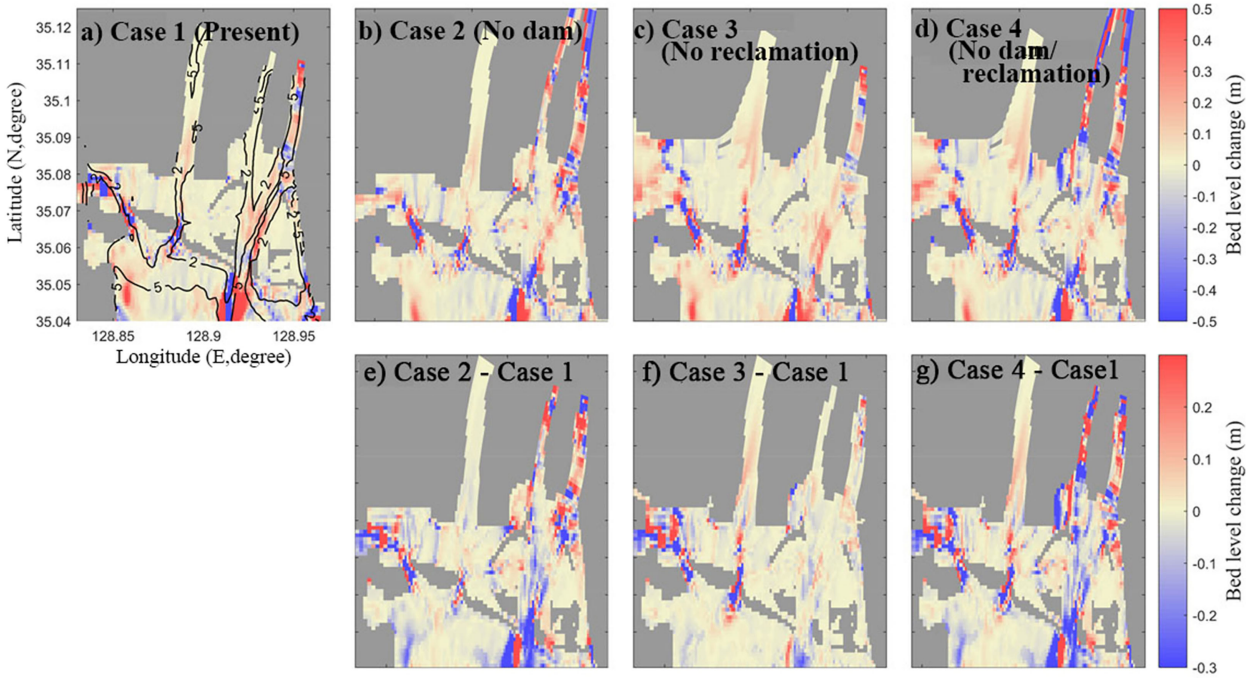


FIGURE 7
The annual change of bed level and the difference between the present (Case 1) and each case. Top: Bed level change over a year for **(A)** Case 1, **(B)** Case 2, **(C)** Case 3, and **(D)** Case 4. Positive is bed deposition and negative is bed erosion. Bottom: **(E)** The difference in the annual bed level change between Case 1 and Case 2, **(F)** Case 1 and Case 3, and **(G)** Case 1 and Case 4. Positive represents greater deposition and negative represents greater erosion compared with the present case.

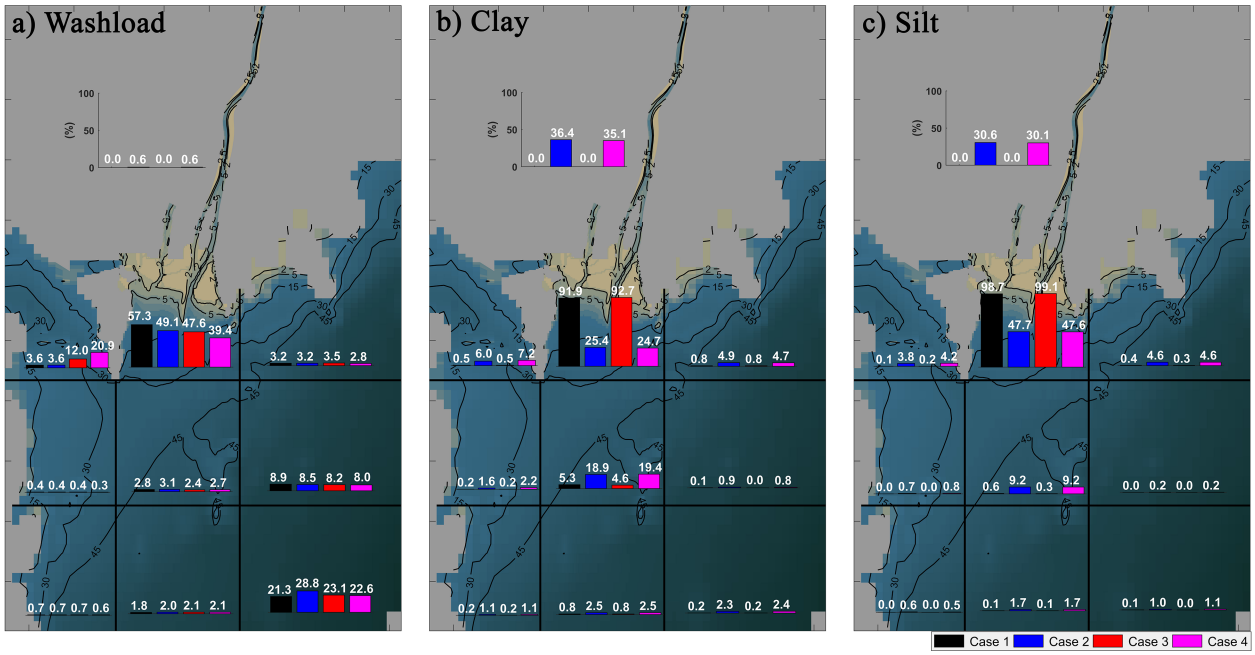


FIGURE 8
Fraction of deposited **(A)** washload, **(B)** clay, and **(C)** silt discharged from the river (%) for the four scenarios for the domain divided into one river, one estuary, and eight coastal/shelf sub-environments. The percent of deposited river sediment in each sub-environment was represented by color for Case 1 (black), Case 2 (blue), Case 3 (red), and Case 4 (magenta).

in the inner estuary (Figure 8A). The remaining washload sediment was transported to the west and further offshore. As for Cases 1 and 3, more than 90% of silt and clay were deposited in the estuary and nearby coastal region (Figures 8B, C) and only a small amount of silt and clay escaped the estuary and dispersed to all other model domains. Without the estuarine dam (Cases 2 and 4), about 35% of clay was deposited in the river, and 25 and 19% of clay were deposited in the estuary and nearshore, respectively. The remaining 20% of clay was dispersed in all other coastal and shelf areas. The heavier silt was deposited in the river and estuary, totaling about 80%. About 10% of the silt was deposited in the nearshore and the remaining 10% of silt was dispersed in the coastal and shelf area (Figure 8C). These results suggested that the presence of the estuarine dam resulted in the increased retention of riverine sediment in the estuary and that the river sediment was more widely dispersed offshore in the absence of the estuarine dam.

# 5 Discussion

## 5.1 Relative impacts of the estuarine dam and land reclamation

The model results indicated that the estuarine dam construction and land reclamation caused different magnitudes of changes to current velocity, SSC, and depositional mass (Table 1). In general, the estuarine dam produced more significant impacts than the land reclamation. The model results showed that the influence of the estuarine dam was more significant in the averaged current speed in the Nakdong Estuary. The mean current velocity doubled when the estuarine dam was removed in the East Nakdong (Figure 9; Table 1). Similar changes in current speed were reported elsewhere when an estuarine dam was constructed (Kim et al., 2006; Zhu et al, 2011). On the other hand, land reclamation had a weak impact on current speed (Figure 9B). Our results correspond to the findings of Yang and Chui (2017) that the reclamation of about 14% of the total area reduced the current speed by only 9%.

SSC was sensitive to the presence of the estuarine dam and land reclamation and the estuarine dam construction mainly impacted the East Nakdong, while impacts of reclamation were more significant in the West Nakdong (Figures 9A, B). The SSC change due to estuarine dam construction and reclamation had a similar magnitude of change, but with opposite trends. The increased SSC for the case that did not include the estuarine dam resulted from the change of hydrodynamics and sediment dynamics in the estuary in two main aspects. First was the enhanced vertical mixing and shear stress due to the increased current velocity, causing the resuspension of sediment from the bottom (Li et al., 2012; Burchard et al., 2019). The other important aspect was that the increased saltwater intrusion in the estuary decreased the vertical salinity gradient, resulting in well-mixed conditions and increased vertical dispersion of suspended sediment. On the other hand, the SSC decreased for the model run that did not include land reclamation even though the velocity was slightly increased (Table 1). This corresponded to previous studies that looked at the impact of land reclamation in other estuaries (van Maren et al., 2016; Gao et al., 2018; Cheng et al., 2020). The land reclamation affected sediment resuspension by changing the sediment sinks, resulting in a loss of accommodation space (Fountoukis and Nenes, 2005; van Maren et al., 2016).

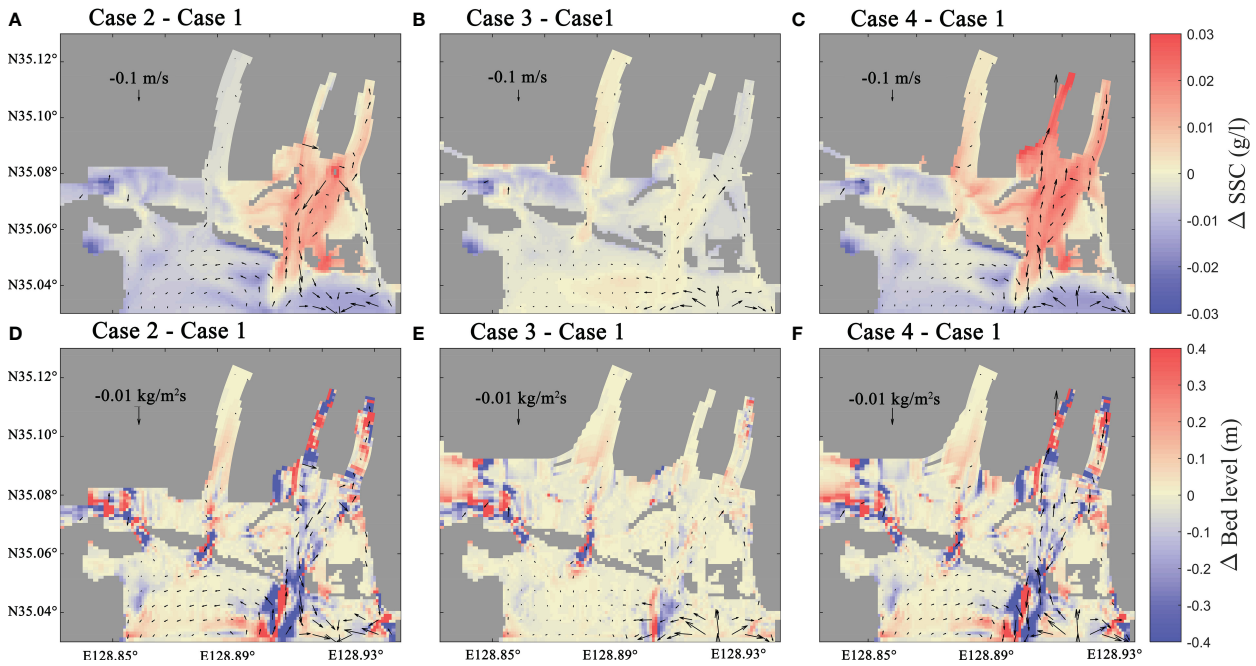


FIGURE 9
The difference of annual and depth-averaged velocity, suspended sediment concentration (SSC), sediment flux, and bed level change over a year between **(A)** Case 1 (present) and Case 2 (no dam), **(B)** Case 1 and Case 3 (no reclamation), and **(C)** Case 1 and Case 4 (no dam/reclamation). Differences between velocity (arrows) and SSC (pseudocolor) are shown on the top row **(A–C)**. Differences between sediment flux (arrows) and bed level change over a year (pseudocolor) are shown on the bottom row **(D–F)**.

The amount of sediment deposited indicated that the presence of the estuarine dam has had more influence than land reclamation on the increased sedimentation in the Nakdong Estuary. On the other hand, the depositional patterns in the East and West Nakdong responded differently to the combined effects of the estuarine dam and land reclamation (Case 4). In the East Nakdong, deposition was reduced, and the amplitude of reduction was larger than the result of the model scenario that only removed the estuarine dam (Table 1). Deposition in the West Nakdong was slightly increased for Case 4 relative to the scenario that only removed land reclamation (Case 3), implying the significant influence of land reclamation there. These results suggested that the location of the human alterations is important to the response of sediment dynamics, and also that the impact of these human alterations can be amplified by their interaction.

Comprehensively examining the above results, it was found that the change in sediment dynamic and morphological change due to the construction of the estuarine dam was relatively stronger than the change due to the land reclamation. Two major factors seem to have played a role in showing these results. The first is the type and location of the estuarine dam. The Nakdong estuary consists of the Noksan Dam, which does not discharge in the west, and the Nakdong estuarine dam, which controls the discharge in the east. In previous studies, this difference was reported to cause a change in sediment transport between the East and West Nakdong (Williams et al., 2013), and the effect of dam discharge was significant in the East Nakdong (Chang et al., 2020). The location of the dam also seems to have a significant impact. Figueroa et al. (2022a) showed that tidal currents vanish adjacent to estuarine dams due to the dead-end channel. For estuarine dams located less than the resonance length from the mouth, the effect of the dead-end channel will tend to reduce the tidal currents over a significant portion of the remnant estuary. The Nakdong estuarine dam is very close to the estuary mouth, only about 6 km upstream. This contributes to this region being greatly affected by the estuarine dam. The second is the location and extent of land reclamation. The land reclamation in the Nakdong Estuary is mainly focused in the West Nakdong and occurred at the estuary mouth. This reclamation at the mouth of the estuary leads to channel straightening to the effect that its shape more closely resembles a wave- or river-dominated estuary (Jung et al., 2021). This environmental change from a tide-dominated to a wave- or river-dominated estuary is corresponding to previous studies (Williams et al., 2013; Chang et al., 2020) and caused the increased influence of land reclamation in the West Nakdong compared to the East Nakdong.

## 5.2 Change in sediment transport mechanisms

To understand the changing sediment transport mechanisms due to the estuarine dam and land reclamation, the sediment fluxes were decomposed for the model scenarios. Figure 10 shows the decomposed sediment fluxes for tide, discharge, and wave events in the main channel. Here, only four decomposed sediment fluxes (mean, tidal pumping, estuarine circulation, and Stokes flux) along with the total flux are shown for Cases 1 and 2 because the tidal

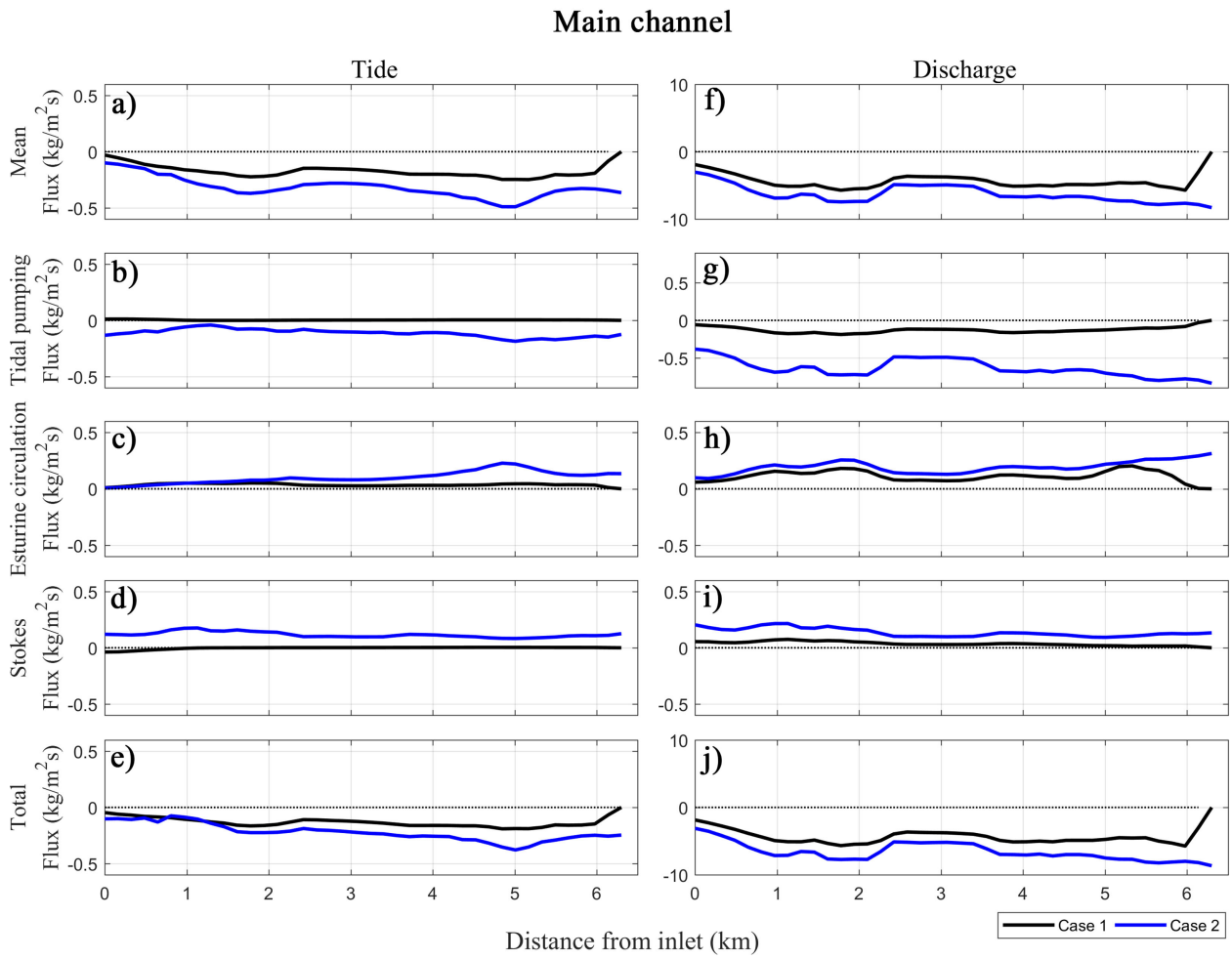


FIGURE 10
Time-averaged, cross-sectionally integrated sediment flux along-channel profiles in the main channel during tide and discharge events. Each panel shows the decomposed sediment fluxes (mean **(A, F)**, Tidal pumping **(B, G)**, Estuarine circulation **(C, H)**, Stokes **(D, I)**) and total flux **(E, J)** for Case 1 (black) and Case 2 (blue) to represent the influence of the estuarine dam. For all cases and flux components, the reader is referred to the supplementary material (Figure S2).

straining was very small, and Cases 3 and 4 were essentially the same as Cases 1 and 2, respectively. The full data can be found in the supplementary material (Figure S2). During the discharge event, the seaward mean flux due to the freshwater discharge is the only dominant mechanism, regardless of the presence of the estuarine dam, along the main channel (Figure 10). During the non-discharge period (tide event), the seaward mean flux was dominant with the presence of the estuarine dam (Case 1). With the removal of the estuarine dam (Case 2), the mean flux and the tidal pumping flux were dominant and directed seaward. The landward estuarine circulation flux increased and the Stokes flux also existed. The magnitude of these landward fluxes was smaller than the seaward mean and tidal pumping fluxes.

The previous studies revealed that the change in the tidal pumping flux and the Stokes flux can be related to the change in tidal properties (e.g., Gao et al., 2014). To estimate the change in tidal properties, the tide amplitude was compared in the three channels and the tidal distortion was calculated by the ratio of $M_2$ amplitude and $M_4$ amplitude (Figure 11). The tidal asymmetry was calculated as $\log(u_F/u_E)^3$ where $u_F$ is the tidal current velocity during flood and $u_E$ is the velocity during ebb. The change in tidal properties after the construction of an estuarine dam affected sediment transport in two aspects.

First, the change in tidal properties modified the Stokes transport. With the construction of the estuarine dam, the tide amplitude increased, especially the $M_2$ amplitude was more amplified than $M_4$. The distortion of the tidal wave was less pronounced due to this increased tidal amplitude (Zhu et al., 2021). The decreased tidal distortion resulted in the decrease of the phase difference between tidal current and sea surface height (Buschman et al., 2010). Therefore, the landward Stokes transport primarily generated by the shift from the mixed to standing wave was decreased with the tidal distortion. The reduction of tidal distortion also caused reduced asymmetry of tidal waves, causing reduced landward Stokes transport (Stanev et al., 2007; Guo et al., 2014; Burchard et al., 2018).

Second, this change in Stokes transport affected the tidal pumping flux. Without the estuarine dam, the landward Stokes

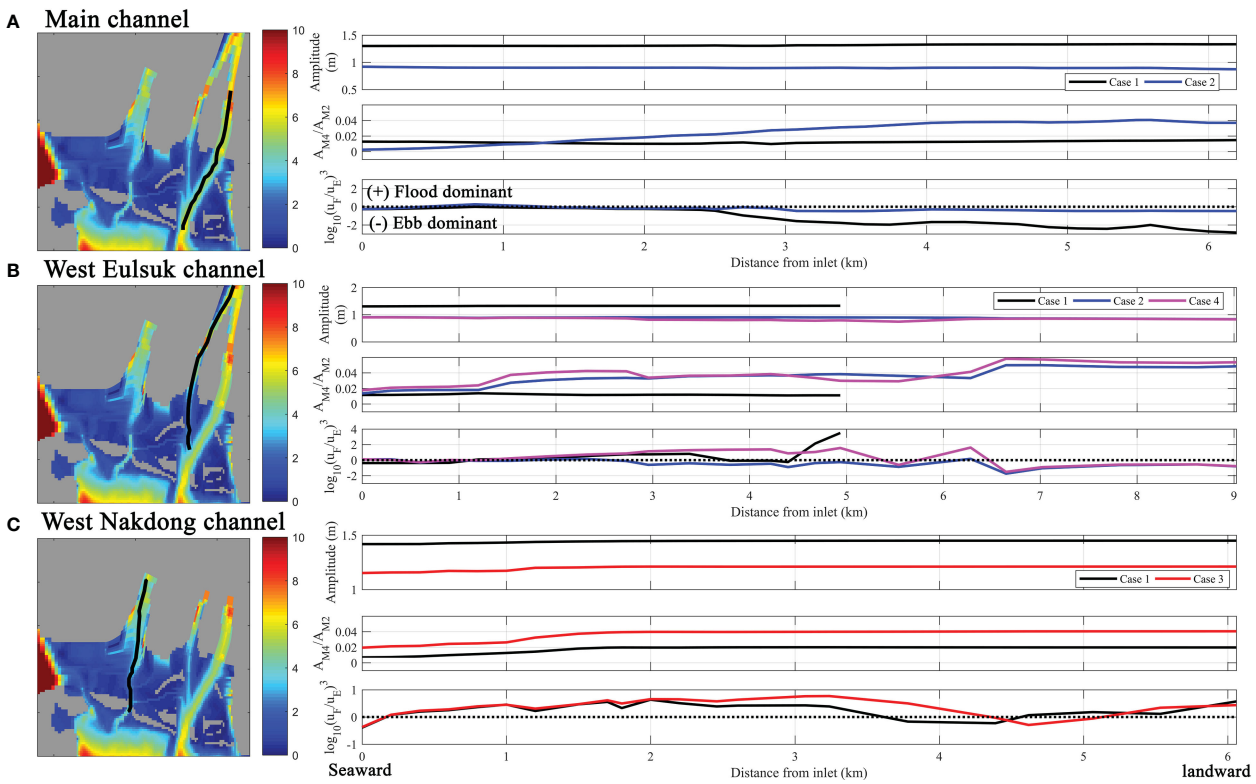


FIGURE 11
Tidal properties in the three channels for different cases. Tide amplitude, distortion, and asymmetry are shown for **(A)** the main channel with Cases 1 and 2, **(B)** the West Nakdong channel with Cases 1, 2, and 4, and **(C)** the West Eulsuk channel with Cases 1 and 2. Tidal distortion was calculated as the ratio between $M_2$ amplitude and $M_4$ amplitude, and tidal asymmetry was calculated based on the tidal current during flood and ebb. For all cases and channels, the reader is referred to the supplementary material (Figure S3).

transport caused landward water and momentum accumulation, generating a negative seaward water level gradient. This water level gradient induces a seaward return flow (Buschman et al., 2010; Guo et al., 2014), which in turn resulted in seaward tidal pumping (Guo et al., 2014; Moftakhari et al., 2016). The decreased landward Stokes drift after the construction of the estuarine dam caused the removal of seaward Stokes return flow, resulting in a decrease in the tidal pumping flux (Figueroa et al., 2022b). Unlike the tidal pumping and Stokes fluxes related to tidal properties, the estuarine circulation flux was directly related to the balance between baroclinic pressure gradient and friction (Geyer and MacCready, 2014; Hansen and Rattray Jr, 1966). This flux decreased with the estuarine dam construction due to the restricted landward bottom density gradient, resulting in decreased baroclinic pressure gradient (Shin et al., 2019). Therefore, the construction of the estuarine dam simplified the sediment transport mechanisms from a tide- and discharge-driven environment to a discharge-dominated environment.

To investigate the change in sediment transport mechanisms in the West Nakdong channel where the most land reclamation occurred, but no freshwater discharge was allowed, Figure 12 shows the decomposed sediment fluxes for tide and discharge events. Here, only three decomposed sediment fluxes (mean, tidal pumping, and Stokes flux) along with the total flux are shown for Cases 1 and 3 because the sediment fluxes of other components were insignificant, and Cases 2 and 4 were essentially the same as Cases 1 and 3, respectively. The total sediment flux in the West Nakdong channel was smaller than in the main channel and directed landward. The tidal pumping flux was the dominant component of the total sediment flux regardless of the land reclamation but was higher without the land reclamation (Figure 12b). Moreover, the tidal pumping flux was greatest at the inlet and decreased landward. The mean and Stokes fluxes also existed, but the magnitude was small. Because the West Nakdong had no river discharge and was far away from the main channel, the sediment flux during the discharge event was similar to the tide event but weaker.

In the West Nakdong where the river discharge was blocked in all model scenarios, the change in tidal properties was the main sediment transport mechanism, resulting in the change in the tidal pumping flux (Figure 11). Basically, the land reclamation caused the change in tidal properties by reducing the tidal storage (van Maren et al., 2023). The land reclamation of the shallow tidal flats resulted in a decrease in the estuarine volume and thus a change in tidal propagation pattern (Chu et al., 2022). Especially, the tidal propagation was accelerated, and the tidal amplitude was increased by increased convergence (Savenije et al., 2008; Van Rijn, 2011; Song et al., 2013; Zhu et al., 2016). The elimination of the tidal flat, where shallow water tidal components such as $M_4$ tide were generated, resulted in more increase in the tidal amplitude of

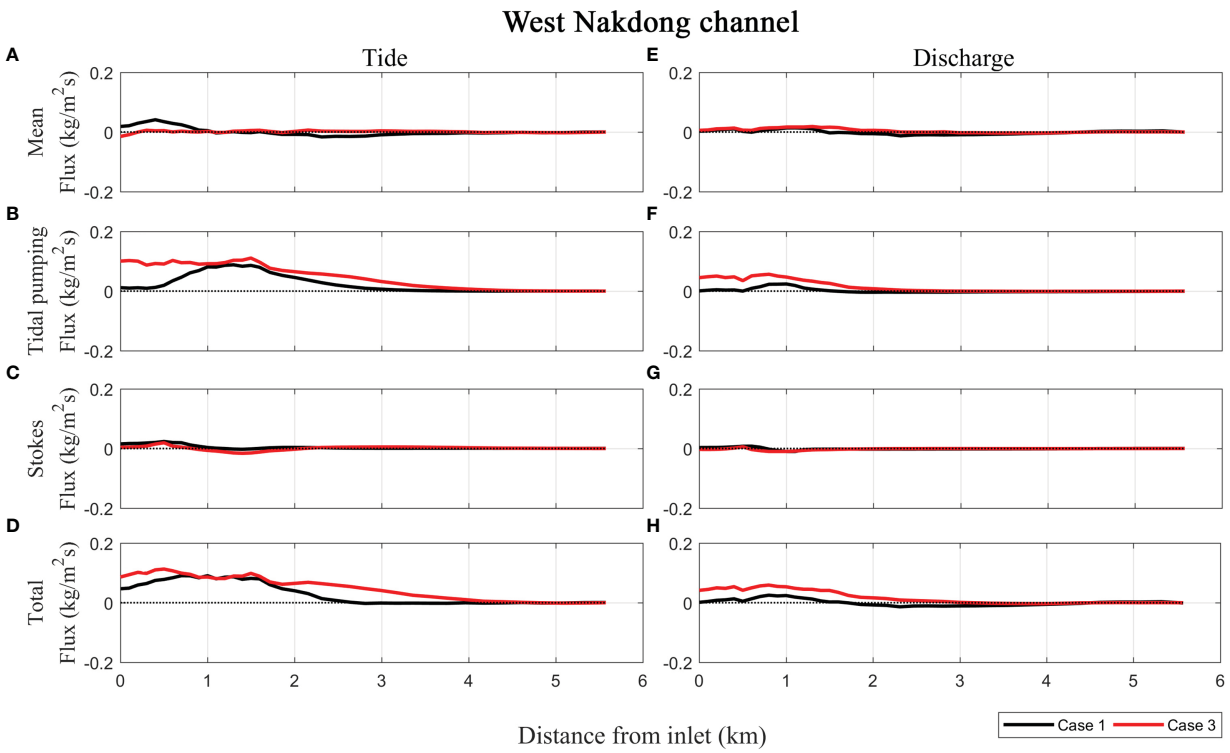


FIGURE 12
Time-averaged, cross-sectionally integrated sediment flux along-channel profiles in the West Nakdong Channel during tide and discharge events. Each panel shows the decomposed sediment fluxes (mean **(A, E)**, tidal pumping **(B, F)** and Stokes fluxes **(C, G)**) and total flux **(D, H)** for Case 1 (black) and Case 3 (red) to represent the influence of the land reclamation. For all cases and flux components, the reader is referred to the supplementary material (Figure S4).

$M_2$ than $M_4$ (Li et al., 2018). The reduction of tidal distortion due to this decreased shallow water tidal components caused the decreased flood dominance in the estuary (Aubrey et al., 1988), which decreased the tidal pumping from offshore (Song et al., 2013; Liang et al., 2018). In addition, it is known that the response of the sediment transport can be different depending on the location of the reclaimed area (Liang et al., 2018). When the reclamation occurred near the inlet, the reduction of the surface area near the inlet promoted the transfer of energy from astronomical tide (such as $M_2$) to shallow water tide (such as $M_4$), enhancing flood dominance. On the other hand, the reclamation of the tidal flats inside the estuary restrained the tidal energy of shallow water tide and thus reduced the flood dominance, which corresponds to the case of the West Nakdong (Liang et al., 2018). This study implies that the location of the land reclamation is an important factor in estuarine sediment transport.

## 5.3 Interaction between estuarine dam and land reclamation in the West Eulsuk channel

The hydrodynamic and sedimentary changes for Case 4 resulted from the combined effects of Cases 1 and 2. Case 4 showed similar characteristics of the removal of the land reclamation in hydrodynamic and sediment dynamics as Case 3 in the West Nakdong. On the other hand, the characteristics in the change of current velocity, SSC, and bel level for Case 4 were similar to those of Case 1 in the East Nakdong where the estuarine dam was removed. However, the amplitude of change in velocity and SSC was enhanced in the West Eulsuk channel and the cumulative sediment flux was directed landward with both alterations because of combined impacts by both alterations. Figure 13 shows the sediment flux of three components (mean, tidal pumping, and estuarine circulation) for two events (tide and discharge events) along the West Eulsuk channel for Cases 2 and 4. The mean flux was dominant and directed seaward for Case 2 during the discharge event, but the magnitude was smaller than the sediment flux in the main channel. However, the sediment flux was insignificant for all components for Case 4, except for the seaward mean flux at the estuarine dam (Figure 13E). For the tide event, the sediment fluxes were very small for all decomposed components for Case 2. However, both the mean flux and the tidal pumping components were a similar magnitude and directed landward during the tide event. The estuarine circulation was weak for Cases 2 and 4. Thus, the sediment flux for Case 2 showed a similar behavior in the main channel, but the sediment flux for Case 4 revealed a similar behavior in the West Nakdong.

In order to estimate the combined effect, the cross-sectionally averaged residual current and the cross-sectionally integrated water flux were calculated (Figure 14). During the tide event, the residual current flowed from the West Nakdong to the East Nakdong and the velocity was increased without the estuarine dam construction (Figures 14A, B). This enhanced residual current without the dam

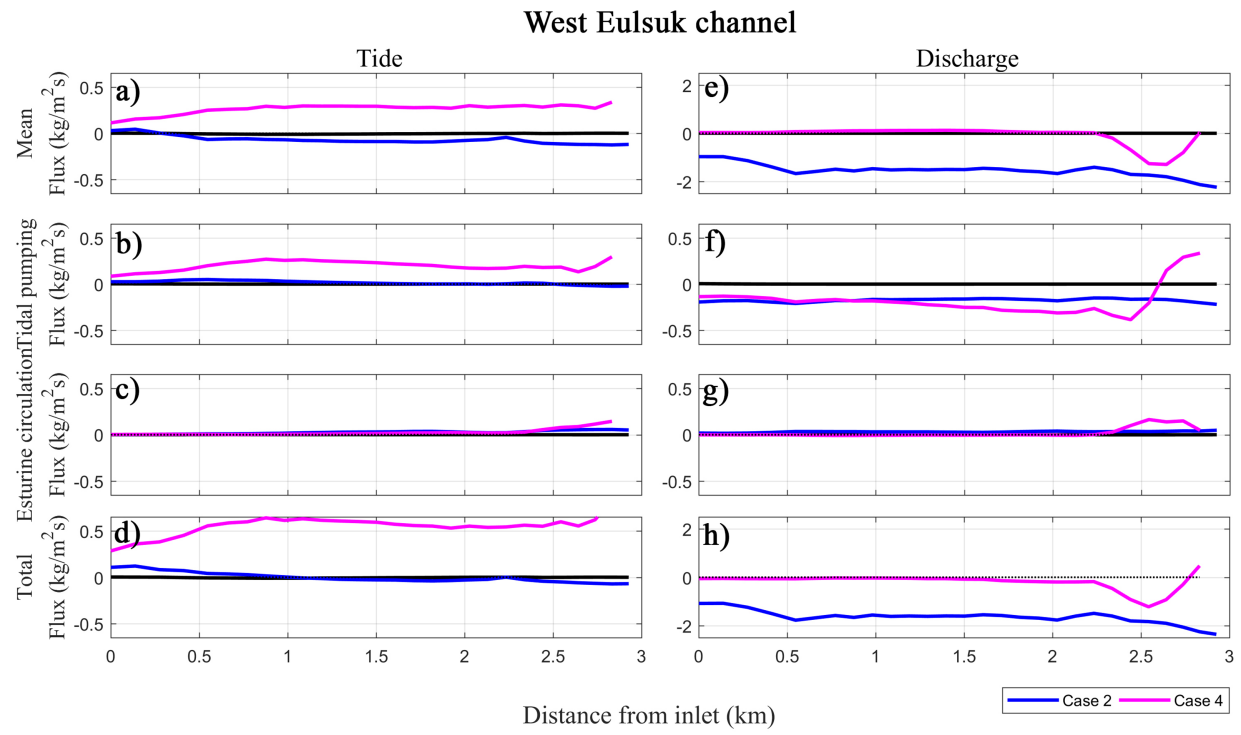


FIGURE 13
Time-averaged, cross-sectionally integrated sediment flux along-channel profiles in the West Eulsuk Channel during tide and discharge events. Each panel shows the decomposed sediment fluxes (mean **(A, E)**, tidal pumping **(B, F)** and estuarine circulation fluxed **(C, G)**) and total flux **(D, H)** for Case 2 (blue) and Case 4 (magenta) to represent the interaction between the estuarine dam construction and the land reclamation. For all cases and flux components, the reader is referred to the supplementary material (Figure S5).

carried more water from the West Nakdong to the East Nakdong (Figures 14B, C). On the other hand, the reclamation reduced the residual velocity but the magnitude of change was smaller than the change without estuarine dam construction (Figures 14A, B). It is important that the amount of water flux without the land reclamation increased, even though the residual velocity was decreased, due to the expansion of the cross-section (Figures 14B, C). Therefore, the combined impact between the enhanced residual current without the dam and the increased water flux without land reclamation resulted in the dramatically increased westward mean flux, which continued to become a landward flux in the West Eulsuk channel. During the discharge event, the mean flux due to river discharge was offset with the mean flux from the West Nakdong without both estuarine dam and land reclamation, while the high mean flux occurred without only estuarine dam (Figure 14C–E). Therefore, the land reclamation amplified the mean flux enhanced by the estuarine dam construction during the tide event and offset during it during the discharge event.

Figure 11 shows the change in tidal properties along the West Eulsuk channel. The tidal amplitude decreased for Case 4 and the tidal distortion and asymmetry were enhanced by the interaction of both alterations compared to either the estuarine dam or the land reclamation alone. Thus, the landward tidal pumping flux increased, as explained in the previous section, by the generation of the shallow water tide (section 5.2). With the removal of the estuarine dam, the tidal deformation induced a decrease in the tidal pumping by enhancing the seaward return flow due to Stokes drift (section 5.1). In the West Eulsuk channel, the Stokes drift was weak, and the tidal pumping was dominantly landward. These results imply that while the West Eulsuk channel was affected by both the estuarine dam and land reclamation, it was more influenced by the land reclamation during the tide event.

Unlike the mechanism of tidal pumping flux in the estuary without dam construction, the flux due to Stokes transport was not changed in the estuary without estuarine dam construction and reclamation (Figure 13). Previous studies have suggested that the process of changing the current velocity by the construction of the estuarine dam is also important (Zhu et al, 2011; Ralston et al., 2019). Without the estuarine dam, the increased current velocity feels more friction, especially with the extended bottom area without land reclamation (Helaire et al., 2019). The enhanced bottom stresses generate shallow water tides causing a decreased flood dominant asymmetry (Figure 11). Therefore, the hydrodynamic change due to the estuarine dam construction interacted with the change of estuary area due to land reclamation, resulting in landward tidal pumping flux.

## 5.4 Implications for future estuary management

Estuaries around the world have undergone significant human developments due to population growth and economic growth. Accordingly, many researchers have studied the effect of such

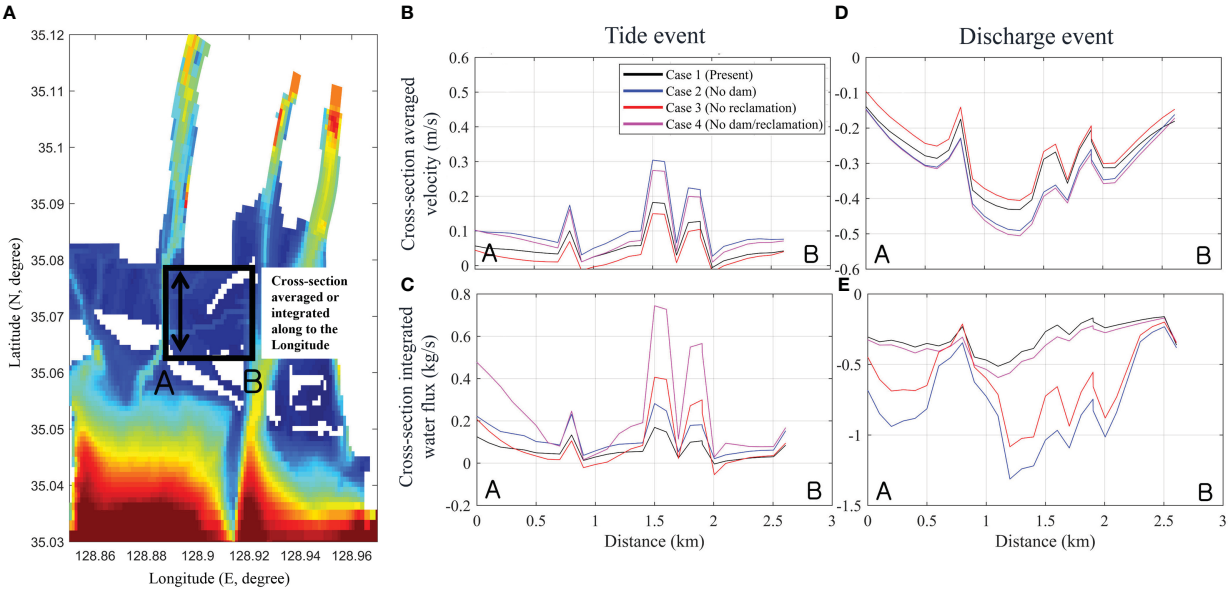


FIGURE 14
Velocity and water flux in the Central Nakdong channel. **(A)** The area where velocity and water flux were calculated. The cross-section averaged velocity and integrated water flux were calculated along the longitude (line A-B). Cross-section averaged velocity from A to B during the tide event from the Nakdong Estuarine dam **(B)** and during the dam discharge event **(D)**. Negative is westward velocity. Cross-section integrated water flux from A to B during the dam discharge event from the Nakdong Estuarine dam during the tide event **(C)** and the with dam discharge **(E)**. Negative is westward water flux.

human developments on sediment transport and morphological changes. In particular, the mean current velocity after the estuarine dam construction dramatically decreased (Kim et al., 2006; Zhu et al., 2011), resulting in a decrease in SSC (Li et al., 2012; Burchard et al., 2019). This change was mainly caused by reduced tidal prism (Zhang et al., 2015; van der Spek and Elias, 2021). After the land reclamation, the current velocity increased slightly (Yang and Qi, 2017) and tidal pumping decreased (Cheng et al., 2020). The decrease in SSC occurred dominantly due to a loss in accommodation space (Fountoukis and Nenes, 2005; van Maren et al., 2016). This study not only reflects the results of previous studies in other estuaries but also revealed new findings to improve knowledge about the influence of human developments on altered estuaries. This study suggests that even a single estuary was able to have different effects from different types of human developments depending on the location where they occur dominantly. In addition, the magnitude of changes caused by the presence of an estuarine dam and reclamation was quantitively compared, revealing that the influence of the presence of the dam had a more significant influence than that of the reclamation in the Nakdong Estuary, and the mechanisms of these changes were revealed by decomposing sediment flux. It was also found that the two human developments interacted with each other and caused intensified impacts.

These results can provide an analog for the impacts of development activities on similar estuaries of the world such as micro-tidal estuaries that has been significantly altered by human development. In particular, our results can be used in two areas: environmental impact assessment for the alteration of an estuary for industrial and residential purposes and for the restoration of altered estuaries. First, estuaries are under pressure for development in underdeveloped and developing countries. It is important to assess the impacts of development on sediment transport and morphological change in advance. Various studies have been used for these purposes (Kidd, 1995; Ballinger and Stojanovic, 2010) and this study can contribute to understanding not only the response of sediment transport but also the interaction between multiple alterations and sediment transport processes. Second, this study can provide considerable knowledge about the sedimentary responses for the restoration of an estuary where multiple human alterations already occurred. Although numerous studies have been conducted for the restoration of altered estuaries, many of them were focused on the improvement of fisheries (Bergstrom et al., 2004; Blomberg et al., 2018) and water quality problems (Smit et al., 1997; Balkis et al., 2010). On the other hand, studies on sedimentary changes for the restoration of an estuary were rare (George et al., 2012) because sedimentary and morphological responses take a relatively long period of time compared to chemical and biological responses. Numerical modeling is a suitable method to compensate for this limitation, and this study enabled us to predict the sedimentary changes that may occur after the restoration. Therefore, it is expected to contribute to efficient decision-making in restoring an estuary by quantitatively investigating the relative contribution of these alterations.

## 6 Conclusion

The goal of this study was to investigate the relative impacts of sediment transport on the estuarine dam and land reclamation in an altered Nakdong Estuary by using a numerical model and determine the change in sediment transport mechanisms by using

sediment flux decomposition. Several important conclusions can be summarized.

1. The estuarine dam construction built in the East Nakdong to control the river discharge decreased by 80% of current velocity and increased vertical stratification by limiting the saltwater intrusion. These changes caused approximately 25 mg/L of suspended sediment reduction. The sediment from river discharge was settled in the Nakdong River and spread to the estuary and offshore. On the other hand, the land reclamation mainly occurred in the West Nakdong and was responsible for relatively smaller changes to current velocity with only a 10% increase, with an increase of 9 mg/L of suspended sediment due to a decrease in sediment accommodation space (15% of water volume). The sediment included in river discharge mostly settled in the inner estuary. These changes in current velocity and SSC resulted in a large change in deposition with the estuarine dams increasing deposition 8 times more compared to land reclamation, while land reclamation reduced deposition by a factor of 1.04 times. The result of this study suggested that the presence of the estuarine dam had more influence on the increased sedimentation in the whole estuary, while the influence of land reclamation was focused to the West Nakdong where the tidal flats mainly were converted to land.

2. A five-component sediment flux decomposition was used to understand the underlying mechanisms responsible for changes to sediment transport due to the estuarine dam and land reclamation. In absence of high river discharge, the sediment flux without the estuarine dam consisted of fluxes due to mean flow, tidal pumping, estuarine circulation, and Stokes transport. After dam construction, sediment flux was simplified into only mean flow due to the change in both tidal properties and stratification, resulting in other mechanisms being diminished. The tidal pumping flux was dominant in the West Nakdong, where most of the land reclamation occurred, without influence from the river discharge. Land reclamation decreased the tidal pumping due to the change in tidal properties, while it didn't change the sediment transport mechanism in the East Nakdong. The Central Nakdong which was influenced by both the estuarine dam construction and land reclamation showed dramatically increased tidal pumping and mean flow suggesting the interaction between those alterations.

3. The sediment dynamics for the case that did not include either the estuarine dam or land reclamation was similar to that for the case that only removed the estuarine dam because the presence of the dam has a stronger impact than the land reclamation. However, the magnitude of the response of sediment dynamics and changes to the mechanisms were more amplified, indicating the importance of interactions between the estuarine dam construction and land reclamation. Especially, the high sediment flux occurred without the estuarine dam in the Central Nakdong, and the expanded Central Nakdong without land reclamation transported more sediment from the West Nakdong to the East Nakdong. The East Nakdong was mostly influenced by the estuarine dam construction and the West Nakdong was influenced more by the land reclamation ii.

## Data availability statement

The raw data supporting the conclusions of this article will be made available by the authors, without undue reservation.

## Author contributions

JC: conceptualization, data curation, formal analysis, investigation, methodology, validation, visualization, writing-original draft preparation. G-HL: conceptualization, data curation, funding acquisition, investigation, project administration, supervision, validation, writing-review and editing. CH: investigation, methodology, validation, writing-review and editing. SF: investigation, validation, visualization, writing-review and editing. NJ: data curation, investigation, visualization. All authors contributed to the article and approved the submitted version.

## Funding

This research was supported by Basic Science Research Program (2017R1D1A1B05033162) and Center for Anthropocene Studies (2018R1A5A7025409) through the National Research Foundation of Korea (NRF).

## Conflict of interest

The authors declare that the research was conducted in the absence of any commercial or financial relationships that could be construed as a potential conflict of interest.

## Publisher's note



## Supplementary material

The Supplementary Material for this article can be found online at: https://www.frontiersin.org/articles/10.3389/fmars.2023.1101658/full#supplementary-material

# References


Aubrey, D. G., Friedrichs, C. T., Aubrey, D. G., and Weishar, L. (1988). "Hydrodynamics and sediment dynamics of tidal inlets. lecture notes on coastal and estuarine studies," in *Seasonal climatology of tidal non-linearities in a shallow estuary*, vol. 29. (New York, NY: Springer). doi: 10.1007/978-1-4757-4057-8_6

Balkis, N., Müftüoğlu, E., Aksu, A., Sur, H. I., and Apak, R. (2010). The chemical oceanographic consequences of environmental restoration projects in the golden horn estuary (Marmara Sea, Turkey). *Environmen Monit. Assess* 164 (1), 67–79. doi: 10.1007/s10661-009-0875-z

Ballinger, R., and Stojanovic, T. (2010). Policy development and the estuary environment: a Severn estuary case study. *Mar. pollut. Bull.* 61 (1-3), 132–145. doi: 10.1016/j.marpolbul.2009.12.020

Barusseau, J. P., Bă, M., Descamps, C., Diop, E. S., Diouf, B., Kane, A., et al. (1998). Morphological and sedimentological changes in the Senegal river estuary after the constuction of the diama dam. *J. Afr Earth Sci.* 26 (2), 317–326. doi: 10.1016/S0899-5362(98)00014-1

Becherer, J., Flöser, G., Umlauf, L., and Burchard, H. (2016). Estuarine circulation vs tidal pumping: sediment transport in a well-mixed tidal inlet. *J. Geophys. Res. Oceans*. 121(8), 6251–6270. doi: 10.1002/2016JC011640

Bergstrom, J. C., Dorfman, J. H., and Loomis, J. B. (2004). Estuary management and recreational fishing benefits. *Coast. Manage.* 32 (4), 417–432. doi: 10.1080/08920750490487430

Blomberg, B. N., Pollack, J. B., Montagna, P. A., and Yoskowitz, D. W. (2018). Evaluating the US estuary restoration act to inform restoration policy implementation: a case study focusing on oyster reef projects. *Mar. Policy* 91, 161–166. doi: 10.1016/j.marpol.2018.02.014

Burchard, H., Lange, X., Klingbeil, K., and MacCready, P. (2019). Mixing estimates for estuaries. *J. Phys. Oceanogr* 49, 10.1175/JPO–D-18-0147.1. doi: 10.1175/JPO-D-18-0147.1

Burchard, H., Schuttelaars, H. M., and Ralston, D. K. (2018). Sediment trapping in estuaries. Ann. *Rev. Mar. Sci. Annu. Rev. Mar. Sci.* 10, 371–395. doi: 10.1146/annurev-marine-010816-060535

Buschman, F. A., Hoitink, A. J. F., van der Vegt, M., and Hoekstra, P. (2010). Subtidal flow division at a shallow tidal junction. *Water Resour. Res.* 46, W12515. doi: 10.1029/2010WR009266

Chang, J., Lee, G., Harris, C. K., Song, Y., Figueroa, S. M., Schieder, N. W., et al. (2020). Sediment transport mechanisms in altered depositional environments of the anthropocene nakdong estuary: a numerical modeling study. *Mar. Geol.* 430, 106364. doi: 10.1016/j.margeo.2020.106364

Cheng, Z., Jalon-Rójas, I., Wang, X. H., and Liu, Y. (2020). Impacts of land reclamation on sediment transport and sedimentary environment in a macro-tidal estuary. *Estuar. Coast. Shelf Sci.* 242, 106861. doi: 10.1016/j.ecss.2020.106861

Chu, N., Yao, P., Ou, S., Wang, H., Yang, H., and Yang, Q. (2022). Response of tidal dynamics to successive land reclamation in the lingding bay over the last century. *Coast. Eng* 173, 104095. doi: 10.1016/j.coastaleng.2022.104095

de Jonge, V. N., Schuttelaars, H. M., van Beusekom, J. E. E., Talke, S. A., and de Swart, H. E. (2014). The influence of channel deepening on estuarine turbidity levels and dynamics, as exemplified by the ems estuary. *Estuarine Coast. Shelf Sci.* 139, 46–59. doi: 10.1016/j.ecss

Díez-Minguito, M., Baquerizo, A., de Swart, H. E., and Losada, M. A. (2014). Structure of the turbidity field in the guadalquivir estuary: analysis of observations and a box model approach. *J. Geophys. Res. Oceans* 119 (10), 7190–7204. doi: 10.1002/2014JC010210

Dyer, K. R. (1997). *Estuaries: a physical introduction* (New York: John Wiley & Sons).

Eidam, E., Sutherland, D. A., Ralston, D. K., Conroy, T., and Dye, B. (2020). Shifting sediment dynamics in the coos bay estuary in response to 150 years of modification. *J. Geophys. Res. Oceans* 126, 10.1029/2020JC016771. doi: 10.1029/2020JC016771

Eyre, B., Hossain, S., and Mckee, L. (1998). A suspended sediment budget for the modified subtropical Brisbane river estuary, Australia. *Estuarine Coast. Shelf Sci.* 47 (4), 513–522. doi: 10.1006/ecss.1998.0371

Figueroa, S. M., Lee, G., Chang, J., and Jung, N. W. (2022b). Impact of estuarine dams on the estuarine parameter space and sediment flux decomposition: idealized numerical modeling study. *J. Geophys. Res. Oceans* 127 (5), e2021JC017829. doi: 10.1029/2021JC017829

Figueroa, S. M., Son, M., and Lee, G. (2022a). Effect of estuarine dam location and discharge interval on estuarine hydrodynamics, sediment dynamics, and morphodynamics. *Front. Mar. Sci.*, 2168. doi: 10.3389/fmars.2022.1035501

Fountoukis, C., and Nenes, A. (2005). Continued development of a cloud droplet formation parameterization for global climate models. *J. Geophys. Res.* 110, D11212. doi: 10.1029/2004JD005591

French, P. W. (2001). *Coastal defenses: processes, problems and solutions* (Oxfordshire, UK: Routledge). doi: 10.4324/9780203187630

Gao, J., Li, J., Wang, H., Bai, F., Cheng, Y., and Wang, Y. (2012). Rapid changes of sediment dynamic processes in yalu river estuary under anthropogenic impacts. *Int. J. Sediment Res.* 27 (1), 37–49. doi: 10.1016/S1001-6279(12)60014-6

Gao, G. D., Wang, H. W., and Bao, X. W. (2018). The impacts of land reclamation on suspended-sediment dynamics in jiaozhou bay, qingdao, China. *Estuar. Coast. Shelf Sci.* 206, 61–75. doi: 10.1016/j.ecss.2017.01.012

Gao, G. D., Wang, H. W., Bao, X. W., Song, D., Lin, X. P., and Qiao, L. L. (2014). Land reclamation and its impact on tidal dynamics in jiaozhou bay, qingdao, China. *Estuar. Coast. Shelf Sci.* 151, 285–294. doi: 10.1016/j.ecss.2014.07.017

George, D. A., Gelfenbaum, G., and Stevens, A. W. (2012). Modeling the hydrodynamic and morphologic response of an estuary restoration. *Estuaries coasts* 35 (6), 1510–1529. doi: 10.1007/s12237-012-9541-8

Geyer, W. R., and MacCready, P. (2014). The estuarine circulation. *Annu. Rev. Fluid Mech.* 46 (1), 175–197. doi: 10.1146/annurev-fluid-010313-141302

Grasso, F., and Le Hir, P. (2019). Influence of morphological changes on suspended sediment dynamics in a macrotidal estuary: diachronic analysis in the seine estuary (France) from 1960 to 2010. *Ocean Dyn* 69, 83–100. doi: 10.1007/s10236-018-1233-x

Grasso, F., Verney, R., Le Hir, P., Thouvenin, B., Schulz, E., Kervella, Y., et al. (2018). Suspended sediment dynamics in the macro tidal seine estuary (France): 1. numerical modeling of turbidity maximum dynamics. *J. Geophys. Res. Oceans* 123, 558–577. doi: 10.1002/2016JC012638

Guerry, A. D., Ruckelshaus, M. H., Arkema, K. K., Bernhardt, J. R., Guannel, G., Kim, C.-K., et al. (2012). Modeling benefits from nature: using ecosystem services to inform coastal and marine spatial planning. *Intl J. Biodivers. Sci Ecosys Serv Manag.* 8 (1-2), 107–121. doi: 10.1080/21513732.2011.647835

Guo, L., van der Wegen, M., Roelvink, J. A., and He, Q. (2014). The role of river flow and tidal asymmetry on 1-d estuarine morphodynamics. *J. Geophys. Res. Earth Surf* 119 (11), 2315–2334. doi: 10.1002/2014JF003110

Hansen, D. V., and Rattray, M.Jr. (1966). *Gravitational circulation in straits and estuaries* (Washington: University of Washington, Department of Oceanography, Seattle).

Helaire, L. T., Talke, S. A., Jay, D. A., and Mahedy, D. (2019). Historical changes in lower Columbia river and estuary floods: a numerical study. *J. Geophys. Res. Oceans* 124 (11), 7926–7946. doi: 10.1029/2019JC015055

Jia, L., Pan, S., and Wu, C. (2013). Effects of the anthropogenic activities on the morphological evolution of the modaomen estuary, pearl river delta, China. *China Ocean Eng.27* 6), 795–808. doi: 10.1007/s13344-013-0065-1

Jung, N. W., Lee, G., Jung, Y., Figueroa, S. M., Lagamayo, K. D., Jo, T.-C., et al. (2021). MorphEst: an automated toolbox for measuring estuarine planform geometry from remotely sensed imagery and its application to the south Korean coast. *Remote Sens* 13 (330), 33. doi: 10.3390/rs13020330

Kidd, S. (1995). Planning for estuary resources: the Mersey estuary management plan. *J. Environ. Plan Manage.* 38 (3), 435–442. doi: 10.1080/09640569512968

Kim, J. (2011). The history of nakdong river development and the foundation of folklore. *J. Kor Folk Soc* 54, 99–128. doi: G704-000983.2011.54..009

Kim, S., Ahn, J., Jung, K., Lee, K., Kwon, H., Shin, D., et al. (2017). Contamination assessment of heavy metals in river sediments (For the surface sediments from nakdong river). *J. Korean Soc Environ. Eng* 33 (4), 460–473. doi: 10.15681/KSWE.2017.33.4.460

Kim, T. I., Choi, B. H., and Lee, S. W. (2006). Hydrodynamics and sedimentation induced by large-scale coastal developments in the keum river estuary, Korea. *Estuar. Coast. Shelf Sci.* 68 (3-4), 515–528. doi: 10.1016/j.ecss.2006.03.003

Li, L., Guan, W., Hu, J., Cheng, P., and Wang, X. (2018). Responses of water environment to tidal flat reduction in xiangshan bay: part I hydrodynamics. *Estuar. Coast. Shelf Sci.* 206, 10.1016/j.ecss.2017.11.003. doi: 10.1016/j.ecss.2017.11.003

Li, P., Yang, S. L., Milliman, J. D., Xu, K. H., Qin, W. H., Wu, C. S., et al. (2012). Spatial, temporal, and human-induced variations in suspended sediment concentration in the surface waters of the Yangtze estuary and adjacent coastal areas. *Estuar. Coast. Shelf Sci.* 35 (5), 1316–1327. doi: 10.1007/s12237-012-9523-x

Liang, H., Kuang, C., Olabarrieta, M., Song, H., Ma, Y., Dong, Z., et al. (2018). Morphodynamic responses of caofeidian channel-shoal system to sequential large-scale land reclamation. *Cont Shelf Res.* 165, 10.1016/j.csr.2018.06.004. doi: 10.1016/j.csr.2018.06.004

Luan, H. L., Ding, P. X., Wang, Z. B., Ge, J. Z., and Yang, S. L. (2016). Decadal morphological evolution of the Yangtze estuary in response to river input changes and estuarine engineering projects. *Geomorphology* 265, 21–23. doi: 10.1016/j.geomorph.2016.04.022

Miles, J. (1961). On the stability of heterogeneous shear flows. *J. Fluid Mech.* 10, 496–508. doi: 10.1017/S0022112061000305

Moftakhari, R. H., Jay, D., and Talke, S. A. (2016). Estimating river discharge using multiple-tide gauges distributed along a channel. *J. Geophys. Res. Oceans* 121, n/a–n/a. doi: 10.1002/2015JC010983

Morris, R., and Mitchell, S. (2013). Has loss of accommodation space in the Humber estuary led to elevated suspended sediment concentrations? *J. Front. Constr Eng* 2, 1–9.

Park, H. B., and Lee, G. (2016). Evaluation of ADCP backscatter inversion to suspended sediment concentration in estuarine environment. *Ocean Sci. J.* 51, 1–17. doi: 10.1007/s12601-016-0010-3

Ralston, D. K., Talke, S., Geyer, W. R., Al-Zubaidi, H. A., and Sommerfield, C. K. (2019). Bigger tides, less flooding: effects of dredging on barotropic dynamics in a highly modified estuary. *J. Geophys. Res. Oceans* 124 (1), 196–211. doi: 10.1029/2018JC014313

Richardson, L. F. (1920). The supply of energy from and to atmospheric eddies. *Proc. R. Soc* 97, 354–373. doi: 10.1098/rspa.1920.0039

Savenije, H. H. G., Toffolon, M., Haas, J., and Veling, E. J. M. (2008). Analytical description of tidal dynamics in convergent estuaries. *J. Geophys. Res. Oceans* 113, https://doi. doi: 10.1029/2007JC004408

Scully, M., and Friedrichs, C. (2007). Sediment pumping by tidal asymmetry in a partially mixed estuary. *J. Geophys. Res.* 112, 10.1029/2006JC003784. doi: 10.1029/2006JC003784

Shin, H. J., Lee, G., Kang, K., and Park, K. (2019). Shift of estuarine type in altered estuaries. *Anthropocene Coasts* 2 (1), 145–170. doi: 10.1139/anc-2018-0013

Smit, H., van der Velde, G., Smits, R., and Coops, H. (1997). Ecosystem responses in the Rhine-meuse delta during two decades after enclosure and steps toward estuary restoration. *Estuaries* 20 (3), 504–520. doi: 10.2307/1352610

Sommerfield, C., and Wong, K. (2011). Mechanisms of sediment flux and turbidity maintenance in the Delaware estuary. *J. Geophys. Res.* 116, 10. doi: 10.1029/2010JC006462

Song, D., Wang, X., Zhu, X., and Bao, X. (2013). Modeling studies of the far-field effects of tidal flat reclamation on tidal dynamics in the East China seas. *Estuar. Coast. Shelf Sci.* 133, 147–160. doi: 10.1016/j.ecss.2013.08.023

Stanev, E. V., Brink-Spalink, G., and Wolff, J. O. (2007). Sediment dynamics in tidally dominated environments controlled by transport and turbulence: a case study for the East Frisian wadden Sea. *J. Geophys. Res.* 112, C04018. doi: 10.1029/2005jc003045

van der Spek, A. J. F., and Elias, E. P. L. (2021). Half a century of morphological change in the haringvliet and grevelingen ebb-tidal deltas (SW Netherlands) - impacts of large-scale engineering 1964-2015. *Mar. Geol* 432, 106404. doi: 10.1016/j.margeo.2020.106404

van Maren, D. S., Beemster, J. G. W., Wang, Z. B., Khan, Z. H., Schrijvershof, R. A., and Hoitink, A. J. F. (2023). Tidal amplification and river capture in response to land reclamation in the Ganges-Brahmaputra delta. *Catena* 220, 106651. doi: 10.1016/j.catena.2022.106651

van Maren, D. S., Oost, A., Wang, Z. B., and Vos, P. (2016). The effect of land reclamations and sediment extraction on the suspended sediment concentration in the ems estuary. *Mar. Geol.* . 376, 147–157. doi: 10.1016/j.margeo.2016.03.007

van Maren, D. S., van Kessel, T., Cronin, K., and Sittoni, L. (2015b). The impact of channel deepening and dredging on estuarine sediment concentration. *Cont Shelf Res.* 95, 1–14. doi: 10.1016/j.csr.2014.12.010

van Maren, D. S., Winterwerp, J. C., and Vroom, J. (2015a). Fine sediment transport into the hyper-turbid lower ems river: the role of channel deepening and sediment-induced drag reduction. *Ocean Dyn* 65, 589–605.

Van Rijn, L. C. (2011). Analytical and numerical analysis of tides and salinities in estuaries; part I: tidal wave propagation in convergent estuaries. *Ocean Dyn* 61, 1719–1741. doi: 10.1007/s10236-011-0453-0

Walther, R., Schaguene, J., Hamm, L., and David, E. (2012). COUPLED 3D MODELING OF TURBIDITY MAXIMUM DYNAMICS IN THE LOIRE ESTUARY, FRANCE. *Coast. Eng Proc.* 1 (33), 22. doi: 10.9753/icce.v33.sediment.22

Warner, J. C., Sherwood, C. R., Signell, R. P., Harris, C., and Arango, H. G. (2008). Development of a three-dimensional, regional, coupled wave, current, and sediment-transport model. *Comput. Geosci* 34, 1284–1306. doi: 10.1016/j.cageo.2008.02.012

Williams, J. R., Dellapenna, T. M., and Lee, G. (2013). Shifts in depositional environments as a natural response to anthropogenic alterations: nakdong estuary, south Korea. *Mar. Geol.* 343, 47–61. doi: 10.1016/j.margeo.2013.05.010

Williams, J. R., Dellapenna, T. M., Lee, G., and Louchouarn, P. (2014). Sedimentary impacts of anthropogenic alterations on the yeongsan estuary, south Korea. *Mar. Geol.* 357, 256–271. doi: 10.1016/j.margeo.2014.08.004

Williams, J. R., Lee, G., Shin, H. J., and Dellapenna, T. M. (2015). Mechanism for sediment convergence in the anthropogenically altered microtidal nakdong estuary, south Korea. *Mar. Geol.* 369, 79–90. doi: 10.1016/j.margeo.2015.08.004

Winterwerp, J. C., and Wang, Z. B. (2013). Man-induced regime shifts in small estuaries–I: theory. *Ocean Dyn* 63 (11-12), 1279–1292. doi: 10.1007/s10236-013-0662-9

Wolanksi, E., and Elliott, M. (2015). *Estuarine ecohydology: an introduction* (Amsterdam: Elsevier Science).

Yang, Y., and Chui, T. F. M. (2017). Hydrodynamic and transport responses to land reclamation in different areas of semi-enclosed subtropical bay. *Cont Shelf Res.* 143, 54–66. doi: 10.1016/j.csr.2017.06.008

Yoon, E. C., and Lee, J. S. (2008). Characteristics of seasonal variation to sedimentary environment at the estuary area of the nakdong. *J. Korean Soc Coast. Ocean Eng* 20 (4), 372–389.

Yoon, H., Park, S., Lee, I., and Kim, H. (2008). Spatiotemporal variations of seawater quality due to the inflow of discharge from nakdong river barrage. *J. Korean Soc Mar. Environ. Energy* 11, 78–85.

Zhang, L., Wu, B., Yin, K., Li, X., Kia, K., and Zhu, L. (2015). Impacts of human activities on the evolution of estuarine wetland in the Yangtze delta from 2000 to 2010. *Environ. Earth Sci.* 73 (1), 435–447. doi: 10.1007/s12665-014-3565-2

Zhu, C., Guo, L., van Maren, D. S., Wang, Z. B., and He, Q. (2021). Exploration of decadal tidal evolution in response to morphological and sedimentary changes in the Yangtze estuary. *J. Geophys. Res. Oceans* 126 (9), e2020JC017019. doi: 10.1029/2020JC017019

Zhu, Q., Wang, Y. P., Ni, W., Gao, J., Li, M., Yang, L., et al. (2016). Effects of intertidal reclamation on tides and potential environmental risks: a numerical study for the southern yellow Sea. *Environ. Earth Sci.* 75 (23), 1472. doi: 10.1007/s12665-016-6275-0

Zhu, Z., Zhang, J., Wu, Y., Zhang, Y., Lin, J., and Liu, S. (2011). Hypoxia off the changjiang (Yangtze river) estuary: oxygen depletion and organic matter decomposition. *Mar. Chem.* 159, 108–116. doi: 10.1016/j.marchem.2011.03.005

# Frontiers in Marine Science

**Explores ocean-based solutions for emerging global challenges**

The third most-cited marine and freshwater biology journal, advancing our understanding of marine systems and addressing global challenges including overfishing, pollution, and climate change.

---

## Discover the latest Research Topics

See more →

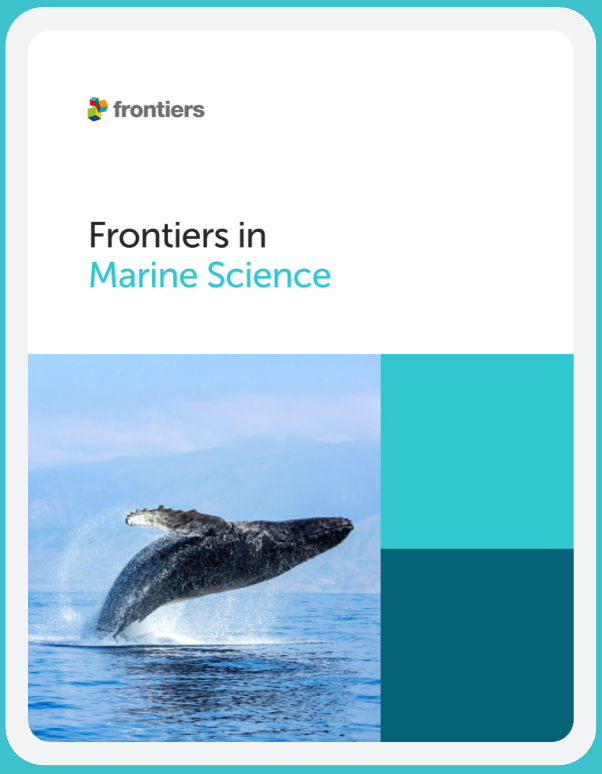


**Frontiers**

Avenue du Tribunal-Fédéral 34
1005 Lausanne, Switzerland
frontiersin.org

**Contact us**

+41 (0)21 510 17 00
frontiersin.org/about/contact